Reconfigurable metasurfaces for wavefronts control - Application to the generation of complex beams

Rui Feng

THESE DE DOCTORAT

NNT : 2022UPAST066

Reconfigurable metasurfaces for wavefronts control - Application to the generation of complex beams

Métasurfaces reconfigurables pour le contrôle des fronts d'onde – Application à la génération de faisceaux complexes

Thèse de doctorat de l'université Paris-Saclay et de l'université Xidian

École doctorale n° 575, Electrical, Optical, Bio-physics and Engineering (EOBE)
Spécialité de doctorat : Electronique et Optoélectronique, Nano- et Microtechnologies
Graduate School : Sciences de l'ingénierie et des systèmes. Référent : Faculté des sciences d'Orsay

Thèse préparée dans l'unité de recherche **Centre de Nanosciences et de Nanotechnologies** (Université Paris-Saclay, CNRS), sous la direction de **Shah Nawaz BUROKUR**, Maître de Conférences/HDR, la co-direction de **Hailin ZHANG**, Professeur, le co-encadrement de **Badr Eddine RATNI**, Maître de Conférences

Thèse soutenue à Xi'an, le 30 mai 2022, par

Rui FENG

Composition du Jury

Anatole LUPU DR CNRS, C2N, Université Paris-Saclay	Président
Guido VALERIO MCF/HDR, GeePs, Sorbonne Université	Rapporteur & Examinateur
Jiafu WANG Professeur, Air Force Engineering University	Rapporteur & Examinateur
Wenchi CHENG Professeur, Xidian University	Examinateur
Anne-Claire LEPAGE MCF, LTCI, Télécom Paris	Examinatrice
Hongyu SHI Professeur Associé, Xi'an Jiaotong University	Examinateur
Shah Nawaz BUROKUR MCF/HDR, LEME, Université Paris Nanterre	Directeur de thèse
Hailin ZHANG Professeur, Xidian University	Co-Directeur de thèse

Acknowledgements

By writing here, my doctoral study will come to an end. I will leave this campus life but my heart is overwhelmed with reluctance. Thanks to all people who accompanied me during my doctoral study.

I would like to express my sincere gratitude towards Prof. Hailin Zhang who is my supervisor at Xidian University. He not only provides me good learning and scientific research environment, but also detailed care and guidance. Prof. Hailin Zhang has a profound professional knowledge foundation and rigorous attitude to academic problems. He always considers the matter in our shoes and respects students' choices. When we are puzzled, he gives us direction and supports our decision. No matter what problems we meet, he always keeps patient and listens to our problems, and then he does his best to help us. I want to sincerely appreciate all guidance and assistance provided by Professor Zhang in these six years.

I would like to express my deep appreciation to my supervisor at University Paris Saclay, Prof. Shah Nawaz Burokur. When I had the idea to go abroad for the joint training, he gave me the opportunity to join his group and the trust he put on me and my abilities. His responsibility for students and rigorous attitude on research really impressed me. During my two-year study in France, he helped me a lot on various themes such as measurement setups and manuscript improvement. I learned a lot from him. Under his tutoring, I solved many difficulties and finally became a doctoral student with independent research capability. His valuable advice and support were necessary for the results I have got.

I would like to offer my special thanks to Prof. Jianjia Yi. I have still clearly remembered that I received his phone call on September 30, 2016, and he invited me to join his project. He is very kind to me and gives me a great deal of help, whether in life, thought, or scientific research. With his recommendation, I then could successfully join the group of Prof. Shah Nawaz Burokur. This would not have come true without his great help. Faced with my limited funds to support my scientific research in the first year in France, he still stuck to using money from his project to subsidize me. When I met the problem that I could not find an appropriate guarantor for a CSC scholarship for the second year in France, he helped me as a guarantor without hesitation. I will never forget this great kindness.

I would also like to thank Prof. Badreddine Ratni, who is a warm-hearted and vigorous

scientific researcher. During my two-year study life in France, he also has supported me a lot in learning and life. I sincerely appreciate his assistance. I would also like to express my thank to Prof. André de Lustrac and Prof. Anatole Lupu for their kindness and invitation to parties, which made my time in France filled with warmth and fun.

I would also like to sincerely thank the members of the ISN State Key Laboratory, Prof. Wenchi Cheng, Prof. Yi Liu, Prof. Zhiyuan Ren, Prof. Xiaofeng Lu, Prof. Meixia Hu, Prof. Fan Qin, Dr. Longwei Liu, Dr. Shuhua Liu, Dr. Liping Liang, and so on. Thank you for your help and guidance in my research, study, and life.

I want to thank all the colleagues at Xidian University, Zhuohui Yao, Danyang Yu, Xin Zhao, Menglan Lin, Pu Yang, Jianyu Wang, Haiyue Jing, Yuzhou Fu, Tianyang Zhang, and so on. Thanks for your support. All of you are important to me in my life.

I would like to thank my friends met in France, Dr. Yulong Fan, Dr. Cheng Zhang, Dr. Binbin Wang, Yaoyao Liang, Quan Yue, Zhengrui Tu, Lei Han, Zehao Pei, Lisha Wan, Xiaoyu Gu, Yingge Zhang, and so on.

In addition, I also want to thank Xiandan Zhang, who will be my wife. In this more than six years relationship, she was always accompanying me. Although we had quarrels, we always accompanied each other.

Finally, I would like to say a big thank you to my parents and family. I appreciate their upbringings and devotion to me for so many years. My parents are farmers and have not graduated from primary school. They have spent half of their life to raise their four kids. Thank you my dear parents. I wish you are always healthy and happy. I will continue to work hard and help my parents and family.

I hope the persons I missed here can accept my appreciation. Thank you for all your help.

Summary (In French)

Comment contrôler de manière flexible les ondes électromagnétiques a toujours été l'objectif recherché. Depuis les débuts de la société humaine, différents matériaux naturels ont été utilisés pour contrôler la lumière. Les propriétés électromagnétiques des matériaux naturels dépendent de la composition moléculaire et de la disposition des matériaux constitutifs, tandis que les métamatériaux sont généralement composés de cellules unitaires artificielles périodiques ou quasi-périodiques sub-longueur d'onde, qui peuvent réaliser des fonctions au-delà des possibilités offertes par les matériaux naturels. Par conséquent, de nombreux phénomènes physiques exotiques, tels que la réfraction négative et l'effet Doppler inverse, peuvent être réalisés à l'aide de métamatériaux. Les métamatériaux ont été largement utilisés dans de nombreux domaines, devenant un outil essentiel pour concevoir de nouveaux dispositifs fonctionnels.

Le développement des métamatériaux électromagnétiques a connu un processus allant des métamatériaux tridimensionnels aux métasurfaces ultraminces bidimensionnelles, puis aux métasurfaces reconfigurables. En 1967, le scientifique soviétique V. G. Veselago avait émis pour la première fois l'hypothèse d'avoir un matériau avec simultanément une permittivité négative et une perméabilité négative, et avait prédit des phénomènes physiques exotiques que les matériaux conventionnels n'ont pas, tels que la réfraction négative et le décalage de fréquence Doppler inversé. Ensuite, le physicien théoricien J. B. Pendry de l'Imperial College de Londres a proposé d'utiliser des fils métalliques disposés périodiquement et des résonateurs fendus pour obtenir une permittivité négative et une perméabilité négative, respectivement. En 2001, le professeur D. R. Smith de l'Université de Duke aux États-Unis a observé avec succès le phénomène de réfraction négative dans des expériences grâce à la combinaison de fils métalliques et de résonateurs fendus. Cette percée historique a suscité l'enthousiasme des chercheurs pour les métamatériaux. Cependant, en raison du volume encombrant et des pertes élevées des métamatériaux, les chercheurs ont réduit la dimension des métamatériaux à un plan bidimensionnel, c'est-à-dire une métasurface. Les métasurfaces présentent les avantages d'un poids léger, d'un profil plat, de faibles pertes et d'une intégration facile et elles permettent de manipuler la phase, l'amplitude et la polarisation des ondesélectromagnétiques incidentes.

Le travail historique dans le domaine de la métasurface est la loi de Snell généralisée proposée par l'équipe de F. Capasso de l'Université de Harvard. En introduisant des phases

abruptes spécifiques sur la métasurface, l'onde incidente peut être réfractée ou réfléchie dans des directions arbitraires. Cette loi a ensuite été largement utilisée dans la conception de dispositifs micro-ondes pour le contrôle de fronts d'ondes. Cependant, ces structures micro-ondes sont toujours soumis à des fonctions limitées, qui ne peuvent pas répondre aux besoins réels des systèmes de communications. Le concept de métasurfaces reconfigurables a donc été proposé. Pour réaliser les métasurfaces reconfigurables, des composants accordables doivent être intégrés dans les métasurfaces, telles que les diodes PIN, les diodes varactors, les systèmes micro-électro-mécaniques (MEMS) et les cristaux liquides. Les métasurfaces reconfigurables, d'une part, héritent de la capacité des métasurfaces passives à contrôler la phase, l'amplitude et la polarisation des ondes électromagnétiques. D'autre part, les métasurfaces reconfigurables peuvent être digitalisées pour une meilleure intégration. En modifiant le stimulus externe du composant accordable, la résonance peut être ajustée, et ensuite la fonction de la métasurface peut être modifiée de manière flexible. En 2014, T. J. Cui de l'Université Southeast en Chine a proposé le concept de métamatériaux codés et digitaux. Il a utilisé des codes binaires pour décrire des métamatériaux au lieu de milieux effectifs équivalents, et a proposé le concept de métamatériaux programmables. Son équipe de recherche a également utilisé des métasurfaces reconfigurables pour réaliser la manipulation dynamique des ondes planes dans la bande de fréquences micro-ondes. Le mécanisme de reconfigurabilité a favorisé l'application des métasurfaces dans les systèmes pratiques.

Dans cette thèse, des métasurfaces reconfigurables sont conçues à l'aide de diodes varactors. Deux métasurfaces reconfigurables fonctionnant en mode réflexion sont utilisées pour l'étude de la génération dynamique et de la manipulation de faisceaux électromagnétiques complexes. La première métasurface est une métasurface reconfigurable unidimensionnelle (1D), qui peut réaliser la modulation de phase uniquement le long d'une direction fixe et qui a une couverture de phase d'environ 320°. La deuxième métasurface est une métasurface reconfigurable bidimensionnelle (2D), dont la cellule unitaire peut être adressée individuellement et elle présente une couverture de phase de près de 340°. Les faisceaux complexes étudiés dans cette thèse comprennent le rayonnement directionnel d'ondes électromagnétiques diffractées à partir d'une ouverture sub-longueur d'onde, les faisceaux d'Airy et de Bessel d'ordre zéro non-diffractants, les faisceaux de vortex transportant un moment cinétique orbital et l'imagerie holographique électromagnétique. La théorie de base des faisceaux complexes est introduite, la distribution de phase des métasurfaces nécessaires pour générer des faisceaux complexes est calculée et la génération

et la manipulation de ces faisceaux électromagnétiques sont réalisées par les métasurfaces reconfigurables conçues.

Dans un premier temps, la génération et la manipulation de faisceaux d'ondes électromagnétiques directionnels à travers une fente sub-longueur d'onde est réalisée. Pour cela, la fente est flanquée de métasurfaces à modulation de phase. Lorsque l'onde incidente éclaire la fente sub-longueur d'onde, l'onde électromagnétique est diffractée dans toutes les directions. Une partie de l'onde électromagnétique diffractée se propage le long de la métasurface, que nous appelons onde de surface. Des études sur les métasurfaces ont permis de convertir des ondes électromagnétiques dans l'espace libre en ondes de surface. Selon le théorème de réciprocité, les ondes de surface peuvent également être converties en ondes rayonnantes se propageant dans l'espace libre en définissant un gradient de phase approprié sur la métasurface. C'est dans cette optique que la métasurface reconfigurable 1D a été utilisée. En réalisant une fente au milieu du plan de masse de la métasurface, deux parties bien distinctes de la métasurface entourent cette fente. La direction des ondes électromagnétiques rayonnées peut donc être régulée de manière flexible en modifiant la tension de polarisation appliquée à la métasurface de chaque côté de la fente. Le rayonnement directionnel à 0° au-dessus de la fente peut être obtenu en attribuant les gradients de phase symétriques sur les deux parties de la métasurface entourant la fente. Ces faisceaux directionnels à 0° sont également obtenus sur une large bande de fréquences allant de 9 GHz à 12 GHz, ce qui démontre l'agilité en fréquence de la métasurface conçue. Pour réaliser les rayonnements directionnels dépointés à 20°, 30° et 40°, des gradients de phase asymétriques sont appliqués sur les deux parties de la métasurface entourant la fente. Le faisceau directionnel d'ondes électromagnétiques à travers une fente sub-longueur d'onde a des applications importantes dans les capteurs champ proche planaires, les lentilles et les dispositifs holographiques, et peut être étendu aux antennes à ondes de fuite micro-ondes.

Ensuite, en exploitant les deux métasurfaces reconfigurables (1D et 2D), la génération et la manipulation de faisceaux non-diffractants d'Airy et de Bessel d'ordre zéro sont étudiés. L'étude paramétrique des faisceaux Airy 1D est réalisée en utilisant la métasurface reconfigurable 1D. La trajectoire de propagation parabolique des faisceaux Airy peut être ajustée en modifiant le paramètre de la fonction Airy. Les propriétés de non-diffraction, d'auto-courbure et d'auto-reformation du faisceau Airy sont vérifiées en simulation et en mesure. En outre, le faisceau Airy 1D est généré sur une large bande de fréquences allant de 9 GHz à 12 GHz. En superposant une distribution de phase calculée pour une déviation de faisceau à la phase originale du faisceau Airy 1D, l'angle de lancement initial du faisceau

d'Airy peut être ajusté à volonté. Une étude paramétrique des faisceaux non-diffractants de type Bessel d'ordre zéro (mais en une dimension) est également réalisée avec la métasurface reconfigurable 1D. La manipulation dynamique de la zone de non diffraction est réalisée en modifiant l'angle d'inclinaison qui intervient dans le calcul du profil de phase. Deux principaux modes de champ lointain de faisceaux de Bessel d'ordre zéro ont été mis en évidence. Lorsque l'angle d'inclinaison de la distribution de phase des est faible, un seul faisceau dans le plan longitudinal apparaît en champ lointain. Inversement, un diagramme de rayonnement avec deux faisceaux apparait dans le plan longitudinal en champ lointain lorsque l'angle d'inclinaison de la distribution de phase est relativement plus grand. Ces deux modes de rayonnement s'expliquent d'une part par le chevauchement décroissant de deux faisceaux Gaussiens avec la distance de propagation et d'autre part par la taille de la tache de chaque faisceau Gaussien qui augmente avec la distance de propagation. Les propriétés de non diffraction et d'auto-reformation du faisceau de Bessel d'ordre zéro sont vérifiées par l'ouverture à mi-puissance du lobe principal et en plaçant un obstacle métallique dans le trajet de propagation du lobe principal. En superposant une distribution de phase de déviation de faisceau à celui du faisceau de Bessel, sa direction peut être modifié.

De plus, les faisceaux d'Airy 2D ont également été étudiés en utilisant la métasurface reconfigurable 2D. Sa génération a été réalisée sur une bande de fréquences allant de 8,5 GHz à 9,5 GHz. De la même façon, l'étude paramétrique des faisceaux de Bessel d'ordre zéro 2D est réalisée et les propriétés observées dans le cas du faisceau de Bessel à une dimension ont pu être vérifiées. Lorsque l'angle d'inclinaison de la phase du faisceau de Bessel est faible, il y a un seul faisceau en champ lointain. Lorsque l'angle d'inclinaison de la phase est grand, une structure en forme d'anneau apparaît en le champ lointain. Mais, ceci n'implique pas qu'il s'agit d'un faisceau vortex, car le faisceau de Bessel d'ordre zéro ne porte pas de moment cinétique orbital. Les faisceaux non-diffractants présentent l'avantage de maintenir le lobe principal constant sur la distance de non diffraction par rapport aux faisceaux gaussiens dont le faisceau est diffracté lors de la propagation dans l'espace libre. Par conséquent, les faisceaux non-diffractants peuvent avoir des applications pratiques concrètes dans les domaines de la transmission d'énergie sans fil et de la détection.

La métasurface reconfigurable 2D a aussi été exploitée pour l'étude et la génération de faisceaux vortex transportant un moment cinétique orbital (OAM), y compris les faisceaux de Laguerre-Gaussien, les faisceaux vortex focalisés et les faisceaux vortex non-diffractant. Dans le cas des faisceaux Laguerre-Gaussien, quatre modes OAM différents ont pu être générés en attribuant des profils de phase judicieusement calculés à la métasurface

reconfigurable. Les faisceaux Laguerre-Gaussien sont intrinsèquement divergents et l'effet de divergence est proportionnel au mode OAM. En superposant un profil de phase de focalisation aux faisceaux Laguerre-Gaussien, les faisceaux vortex focalisés avec différents modes OAM ont été générés avec succès. De même, en superposant un profil de phase du faisceau non-diffractant de Bessel d'ordre zéro aux faisceaux Laguerre-Gaussien, des faisceaux vortex non-diffractants avec différents modes OAM sont réalisés. Le faisceau vortex non-diffractant présente d'ailleurs le plus petit angle de divergence par rapport aux deux autres types de faisceaux de vortex mentionnés ci-dessus. De plus, la génération simultanée de quatre faisceaux vortex dirigés dans des directions différentes est également étudiée. Le faisceau vortex transportant le moment cinétique orbital offre un nouveau degré de liberté pour la manipulation d'ondes électromagnétiques, ce qui devrait encore améliorer la capacité des canaux de transmission et présente des perspectives d'application potentielles dans les futurs systèmes de communications.

Pour finir, l'algorithme pondéré de Gerchberg-Saxton (GSW) a été utilisée pour réaliser une imagerie holographique électromagnétique avec la métasurface reconfigurable 2D. Les images holographiques composées de 2, 3 et 4 points focaux avec des amplitudes uniformes sont réalisées dans différents plans d'imagerie à la fréquence de fonctionnement de 8,5 GHz. Ensuite, en ajustant le rapport d'énergie de chaque point focal, le codage de quantification de l'énergie dans différents canaux a pu être réalisé. Théoriquement, le codage d'énergie de n'importe quel nombre de bits peut être réalisé selon l'algorithme GSW. Le codage d'énergie 1 bit et 2 bits dans différents canaux a été validé numériquement et expérimentalement pour prouver le concept. Afin de vérifier davantage que le codage d'énergie est efficace pour tous les canaux dans l'espace libre, deux configurations ont été testées : codage d'énergie 2 bits sur une ligne droite et sur les quatre coins d'un carré. L'excellente performance du codage d'énergie 2 bits est démontrée dans deux cas. De plus, des images holographiques des nombres « 1 », « 2 » et « 3 » dans différents plans d'imagerie ont été validées à 9 GHz. De même, les images holographiques des lettres « C », « T » et « L » sont accomplies dans différents plans d'imagerie à la fréquence de fonctionnement de 9,5 GHz. Cette technologie d'imagerie holographique électromagnétique haute résolution basée sur les métasurfaces a des applications potentielles pour les communications sans fil en champ proche, l'identification par la radiofréquence et le traitement du signal.

En conclusion, plusieurs exemples de manipulation de fronts d'ondes ont été validés dans cette thèse. Ceci a été rendu possible grâce au développement et à la réalisation de métasurfaces reconfigurables. Notamment, la conversion d'ondes de surface en ondes

propagatives a été réalisée en exploitant la diffraction à travers une fente sub-longueur d'onde et une modulation de phase sur la métasurface. La génération et le contrôle dynamiques de faisceaux non-diffractants type faisceau d'Airy et de Bessel d'ordre zéro et aussi des faisceaux vortex ont aussi été réalisés. La métasurface reconfigurable 2D a pu aussi être utilisée en imagerie holographique, particulièrement en codage d'énergie multi-bits dans différents canaux. Tous ces résultats démontrent la capacité de nos métasurfaces reconfigurables à contrôler les ondes électromagnétiques. Avec le développement rapide de l'internet mobile, l'internet de tout est l'objectif ultime que l'on recherche. La reconfigurabilité des métasurfaces permettrait de connecter sans liaison filaire à divers appareils électroménagers et appareils électroniques. Grâce à la combinaison de la technologie des semi-conducteurs et des métasurfaces plates, les métasurfaces reconfigurables seront plus légères et plus faciles à intégrer et devraient être largement utilisées dans notre vie quotidienne à l'avenir.

Contents

List of figures

List of tables

List of symbols

Symbols	Names
k_{SW}	Wavenumber of the surface wave
k_t	Wavenumber in incident region
k_i	Wavenumber in refracted region
ξ	Normalized propagation distance
s	Dimensionless transverse coordinate
Ai(x)	Airy function
$J_0(x)$	Zeroth-order Bessel function of the first kind
$\lvert\cdot\rvert$	Absolute value

List of abbreviations

Abbreviations	Full names
EM	Electromagnetic waves
1D	One-dimensional
2D	Two-dimensional
OAM	Orbital angular momentum
GSW	Weighted Gerchberg−Saxton
PB	Pancharatnam-Berry
MEMS	Micro-electro-mechanical-systems
LCs	Liquid crystals
VNA	Vector network analyzer
HFSS	High frequency structure simulator
PCB	Printed circuit board
FPC	Flexible printed circuit
SPP	Surface plasmon polariton
FWHM	Full width at half maximum
CDMA	Code division multiple access
OFDM	Orthogonal frequency division multiplexing
MIMO	Multi input multi output
CGH	Computer Generated Holography
FPGA	Field-programmable gate array

General introduction

In the field of electromagnetics, how to flexibly control the characteristics of electromagnetic waves (EM) to serve the communication and electronics industries has been a very challenging research topic. The introduction of the concept of artificial metasurface provides a new idea to tailor electromagnetic waves. Metasurface, a two-dimensional artificial structure composed of subwavelength elements, can achieve the flexible manipulation of phase, magnitude, and polarization of EM waves. Nevertheless, the functionality of generally designed passive metasurfaces is limited due to the fact that the resonance of the constituents are fixed once the passive metasurface is fabricated. The narrow frequency band of operation also limits the application of passive metasurfaces. However, reconfigurable metasurfaces, where the resonance of the constituents can be adjusted by changing the external stimuli, overcome these limitations, thus making metasurfaces attracting enormous attention for potential applications in wireless communications and energy transfer. In this thesis, two kinds of reflective reconfigurable metasurfaces, a one-dimensional (1D) one and a two-dimensional (2D) one, are designed in the microwave domain by using electrical mechanism through the incorporation of varactor diodes. These two metasurfaces allow a modulation of the reflection phase, only along one axis in the case of the 1D reconfigurable metasurface and along two axes in the case of the 2D reconfigurable metasurface. While the unit cells on the 1D metasurface are controlled in a row by row manner, those of the 2D metasurface can be individually addressed. Five different applications of complex beams, including directional beaming of diffracted electromagnetic waves from a subwavelength aperture, Airy beam, zeroth-order Bessel beam, vortex beam, and holographic imaging, are explored based on these two metasurfaces. The details of the five tested applications are summarized as:

1. The first application is the directional beaming of electromagnetic waves diffracted through a subwavelength aperture. This work constitutes the first one to realize the dynamic directional beaming from a subwavelength aperture using a reconfigurable metasurface, especially in the microwave domain. The on-axis beaming of electromagnetic waves from the subwavelength aperture is realized by applying symmetric phase profiles to the two parts of the 1D reconfigurable MS surrounding the subwavelength aperture. The on-axis beaming is also performed at different working frequencies to validate the frequency agility property of the metasurface. In addition, the off-axis beaming in different directions is realized by

applying asymmetric phase profiles on the two sides of the subwavelength aperture.

2. The second application is the generation and manipulation of the diffraction-free Airy beam by applying the 1-bit coding scheme on the reconfigurable metasurfaces. Indeed, the reconfigurable metasurface can be used as a 1-bit coding metasurface by appropriately adjusting the voltage applied to the metasurface. Both the one-dimensional (1D) and two-dimensional (2D) Airy beams are dynamically generated and manipulated. Firstly, the influence of Airy function parameter on the 1D Airy beams generation is explored before validating the generation over a wide frequency band. The diffraction-free, self-bending, and self-healing properties of Airy beams are also investigated. The steering of Airy beams is studied to further show the flexible regulation ability of the designed 1D reconfigurable metasurface. Secondly, the 2D Airy beams generation is also studied and analyzed using the 2D reconfigurable metasurface. The 2D Airy beams are also generated in a wide frequency band.

3. The third application is the flexible generation and control of zeroth-order Bessel beams. Two far-field radiation modes of the zeroth-order Bessel beams are reported, which are the single beam mode for the small phase tilt angle scenario, and the dual-beam mode for the large phase tilt angle scenario. Both the 1D Bessel-like and 2D Bessel beams are explored. The arbitrary control of the diffraction-free zone is studied by using different phase configurations on the 1D metasurface. The far-field patterns of different phase configurations are explored and the reason for the difference among them is clearly explained. The diffraction-free and self-healing properties of 1D Bessel-like beams are also analyzed. Furthermore, the beam steering and flexibly control of 1D Bessel-like beams are realized. The dynamic control of diffraction-free areas of 2D Bessel beams is also explored.

4. The fourth application is the dynamic generation of vortex beams carrying orbital angular momentum (OAM). Three different types of single vortex beams radiating in the direction normal to the metasurface, including Laguerre-Gaussian beam, focusing vortex beam, and non-diffracting vortex beam, are explored. By comparing the three types of vortex beams with the same mode, the diffraction-free vortex beam is shown to have the smallest divergence angle. Then, the generation of non-diffracting vortex beam over a wide frequency band is achieved.

5. The fifth and last application considered in the thesis is the digital holographic imaging generation and multibit spatial energy modulation. The dynamic generation of holographic imaging using the modified weighted Gerchberg−Saxton (GSW) algorithm is validated using the 2D reconfigurable metasurface. Three different types of holographic

imaging, including focusing spots, Arabic numbers, and Alphabet letters, are explored at different detecting planes and operating frequencies. Besides, the multibit spatial energy modulation in different channels is proposed and validated. It is the first time that multibit spatial energy modulation in different channels is achieved.

Chapter 1 State of the art on artificial metamaterials and metasurfaces

1.1 Introduction

All along, flexible manipulation of electromagnetic waves is the dream that people are pursuing. The ability to control electromagnetic waves has been gradually improved with the deeper understanding of the theory and properties of electromagnetic waves, but this control is still quite limited due to the electromagnetic parameters of natural materials that are relatively fixed. The emergence of metamaterials extremely enhanced the ability to tailor electromagnetic waves. The field of metamaterials is a scientific breakthrough with far-reaching significance. It brings a brand-new structural method that can be utilized to design exotic devices by using artificial structures, resulting in many extraordinary physical properties.

Electromagnetic metamaterials are mainly divided into dielectric metamaterials and metal-based metamaterials. Metal-based metamaterials are the most typical structure in the development process of metamaterials. The basic idea of the metal-based metamaterial is that metal is used to design the array consisting of periodic or quasi-periodic unit structures of a certain shape. The size of the unit structure is much smaller than the wavelength of the incident electromagnetic wave, allowing the designed array to be equivalent to a uniform medium. However, dielectric metamaterials combine natural materials and equivalent dielectric theory, and they focus on the electromagnetic response of the dielectric material with specific geometry. Those distinctive electromagnetic properties caused by the specific geometry of the material itself expand the working frequency band of metamaterials. With the rapid development of communication technologies, the demand for multi-functional adjustable communication devices is increasing. Tunable devices based on the metamaterials are achieved by integrating the active components, for example, diodes, liquid crystal, graphene, phase-variable materials, ferrites, and variable-position cover layers.

A great amount of practical applications using metamaterials have been proposed in the fields of civil technology, aerospace, communication technology, and new energy technology. At present, research in metamaterials field is highly valued all over the world. For example, the American magazine 《Science》 lists metamaterials as one of the ten important scientific advances in the first decade of this century. Therefore, electromagnetic metamaterials have

become an important direction in scientific research, which are likely to become a powerful means to discover new functions of materials, to lead new directions in the industry, to improve the overall performance of materials, and to break through the bottleneck of scarce resources.

1.2 Metamaterials

1.2.1 Concept of Metamaterials

Metamaterials, which have specific properties that might not exist in natural materials, are artificial structured materials. A metamaterial is composed of sub-wavelength elements and its unique electric or magnetic property is determined by the materials and geometry of the elements instead of the arrangement of the particles. Beam control using metamaterials is generally realized by the spatial varying electromagnetic parameters (ε and μ). Therefore, a certain thickness of metamaterials is required for the manipulation of the illuminating wave, which inevitably brings loss and disadvantages of bulky size and non-negligible weight.

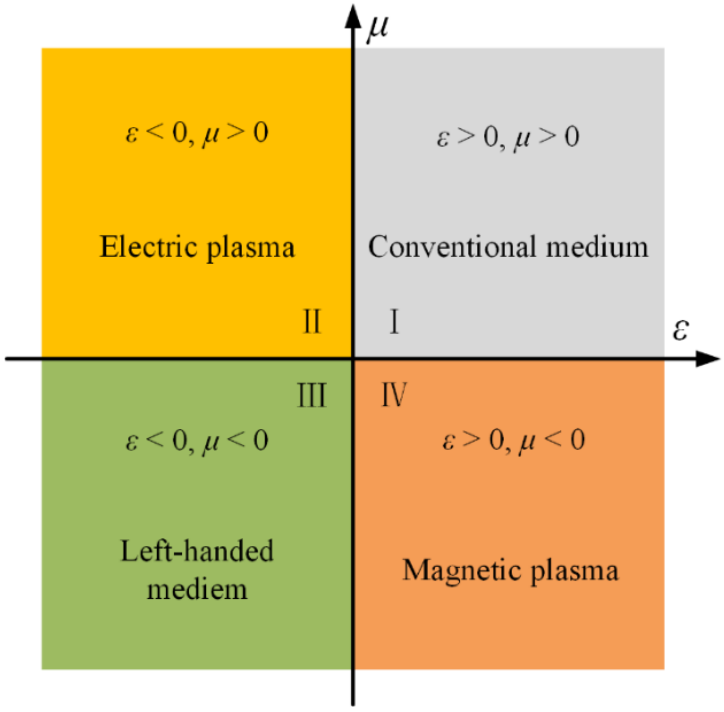

Figure 1.1 Four types of materials with different electric permittivity ε and magnetic permeability μ.

In electromagnetic theory, the fundamental electromagnetic properties of a medium can be described by the electric permittivity ε and magnetic permeability μ that determine the

interaction between the electromagnetic wave and medium. The medium can be divided into four categories according to different values of the permittivity and permeability as depicted in Figure 1-1, where the *x*-axis denotes the permittivity and *y*-axis represents the permeability. The interaction between the medium and those four different cases can be concluded from the Maxwell's equation. The material in which both the permittivity and permeability are positive is called right-handed or double positive material. Most natural materials are right-handed materials. The materials in second quadrant are epsilon-negative. Electric plasma in some natural materials exhibits the epsilon-negative characteristics in certain frequency ranges, such as precious metals at optical wavelengths and ferroelectric materials. The fourth quadrant denotes permeability-negative characteristics, which are exhibited in some optically active materials or ferrite materials. When both the permittivity and permeability are negative as in the third quadrant, the electric vector E, magnetic vector H and wave vector *k* of electromagnetic wave follow the left-handed rule.

The left-handed material that does not exist in nature was first hypothesized by V. G. Veselago in 1968[1]. However, this work did not attract enough attention at that time. In 1996, J. B. Pendry first verified the negative permittivity in microwave frequency band by designing a periodic structure built of thin wires[2]. The negative magnetic permeability[3] was realized using split ring resonators in a square array by J. B. Pendry's group in 1999. As depicted in Figure 1-2, the first metamaterial consisting of copper strips and split ring resonators was proposed by D. R. Smith and the negative index of refraction was experimental validated in 2000[4]. In 2006, J. B. Pendry proposed the transformation optics theory[5], which is based on the form invariance of Maxwell's equations and the coordinate transformation method. Electromagnetic waves can be transmitted in any desired direction by suitable designing the electric permittivity and/or magnetic permeability of the material.

Figure 1.2 Photograph of the left-handed metamaterial (LHM) sample[4].

1.2.2 Applications of Metamaterials

The proposition of transformation optics theory has greatly promoted the development of metamaterials. An extremely important role of metamaterials in recent years is that they provide an effective means for controlling the propagation of electromagnetic waves along a predetermined path. Metamaterials have attracted wide attention and passion in physics, electromagnetics, and related fields due to their exotic abilities to manipulate electromagnetic waves. Plenty of applications have been realized, such as optical illusion devices[6-10], electromagnetic wave concentrators[11-13], perfect imaging devices[14-18], super-scatters and super-absorbers[19-24], electromagnetic cavities[25-27], special waveguides[28-32], and cloaking devices[33-40].

In this section, we list several typical applications of metamaterials, such as two-dimensional (2D) electromagnetic cloaks[40], broadband high-resolution imaging lenses[41], and three-dimensional (3D) broad-angle transformation-optics lenses[42].

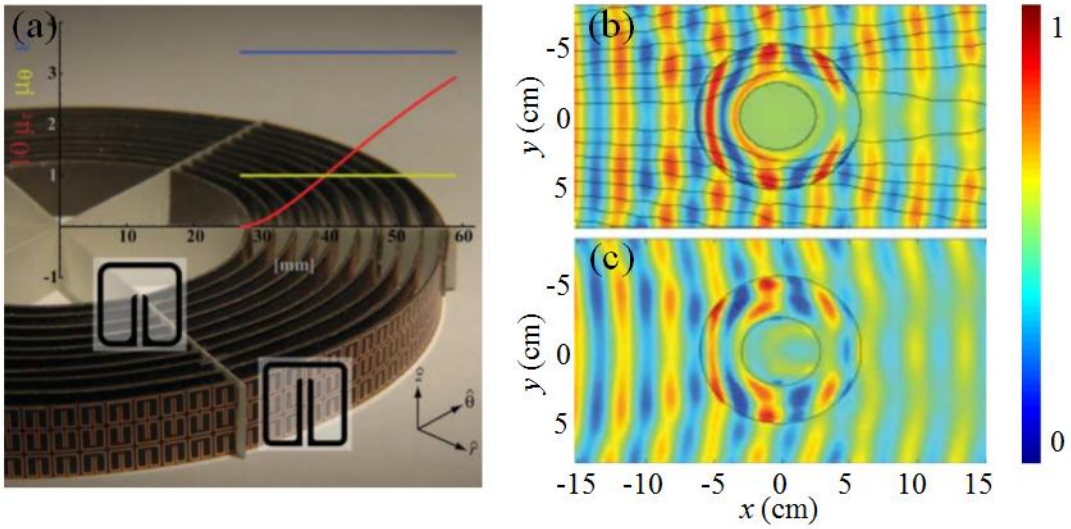

Figure 1.3 (a) 2D microwave cloak composed of SRR. (b-c) Simulation and measurement of the cloak surrounding a Cu cylinder[40].

One of the most fascinating applications of metamaterials is the invisibility cloak. When an incident wave illuminates an object, the wave is scattered and changes its original propagating trajectory, rendering it visible and detectable. However, metamaterials can be used to realize gradient refractive index. The wave illuminating the metamaterial-based cloaked object can propagate along the pre-designed trajectory with the elaborately refractive index distribution, such that the incident wave propagates forward around the object instead of being scattered. Following the published work where an invisibility cloak

was possible in theory[5] based on the transformation optics, the first practical realization of two-dimensional cloak was achieved using artificially structured SRR metamaterials and transformation optics concept by J. B. Pendry *et al.* in 2006 as presented in Figure 1-3[40]. This device can 'hide' a copper cylinder from an incident wave, with reduced scattering and reduced shadow.

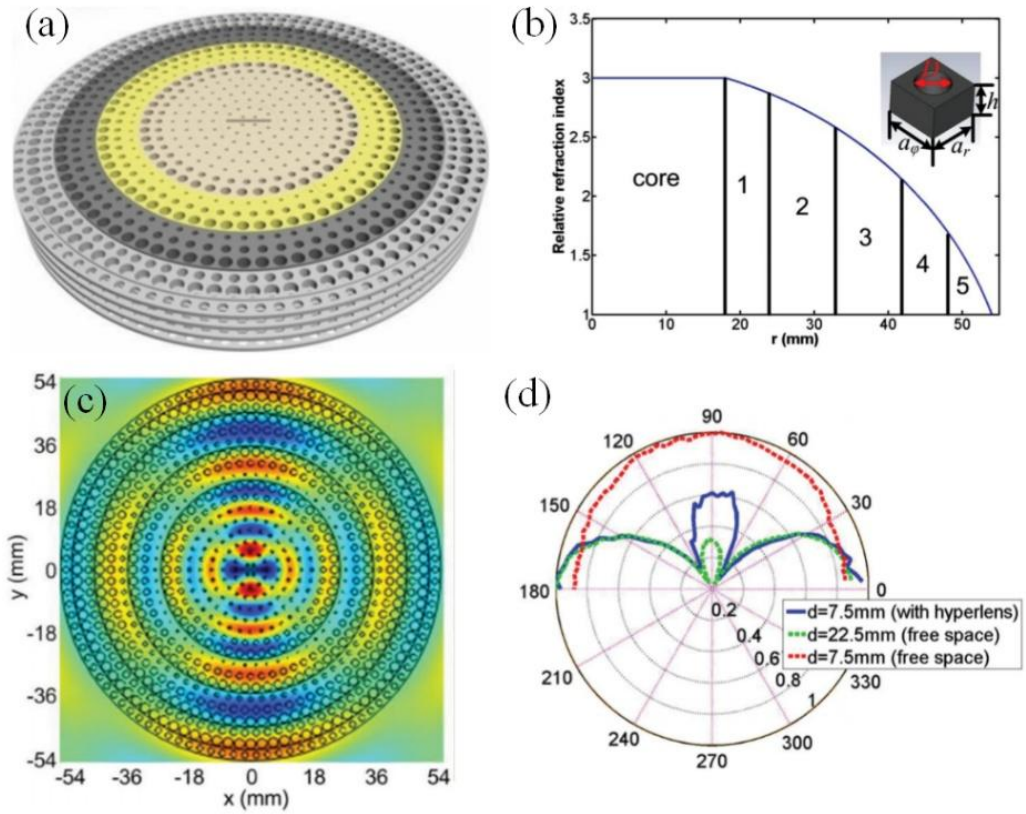

Figure 1.4 (a) Schematic of the broadband high-resolution imaging lens. (b) Curve of refractive index with respect with to *r*. (c) Simulated result inside the lens. (d) Measured result along the observation circle with radius of 60 mm[41].

By using the theory of transformation optics, W. X. Jiang *et al.* proposed a broadband all-dielectric magnifying lens to realize far-field subwavelength imaging with high resolution[41]. The imaging lens is constructed by multiple dielectric layers with drilled holes in them as shown in Figure 1-4. Due to the low-loss and broadband characteristics of the dielectric layers, the operating frequency of this high-resolution imaging lens spans from 7 to 10 GHz. The subwavelength space between two objects can be amplified by this imaging lens such that a magnified image is produced in the far-field region, where a conventional imaging system can then be used to detect the two different objects. This high-resolution

imaging mechanism may also open an avenue to the high-resolution optical imaging.

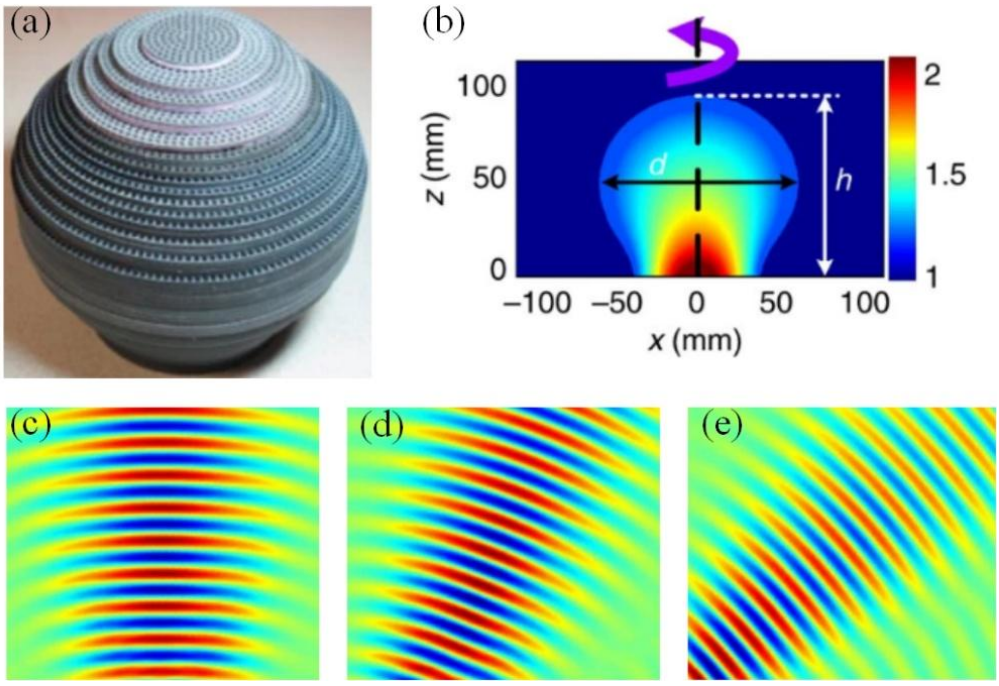

Figure 1.5 (a) Photography of the 3D broad-angle transformation-optics lens. (b) Refractive index distribution in *xoz* plane. (c)-(e) Measured results with the position change of feeding source at 15 GHz[42].

In 2010, T. J. Cui *et al.* proposed a 3D transformation-optics lens used for beam scanning in a large angle range in radio frequency band[42]. This 3D lens was constructed by non-resonant metamaterials with inhomogeneous holes as displayed in Figure 1-5(a). Figure 1-5(b) shows the refractive distribution of the 3D lens in *xoz* plane and the 3D lens is constructed by the rotation of this distribution around the *z*-axis. By changing the position of the feeding source, the beam can be defelcted to different angles. The outstanding performance of this 3D lens is validated for different polarizations over a wide frequency band ranging from 12.4 to 18 GHz. It has a potential in the application of high-gain antenna with larger scanning angles.

1.3 Metasurfaces

Even if metamaterials can realize specific properties that may not exist be possible with conventional materials, they suffer from the problems of bulky size, low efficiency, and complex manufacturing. The emergence of ultra-thin metasurface, the 2D counterparts of

metamaterials, has attracted a great deal of research interests owing to its high efficiency and simple manufacturing properties. Metasurfaces can be constructed by only dielectric (all-dielectric metasurfaces) or combination of both dielectric and metal. In this thesis, we focus on the metal-based metasurfaces.

Metasurfaces have the specific abilities of flexibly regulating the amplitude, phase, and polarization of illuminating electromagnetic waves. Compared to wave control of metamaterials that need a certain thickness, the phase and wavefront manipulation is achieved by the abrupt phase change for the metasurface within an ultrathin dimension. The abrupt phase change of the metasurface comes from the resonance effect of its subwavelength unit cell that is usually composed of subwavelength resonators. When the electromagnetic wave illuminates the metasurface composed of metal resonators, the resonator is excited to produce surface electromagnetic waves, causing the charge oscillation in the unit cell, which is called the surface plasmon resonance phenomenon. Then, the discontinuous phase between the incident and outgoing electromagnetic waves is constructed.

1.3.1 Classification of metasurfaces

The landmark work of establishing the new electromagnetic artificial metasurface concept is the definition of generalized Snell's law and the accurate regulation of electromagnetic wave proposed by Capasso's group from Harvard University in 2011[43]. By adding a predesigned phase gradient on the metasurface, the direction of illuminating wave can be flexibly controlled. Since then, plenty of fascinating devices for the tailoring of electromagnetic waves has been proposed including polarization convertors[44-48], beam deflectors[49-53], perfect absorbers[54-57], and imaging holography[58-62]. According to the working mechanism, the metasurface can be classified into several categories, including plasmonic resonant phase type metasurfaces, geometric-phase metasurfaces using Pancharatnam-Berry (PB) phase principle, and Huygens' principle based metasurfaces.

Plasmonic resonant phase type metasurfaces are composed of electric dipoles elements. The abrupt phase of the illumination wave passing through metasurface is caused by the scattering of the element. The period of the element is smaller than the operating wavelength to avoid the diffraction effect. The typical structure is the V-shaped and C-shaped nano-antennas. Capasso et al. elaborately designed a 'V' type unit structure that is used to realize the abrupt phase change in the interface as shown in Figure 1-6(a)[43]. The anomalous reflection and refraction of the incident wave were realized by using the metasurface consists

of 'V' type elements based on the proposed generalized Snell's law. In 2013, W. Zhang realized the anomalous refraction using a transmissive metasurface based on C-shape split-ring resonator units whose phase can be adjusted by changing the opening angle of the split as presented in Figure 1-6(b)[63]. Besides, according to the Babinet's principle, the complementary element, such as the subwavelength apertures in a metallic film, can be used to realize a metasurface. This type of metasurface is relatively simple in design and have the advantages of high tolerance to fabrication errors.

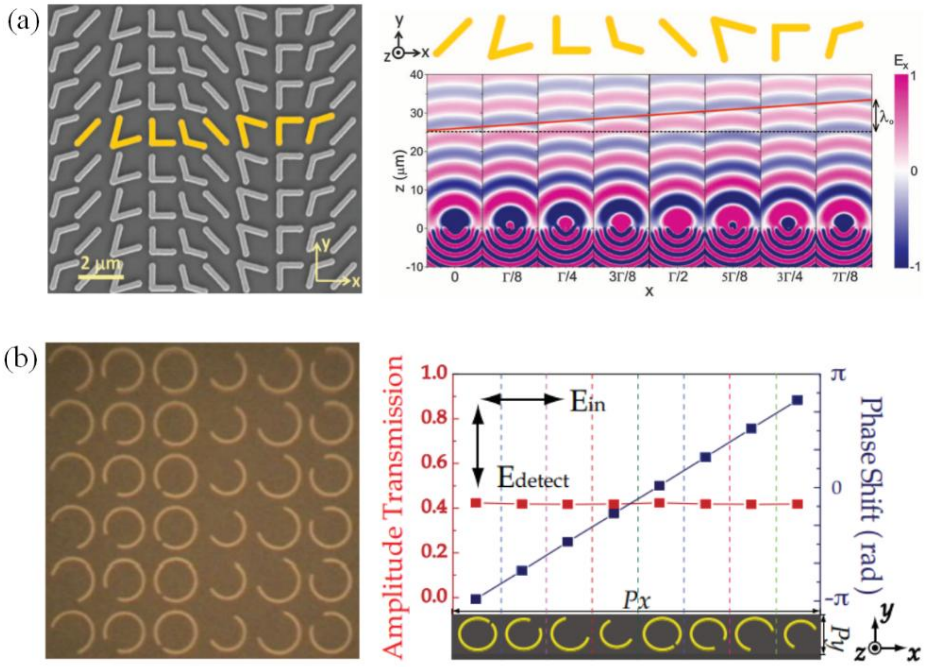

Figure 1.6 (a) Sample of the metasurface composed of V type structures. The simulation of the scattered electric field for the supercell consists of V type structures[43]. (b) Photograph of the metasurface consisting of C-shaped structures. The phase coverage of the C-shaped structures is approximately 2π[63].

The geometric-phase metasurface depends on the geometric phase, also known as the PB Phase. In 1956, S. Pancharatnam first proposed the geometric phase effect[64], which shows that the movement of polarized light along a closed path produces an additional phase determined by the area subtended by the path on the Poincaré sphere. In 1984, M.V. Berry from the University of Bristol introduced the similar geometric phase in the case of cyclic and adiabatic transformation[65]. Since that, the concept of geometric phase was soon applied to other cases with parameter variations[66]. Due to those two pioneering works, the geometric phase was named after two scientists, Pancharatnam-Berry Phase. The PB phase

is derived from the spatial control of the polarization state of the circularly polarized incident wave interacting with the element of metasurface. Such a phase can be adjusted by rotating the element around its origin and the PB phase φ with respect to the orientation angle θ satisfies $\varphi = 2\theta$. Therefore, it is convenient to construct a metasurface using the PB phase principle by rotating the element without changing its dimension under the circularly polarized illumination.

The Huygens' metasurface consists in simultaneous electric dipole and magnetic dipole in the constitutive element. The maximum phase change caused by the electric dipole or the magnetic dipole are both π without taking the polarization into consideration. When the two corresponding resonant frequencies of electric dipole and magnetic dipole are exactly the same, the phase coverage of 2π can be achieved. In 2013, Grbic designed a Huygens' metasurface, which provides both electric and magnetic polarization currents to generate prescribed wave fronts as shown in Figure 1-7[49]. The efficiency of the focusing and deflection of the incident wave can reach nearly 100% in such type of metasurfaces. Since the Huygens' metasurface can be designed as a transmissive one with extremely high efficiency, it has real potential interests in antenna systems.

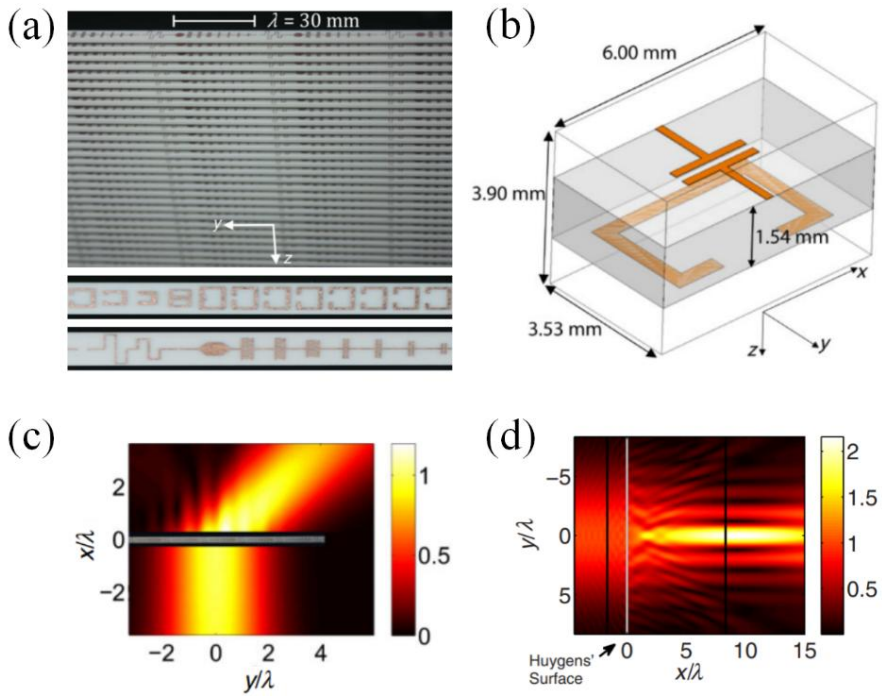

Figure 1.7 Huygens' metasurface with nearly 100% efficiency. (a) Image of the fabricated Huygens' metasurface. (b) Model of the unit cell. (c)-(d) Results of beam deflection and Bessel beam generation[49].

1.3.2 Reconfigurable metasurfaces

The ability of a metasurface to manipulate electromagnetic waves is imposed by the geometry of the metallic pattern on the dielectric substrate. After the metasurface is fabricated, its function of wave manipulation is fixed and cannot be changed. Besides, the resonance of passive metasurface is not tunable such that it is always subjected to a limited working frequency band and functionality. Therefore, many efforts are devoted to propose a reconfigurable metasurface that can dynamically manipulate EM waves and work in a wide frequency band. Various tuning mechanisms can be applied to metasurface for the reconfigurability, such as thermal[67–71], optical[72–80], mechanical stretching[81–90], Micro-electro-mechanical-systems (MEMS)[91-95], and electrical[96-101].

The thermally metasurface can be realized by combining passive metasurface with thermally sensitive materials like phase-change materials and superconductors. In 2009, Driscoll *et al.* realized a thermally reconfigurable metasurface consists of metallic split-ring resonators placed on a VO_2 substrate as shown in Figure 1-8(a) and experimentally demonstrated 20% resonance frequency shift by changing temperature as displayed in Figure 1-8(b)[67].

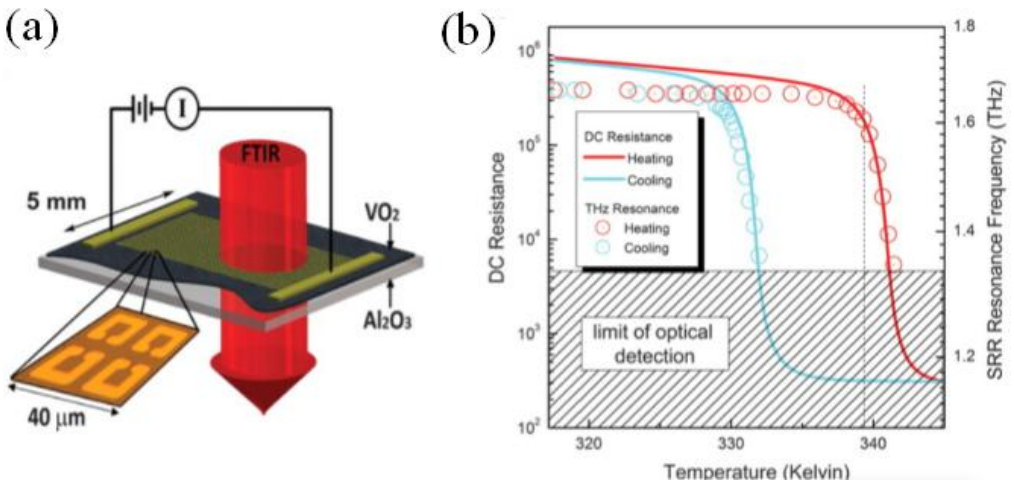

Figure 1.8 (a) The VO_2-hybridized thermally tunable metasurface. (b) Curves of the DC resistance and SRR resonance frequency versus temperature[67].

The optical reconfigurable metasurface means that the metasurface is typically constructed with meta-atoms involving optically sensitive materials whose conduction carriers is sensitive to external optical pumping. M. R. Shcherbakov *et al.* realized the optical reconfigurable metasurface formed by Silica/GaAs/AlGaO nanopillars grown on a bulk

GaAs substrate as presented in Figure 1-9[80]. The absolute reflection magnitude of the optical reconfigurable metasurface can be modulated by 35% and the recovery tome is about 6 ps.

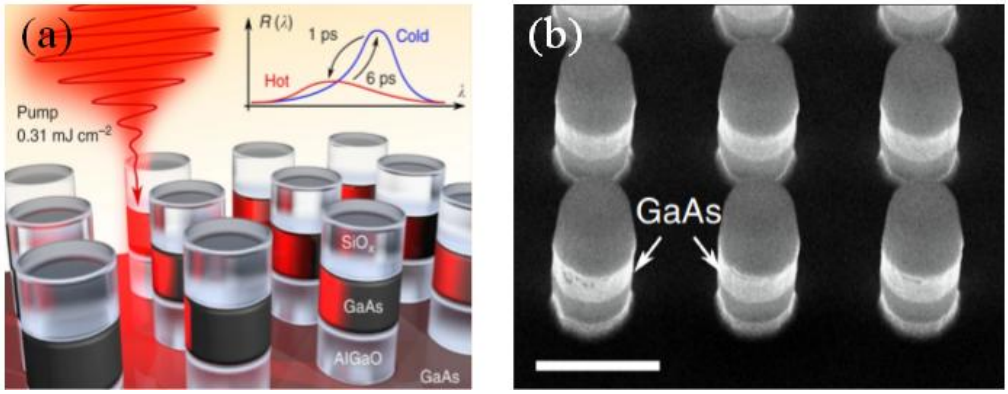

Figure 1.9 (a) Ultrafast all-optical tuning of Mie-resonant mode in a GaAs involved dielectric optically tunable metasurfaces. (b) Sample of the metasurface[80].

The dynamically control of the resonance of microelectromechanical systems (MEMS) based metasurfaces can be realized by changing the geometrical structure of the meta-molecules. The pioneering work on MEMS metasurface is done by Tao *et al.* who proposed a THz thermomechanical switchable metasurface in 2009[91]. The MEMS metasurface is composed of metallic split ring structures arranged on the biomaterials cantilevers as shown in Figure 1-10. Those SSRs can be flipped out the metasurface plane with the external stimuli, which result in a change of the responses of the metasurface.

In this thesis, we focus on microwave reconfigurable metasurfaces using the electrical control mechanism. The electrically tunable metasurface can be realized by integrating the meta-atom with different electrically sensitive components such as PIN diode, varactor diode, graphene, liquid crystal, and semiconductor. PIN diodes are generally used to switch from a reflection state to a transmission state. In 1996, T. K. Chang incorporated a switched PIN diode into the FSS elements to realize the control of the frequency response[102]. The fundamental principle of this FSS element design is to make a geometry difference of elements between the two states of PIN diode, thus the significant difference of frequency response can be achieved. A switchable electromagnetic wave reflector/absorber incorporating PIN diodes for different polarizations was proposed by Zhu B. *et al.* in 2010 [103]. Two sets of electric-LC resonators are employed with orthogonal orientation on the top layer of the unit cell such that it can respond to both EM polarizations of the incident waves.

The PIN diode is used to connect the two electric-LC resonators with same orientation for the resonance control propose. The nearly total reflection of this metasurface can be converted to total absorption for a particularly polarized incident wave by switching the state of the corresponding PIN diodes incorporated in metasurface.

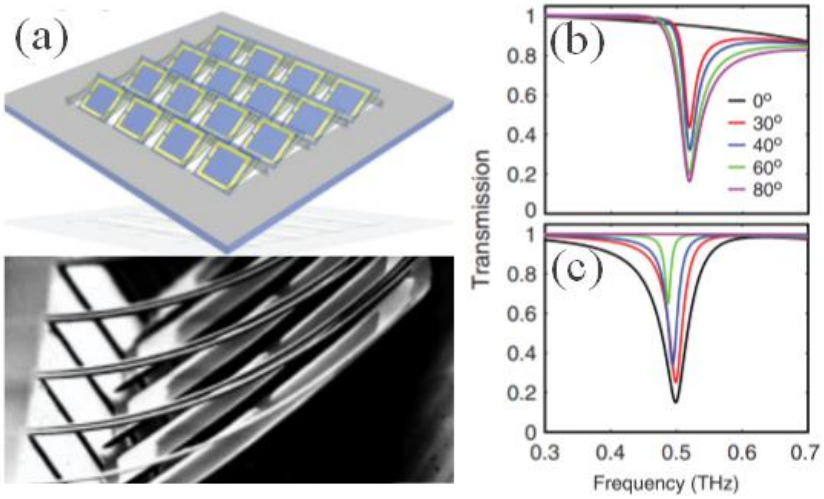

Figure 1.10 (a) Mechanically switchable metasurfaces. (b) Magnetic response of various bending angles. (c) Electric response of various bending angles[91].

Figure 1-11 shows a 2-bit programmable metasurface employing PIN diodes[104]. Two PIN diodes are embedded in the gap between the two strips and hexagonal of unit cell to realize the 2-bit control. Interestingly, this metasurface can realize 4-bit or even arbitrary higher-bit by the time-domain coding approach. The 360° equivalent phase coverage can be obtained using this method.

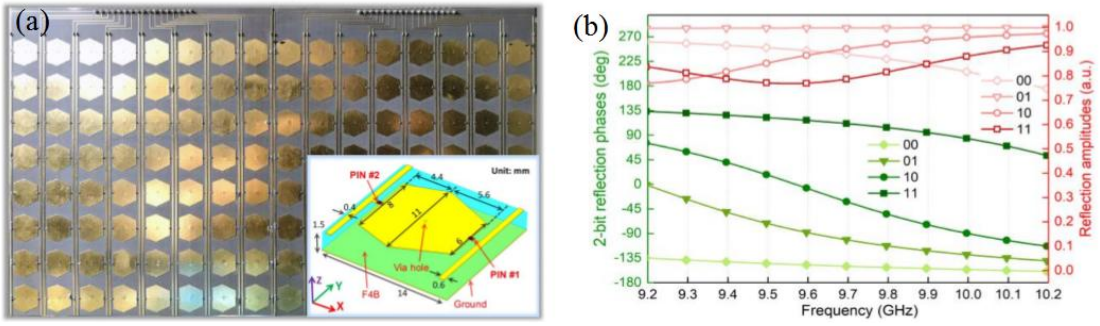

Figure 1.11 (a) Photograph of the 2 bit-programable metasurface integrated with PIN diodes. (b) Amplitude and phase response of the meta-atom[104].

In the Figure 1-12, an active metasurface having the ability to control the reflections, transmissions, and polarizations of incident wave is designed. The periodic metallic short wires are printed on the top layer while the PIN diode is embedded on the bottom layer. The measured transmission amplitude T_{xy} and reflection amplitude R_{yy} are presented in Figures 1-12(d)-(e), where both T_{xy} and R_{yy} are higher than 0.9 at 2.1 GHz. The working state of diode is switched from on to off by adjusting the applied bias voltage, and the reflection with the same polarization of incident wave (co-polarized reflection) is switched to a transmission with orthogonal polarization (cross-polarized transmission) at around 2.1 GHz[105].

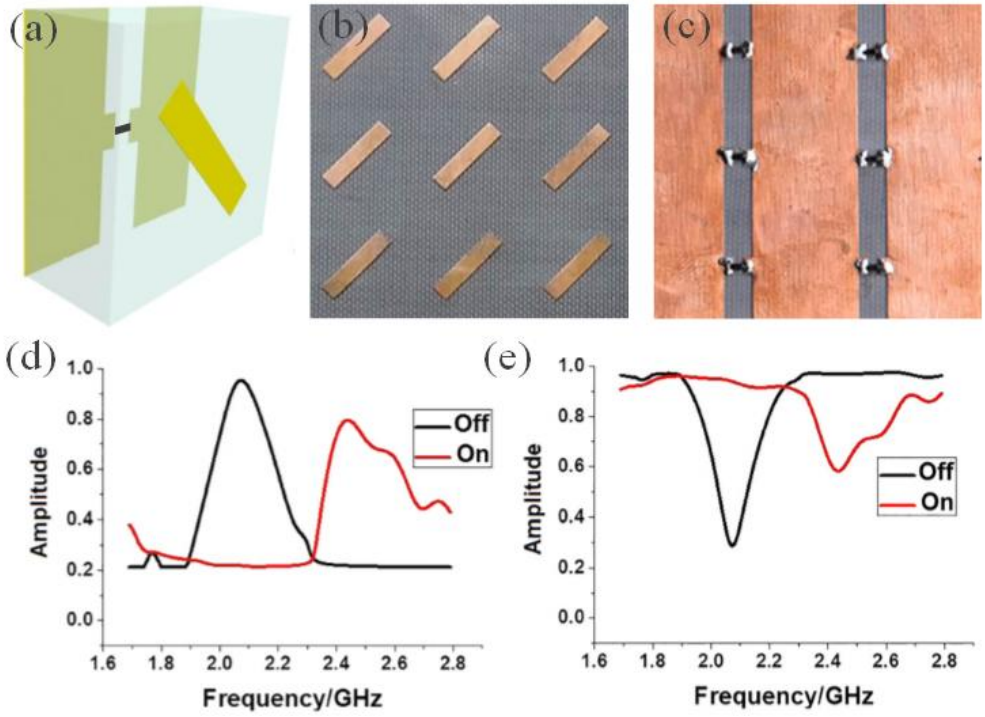

Figure 1.12 (a) Schematic illustration of unit cell integrated PIN diode. (b)-(c) Top layer and bottom layer of the fabricated active metasurface. (d) Measured amplitude of T_{xy} for the two states of PIN diode. (e) Measured amplitude of R_{yy} for the two states of PIN diode[105].

Varactor diode is another component that is frequently adopted in designing reconfigurable metasurface at microwave frequency domain. In the microwave field, varactor diodes are usually incorporated in the meta-atoms such that the capacitance can be controlled by varying the DC bias voltages. As depicted in Figure 1-13(a), an electronically reflector based on metasurface incorporated with varactor diodes is proposed by D. F. Sievenpiper *et al.* in 2003[106]. The varactor diode is integrated in the gap between the neighboring two patches. Half of the patches are connected to the ground and the other half

are attached to the bias line. The fabricated metasurface is depicted in Figure 1-13(b). The resonance frequency can be adjusted by changing the bias voltage applied to the varactor diode. The beam steering based on this active metasurface is realized by a tunable phase gradient on the metasurface by changing the applied bias voltage. Figure 1-13(c) shows the measured radiation patterns and the steering angles of the beams are 0°, 20°, and 40°, respectively.

Figure 1-14(a) shows a FP cavity consists of a tunable metasurface as a partially reflecting surface and an array of wideband sources[107]. The varactor diode is inserted in the gap between the two strips on the bottom layer. The fabricated electronically reconfigurable metasurface is presented in Figure 1-14(b). The resonance frequency and phase characteristics of the metasurface can be adjusted by varying the dc bias voltage applied on the metasurface. The experimental measurements are performed in an anechoic chamber and the related results are depicted in Figure 1-14(c), where the far-field intensity maps versus operating frequency and elevation angle are plotted and the radiation patterns versus elevation angle are also displayed. It is clear that the FP cavity can realize its property in a wide frequency band ranging from 1.9 to 2.31 GHz.

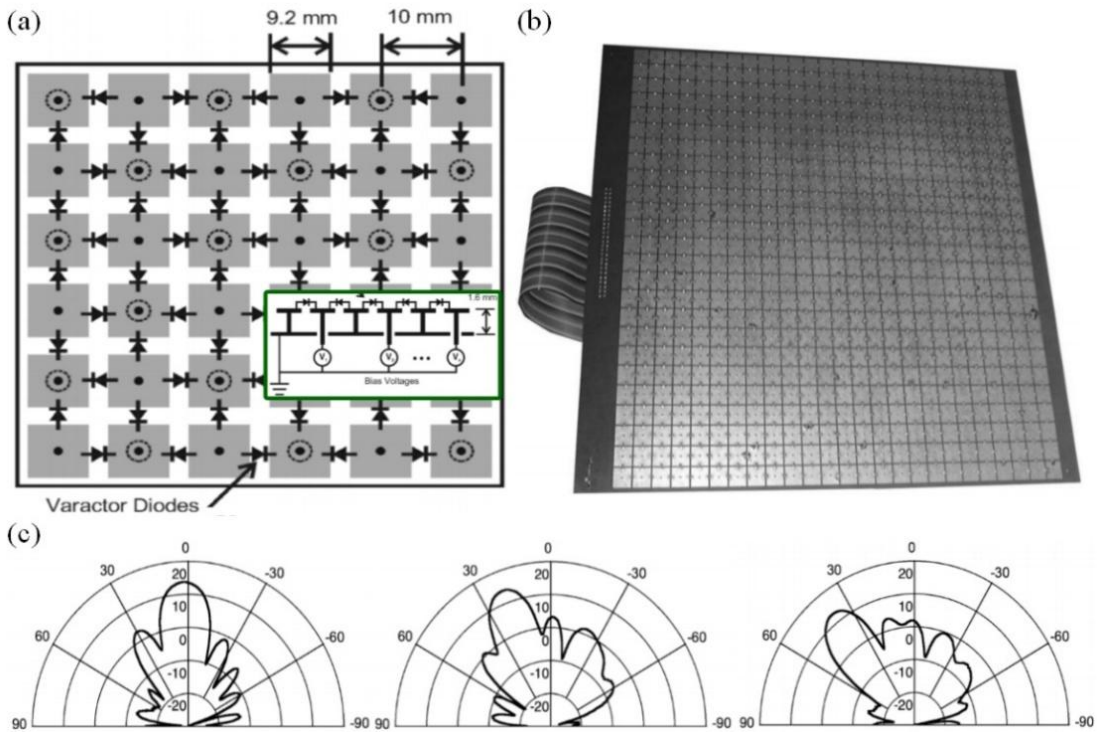

Figure 1.13 (a) Schematic of the structure of the active metasurface. The insect shows the cross section of the metasurface. (b) Photograph of the metasurface. (c) Beam steering at 0°, 20°, and 40°[106].

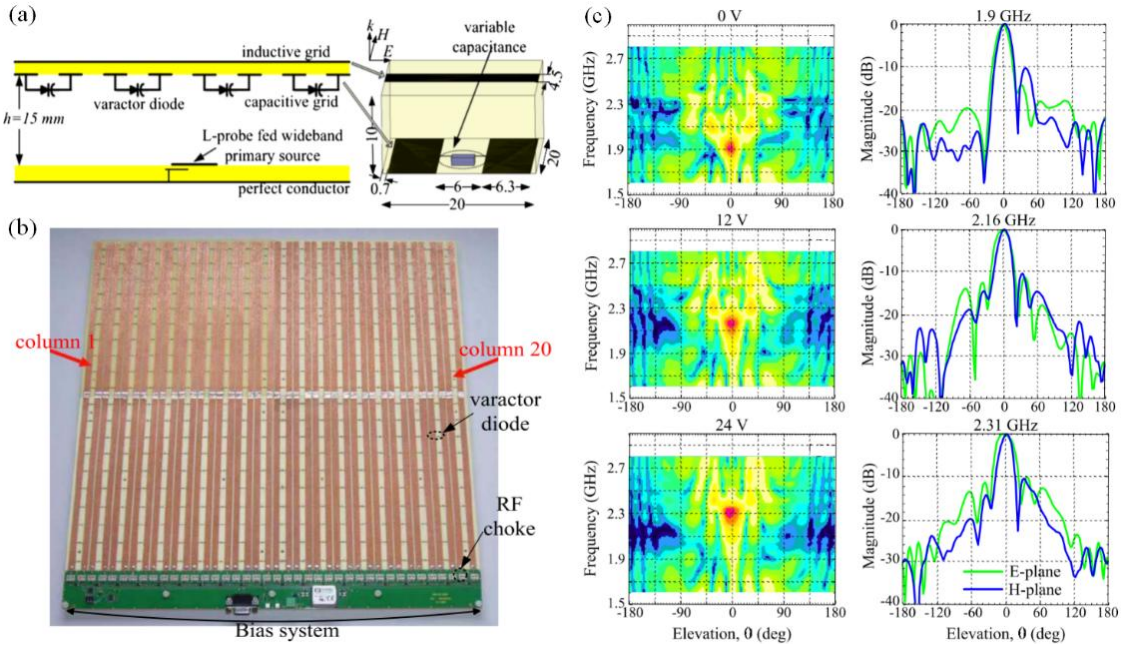

Figure 1.14 (a) Schematic view of the FP cavity. (b) Photograph of the electronically reconfigurable metasurface reflector. (c) Measured far-field intensity maps and radiation patterns[107].

Figure 1-15 shows a reconfigurable Huygens' metalens, whose unit cell includes three varactor diodes which are used for the electric and magnetic resonance[108]. The phase and amplitude response of the unit cell at 6.9 GHz are depicted in the insert of Figure 1-15(a), where we can observe an approximately 360° phase coverage for the capacitance values varying from 0.05 to 3 pF. This reconfigurable Huygens' metalens can achieve the focusing of EM waves in a pre-designed trace and the two focal spots simultaneously in a 2D space with a high efficiency by adjusting the bias voltage. The experimental measurements of the magnitude distribution of the focal spot moving along a trace of letter 'N' are implemented in the elaborately designed setup as illustrated in Figure 1-15(b). The corresponding measured magnitude distributions of focal spot at different positions of the trace of letter 'N' are presented in Figure 1-15(c), where three voltage distributions applied on the Huygens' metalens are shown in the right column.

Graphene, a two-dimensional material with only one atomic layer, can be used to realize an electrically reconfigurable metasurface in microwave, THz and mid-IR regimes [109-113] due to its wide-range electrically tunable conductivity. The first gate-controlled active graphene-assisted metasurface was proposed and experimental verified by Lee *et al.* in 2012, as shown in Figure 1-16(a)[109]. A monolayered atomically thin graphene surrounded by a hexagonal metallic meta-atoms layer and metallic wire gate electrodes are integrated in

the polymeric substrate. The tuning ability of graphene is greatly enhanced due to the combination between the graphene and the electric metasurface, such that a modulation of amplitude of up to 47% and phase up to 32.2° of the transmitted wave was achieved using this graphene metasurface.

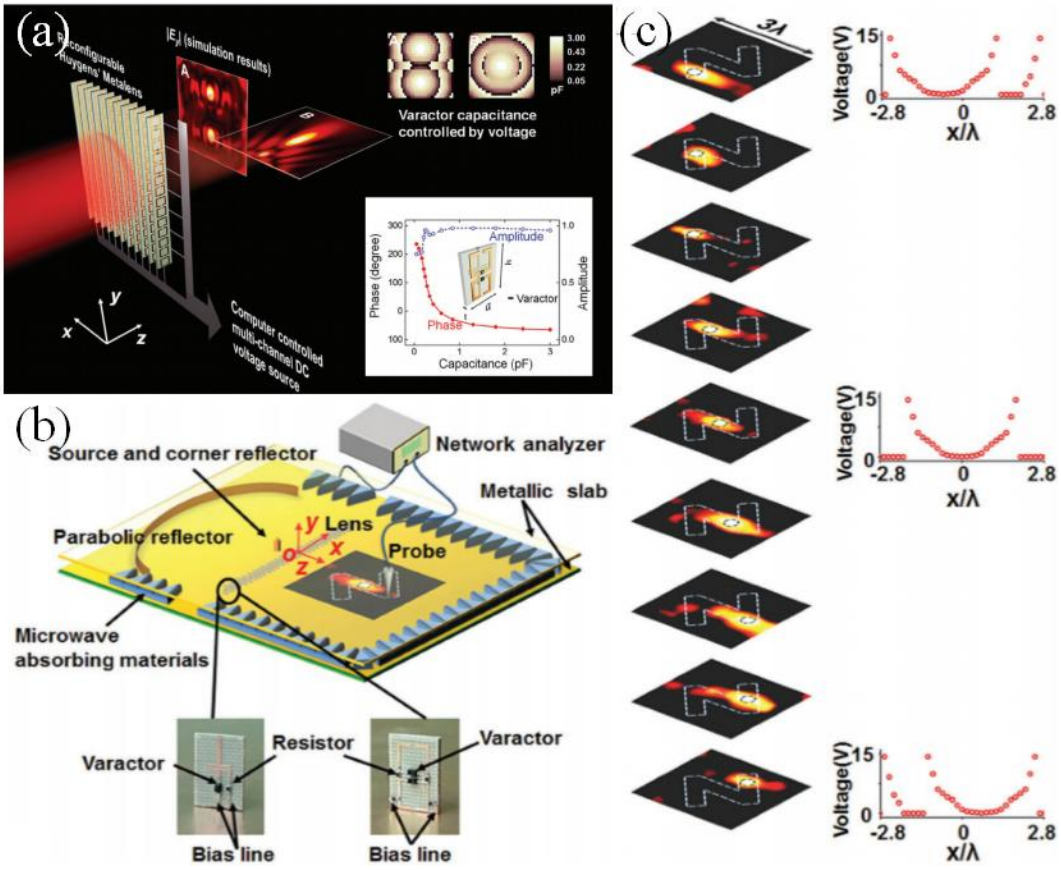

Figure 1.15 (a) Illustration of the focusing of the incident EM waves using the reconfigurable Huygens' metasurface. The insert shows the phase and amplitude response of the unit cell at 6.9 GHz. (b) Measurement setup. (c) Measurements of the focal spot moving along the trace of letter 'N'[108].

In the microwave regime, graphene also plays a vital role in the design of tunable metasurfaces. H. Chen *et al.* realized the beam manipulation of incident EM waves using a reconfigurable graphene-assisted metasurface, as illustrated in Figure 1-17(a)[112]. The unit cell of this metasurface is composed of four layers, including a graphene sandwich layer, a metallic patch layer, a substrate layer, and a metallic ground layer. The detailed view of the graphene sandwich layer is displayed in Figure 1-17(c), where we can see it consists of two polyvinyl chloride substrates (green layer), one diaphragm paper soaked with ionic liquid (white layer), and two patterned graphene monolayers. The π phase difference of the

graphene-based unit cell, which used for the 1-bit coding metasurface, can be achieved at around 9.6 GHz as shown in Figure 1-17(b). By assigning different voltage sequences on the reconfigurable graphene metasurface, the beam splitting is realized at 9.6 GHz and the corresponding measured far-field patterns are presented in Figures 1-17(d) and (e). The radiation direction of the reflected beam can be adjusted from 23° to 53° by varying the bias voltage sequences.

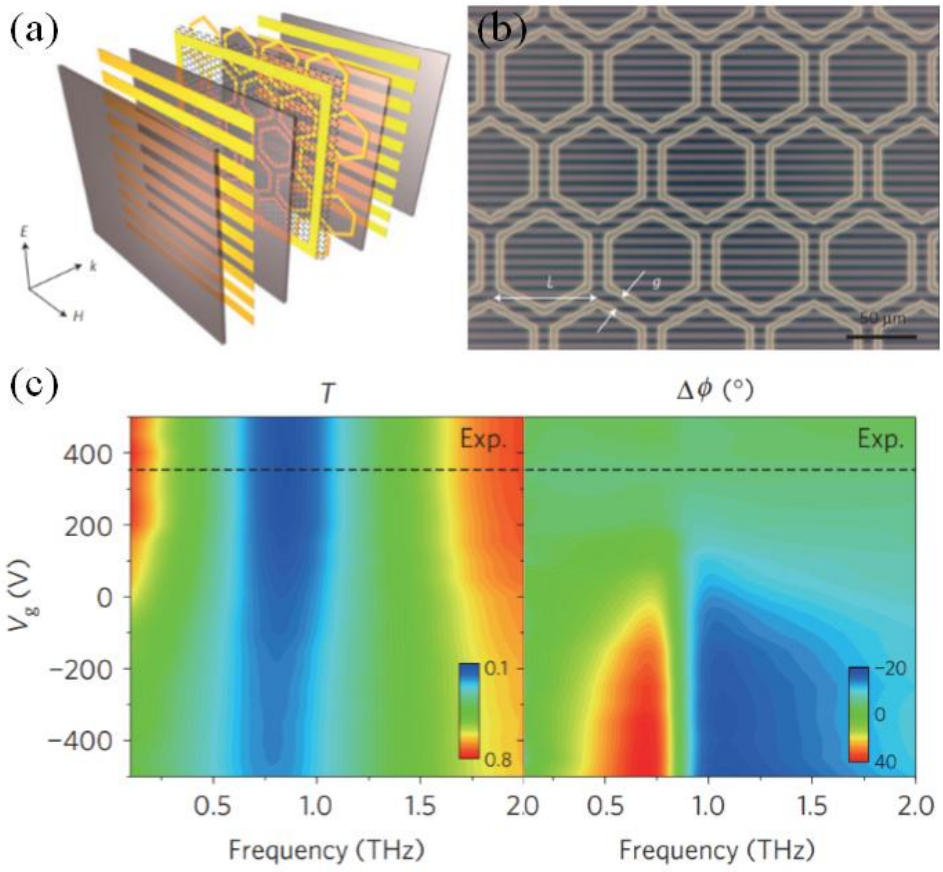

Figure 1.16 (a) Schematic of the structure of active graphene metasurface. (b) Fabricated active graphene metasurface without the top electrode. (c) Measured absolute amplitude and relative phase responses versus frequency and biased voltage[109].

Liquid crystals (LCs) are also efficient electrically sensitive components having the ability to realize tunable metasurfaces. The variation of the orientation angles of the elongated molecules in the LCs by changing the external electric field lead to the reconfigurability of LCs metasurface. In 2010, F. Zhang *et al.* designed a reconfigurable short wire-pair metasurface with a nematic LC integrated into the gap of two copper metasurface patterns in microwave regime[114]. Figure 1-18(a) shows the LC-based tunable

unit cell, which is composed of two Teflon fiberglass layers, two metallic pattern layers placed on the surface of Teflon fiberglass, and one nematic LC layer. The fabricated LC-based reconfigurable metasurface is presented in Figure 1-18(b). By applying different bias voltages on the metasurface, the measurements of the magnitude and phase responses versus frequency are carried out and depicted in Figure 1-18(c). It is clear that the resonance frequency can be easily adjusted from 9.91 GHz down to 9.55 GHz by varying the bias voltage from 0 to 100V. In 2012, a perfect absorber in the THz regime based on the LC tunable metasurface was proposed and experimental demonstrated by D. Shrekenhamer *et al.* as depicted in Figure 1-13(a)[115]. By changing the external bias voltage, a 30% amplitude tuning of the absorption at around 2.62 THz and a frequency tunability greater than 4% was realized as shown in Figures 1-19(d) and (e).

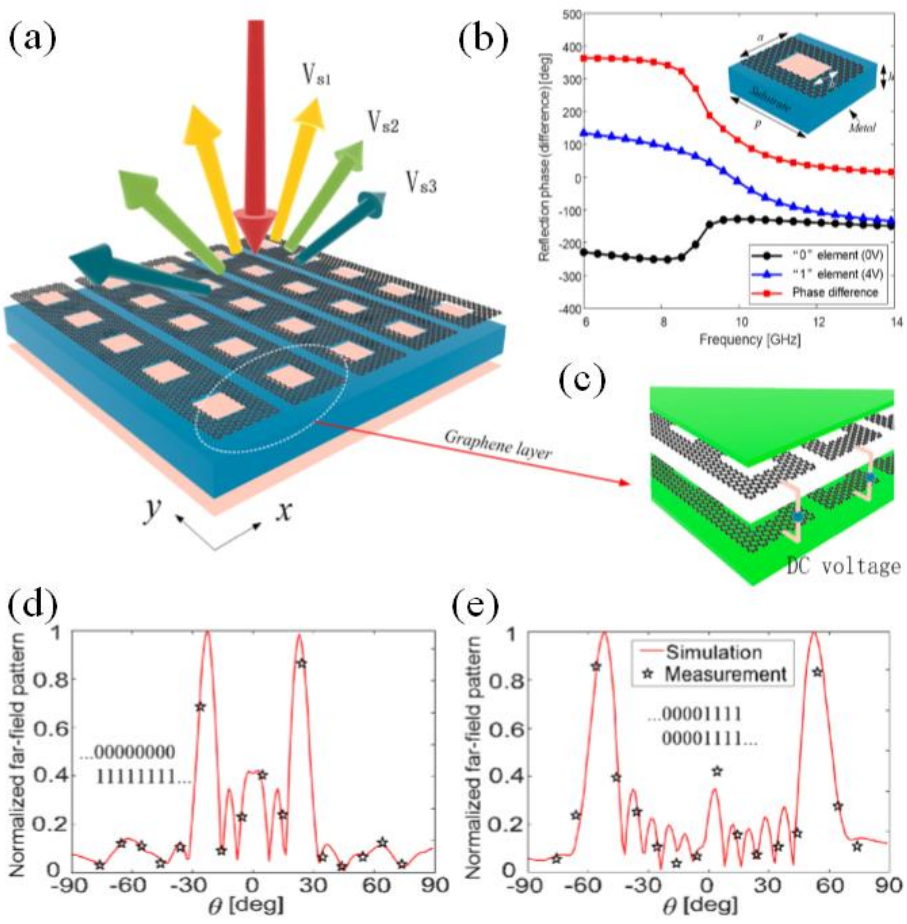

Figure 1.17 (a) Schematic of the reconfigurable graphene metasurface for the manipulation of EM waves. (b) Reflection phase response of the graphene unit cell. (c) Detailed structure of the graphene layer connected to a DC voltage source. (d)-(e) Normalized far-field patterns of different phase profiles[112].

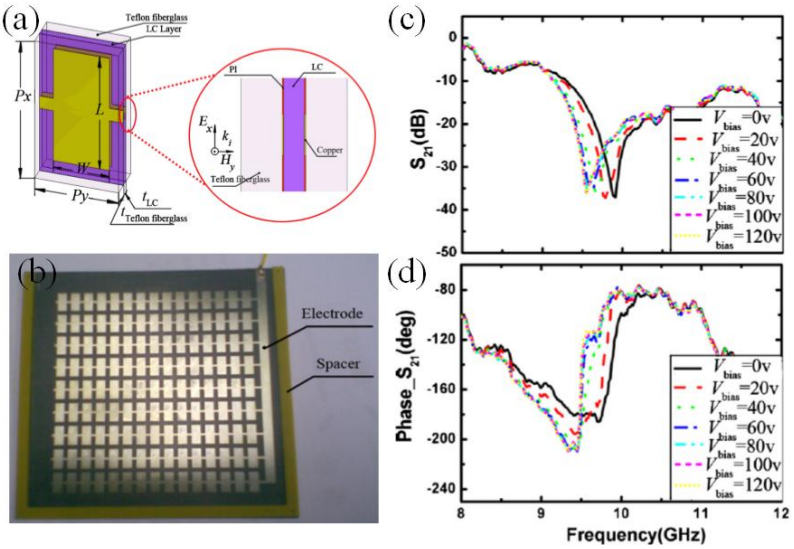

Figure 1.18 (a) 3D view of the tunable unit cell. The insert shows the side view of the tunable unit cell. (b) Photograph of the fabricated metasurface integrated liquid crystals. (c)-(d) Measured transmission amplitude and phase responses[114].

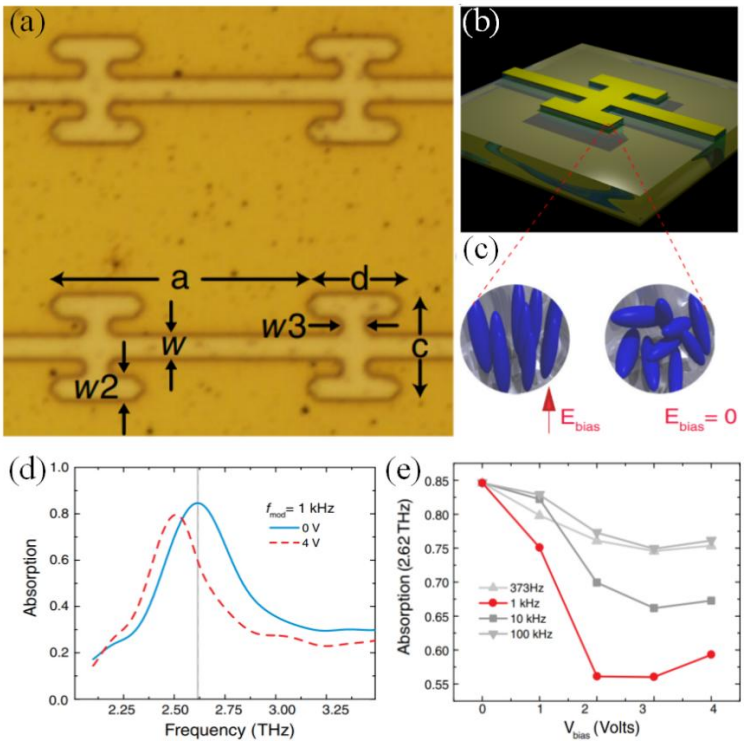

Figure 1.19 (a) Photograph of the LC tunable metasurface. (b) Schematic of the unit cell. (c) Arragements of LC with and without bias voltage. (d) Absorption versus frequency of two bias voltages with fixed modulation frequency (f_{mod}). (e) Absorption versus bias voltage for different modulation frequencies[115].

Besides, the doped semiconductor or transparent conducting oxide materials can also be used in the design of reconfigurable metasurface in IR and optical regimes. In 2006, Chen *et al.* proposed a reconfigurable metasurface using the semiconductor as active component as shown in Figure 1-20 (a)[116]. The metallic pattern of the metasurface is etched on a thin n-type gallium arsenide (GaAs) layer grown on a semi-insulating gallium arsenide (Si-GaAs) wader. The transmission amplitude responses of the metasurface for different bias voltages are presented in Figure 1-20(b). By changing the external bias voltage, the transmission amplitude can be dynamically adjusted in a wide frequency band.

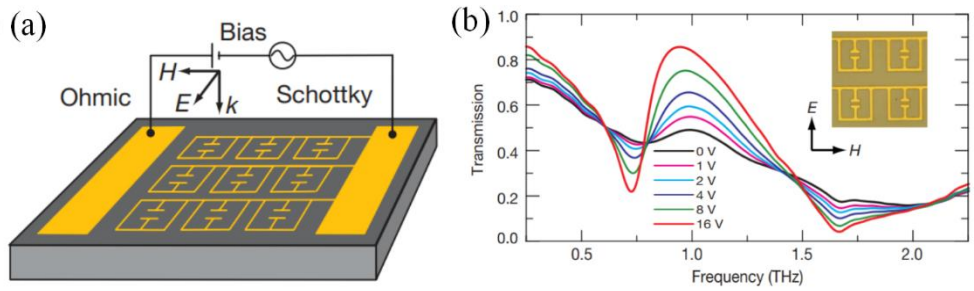

Figure 1.20 (a) Schematic of the tunable metasurface. (b) Transmission amplitude responses for different bias voltages versus frequency[116].

1.4 Conclusion

In this chapter, I review the concept and development history of metamaterials. The corresponding typical applications based on metamaterials are presented and analyzed in detailed. Then, the advantages and disadvantages of the metamaterials are discussed. Metasurfaces, the two-dimensional counterparts of metamaterials, are classified into three categories, plasmonic resonance metasurfaces, geometric-phase metasurfaces, and Huygens' metasurfaces. The corresponding applications of the three kinds of metasurfaces are also presented. Due to the fixed functionalities of the fabricated devices based on the passive metamaterials and metasurfaces, the reconfigurability mechanism in metasurfaces is further introduced. Different mechanisms, including thermal, optical, mechanical stretching, Micro-electro-mechanical-systems (MEMS), and electrical, are discussed in the design of reconfigurable metasurfaces. In the following chapters, I will investigate the properties of a one-dimensional modulated reconfigurable metasurface and two-dimensional modulated reconfigurable metasurface. Several applications are realized by the two reconfigurable metasurfaces.

Chapter 2 Simulation and measurement tools and design of reconfigurable metasurfaces

In chapter 1, the literature about the reconfigurable metasurfaces has been reviewed. Due to the limited functionality and narrow frequency band of passive metasurfaces, we propose the design of two reconfigurable metasurfaces utilizing the electrical reconfigurability mechanism in this chapter. The first one is a one-dimensional (1D) reconfigurable metasurface incorporating varactor diodes, which is controlled column by column and can only be modulated along one direction. The second one, an improvement of the first one, is a two-dimensional (2D) reconfigurable metasurface whose unit cells can be individually addressed. These two designed reconfigurable metasurfaces for a working frequency around 10 GHz are further utilized to generate and manipulate complex beams, including Airy beams, Bessel beams of zeroth-order and higher order, and also to generate holographic images, as it will be shown in the next chapters. However, before presenting the design of these two metasurfaces, we will briefly introduce the tools and setups exploited for simulation purposes and experimental validations.

2.1 Numerical softwares

In this section, we present the softwares that have been exploited for the design of the metasurfaces and for the generation of complex beams.

2.1.1 Ansys HFSS

Ansys HFSS software, a commercial 3D structure electromagnetic field simulation software[117], can be used to design periodic arrays and calculate parameters, such as gain, directivity, near-field distributions and far-field patterns. Besides, this software has the function to plot polarization characteristics, including spherical field components, circular polarization field components and axial ratios.

In this thesis, simulations of tunable unit cells and wavefronts tailoring using metasurfaces are implemented by Ansys HFSS. The varactor diode is used as a tunable component in our two reconfigurable metasurfaces. However, the difficulty we encountered is modeling the active component (the varactor diode). The lumped RLC boundary condition in the HFSS tool is one of the solutions. The schematic of the simulation of a tunable unit

cell is shown in Figure 2-1, where Floquet port on the top face is used as excitation port to emit a plane wave and Primary-Secondary boundary is used as the periodic boundary condition for the optimization of the geometric dimensions of unit cells. For the simulations of tailoring wavefronts using metasurface, the radiation boundary condition is applied on all the faces as shown in Figure 2-2.

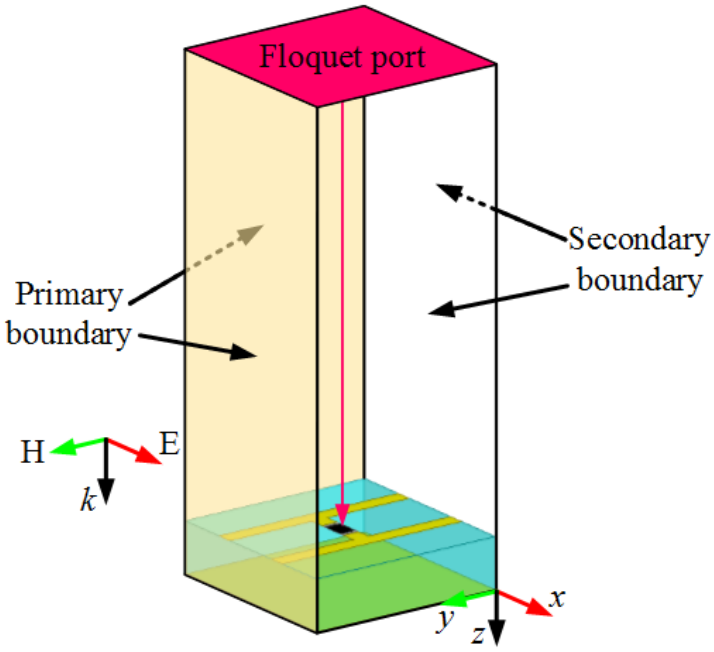

Figure 2.1 HFSS configuration for the simulations of unit cells.

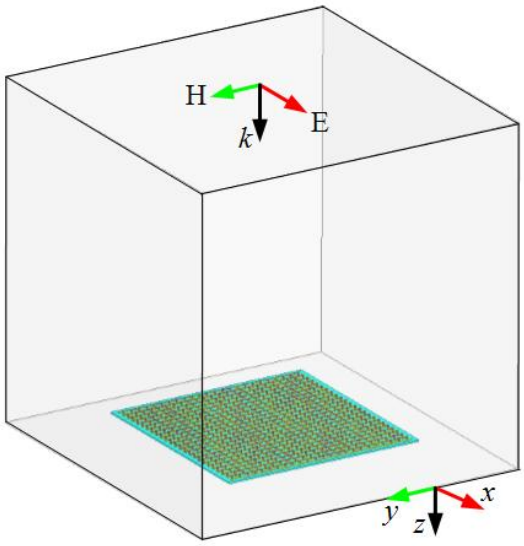

Figure 2.2 HFSS configuration for the simulations of tailoring wavefronts using metasurface.

2.1.2 MATLAB

MATLAB coded by MathWorks company is a commercial math software used in data analysis, wireless communication, deep learning, image processing and computer vision, signal processing, business finance and risk management, robotics, control systems and other fields[118]. In this thesis, this software is mainly used as the tool to calculate the phase profiles according to the equations of the complex beams.

Besides, Matlab can also produce a vbs (Microsoft Visual Basic Script Edition) file that can be run in HFSS to construct the 3D model automatically. HFSS-MATLAB-API is a tool library to control the execution of HFSS via the HFSS script interface. This tool library provides a series of MATLAB functions, which can be used to create 3D models by generating the required HFSS script. When a script is generated in this way, it can be executed in HFSS and the corresponding 3D model can be generated. In fact, any three-dimensional model that is established in HFSS software can be implemented using this function library. Therefore, this HFSS-MATLAB-API can reduce the time consumption in the creation of 3D models in HFSS software.

2.2 Experimental measurement setup

In this thesis, first, the experimental characterization of the reconfigurable metasurface is performed to demonstrate the simulated amplitude and phase responses of the unit cell. We simultaneously obtain the measured phase and amplitude responses versus frequency and bias dc voltage, those are the basic data for the calculation of voltage profiles applied on the reconfigurable metasurfaces. Then, to investigate the generation and manipulation of complex beams using reconfigurable metasurfaces, two experimental setups including near-field setup and far-field setup in a microwave anechoic chamber are utilized for related measurements. The near-field measurement setup is utilized to show the electric field information in the near-field region, while the far-field experimental setup is used to measure the radiation patterns of reconfigurable metasurfaces applied appropriate phase profiles.

2.2.1 Setup for metasurface characterization

The experimental characterization of the reflective reconfigurable metasurface is performed in the anechoic chamber as described as shown in Figure 2-3. Two 2 - 18 GHz wideband horn antennas[119] are used; one as the receiver and one as the transmitter and connected to the vector network analyzer. The horn antennas are placed in front of the top

layer of the reconfigurable metasurface integrated with varactor diodes and have the tilt angle of 5° with the normal direction of the metasurface as depicted in Figure 2-3 (b). Then, a copper sheet having the same size as the metasurface is measured, which is used as a reference.

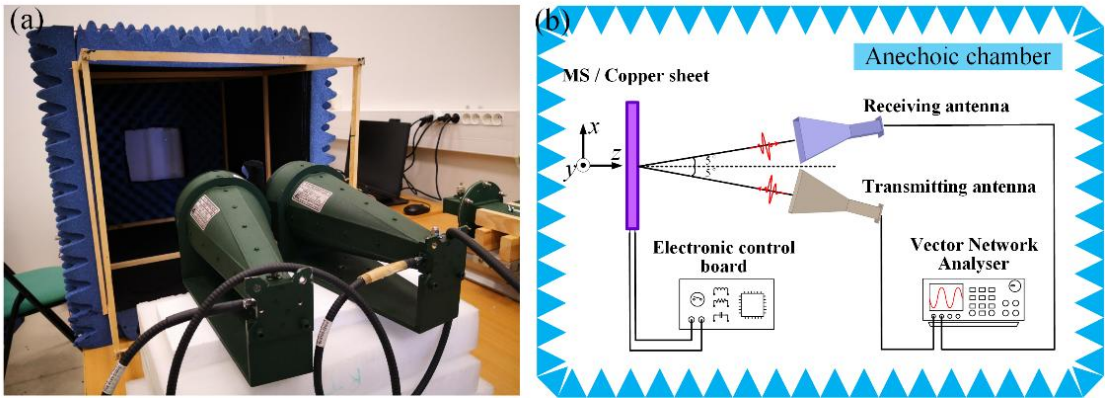

Figure 2.3 (a) Photography of the setup of the characterization of the two-dimensional reconfigurable metasurface. (b) Schematic of the setup of the characterization of the two-dimensional reconfigurable metasurface.

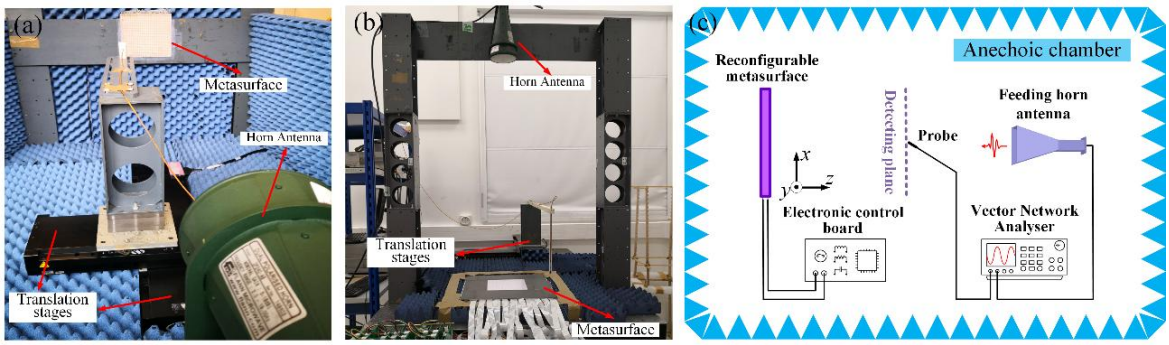

Figure 2.4 (a) Photography of the near-field measurement setup in the case of a reflective metasurface. (b) Schematic of the near-field measurement setup.

2.2.2 Near-field setup

The near-field experimental system is used to collect the near-field information of generated complex beams as shown in Figure 2-4. The system is composed of a horn antenna, a near-field sensing probe, translation stages and a 2-port vector network analyzer (VNA). In order to conduct the experimental measurements, the horn antenna and probe are connected to the two ports of a network analyzer using coaxial cables. The quasi-plane incident wave as a primary source is emitted from the 2 - 18 GHz wideband horn antenna.

The fiber-optic probe[120] is mounted on the orthogonal linear computer-controlled translation stages and is used as receiver to measure both the amplitude and phase of the electric field. The computer-controlled translation stages are stepped with an increment of 2 mm, which allows to perform a full two-dimensional electric field mapping over a total scanning area of 400 x 400 mm^2 in a plane.

2.2.3 Far-field setup

The far-field measurement setup is presented in Figure 2-5. Two horn antennas placed in the same horizontal plane and performing as transmitter and receiver, respectively, are connected to the network analyzer using coaxial cables. The transmitter antenna and metasurface is fixed on the rotating plate which allows a rotation varying from -180° to +180°. While the receiver is mounted on a slide rail allowing to adjust the distance from the transmitter. In this way, far-field patterns can be measured in the most commonly used E- and H-planes (planes containing electric field vector and magnetic field vector, respectively).

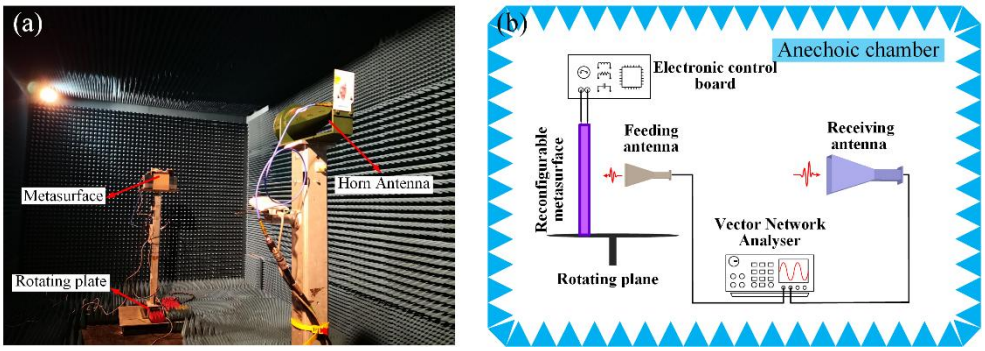

Figure 2.5 (a) Photography of the far-field measurement setup. (b) Schematic of the far-field measurement setup.

2.3 One-dimensional reconfigurable metasurface

Compared to the transmissive reconfigurable metasurface, which generally needs several layers to realize the nearly 2π phase coverage, the reflective reconfigurable can achieve the approximately 2π phase coverage with only one layer. In this section, we describe the 1D reflective reconfigurable metasurface that can be controlled column by column along only one direction by incorporating varactor diodes. This metasurface is used for the experimental validation of different functionalities in this thesis. For instance, it is exploited to generate and regulate directional beaming from a subwavelength aperture, a 1D Airy beam, and 1D zeroth-order Bessel-like beam. This metasurface was previously

designed during the PhD thesis of B. Ratni[121] and was applied for reflector antennas and polarizers[122-124].

2.3.1 Design of the unit cell

The unit cell of the 1D reconfigurable metasurface is depicted in Figure 2-6. All the metallic patterns are etched on a low-loss dielectric substrate (ε_r = 4.5, tan δ = 0.003) with thickness h = 1.52 mm. The top layer consists of two parallel separate metallic strips sharing the same width w = 0.5 mm and a varactor diode is embedded in the gap between the two metallic strips. The model of MACOM MGV 125-08[125] whose capacitance value ranges from 0.055 to 0.6 pF, is selected for the varactor diode in simulation and fabrication. The bottom layer is a square metallic ground plane intended to reflect the incident EM wave. An inductive part is also created due to magnetic flux between the ground plane and the wire array (top layer). The period p of the unit cell is 6 mm, which corresponds to $\lambda/5$ at the working frequency of 10 GHz.

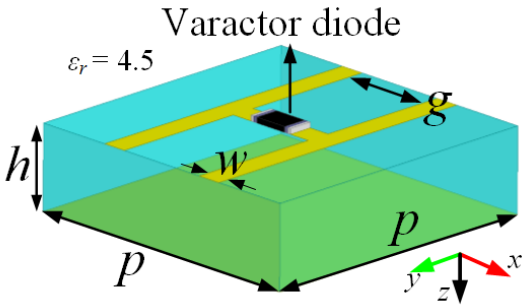

Figure 2.6 Perspective view of the unit cell. The geometrical dimensions are w = 0.5 mm, g = 1.9 mm, p = 6 mm and h = 1.52 mm. A varactor diode is embedded in the gap between two metallic strips on the top layer.

2.3.2 Characterization

The simulation of unit cell with optimized geometries is carried out by using the high frequency structure simulator (HFSS) commercial code by ANSYS, where the Floquet port is used as a plane wave source illuminating in the -z-direction with an x-polarized electric field and periodic boundary conditions are applied along the x- and y-directions to mimic an infinite periodic array for the S-parameter. Four capacitance values are selected for the simulated reflection magnitude and phase responses: 0.055 pF, 0.09 pF, 0.3 pF and 0.6 pF, corresponding to the bias voltage of 0 V, 5 V, 15 V, and 20 V, respectively.

The characteristics of the unit cell are investigated for both horizontal and vertical polarizations of electric field. When the E-field is oriented perpendicular to the strips of the capacitive grid in the top layer (*x*-polarized E-field), as shown in Figure 2-7(a), the *LC* resonance of the unit cell is created by the capacitance of varactor diode together with the inductive response of the structure. The equivalent *RLC* circuit of the designed unit cell is shown in Figure 2-7(b). The dimension of the gap *g* between the two separated metallic strips on the top layer is optimized in such a way that the intrinsic capacitance of the whole microstrip *LC* structure is very low compared to the capacitance introduced by the varactor diode. Therefore, the only capacitance value that influences the resonance frequency of the *RLC* circuit is the one that comes from the varactor diode. The resonance frequency can therefore be flexibly controlled by changing the voltage applied to the varactor diode.

The phase and amplitude responses of the unit cell with the *x*-polarized incidence are presented in Figures 2-7(c) and (d). It can be clearly observed that the resonance frequency spans from 8.5 to 11.6 GHz when the capacitance value is varied within the dynamic capacitance range of the varactor diode. The approximate 320° phase variation is obtained over a wideband ranging from 9 to 12 GHz.

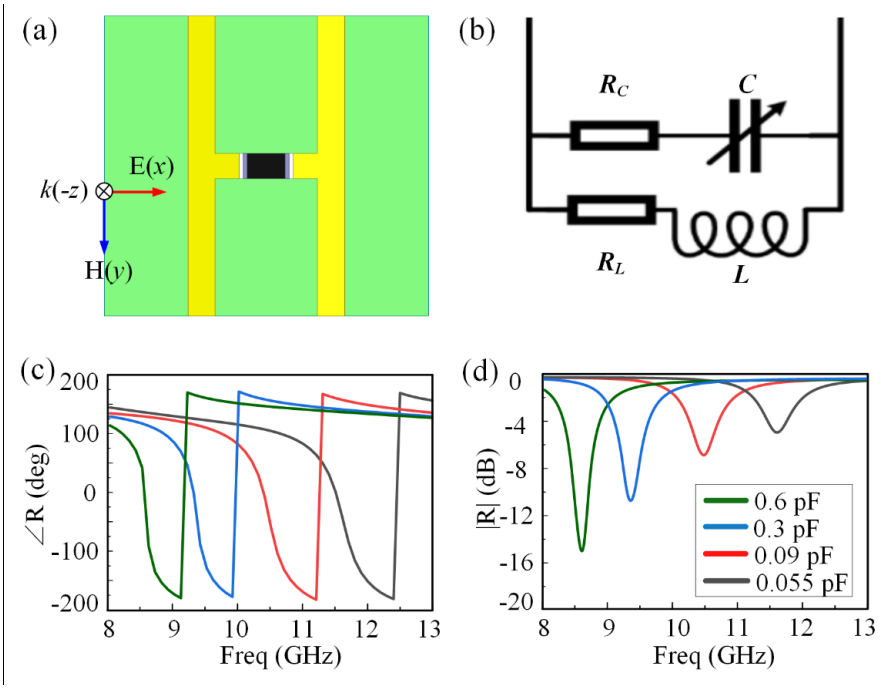

Figure 2.7 (a) Top layer of the unit cell. (b) Corresponding equivalent circuit of the unit cell with the *x*-polarized incident wave. (c)-(d) Simulated reflection magnitude and phase response of the unit cell for different capacitance values with the *x*-polarized incident wave.

Then, when the E-field is oriented parallel to the metallic strips of the capacitive grid in the top layer (*y*-polarized E-field), as shown in Figure 2-8(a), the varactor diode can not be considered as a tunable capacitor and the corresponding equivalent circuit is shown in Figure 2-8(b). The phase and magnitude responses of the unit cell are presented in Figures 2-8(c) and (d). When the capacitance change, nearly perfect reflection and the approximately constant phase of 170° can be observed over a wideband ranging from 9 to 12 GHz. Therefore, only an inductive response is obtained with the *y*-polarized incident wave.

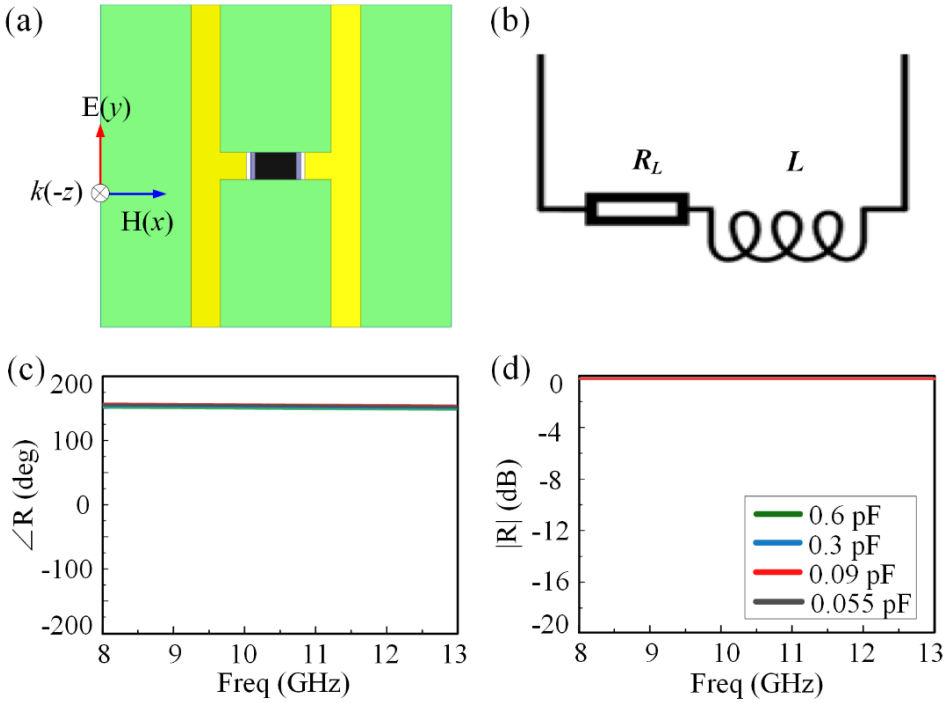

Figure 2.8 (a) Top layer of the unit cell. (b) Corresponding equivalent circuit of the unit cell with the *y*-polarized incident wave. (c)-(d) Simulated reflection magnitude and phase responses of the unit cell for different capacitance values with the *y*-polarized incident wave.

The unit cell is also investigated under oblique illumination of the incident wave in the *xoz* plane in the case of the *x*-polarized E-field configuration. The good stability of phase response can be observed in Figure 2-9 for different incident angles 0°, 25°, and 50°.

Then, the one-dimensional reconfigurable metasurface is fabricated using the conventional printed circuit board (PCB) technology as presented in Figure 2-10. The reconfigurable metasurface consists of 30 columns with lateral dimensions of 18 cm × 18 cm, and each column is composed of 30 unit cells. The inset of Figure 2-10 shows all the unit cells in each column are connected together by two metallic strips such that the same

voltage is applied to each column. The voltage applied to the reconfigurable metasurface can be adjusted by changing the output of the electronic control board which is connected to the metasurface using the feed lines.

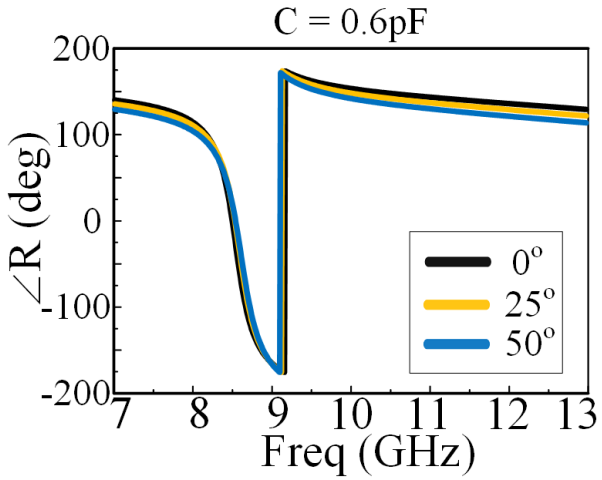

Figure 2.9 Reflection phase response for different incident angles in *xoz* plane with C = 0.6 pF.

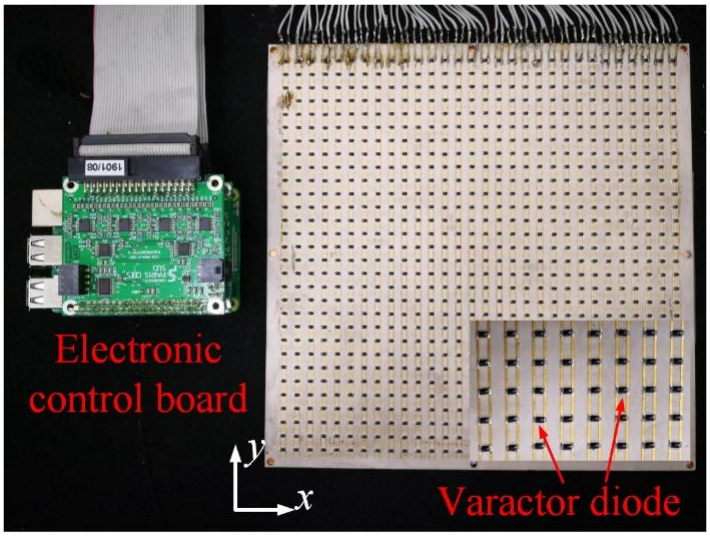

Figure 2.10 Photography of the 1D modulated reconfigurable metasurface.

The measured reflection response of the metasurface for the *x*-polarized E-field is presented in Figure 2-11. Four different bias voltages are used to evaluate the characterization of the one-dimensional reconfigurable metasurface. The resonance frequency ranging from 8.5 to 11.6 GHz can be observed in the phase response. The

approximate 320° phase coverage can be achieved in a wide frequency band. The reflection amplitude is not very high due to the ohmic loss of varactor diode. We can also obverse that the amplitude is not uniform for different voltages. The influence of amplitude on the beam generation will be discussed in Chapter 4. The measurements show a good agreement with the simulations.

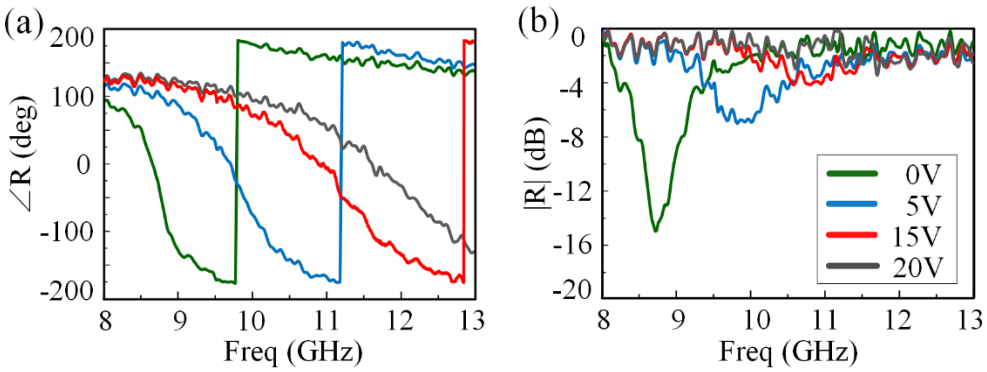

Figure 2.11 (a)-(b) Measured reflection phase and magnitude of the unit cell for different bias voltages.

2.4 Two-dimensional reconfigurable metasurface

In this subsection, to realize the generation of 2D complex beams, a two-dimensional reflective reconfigurable metasurface that can be modulated in two directions is then designed integrated with varactor diodes. The unit cells on the 2D reconfigurable metasurface can be individually addressed by an elaborately designed DC bias system.

2.4.1 Design of unit cell

The two-dimensional modulated reconfigurable metasurface is designed for the more complicated applications, for example, 2D Airy beams, vortex beams, Bessel beams, and imaging holography. We propose a tunable reflective unit cell that can be individually controlled as shown in Figure 2-12. The low-loss dielectric substrate ($\varepsilon_r = 3.5$, $\tan\delta = 0.0037$) is adopted as substrate of the unit cell. The thickness of two substrates is 1 mm and 0.25 mm, respectively. The top layer contains two parallel metallic strips and one varactor diode embedded in the gap with the assistance of two metallic arms. Two through vias from the bottom layer to the top layer are used to connect the feed lines and the positive and negative electrodes of the varactor diode. The middle layer is a metallic plane that is used to allow a magnetic flux between it and the top layer and also to reflect the illuminating wave. In order

to isolate the through vias and the middle metallic plane, two annular regions are removed from the middle metallic layer, as shown in Figure 2-12(a). The red cylinder in Figure 2-12(b) represents the through via connecting the negative electrode of varactor diode and feed line applied positive voltage. Conversely, the dark blue via is utilized to connect the positive electrode of the varactor diode to the ground. The detailed geometrical dimensions of the unit cell are given in Figure 2-12. 15 feed lines, having the same width of 0.16 mm, are printed on the bottom layer as depicted in Figure 2-12(d). The black feed line is connected to the ground while the others 14 lines are used for the input of DC voltages. The reason of 14 lines for positive DC voltages and only 1 red through via for each unit cell is that the feed lines should be isolated for the individual addressing of each unit cell on the metasurface. The feedlines can not be multiplexed. If 14 unit cells are expected to be addressed individually, there must be 14 feedlines.

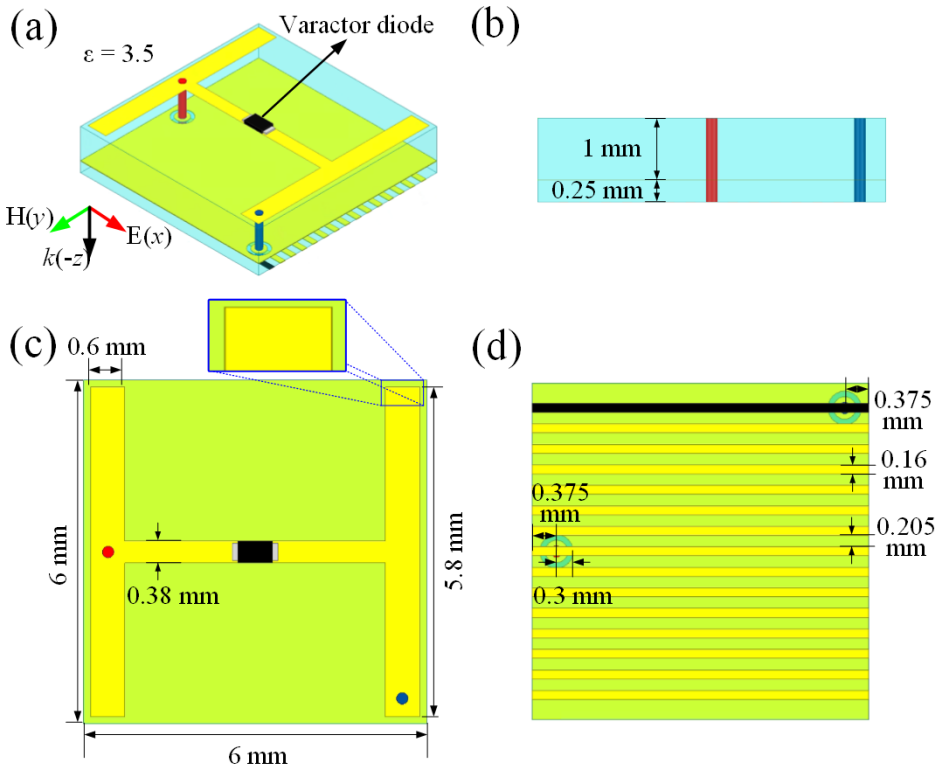

Figure 2.12 Structure of the unit cell used to comprise the two-dimensional reconfigurable metasurface. (a) 3D view. (b) Side view. (c) Top view. (d) Bottom view.

The unit cell used to construct the 2D modulated reconfigurable metasurface is simulated utilizing HFSS, where the incident plane wave with an *x*-polarized electric field is illuminated from a Floquet port along the -*z*-direction. Periodic boundary conditions are set

along the *x*- and *y*-directions to simulate an infinite array. The reflection phase and magnitude responses are plotted and shown in Figure 2-13. The phase response curves plotted for four different considered capacitance values of the varactor diode are not smooth in the predesigned frequency band.

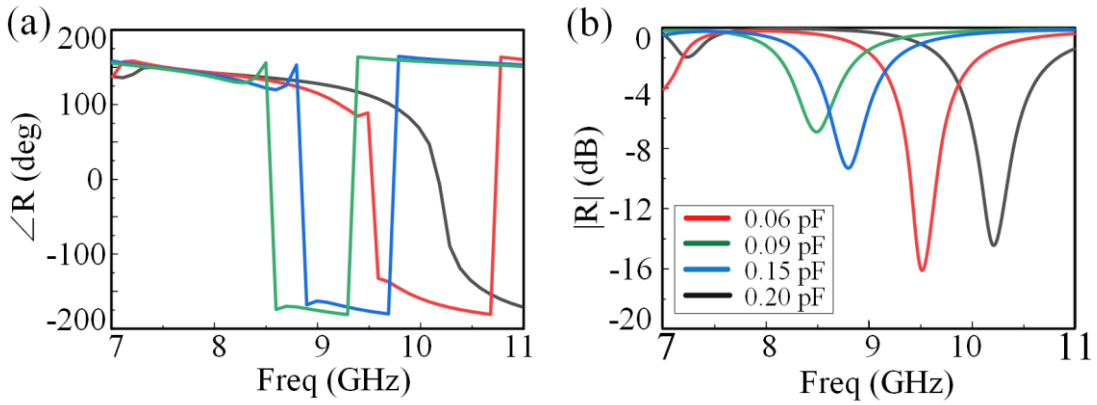

Figure 2.13 Numerical simulated reflection phase and magnitude response of the active unit cell in the wide frequency band ranging from 7 to 11 GHz.

In order to solve the problem of the non-smooth phase response curves mentioned above, we remove the dark blue through via. The positive electrodes of varactor diodes on the metasurface are connected together by the right metallic strip on the top layer as shown in Figure 2-14(c), where the left metallic strip is isolated while the right metallic strip is continuous and connected to the ground of the DC source. Therefore, all the 15 feed lines on the bottom layer can be connected to the positive DC voltages, allowing 15 unit cells independent control along the *x*-direction by moving the red through via.

The numerically simulated reflection phase and magnitude responses of the second unit cell are performed and presented in Figure 2-15. The phase response curves are smooth for the four selected capacitance values of the varactor diode, which means that a good phase response is obtained. The resonance frequency shifts from 7.6 to 10.6 GHz. As the location of the unit cell changes on the metasurface, the position of the through via connected to the power supply also changes. Thus, we investigate the phase response of the unit cell with the position change of the red through via along the *y*-direction. However, the phase of the unit cell has a big shift with the position change of the red through via as illustrated in Figure 2-16. Therefore, this active second unit cell cannot be considered ideal for the 2D modulated metasurface.

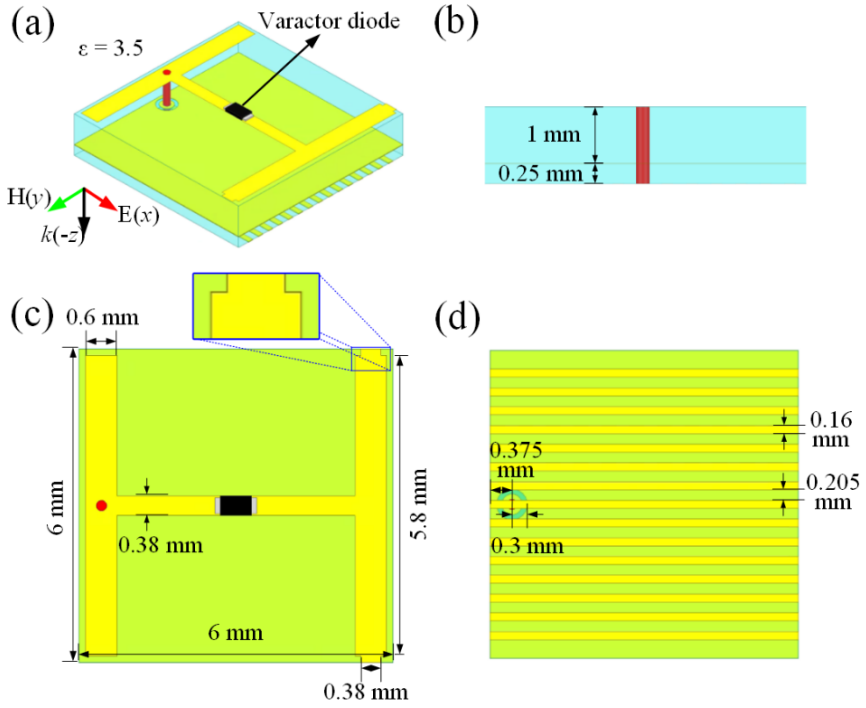

Figure 2.14 Schematic of the active unit cell with the positive electrodes of varactor diodes connected together on the top layer using the continuous right metallic strip. (a) 3D view. (b) Side view. (c) Top view. (d) Bottom view.

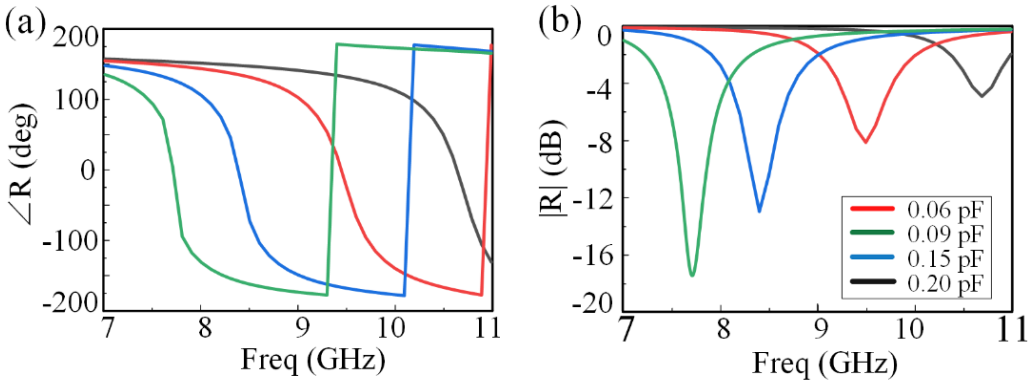

Figure 2.15 Reflected coefficient of the unit cell in the wide frequency band ranging from 7 to 11 GHz.

Then, we consider suppressing the influence of position change of the through via on the phase response. To realize only a very small variation when the position of the red through via changes, 15 vias are drilled in the top substrate and arranged into two rows as shown in Figure 2-17(a). 14 of them are blind vias and one of them is through via. As such, two rows of blind vias, whose inner wall is metalized to be used as feedlines of the varactor diode, are located on the left side of the unit cell. The depth of those blind vias is the same

as the thickness of the top substrate as shown in Figure 2-17(b). The through via is represented by the red cylinder, which is used to connect the feed line and negative electrode of the varactor diode as shown in Figure 2-17(b). The bottom layer is composed of 15 metallic strips used as feed lines as shown in Figure 2-17(d).

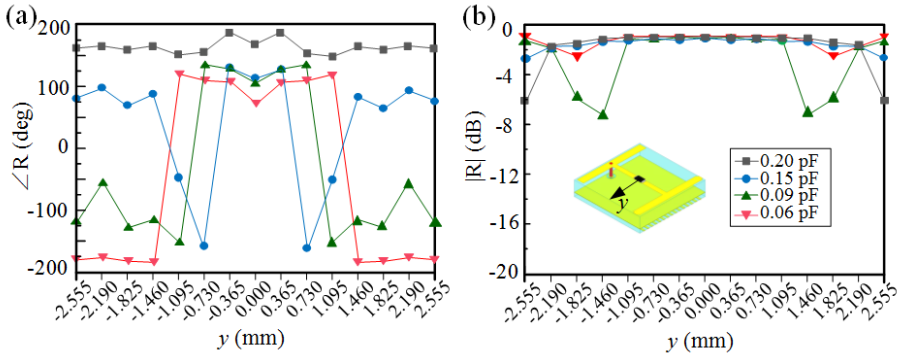

Figure 2.16 Phase and magnitude distributions for different capacitances with the position of the through via varying from -2.555 mm to 2.555 mm along the *y*-direction at 9 GHz.

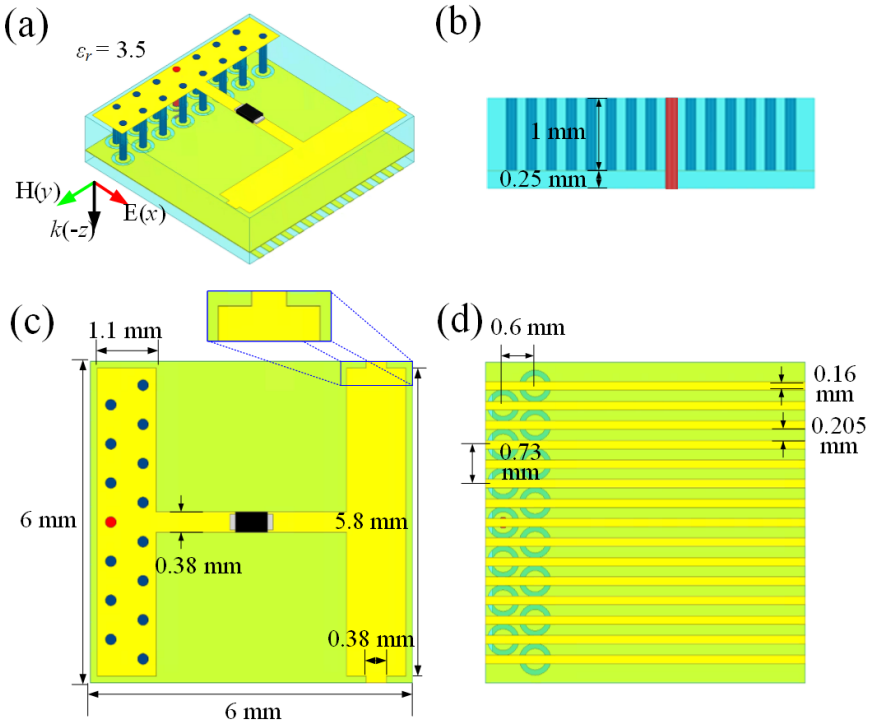

Figure 2.17 The unit cell for the two-dimension modulated reconfigurable metasurface. (a) 3D view. (b) Side view. (c) Top view. (d) Bottom view.

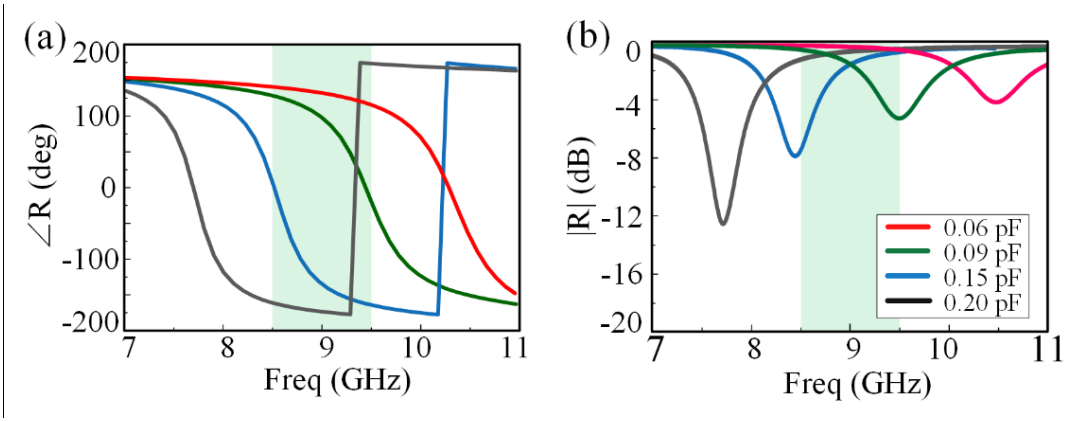

Figure 2.18 Reflection phase and magnitude response of the unit cell used to comprise a 2D reconfigurable metasurface.

The measured phase and magnitude response of the unit cell is presented in Figure 2-18. The approximately 340° phase coverage can be observed from 8.5 to 9.5 GHz as illustrated in the green region. The phase response of the new unit cell with the position change of the through via is simulated at 9 GHz as shown in Figure 2-19. Compared to the phase response of the unit cell without the blind vias in the top substrate, it is clear that the phase response has only a small variation with the position change of the red through via along the *y*-direction.

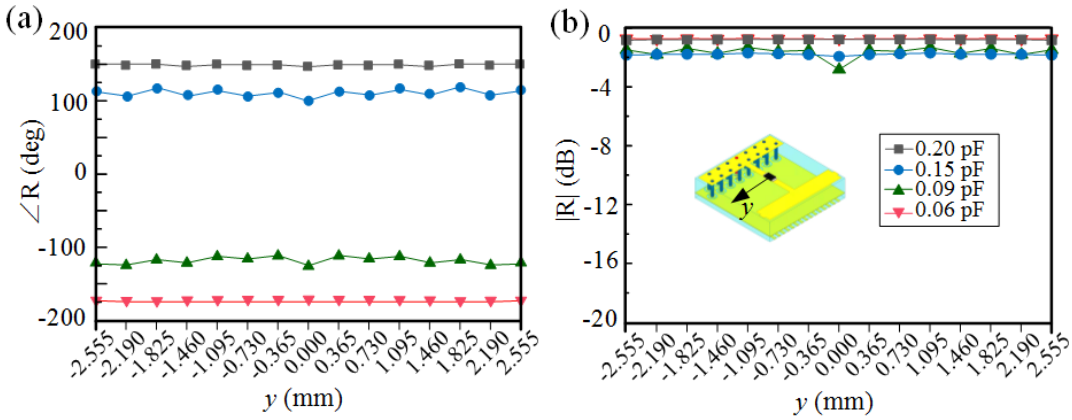

Figure 2.19 Phase and magnitude distributions for different capacitances with the position of the through via varying from -2.555 mm to 2.555 mm along the *y*-direction at 9 GHz.

The unit cell for an individually addressable metasurface is designed as discussed above. To comprise the two-dimensional reconfigurable metasurface using the tunable unit cell, we elaborately design the voltage bias system as illustrated in Figure 2-20, where the structure

in yellow color denotes the metallic lines and the structure in orange color represents the area soldered with flexible printed circuit (FPC) connector. 20 FPC connectors, each containing 45 lines, are utilized in the metasurface. Therefore, there are 900 lines in the bottom layer in total, which enables the possibility of addressing 30 × 30 unit cells in the metasurface. In this way, each unit cell can be individually addressed by changing the corresponding input voltage. The network of feeding lines is decomposed into two parts (right and left) by a slit with a width of 0.2 mm as shown in the inset in the bottom left of the Figure 2-20, such that each part of the metasurface controls 30 × 15 unit cells. The two-dimensional reconfigurable metasurface is then fabricated using the traditional printed circuit board (PCB) technology as shown in Figure 2-21. The total dimension of the fabricated reconfigurable metasurface is 43 cm × 43 cm. The dimension of the usable area of the reconfigurable metasurface is 18 cm × 18 cm and the black area represents the absorbing materials placed around the usable area to eliminate parasitic reflections.

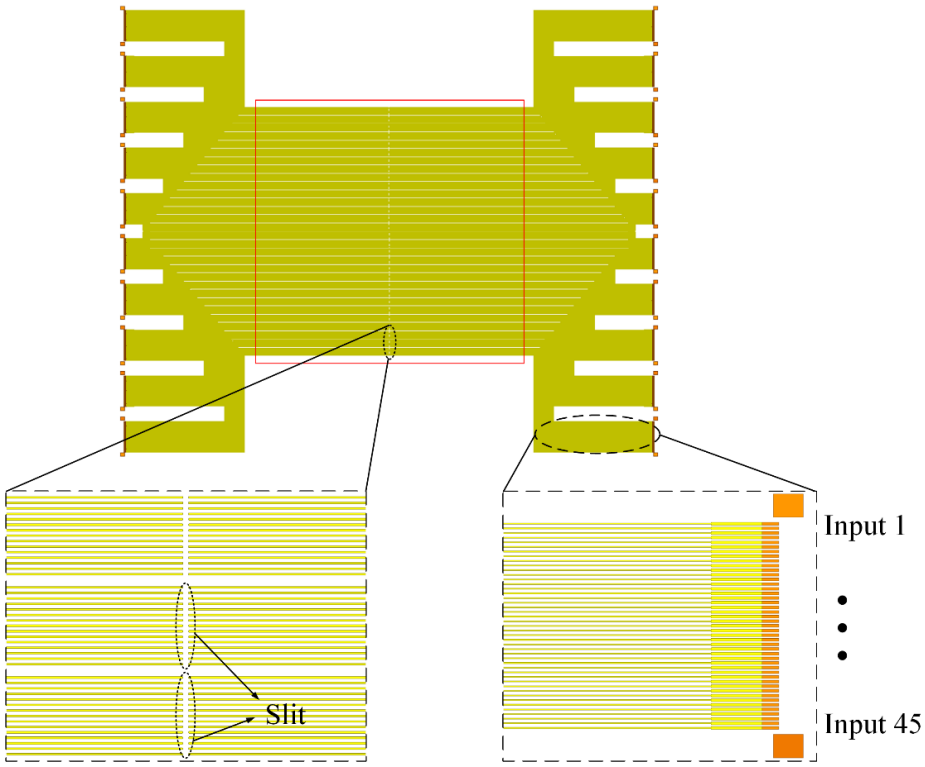

Figure 2.20 Schematic layout of the bias circuit layer (below the ground plane) of the reconfigurable metasurface. 20 flexible printed circuit (FPC) connectors are used in the bias circuit layer. The zoomed inset on the bottom left shows the slit in the middle of the bias layer, used to isolate the voltage on the right and left parts of the metasurface. The zoomed inset on the bottom right shows the details of the feed lines connected to the FPC connectors.

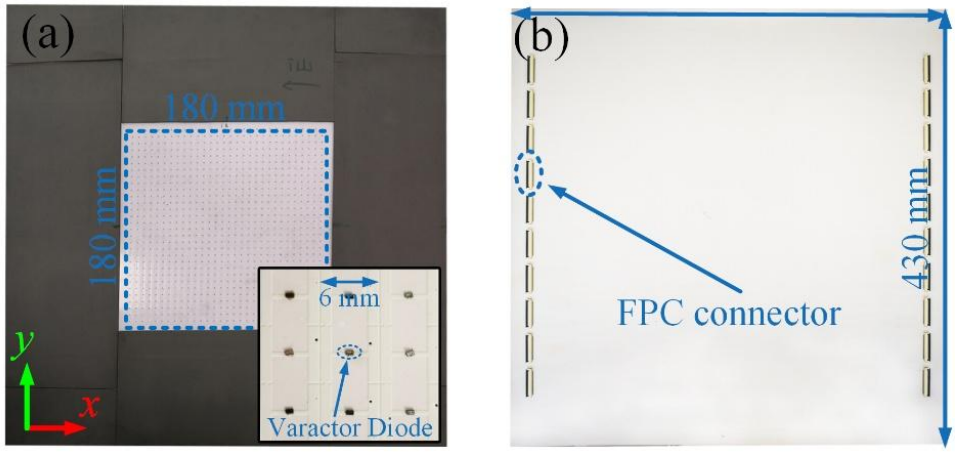

Figure 2.21 Photographs of the 2D reconfigurable metasurface. a) Top view of the fabricated metasurface. b) Bottom view of the fabricated metasurface composed of the bias lines and flexible printed circuit (FPC) connectors. Zoomed detail of the fabricated metasurface displaying the varactor-integrated unit cell.

An electronic control system, which is composed of 60 control boards, is connected to the reconfigurable metasurface to control the voltages applied to the varactor diodes as illustrated in Figure 2-22. Each electronic control board is utilized to control 15 unit cells. The output voltages of the 15 pins of the electronic control board can be flexibly programmed through a computer.

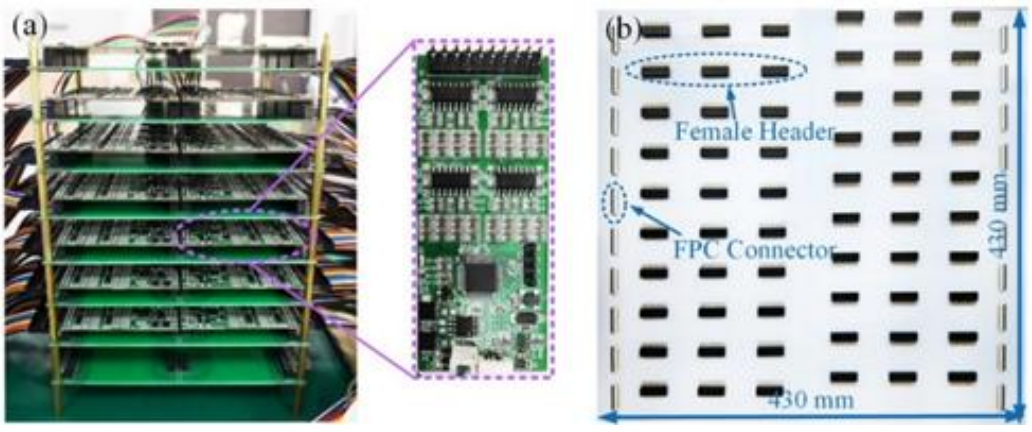

Figure 2.22 (a) Photograph of the electronic control system. The inset is a single electronic control board whose 15 pins are used for the voltage control of 15 meta-atoms. 60 boards are integrated in the electronic control system. (b) The interface board used to link the metasurface to the electronic control system, with the FPC connectors connected to the metasurface and the female header connected to the electronic control board.

2.4.2 Experimental Characterization

The DC voltage bias system is composed of a 24 V DC source, electronic control boards, interface board, and the corresponding connection lines. The output voltages of the electronic control board can be adjusted from 0 to 24 V. However, we set the output voltages in the range from 0 to 18 V for the characterization of the two-dimensional metasurface due to the property of the utilized varactor diode. To realize the characterization of the two-dimensional metasurface, the voltage for all the channels are set as the same simultaneously. The electronic control boards are controlled by a computer via an USB-RS-485 parallel link. As presented in Figure 2-23, four voltages are selected to show the experimental characterization of the two-dimensional reconfigurable metasurface. The experimental characterization is performed in the frequency band spanning from 7 to 11 GHz. The resonance frequency of the metasurface varies from 7.6 to 10.3 GHz when the bias voltages change from 1.5 to 18 V. These selected four voltages correspond to a variation of the capacitance between 0.02 to 0.22 pF. The approximately 340° phase coverage can be observed in the wide frequency band ranging from 8.5 to 9.5 GHz.

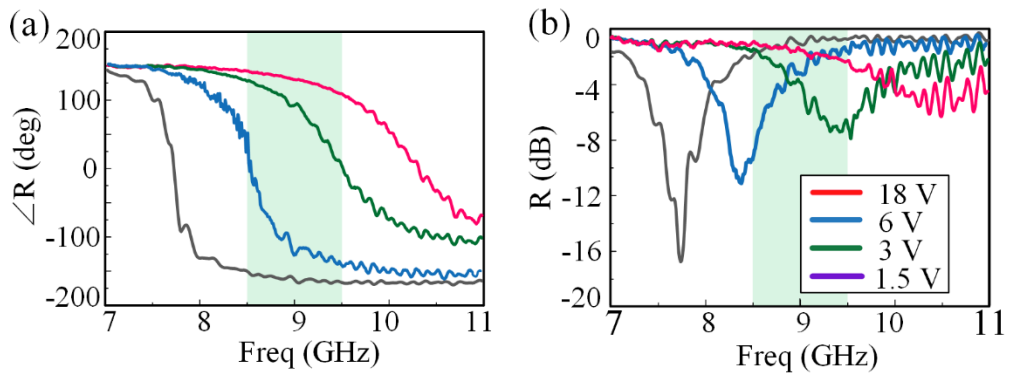

Figure 2.23 Experimental characterization of the two-dimensional reconfigurable metasurface. (a) Phase response of the metasurface. (b) Magnitude response of the metasurface.

2.5 Conclusions

In this chapter, I have in a first step presented the simulation and experimental environments exploited during my thesis for the design and characterization of metasurfaces. Then, two different reconfigurable metasurfaces have been presented. The first one is a 1D reconfigurable metasurface that is controlled column by column, and the second one is a 2D reconfigurable metasurface whose unit cells can be individually addressed by an elaborately

designed DC bias system. Both numerical and experimental characterizations of the two reconfigurable metasurfaces have been detailed, displayed, and analyzed. The approximately 320° phase coverage was achieved over a wide frequency band ranging from 9 to 12 GHz for the 1D reconfigurable metasurface. After several optimizations and using blind via technique, the approximately 340° phase coverage was realized over a wide frequency band ranging from 8.5 to 9.5 GHz for the 2D reconfigurable metasurface.

Chapter 3 Directional beaming of electromagnetic waves through a subwavelength aperture

3.1 Introduction

In chapter 1, I have presented several examples of metasurfaces that have been widely developed for a wide range of applications during the last two decades. In this chapter, I will discuss the directional beaming from a subwavelength aperture flanked by two metasurfaces. First, I describe the electromagnetic (EM) field distribution after an incident plane wave passes through a subwavelength aperture. According to the diffraction theory, a fundamental physical phenomenon studied for centuries, EM waves passing through a subwavelength aperture would be scattered in all directions. Compared to the incident wave, the diffracted wave is weak since only a part of the wave passes through the aperture and EM fields present an evanescent decay in the aperture[126]. When, the wave passes through a subwavelength aperture, a part of the diffracted wave propagates along the metal surface, which is referred to as surface plasmon polariton (SPP) in the optical regime. The SPP is a hybrid mode formed by the collective oscillation of EM waves and free electrons at the interface between the dielectric and metal[127]. The electric field exponentially attenuates along the *z*-direction as shown in Figure 3-1. However, the SPP is impossible to be directly excited on a smooth metal surface. It is necessary to compensate the wave vector mismatch by drilling holes[128-131], grating coupling[132-136], prism coupling[137-139], waveguide mode coupling[140-143], near-field excitation[144,145], and so on.

In 2004, J. B. Pendry *et al.* concluded that the perfect conductor with an array of drilled square holes at the surface could support surface modes[128], as illustrated in Figures 3-2(a) and (b). The surface plasmon modes can also be excited by coupling with a dielectric grating. The reflection characterizations of such designed dielectric gratings on a silver film were investigated by S. Kim *et al.* for different incident angles of an illuminating wave, as depicted in Figure 3-3(a)[136]. Three gratings (A, B, and C) where the length of the dielectric and gap are the same in the *x*-direction and which share same thickness of 80 nm and refractive index of 1.72, were studied in the optical regime. The period of gratings A, B, and C is 305 nm, 376 nm and 503 nm, respectively. The peak of the reflection curve indicates a strong coupling of the incident wave to the surface modes. The strong absorptions of the gratings A, B, and C occur at -20.3°, 0°, and 20.0°. According to the theory of reciprocity, surface modes can

be converted to radiation modes at the specific angle of the strong absorption. By assigning symmetric dielectric gratings on the two sides of the subwavelength slit, on-axis directional beaming can be realized, as shown in Figure 3-3(b). When asymmetric dielectric gratings are assigned on the two sides of the subwavelength slit, the off-axis directional beaming is achieved as displayed in Figure 3-3(c).

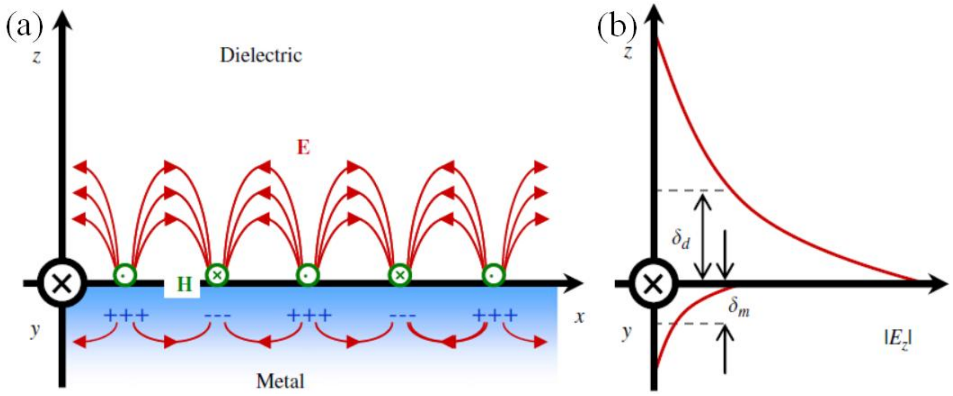

Figure 3.1 (a) Electric field and charge distribution of SPP at the boundary between dielectric and metal. (b) Attenuation property of electric field at the boundary[127].

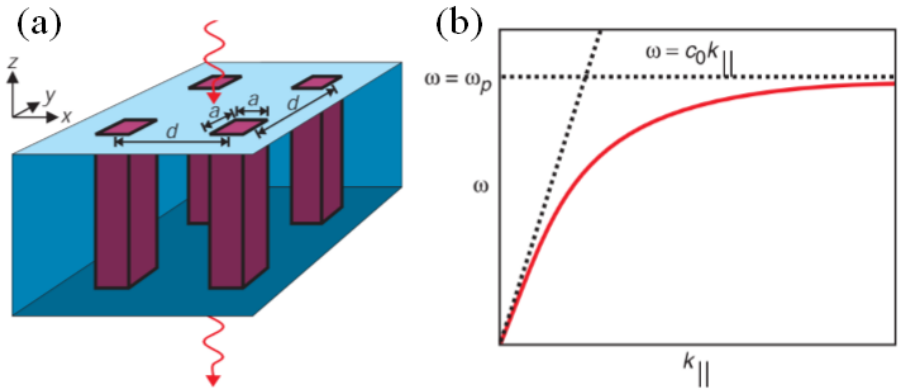

Figure 3.2 (a) Schematic of the perfect conductor with subwavelength square holes. (b) Dispersion curve of the SPP-like at the interface[128].

In addition, SPPs can also be excited in the terahertz and microwave domains. In 2012, L. Zhou *et al.* utilized phase-gradient metasurfaces composed of H-type unit cells to convert propagating waves to surface waves at microwave frequencies, as displayed in Figure 3-4[146]. The simulated and measured radiation patterns are presented in Figures 3-4(c) and (d), where anomalous reflection can be observed when the incident angle is less than a certain

angle of incidence called critical angle. However, no beam appears in the radiation pattern for the incident angle greater than the critical angle. Such kind of metasurface can compensate the momentum mismatch between surface modes and radiation modes by assigning an appropriate phase gradient on the metasurface. In this way, propagating wave to surface wave conversion can be achieved for any incident angle greater than the critical threshold. According to the reciprocity theory, surface waves can also be converted to propagating waves by applying elaborately designed phase gradient on the metasurface. J. J. Xu *et al.* proposed a spoof SPP emitter to achieve the conversion from SPP to the spatial radiated wave[147]. The spatial propagating waves radiated to different directions are realized with using different phase gradient metasurfaces on the ultrathin metallic strips as shown in Figure 3-5.

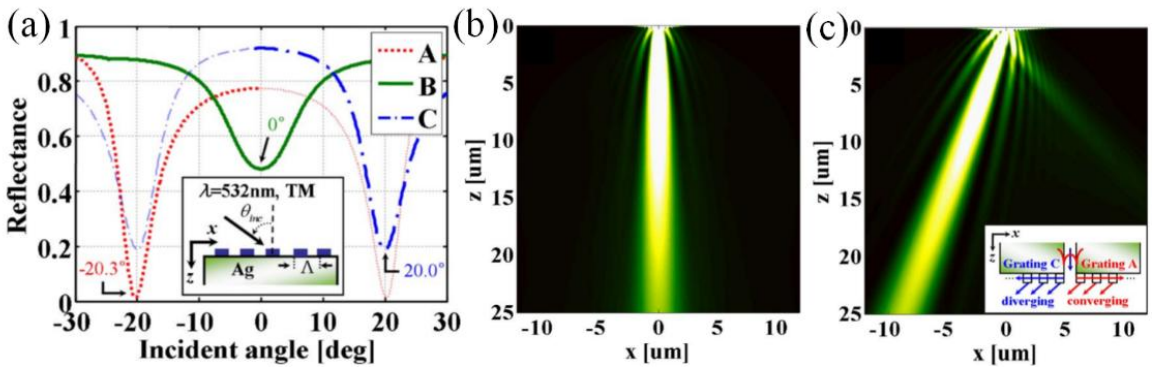

Figure 3.3 (a) Reflection characterizations of the silver attached different dielectric gratings in a wide incident angle ranging from -30° to 30°. (b) On-axis beaming using grating B. (c) Off-axis beaming using gratings A and C[136].

In this chapter, the dynamic tunable directional beaming of EM waves from a subwavelength aperture is studied by exploiting the designed one-dimensional reconfigurable metasurface. The generalized Snell's law is used to analyze the momentum mismatch between surface wave and radiated wave. By applying the appropriate phase gradient on the reconfigurable metasurface, directional beaming from the subwavelength slit illuminated by an incident plane wave can be achieved. On-axis directional beaming from the slit is generated over a wide frequency range and off-axis directional beaming, including 20°, 30°, and 40°, are realized at 10 GHz. Both the numerical simulations and experimental measurements are utilized to validate the proposed method of realizing directional beaming at specific angles using the reconfigurable metasurface.

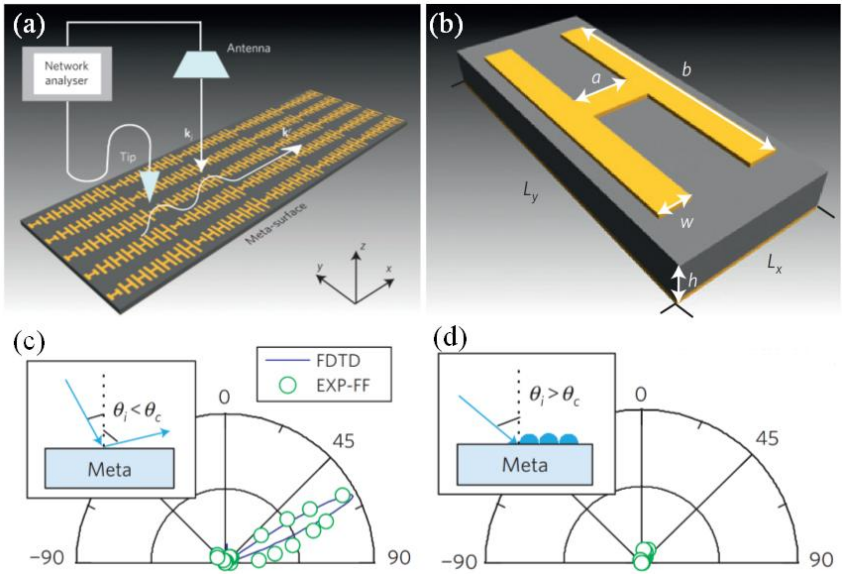

Figure 3.4 (a) Schematic of the conversion of propagating wave to surface wave. (b) Unit cell of the phase gradient metasurface. (c) Radiation patterns with an incident angle less than the critical angle. (d) Radiation patterns with an incident angle greater than critical angle[146].

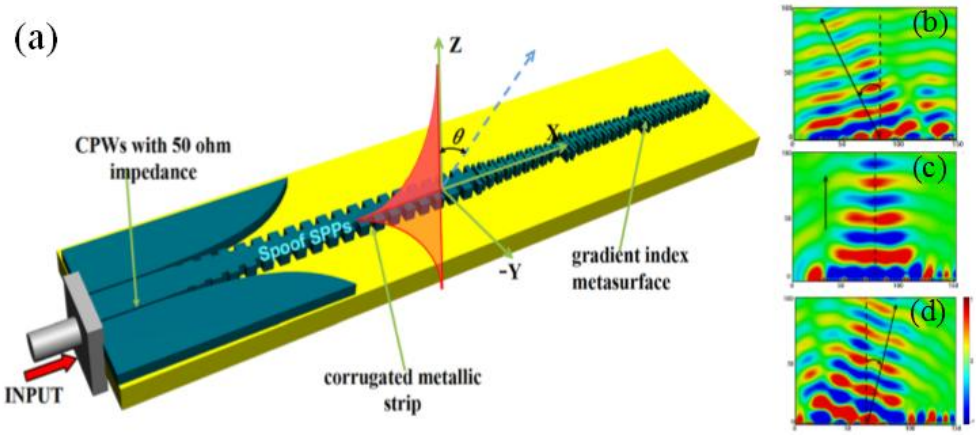

Figure 3.5 (a) Schematic of the spoof SPP emitter. (b) Near-field results for the propagating waves in different directions[147].

3.2 Generalized Snell' law

In this section, I will describe the generalized Snell's law, a fundamental theory in beam manipulation using metasurfaces. There was no unified theory for the analysis and design of beam-steering metasurfaces until the generalized Snell's law was proposed by F. Capasso's group in 2011[43]. The key to manipulate EM waves is the introduction of the abrupt phase

shift at the interface between two media. The abrupt phases are appropriately arranged to form a phase gradient, which changes the isophase surface of the electromagnetic wave in such a way that the purpose of tailoring the direction of electromagnetic waves can be achieved.

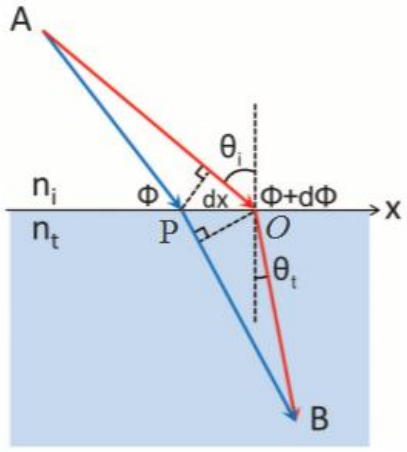

Figure 3.6 Schematic of the generalized Snell's law of refraction[43].

Let us assume two points, A and B, and two infinitely close optical paths, APB and AOB, as shown in Figure 3-6. According to Fermat's law (light travels along the least optical path), the blue and red propagation paths APB and AOB are equal. The phase difference $\Delta\phi$ between A and B can be expressed as:

$$\Delta\phi = \int_A^B n(r)\, dx \tag{3-1}$$

where $n(r)$ is the local index of refraction and r is the vector of propagating path. When an abrupt phase shift $\phi(r)$ is introduced in the optical path by suitably arranging the interface between two media, the total phase shift can be described as:

$$\Delta\phi = \phi(r) + \int_A^B n(r)\, dx \tag{3-2}$$

Two paths are infinitely close to the actual light path, so dx represents the distance between the crossing points P and O at the interface. Then, the phase satisfies:

$$k_0 n_i \sin(\theta_i)\, dx + (\phi + d\phi) = k_0 n_t \sin(\theta_t) dx + \phi \tag{3-3}$$

where θ_i and θ_t are the angles of incident and refracted waves. n_i and n_t are the refractive indices of the two media and k_0 is the wave vector in free space.

If the phase gradient along the interface is set as constant, the general Snell's law of refraction can be deduced as:

$$\sin(\theta_t)n_t - \sin(\theta_i)n_i = \frac{\lambda}{2\pi}\frac{d\phi}{dx} \tag{3-4}$$

Similarly, the generalized Snell's law of reflection can be written as:

$$\sin(\theta_r)n_r - \sin(\theta_i)n_i = \frac{\lambda}{2\pi}\frac{d\phi}{dx} \tag{3-5}$$

where θ_r is the angle of a reflected wave and n_r is the refractive index of the medium in the reflective region ($n_r = n_i$).

Unlike the traditional reflection and refraction law, an artificial abrupt phase is introduced along the interface in the generalized Snell's law. Thus, the angle of refracted and reflected beam can take a desired value. Therefore, the flexible manipulation of electromagnetic waves can be easily achieved according to the generalized Snell's law.

3.3 Concept of directional beaming

In this section, I describe the theory of directional beaming from a subwavelength slit flanked by metasurfaces. The surface wave is generated by the subwavelength slit illuminated by an incident wave. With the momentum mismatch compensation provided by the phase gradients from the metasurfaces, the surface waves can be converted into a free-space beam propagating far away at a specific angle as illustrated in Figure 3-7.

Beaming is a phenomenon that can be considered opposite to the conversion process from radiating waves to surface waves. According to the generalized Snell's law as described in equation (3-5), the relationship between the incident and refracted waves can be described as:

$$k_t \sin(\theta_t) - k_i \sin(\theta_i) = d\phi/dx \tag{3-6}$$

where θ_i and θ_t are the angles of incident and refracted waves, respectively. k_i and k_t are the

wavenumber in incident and refracted region. In our design, $k_i = k_t = k_o = 2\pi/\lambda_o$, λ_o is the wavelength in free space. $d\phi/dx$ is the phase gradient applied to the metasurface. When the phase gradient of a metasurface is fixed, the critical angle for a surface wave generation can be calculated using the equation (3-6).

According to the reciprocity theory, surface waves can be converted to propagating waves at a specific angle. When we analyze the conversion from surface waves to radiated waves utilizing the generalized Snell's law, the incident wave is the surface wave and incidence angle θ_i is 90°. Hence, the generalized Snell's law can be rewritten as:

$$k_0 \sin(\theta) - k_{SW} = d\phi/dx \tag{3-7}$$

where k_{SW} and k_0 is the wavenumber of the surface wave and the radiated wave, respectively. θ represents the angle of the radiated wave in free space.

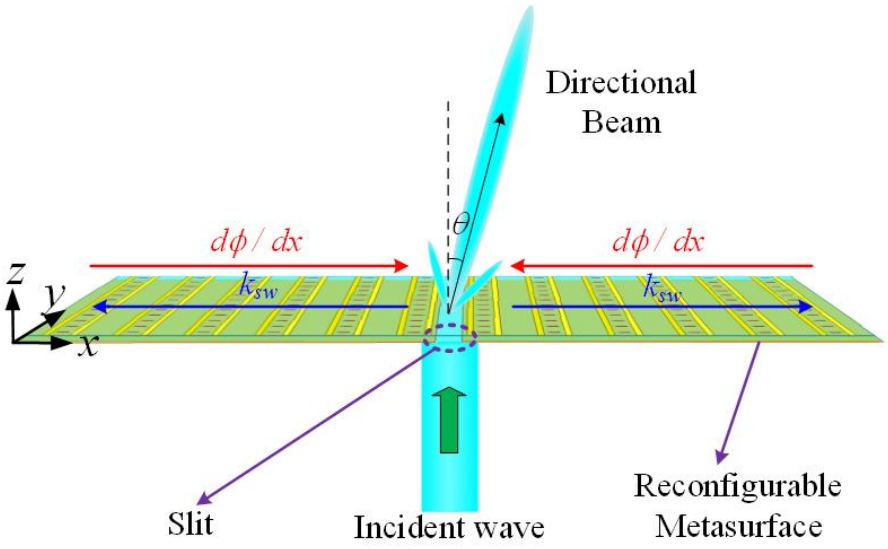

Figure 3.7 Illustrative sketch of directional beaming of diffracted electromagnetic waves from a subwavelength slit flanked by metasurfaces. A plane wave illuminates the slit, generating the surface waves[148].

Equation (3-7) shows that directional beaming of diffracted waves at an angle θ can be obtained by conversion of surface waves. In order to demonstrate that there are surface waves on the metasurfaces flanking the slit, we consider the configuration as displayed in Figure 3-8(a), where a similar constant phase is applied on both metasurfaces. The slit is illuminated by a plane wave at 10 GHz. As shown in Figure 3-8(b), a small part energy of

the incident wave passes through the slit and is diffracted in all directions. The surface wave, which is a part of the diffracted wave that is weaker than the incident wave, can be apparently observed on the surface of the metasurfaces marked by the black dotted ellipse.

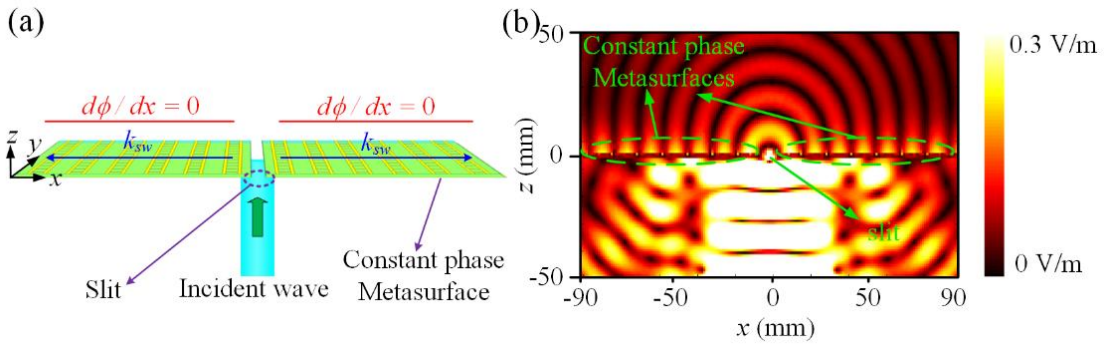

Figure 3.8 (a) Schematic of the diffraction from a slit flanked by two constant phase metasurfaces. (b) Simulated electric field showing the existence of surface waves propagating along the metasurfaces with constant phase[148].

3.4 On-axis beaming

As discussed in the above section, the surface wave propagating along the metasurfaces flanking the slit can be converted to a propagating wave by compensating the momentum mismatch. To realize the directional beaming at boresight in free space, the angle of radiated wave θ is set to 0°. Therefore, according to equation (3-7), the 0° directional beaming at different frequencies must satisfy:

$$k_{SW} + d\phi/dx = 0 \tag{3-8}$$

where k_{SW} varies with the operating frequency shift.

For a possible demonstration of the beaming feature, an implementation with the 1D reconfigurable metasurface designed and presented in Chapter 2 is considered. According to the reciprocity theory, the surface wave propagating along metasurface can be converted into a radiation wave in the position of dip with a phase gradient to compensate momentum mismatch between the surface wave and radiation wave. Therefore, the supercell that has to be designed for a specific phase gradient must show a minimum in the reflection amplitude. It should be noticed that there is no formula for the relationship between the phase gradient

and the dip position. I therefore have to numerically optimize the phase gradient to match the target dip position. A supercell composed of 3 unit cells is thus designed for the reflection coefficient curve employing the finite element method based HFSS software as shown in Figure 3-9(a). A Floquet port on the top face is used as a plane wave source with an *x*-polarized electric field and the incident angle of the plane source varies in *xoz* plane within a range from -40° to 40°. The reason why I did not just fix the incident angle of plane waves to 0° (similar to the single unit cell simulation) is that I need to find the dip position in the reflection amplitude curve. Periodic boundary conditions are applied along the *x*- and *y*-directions.

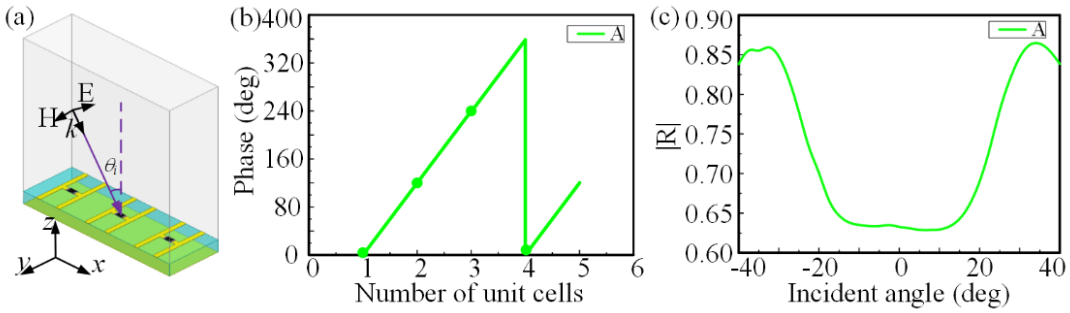

Figure 3.9 (a) Supercell illuminated by an incident plane wave with the incident angle changing from -40° to 40°. (b) Phase gradient of configuration 'A'. (c) Reflection coefficient curve of phase configuration 'A' corresponding to the on-axis beaming at 10 GHz.

To realize the on-axis beaming from the slit illuminated by a plane wave, the phase configuration 'A' is designed and optimized at 10 GHz as shown in Figure 3-9(b). The phase gradient of configuration 'A' ($d\phi/dx = 1.67k_0$), can be calculated by dividing the total phase difference on the supercell over the dimension of the supercell along the phase change direction as summarized in Table 1. The simulated reflection coefficient curve of phase configuration 'A' is depicted in Figure 3-9(c). The distinct phase dip, which indicates that a portion of the incident wave is converted into surface waves at this point, can be observed at 0°. The incident wave and converted surface wave satisfy equation (3-8) at the position of the 0° dip such that the propagation constant k_{SW} of $-1.67k_0$ is equal to the negative phase gradient ($k_{SW} = -d\phi/dx$). Here, the negative sign of k_{SW} denotes the direction of propagation constant is opposite to the phase gradient. According to the reciprocity theory, the deflection angle θ of the radiated wave is 0° (on-axis) due to the fact that the phase gradient can be set equally opposite to the propagation constant of the surface wave. Otherwise, surface waves

are bounded on the metasurface and cannot be converted into radiation waves.

Table 3.1 Parameters of the metasurface for beaming in boresight direction at 10 GHz

Scenario	Unit cells	Phase (deg)	$d\phi/dx$ / k_{sw}	Capacitance (pF)	Bias voltage (V)
No beaming	Cell 1	240	$1.67k_0$ /$1.67k_0$	0.28	4.7
	Cell 2	120		0.14	20
	Cell 3	0		0.24	6.9
A	Cell 1	0	$1.67k_0$ / - $1.67k_0$	0.24	6.9
	Cell 2	120		0.14	20
	Cell 3	240		0.28	4.7

To numerically verify the theory of directional beaming, simulations are performed and the corresponding simulation configuration is presented in Figure 3-10(a). I consider the designed 1D reflective reconfigurable metasurface, which has been presented in chapter 2, to realize the directional beaming. Therefore, a subwavelength slit along the *y*-direction should be made in the center of the bottom metallic layer of the reconfigurable metasurface, allowing the diffraction with the incident wave illuminating the slit. The dimension of the unit cell has been described in chapter 2, so the maximum width of the slit w_s can be 3.1 mm for our designed metasurface. A balance between the energy passing through the slit and the phase response of the unit cell is made such that the width slit is 2.2 mm. As we can observe, a single row (30 unit cells) of the metasurface (30 × 30 unit cells) with periodic boundary conditions applied along the *y*-direction is used to simulate its operation. In the case of a single row, the simulation time is significantly reduced due to the lower number of lumped *RLC* elements used to model the varactor diode.

The simulations of no beaming and on-axis beaming scenarios are performed with the capacitance values applied to the meta-atoms of the reconfigurable metasurface. When the phase gradient 'A' has the same direction as the propagation constant of the surface wave, the surface wave is bounded on the metasurface as shown in Figure 3-11(a) due to $k_{SW} + d\phi/dx = 3.34k_0$. However, when I set the phase gradient 'A' in a direction that is opposite to k_{SW}, the on-axis beaming can be observed as illustrated in Figure 3-11(c) due to $k_{SW} + d\phi/dx = 0$ being satisfied. Besides, the simulated far-field radiation pattern of the phase configuration 'A' at 10 GHz is shown in Figure 3-11(e). Although there are side lobes, we can observe the main lobe appearing at 0°.

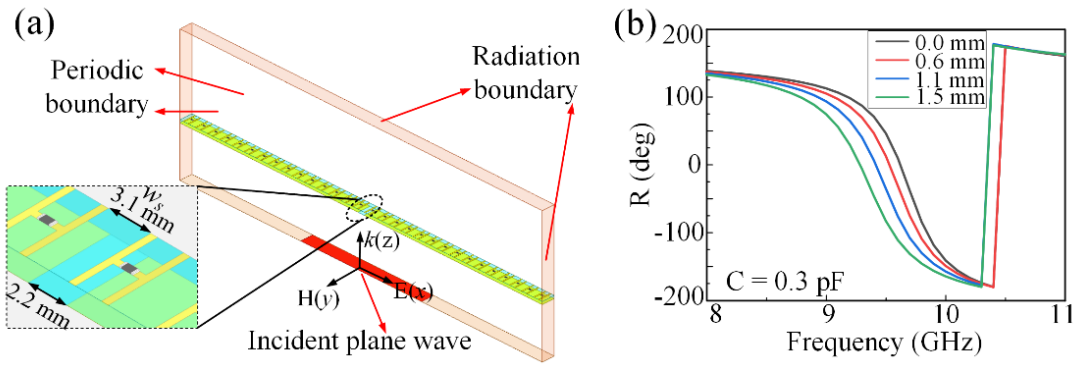

Figure 3.10 (a) Simulation configuration for the directional beaming from a subwavelength slit. (b) Reflection phase responses of the unit cell for the four values $w_s/2$ = 0 mm, 0.6 mm, 1.1 mm, and 1.5 mm.

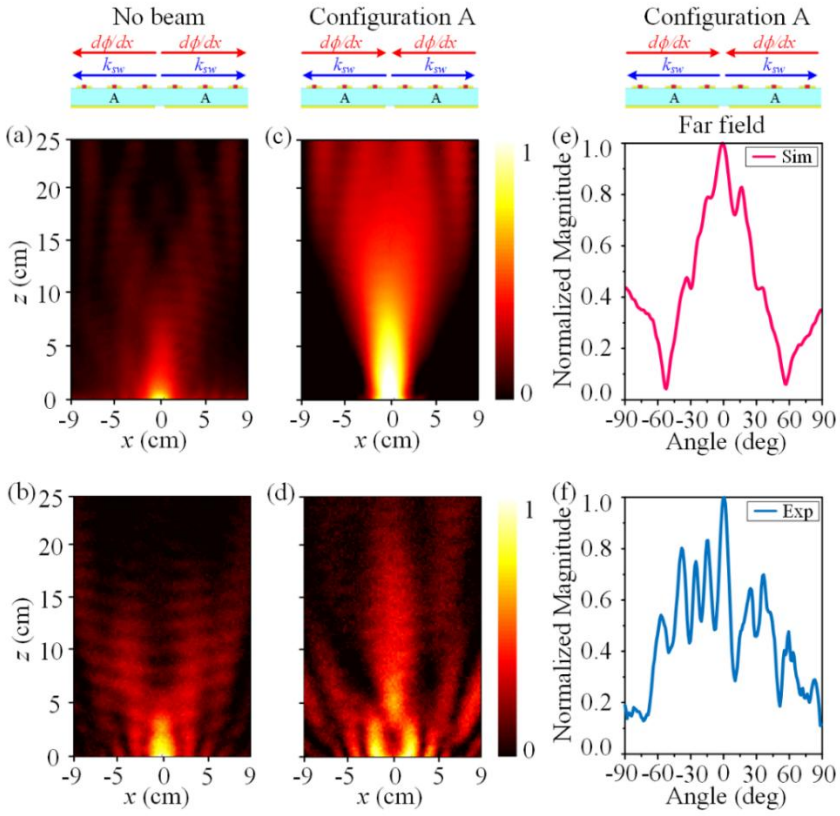

Figure 3.11 Simulated and measured near-field magnitude distributions and far-field radiation patterns at 10 GHz. (a)-(b) Near-field magnitude distribution of no beaming scenario. (c)-(d) Near-field magnitude distribution of on-axis beaming scenario. (e)-(f) Radiation pattern of on-axis beaming scenario.

To experimentally validate the concept of directional beaming, the fabricated one-dimensional reconfigurable metasurface is used for the measurements with a subwavelength slit on the bottom layer of metasurface as presented in Figure 3-12(b), where the dimension of this slit along the *y*-direction is 2.2 mm. Although I have described the measurement setup in chapter 2, it should be noticed that this setup is slightly different from that in chapter 2 due to the fact that the horn antenna and probe are placed on two sides of the metasurface (in a transmission measurement configuration). The experimental near-field measurements are carried out in the anechoic chamber and the schematic of the measurement setup of the directional beaming is depicted in Figure 3-12(c). A horn antenna used as the source of an incident wave is placed on the bottom side of the reconfigurable metasurface. The probe utilized to collect the phase and magnitude information of the electric field is placed on the varactor diode side of the metasurface and is fixed on computer-controlled translation stages allowing a scanning area of 180 mm × 250 mm for this measurement. Both the probe and horn antenna are connected to the two ports of a vector network analyzer.

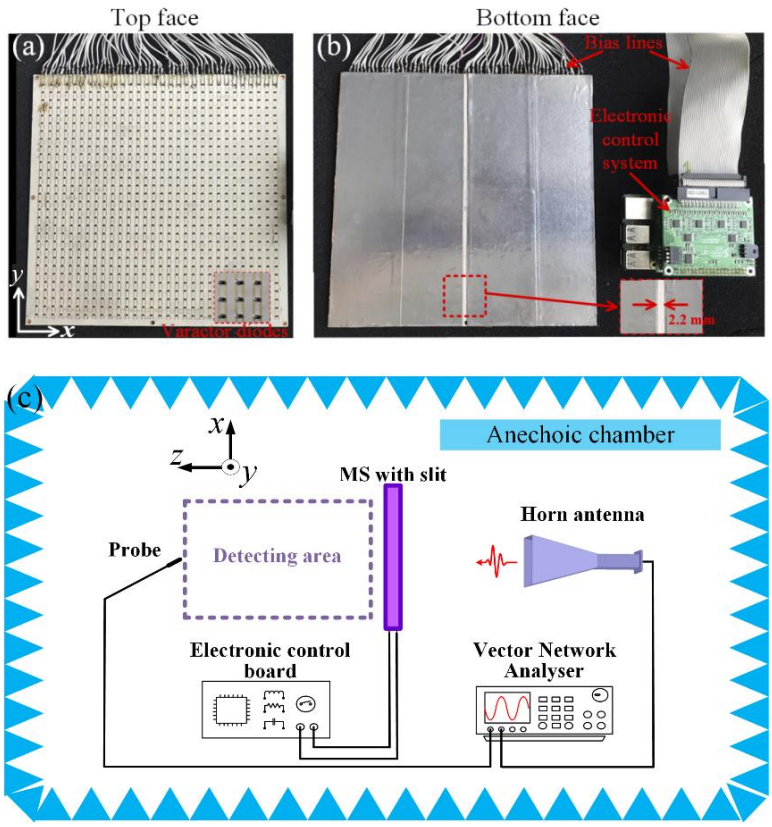

Figure 3.12 Photography of metasurface with a subwavelength slit on the background film. (a)Top face of the metasurface. (b) Bottom face of the metasurface. (c) Schematic of the experimental near-field measurement.

To achieve the boresight beaming in the experimental measurement, the voltage distribution corresponding to phase configuration 'A' is calculated according to the relationship extracted between phase and voltage of the unit cell, as discussed in Chapter 2 and shown in Table 1. When we apply the corresponding DC bias voltages on the reconfigurable metasurface, the phase gradient can be realized on the metasurface. The corresponding measured near-field and far-field results are shown in Figure 3-11(d)-(f), where we can see a good agreement with the simulations. However, compared to the simulations, more side lobes can be observed in measurements. The difference can be due to the imperfect flanking of the slit, since the unit cell which is on each side of the slit does not have the same period as the other cells. Indeed, since in reality we do not have two metasurfaces flanking the slit but only one with a slit made in the middle between two cells, the period of the cell on each side of the slit is reduced (see Figure 3-10).

3.5 Frequency agility

In this section, I verify the broadband property of the designed one-dimensional reconfigurable metasurface. Here, the on-axis directional beaming is further achieved at 9 GHz, 11 GHz, and 12 GHz.

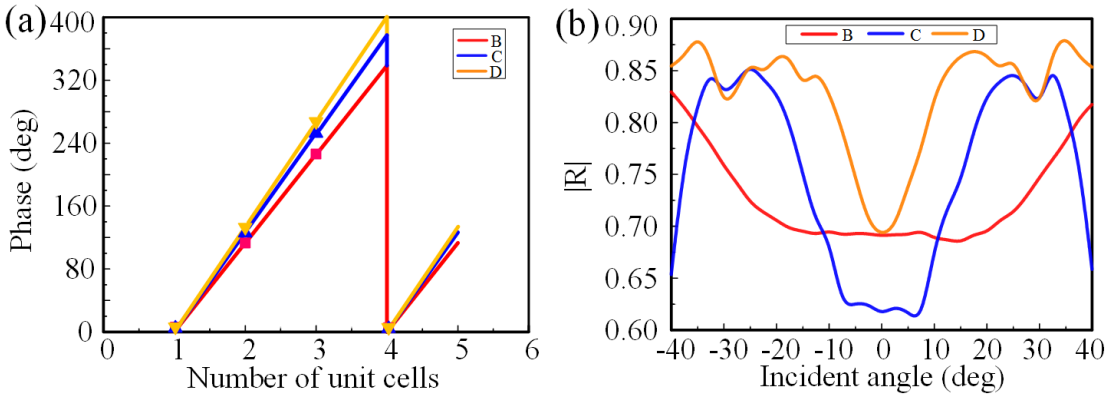

Figure 3.13 (a) Phase gradients of configurations 'B' to 'D'. (b)Reflection coefficient curves of configurations 'B' to 'D' corresponding to the on-axis beaming at 9 GHz, 11GHz and 12 GHz.

The supercells composed of 3 unit cells are designed and simulated for the three reflection coefficient curves corresponding to phase configurations 'B', 'C' and 'D'. The optimized phase gradients of configurations 'B', 'C' and 'D' are shown in Figure 3-13(a). The simulated reflection curves of the three configurations are displayed in Figure 3-13(b),

where the dips appear at 0°. The phase gradients of configurations 'B' to 'D' can be calculated as $1.749k_0$, $1.598k_0$, and $1.543k_0$. According to equation (3-8), the corresponding propagation constant k_{SW} of configurations 'B' to 'D' is respectively $-1.749k_0$, $-1.598k_0$, and $-1.543k_0$.

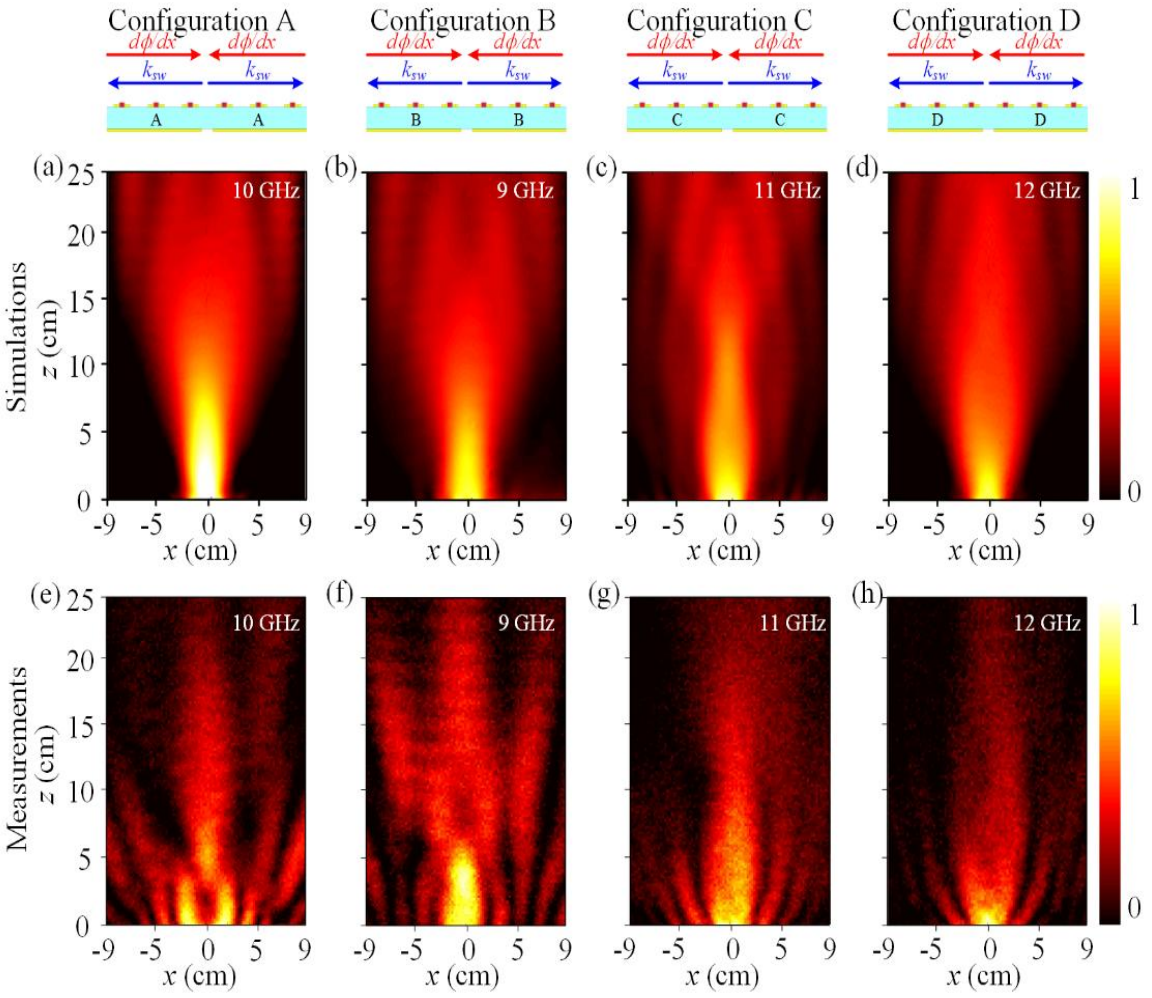

Figure 3.14 Simulated and measured results at different frequencies. (a)-(d) Simulated near-field magnitude distributions of on-axis beaming in *xoz* plane. (e)-(h) Measured near-field magnitude distributions of on-axis beaming in *xoz* plane. (i)-(l) Far-field radiation pattern at different frequencies.

By setting phase gradients opposite to propagation constant of k_{SW} on the two parts of the reconfigurable metasurface surrounding the subwavelength slit, the simulations of on-axis beaming are carried out at 9 GHz, 11 GHz, and 12 GHz, respectively. To make a clear comparison, the simulated on-axis beaming of the phase configurations 'A' to 'D' corresponding to 9 GHz, 10 GHz, 11GHz, and 12 GHz are displayed in Figures 3-14(a)-(d), where the distinct beams can be observed in the 0° direction at the four frequencies.

Table 3.2 Parameters of the metasurface for the beaming in boresight direction at different frequencies.

Configurations	Unit cells	Phase (deg)	$d\phi/dx$ / k_{sw}	Capacitance (pF)	Bias voltage (V)
B (@ 9 GHz)	Cell 1	0	1.75k_0 /-1.75 k_0	0.47	3
	Cell 2	113		0.3	13.3
	Cell 3	226		0.6	1.9
C (@ 11 GHz)	Cell 1	0	1.60k_0 /-1.60 k_0	0.15	12.4
	Cell 2	117		0.36	0
	Cell 3	233		0.17	7.4
D (@ 12 GHz)	Cell 1	0	1.54k_0 /-1.54 k_0	0.11	20
	Cell 2	133		0.65	0
	Cell 3	267		0.12	14.8

Table 3.3 Parameters of the metasurface for the 20^o beaming at 10 GHz.

Configurations	Unit cells	Phase (deg)	$d\phi/dx/k_{sw}$	Capacitance (pF)	Bias voltage (V)
E	Cell 1	0	1.25k_0/-0.91k_0	0.244	6.9
	Cell 2	90		0.197	19.7
	Cell 3	180		0.389	2
	Cell 4	270		0.272	5.2
F	Cell 1	40	0.83k_0/-1.17k_0	0.23	8.5
	Cell 2	100		0.1847	20
	Cell 3	160		0.625	0
	Cell 4	220		0.3	3.8
	Cell 5	280		0.2684	5.4

The frequency agility of the fabricated reconfigurable metasurface at different frequencies is experimentally validated for beaming. Three voltage distributions corresponding to the different configurations, as summarized in Table 2, are symmetrically applied on the two parts of the one-dimensional reconfigurable metasurface flanking the subwavelength slit for boresight beaming at 9 GHz, 11 GHz and 12 GHz. Figures 3-14(e)-(h) show the measured beaming in the boresight direction at 9 GHz, 10 GHz, 11 GHz, and 12 GHz, respectively.

All of these results validate the on-axis beaming from a subwavelength slit through the

use of phase-gradient metasurface over a wide frequency band. Besides, in the next subsection, the off-axis directional beaming is studied.

3.6 Off-axis beaming

I further analyze the off-axis beaming from the subwavelength slit surrounded by the reconfigurable metasurface. Three different deflection angles θ, including 20°, 30°, and 40°, are selected for the off-axis beaming. By optimizing the phase gradient of the supercell, the condition, $k_0 \sin(\theta) - k_{SW} = d\phi/dx$, can easily be satisfied to achieve the off-axis directional beaming.

Table 3.4 Parameters of the metasurface for the 30° beaming at 10 GHz.

Configurations	Unit cells	Phase (deg)	$d\phi/dx/k_{sw}$	Capacitance (pF)	Bias voltage (V)
G	Cell 1	0	$1.18k_0$ /-$0.68k_0$	0.244	6.9
	Cell 2	86.7		0.201	16
	Cell 3	173.4		0.4235	1.8
H	Cell 1	30	$0.92k_0$/-$1.42k_0$	0.264	8
	Cell 2	294		0.234	5.6
	Cell 3	228		0.19	3.9
	Cell 4	162		0.616	0
	Cell 5	96		0.294	20

In order to achieve the off-axis directional beaming at 20°, 30°, and 40°, the configurations 'E'-'J' are designed and summarized in Tables 3.5, where the phase, capacitance values, and bias voltages of the different configurations are displayed. The optimized phase gradients of configurations 'E'-'J' are displayed in Figure 3-15(a). The simulated reflection responses of the configurations 'E'-'J' at 10 GHz versus the incident angle of a plane wave varying from -50° to 50° are depicted in Figure 3-15(b). The reflection dips in the reflection coefficient curves indicate where oblique incident waves are converted to surface waves. The realization of the off-axis beaming needs different phase gradients assigned on the two sides of the subwavelength slit. The phase gradients of configurations 'E' and 'F', $d\phi/dx$, are calculated as $1.25k_0$ and $0.83k_0$. According to the dip positions (θ) in the reflection curves and equation (3-7), the propagation constant k_{SW} of phase gradients 'E'

and 'F' are -0.908k_0 and -1.172k_0 at 10 GHz. By assigning the phase gradients E and F opposite with the direction of propagation constant k_{SW}, the 20° directional beaming can be realized. Similarly, the phase gradients and propagation constants of configurations 'G'-'J' are calculated and summarized in Tables 3.4 and 3.5.

Table 3.5 Parameters of the metasurface for the 40° beaming at 10 GHz.

Configurations	Unit cells	Phase (deg)	$d\phi/dx/k_{sw}$	Capacitance (pF)	Bias voltage (V)
I	Cell 1	0	1.11k_0/-0.47k_0	0.244	6.9
	Cell 2	85		0.203	15
	Cell 3	170		0.39	1.5
	Cell 4	255		0.3	5
J	Cell 1	0	0.83k_0/-1.47k_0	0.24	6.9
	Cell 2	60		0.22	10.5
	Cell 3	120		0.13	20
	Cell 4	180		0.39	2
	Cell 5	240		0.29	4.6
	Cell 6	300		0.26	5.7

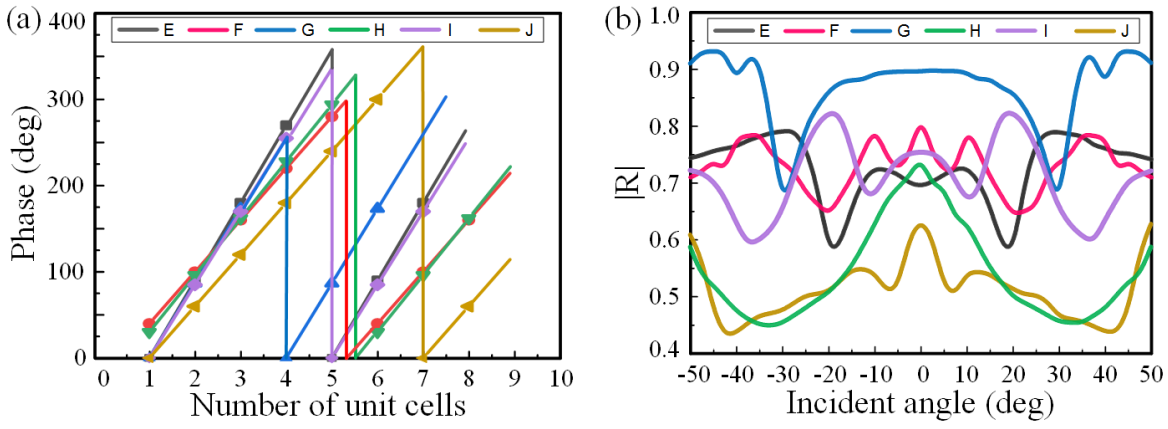

Figure 3.15 (a) Phase gradients of configurations 'E' to 'J'. (b) Reflection efficient curves of configurations 'E' to 'J' utilized for the off-axis beaming. The phase configurations 'E' and 'F', 'G' and 'H', and 'I' and 'J' are used for the directional beaming at 20°, 30°, and 40°, respectively.

The numerical simulations of the off-axis beaming are carried out with the software HFSS by assigning the appropriate capacitance values on the metasurface. The capacitance values of the phase gradients 'E'-'J' are calculated and summarized in Table 3-5. By applying the phase gradients 'E' and 'F' opposite to the propagation constant of the surface wave, the 20° beaming can be achieved at 10 GHz as shown in Figure 3-16(a). Likewise, when the phase gradients 'G'-'J' are assigned opposite to the propagation constant of the surface wave, the 30° and 40° beaming are realized at 10 GHz as displayed in Figures 3-16 (b) and (c).

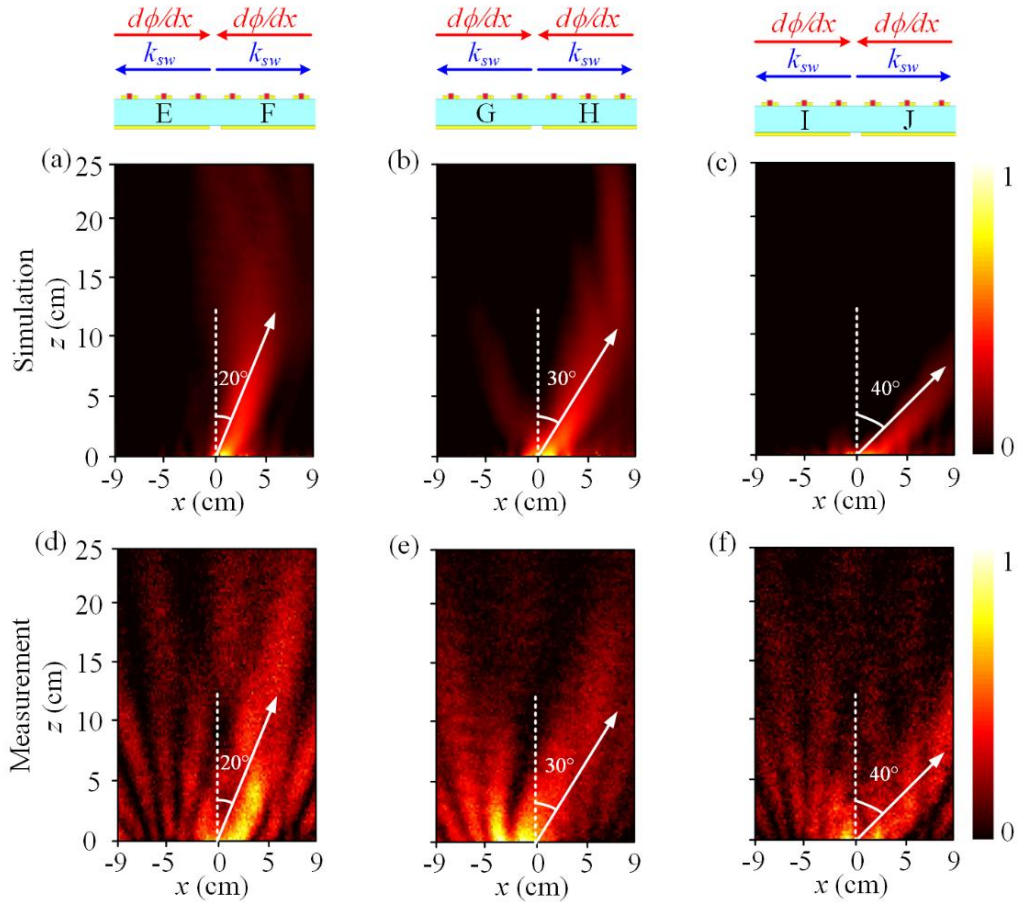

Figure 3.16 Simulated and measured results of off-axis beaming with deviation angles of 20°, 30°, and 40° at 10 GHz. (a)-(c) Simulated near-field results in *xoz* plane. (d)-(e) Measured near-field results in *xoz* plane. (g)-(i) Normalized far-field radiation patterns.

I use the fabricated one-dimensional reconfigurable metasurface to validate the method of realizing the off-axis directional beaming from a slit surrounded with metasurface. The bias voltages of the phase gradients 'E'-'J' are calculated and summarized in Table 3-5. By applying the bias voltages on the reconfigurable metasurface, the experimental

measurements of the off-axis beaming are implemented in the anechoic chamber. The corresponding measured near-field results are depicted in Figures 3-16(d)-(f). Although there are side lobes, we can see the main lobes direct to 20°, 30°, and 40°, respectively. The experimental measurements show a good agreement with the numerical simulations, validating the proposed off-axis beaming using the reconfigurable metasurface.

3.7 Conclusion

In this chapter, first, I realized the on-axis directional beaming of electromagnetic waves from a subwavelength slit by using the reconfigurable phase-gradient metasurface at 10 GHz. Then, I demonstrated that the on-axis beaming from a subwavelength slit can be achieved in a wide frequency band ranging from 9 to 12 GHz by varying the bias voltages applied to the metasurface. Finally, I demonstrated that the 20°, 30°, and 40° directional beaming can be achieved at 10 GHz by assigning asymmetrical phase gradients around the subwavelength slit. This interesting design can find applications in near-field flat sensors, lenses, hologram devices, and can be further extended to microwave leaky-wave antennas. In conclusion, these studies allow us to demonstrate that the diffracted electromagnetic waves from a subwavelength slit can be re-utilized for directional radiation. However, during those studies, I found that there is no formula for calculating the relationship between the phase gradient of a supercell and the position of the dip in a reflection curve. Therefore, lots of simulations are done to optimize the unit cells. In future works, it would be interesting to address this issue.

Chapter 4 Tailoring of diffraction-free beams

Diffraction is a fundamental physical property of EM beams in propagation. This property is unfavorable for long-distance and high-quality propagation of EM beams due to the fact that diffraction results in beam expansion and energy diffusion. Therefore, minimizing or even eliminating the diffraction effect of beams during propagation is of great significance to the rapid development of modern communication technology and energy transmission. The generation of diffraction-free beams provides a method to improve the propagation distance. The Airy beam and Bessel beam are two types of diffraction-free beams. In this chapter, I will explore the dynamic generation and control of the Airy beam and Bessel beam in the microwave domain using the two designed reconfigurable metasurfaces described in chapter 2.

4.1 Introduction on diffraction-free beams

Diffraction-free beams, whose main beam does not spread over travelling distances, have the ability to improve the propagation distance and thereby reducing the diffraction effect. The diffraction-free beams include Airy beams, Bessel beams, Mathieu beams, Weber beams, and so on. The Airy beam is a paraxial beam, which is calculated from the Schrödinger equation. The Bessel beams, Mathieu beams, and Weber beams are nonparaxial beams, which are the exact solutions of the Helmholtz equation[149]. In this chapter, I focus on the exploration of Airy beams and Bessel beams.

4.1.1 Airy beams

The Airy beam is a special kind of diffraction-free beam, which has emerged in recent years. The related research on Airy beams mainly focuses on the infrared and visible light domains, which can be dated back to 1979. Berry *et al.* theoretically demonstrated that the Airy function is the solution of the Schrödinger equation and that the waves satisfying the distribution of the Airy function exhibit the diffraction-free and self-bending properties[150]. However, the ideal diffraction-free Airy beam is difficult to be fulfilled in physics due to the fact that it is associated with infinite energy. In 2007, Siviloglou *et al.* realized the Airy beam carrying finite energy in the optical domain by truncating the ideal Airy beam[151-152]. The ideal infinite-energy Airy beam is shown in Figure 4-1(a), and the finite-energy Airy

truncated by the exponential function is presented in Figure 4-1(b). The distinct parabolic propagation trajectory of the finite-energy Airy beam can be observed and the quasi-invariant intensity can maintain several diffraction lengths, which means that the truncated Airy beam exhibits the good characteristics of the infinite-energy Airy beam over a finite distance. Since then, Airy beams has attracted enormous attention, and various applications have been explored and implemented, such as optical micromanipulation[153-157], laser micromachining[158-160], forming optical bullet[161-164], and microscopy[165-168].

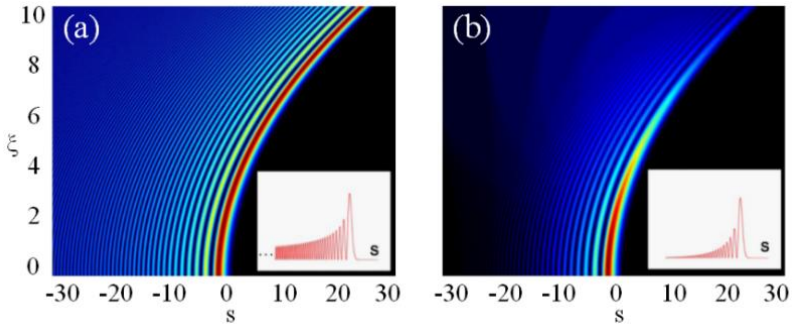

Figure 4.1 Simulations of Airy beam. (a) Ideal Airy beam with infinite energy. (b) Finite-energy Airy beam by truncating the ideal Airy beam. The insets show the corresponding input intensities[152].

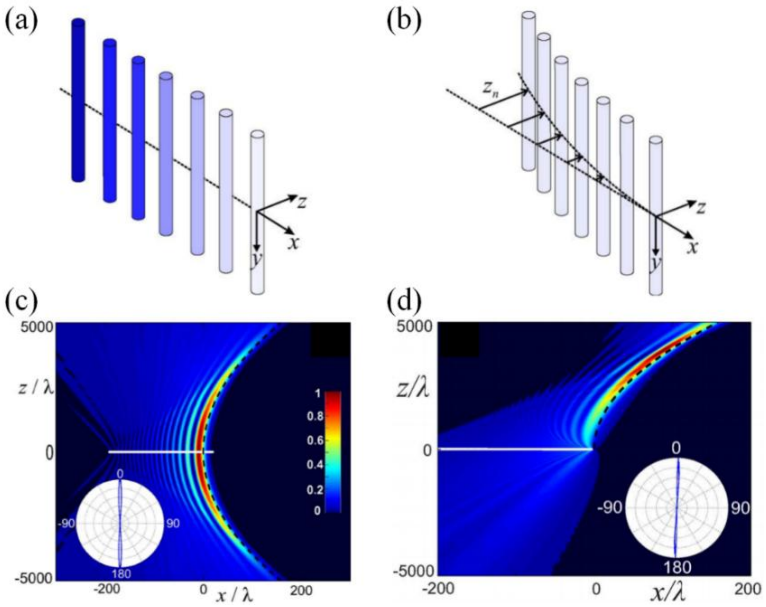

Figure 4.2 (a) Linear phased array with the chirp variation depicted by a color gradient. (b) In-phase array with the curved distribution. (c) Finite-energy Airy beam generated by the linear phased array. (d) Finite-energy Airy beam generated by the in-phase curved array[169].

Outstanding research works on Airy beams have also been performed in the microwave domain. I. D. Chremmos *et al.* introduced the Airy beam in the radiofrequency regime by designing a Fresnel zone abruptly-autofocusing antenna array[169]. As illustrated in Figure 4-2, two antenna arrays were proposed for the Airy beam generation with a pre-specified parabolic trajectory. The first array has a power-law phase variation with a linear phased array, while the second one is a curved array with in-phase radiating antennas. The two mirror-symmetry Airy beams are realized in the two spaces $z > 0$ and $z < 0$ by utilizing the linear phased array located in the $z = 0$ plane, as shown in Figure 4-2(c). The Airy beam is only achieved in the space $z > 0$ for the in-phase array arranged in a curve due to the fact that the symmetry with respect to the $z = 0$ plane is broken, as presented in Figure 4-2(d). However, the Airy beam generated using these two antenna arrays is bounded in the longitudinal plane orthogonal to the antenna arms. To break this limitation, metasurfaces arranged in a plane are introduced to fulfill the Airy beam.

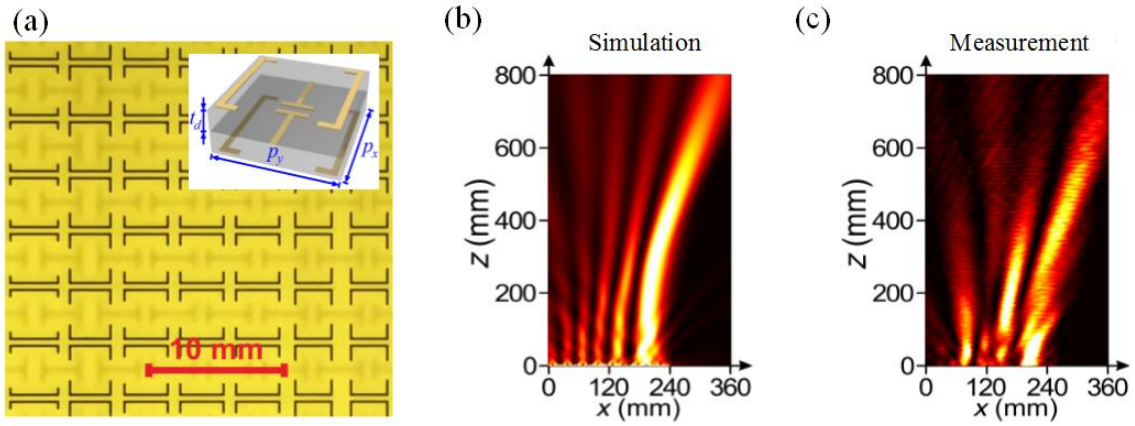

Figure 4.3 (a) A part of the fabricated Huygens' metasurface. The insert shows the unit cell comprising the Huygens' metasurface. (b)-(c) Simulated and measured Airy beam[170].

W. Hao *et al.* designed a Huygens' metasurface for the Airy beam generation[170]. The unit cell comprising the Huygens' metasurface is composed of a microstrip capacitance pattern sandwiched by a double-pair of U-shaped resonators, as shown in the inset of Figure 4-3(a). In this metasurface, the electric and magnetic responses of the metasurface can be independently controlled by elaborately changing the geometrical parameters. By tailoring the unit cells to imitate the electric field envelope of the Airy beam, both the simulated and measured Airy beams are achieved utilizing the Huygens' metasurface with high transmission efficiency, as presented in Figures 4-3(b) and (c). A clear parabolic trajectory

can be observed. In this design, the authors modulated both phase and amplitude for the generation of Airy beams. However, the Airy beam can be achieved by phase only modulation[171-173].

Z. Li *et al.* realized the Airy beam using the phase-only modulation and simultaneous phase and amplitude modulation[171]. The designed unit cell is composed of a rectangle bar and a substrate as shown in Figure 4-4(a). The phase and amplitude can be tailored independently by changing the rotation angle and length of the rectangle bar under a circularly polarized incidence. Figures 4-4(d) and (e) exhibit the simulated Airy beams with phase only modulation and simultaneous phase and amplitude modulation, respectively. We can see that the Airy beam generated using phase only modulation shows the diffraction-free and self-bending properties although the side lobes are worse than the Airy beam generated using simultaneous phase and amplitude modulation.

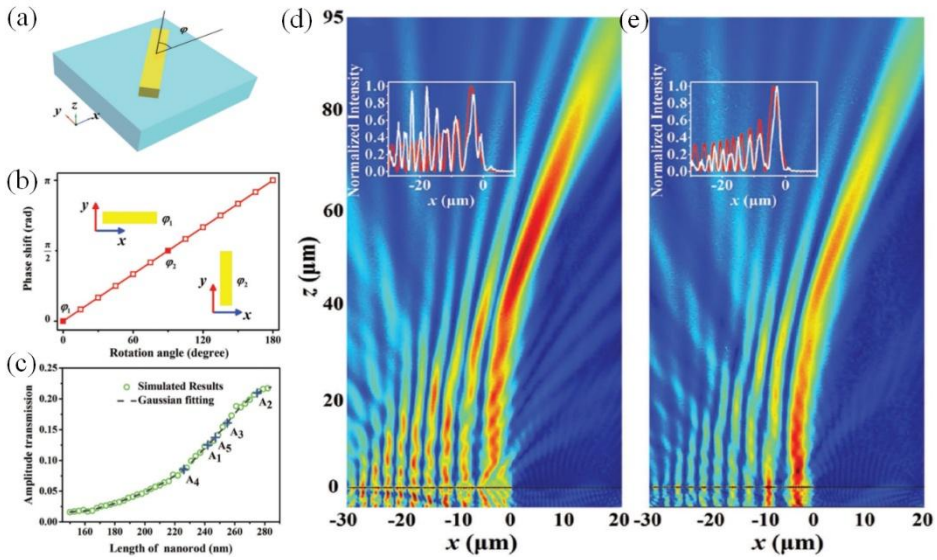

Figure 4.4 (a) Schematic of the unit cell. (b) Phase response versus rotation angle of rectangle bar. (c) Transmission amplitude response versus length of rectangle bar. (d) Simulated Airy beam using phase-only modulation. (e) Simulated Airy beam using both phase and amplitude modulation[171].

4.1.2 Bessel beams

The diffraction-free Bessel beam has been studied for decades. In 1987, Durnin *et al.* found a set of propagation-invariant solutions of free space Helmholtz equation and they first experimentally realized the zeroth-order Bessel beam by illuminating an annular slit with a plane wave[174]. Since then, Bessel beams have attracted a great deal of interest due

to their unique diffraction-free and self-healing properties. The diffraction-free feature of the Bessel beam means that the beamwidth maintains constant during propagation, while the self-healing property reveals that the propagating feature of the Bessel beam is not affected by a small obstacle placed on the propagation path of the main beam, as illustrated in Figure 4-5[175]. Those 'unusual' characteristics allow Bessel beams to be applied in the fields of laser machining[176-180], microscopy[181-185], microwave drilling[186-187], radar[188-189], and so on. To generate Bessel beams, plenty of methods were proposed including sub-wavelength apertures[190], resonant-cavity[191], spherical aberration[192], and axicon[193]. The structure of sub-wavelength apertures and resonant-cavity is simple and easily implemented, but they are inefficient for the utilization of incident waves due to the fact that only a part of the incident wave can pass through the apertures. The spherical aberration method has the advantage of high efficiency. However, it has the issue of complex manufacturing and complicated design parameters. For the axicon, although it has the advantage of high efficiency, it is not flat and the thickness is large.

To solve these issues of the traditional devices, metasurfaces with an axicon phase profile are used to generate the Bessel beam. In 2015, T. J. Cui *et al.* realized the Bessel beam by the backward leaky waves produced from a holographic metasurface in the microwave frequency regime, as shown in Figure 4-6(a)[194]. A monopole located in the center of the metasurface is used to excite the surface waves propagating along the metasurface, which can then be converted to leaky waves by appropriately arranging the surface impedance distribution. The surface impedance of the unit cell comprising the holographic metasurface can be tailored by changing the size of the metallic patch. A part of the fabricated metasurface is presented in Figure 4-6(c), and the corresponding measured near-field results of the Bessel beam are depicted in Figure 4-6(d), where the evident beam in the center can be seen along the *z*-axis.

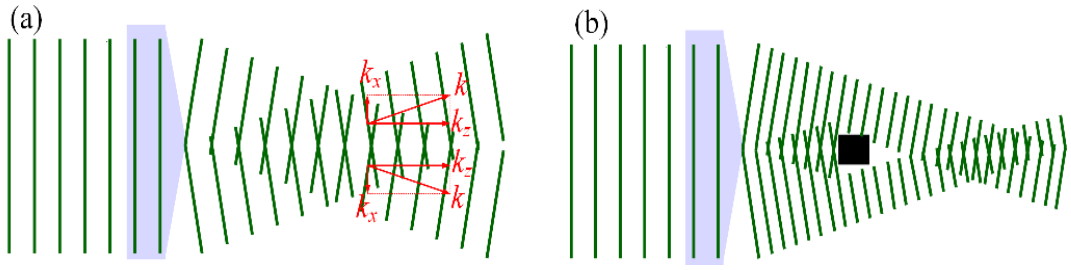

Figure 4.5 Schematic of the diffraction-free and self-healing properties. (a) Diffraction-free property. (b) Self-healing property[175].

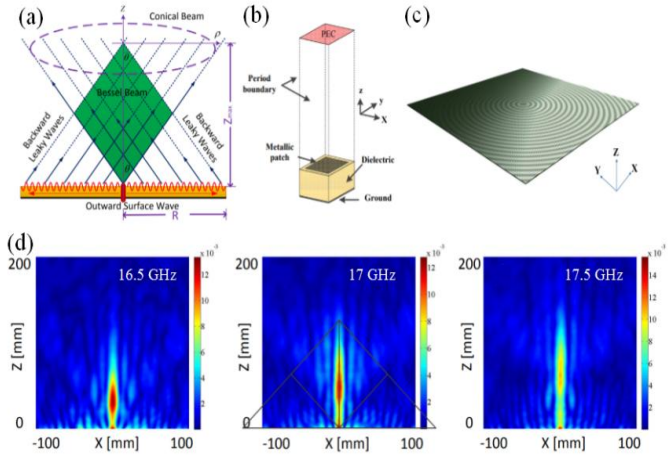

Figure 4.6 (a) Schematic of the Bessel beam generation using the holographic metasurface. (b) Schematic of the unit cell. (c) Fabricated holographic metasurface. (d) Measured near-field results at different frequencies[194].

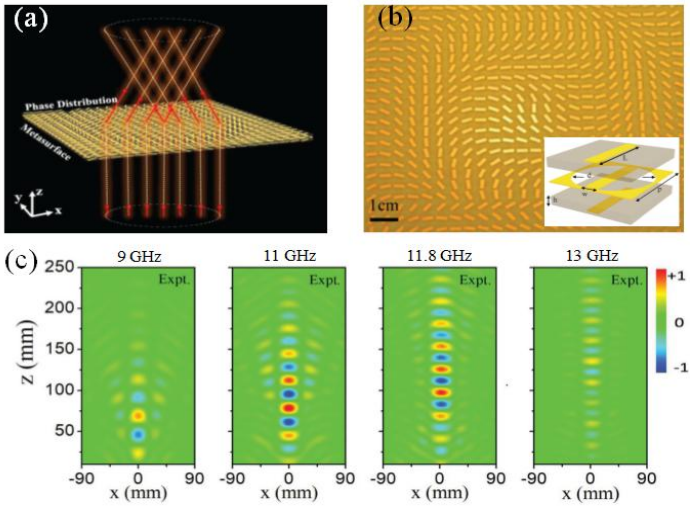

Figure 4.7 (a) Schematic of the Bessel beam generation using transmissive Pancharatnam-Berry metasurface. (b) Fabricated metasurface. (c) Measurements of the Bessel beam at different frequencies[195].

In 2018, L. Zhou's group proposed the ultra-thin transmissive Pancharatnam-Berry (PB) metasurface to generate Bessel beams in the microwave frequency band. The schematic of the Bessel beam generation is shown in Figure 4-7(a)[195]. The fabricated metasurface is presented in Figure 4-7(b), where the inset shows the unit cell is composed of three metallic pattern layers and two substrates. By changing the orientation of the metallic rectangle bars, the phase can be adjusted according to the PB phase mechanism. The experimental

measurements of the Bessel beams at different frequencies are performed and the corresponding real part of electric field distributions are shown in Figure 4-7(c), where the clear diffraction-free regions can be observed at 11 GHz and 11.8 GHz while the Bessel beams deteriorate at 9 GHz and 13 GHz. By using the ultra-thin transmissive PB metasurface, they achieved the Bessel beam generation in a wide frequency band ranging from 10.7 to 12.3 GHz.

However, these interesting Airy beam and zeroth-order Bessel beam generators based on passive metasurfaces are subjected to limited functionality. In this chapter, the dynamic generation and regulation of Airy beams and zeroth-order Bessel beams are fulfilled by utilizing the designed two reconfigurable metasurfaces. For our application of the zeroth-order Bessel beam generated using the one-dimensional reconfigurable metasurface, it is not rigorous to call it a Bessel beam due to the Bessel beam is generally a 2D rotationally symmetric beam. Therefore, this 1D Bessel beam is named as Bessel-like beam in this thesis.

4.2 Theoretical formulation of diffraction-free beams

4.2.1 Theoretical formulation of Airy beams

I begin the theory analysis by considering the normalized paraxial equation of diffraction (potential-free Schrödinger equation)[152]:

$$i\frac{\partial \phi}{\partial \xi} + \frac{1}{2}\frac{\partial^2 \phi}{\partial s^2} = 0 \tag{4-1}$$

where ϕ is the envelope of the electric field. $s = x/x_0$ is the dimensionless transverse coordinate. x_0 is the transverse constant. $\xi = z/kx_0^2$ is the normalized propagation distance along the z-direction. $k = 2\pi/\lambda_0$ is the wavenumber in free space. Airy wave packet, a solution for a quantum particle in free-space described by Schrödinger equation, can be used as an analogy for Airy beams. The electric field envelope of a finite energy one-dimensional (1D) Airy beam can be described as[152]:

$$\begin{aligned}\phi(\xi, s) = \mathrm{Ai}[s - (\xi/2)^2 + ic\xi]\exp[sc - ((c\xi^2)/2) - i(\xi^3/12) \\ + i((c^2\xi)/2) + i(s\xi/2)]\end{aligned} \tag{4-2}$$

where Ai is the Airy function, parameter c is the decay factor and it is a small positive value to ensure containment of the infinite Airy tail ($c \ll 1$). In order to generate the Airy beam

using an ultrathin metasurface, I study the initial field envelope of the Airy beam, which is expressed as:

$$\phi(x, \xi = 0) = \mathrm{Ai}(bx)\exp(ax) \tag{4-3}$$

where $b = 1/x_0$ and $a = c/x_0$.

As described in introduction, Airy beams can be generated by modulating only the phase along the metasurface. The 1-bit phase-coding scheme is utilized for the Airy beam generation in this chapter. I fix the phase equal π/2 when the amplitude of the Airy function is positive. In contrast, the phase is -π/2 for a negative value of the amplitude of the Airy function. The phase profile as a function of the *x*-coordinate is described as:

$$\varphi = \mathrm{angle}\,[\phi(x,\ \xi = 0)] - \pi/2 \tag{4-4}$$

When $\phi(x, \xi = 0)$ is a positive number, angle [ ] returns 0. On the contrary, when $\phi(x, \xi = 0)$ is a negative number, angle [ ] returns π. To simply explain the phase calculation, I take parameters $a = 4$ and $b = 44.1$ as an example due to the fact that the Airy function has exactly 5 zero points in the *x*-axis from -180 mm to 0 mm, as shown in Figure 4-8(a). The electric field envelope oscillating along the *x*-axis with the exponential decaying magnitude is represented by the red curve and the 1-bit coding phase profile calculated according to equation (4-4) is depicted by the blue line. It is clear that the phase alternates between the two values, $\pi/2$ and $-\pi/2$. Therefore, we can easily extract the phase profile of 1D Airy beams with any value of parameter *b*.

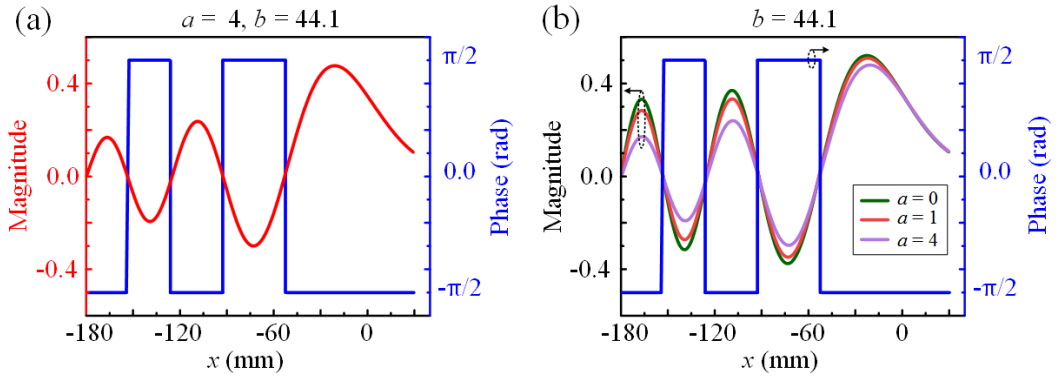

Figure 4.8 (a) Electric field envelope (red) and 1-bit coding phase profile (blue) of the 1D Airy beam. (b) Electric field envelopes for different parameter *a* with a fixed $b = 44.1$.

4.2.2 Theoretical formulation of Bessel beams

In order to get the electric field expression of Bessel beams, I begin with the wave equation in free space[196]:

$$\left(\nabla^2 - \frac{1}{c^2}\frac{\partial^2}{\partial t^2}\right)E(\mathbf{r},t) = 0 \tag{4-5}$$

The solution of equation (4-5) in the region $z \geq 0$ is[196]:

$$E(x, y, z \geq 0, t) = \exp[i(k_z z - \omega t)] \int_0^{2\pi} A(\phi)\exp[ik_r(x\cos\phi + y\sin\phi)]d\phi \tag{4-6}$$

where $k_z^2 + k_r^2 = k_0^2$, k_z and k_r is the propagation constant along the z-axis and transverse direction, respectively. k_0 is the propagation constant in free space. $A(\phi)$ represents the amplitude of the electric field and it is independent with ϕ in the cylindrical coordinate system. The zeroth-order Bessel function of the first kind can be expressed as[197]:

$$J_0(x) = \frac{1}{2\pi}\int_{-\pi}^{\pi}\exp(ix\sin\phi)\, d\phi \tag{4-7}$$

Then, the electric field of Bessel beams (4-6) can be rewritten as[196]:

$$\begin{aligned} E(r, z > 0, t) &= 2\pi A \exp[i(k_z z - \omega t)] \int_0^{2\pi} \exp[ik_r(x\cos\phi + y\sin\phi)]\frac{d\phi}{2\pi} \\ &= 2\pi A \exp[i(k_z z - \omega t)] J_0(k_r r). \end{aligned} \tag{4-8}$$

To generate Bessel-like beams, I use the metasurface in this thesis to imitate a one-dimension axicon, which is a traditional method to produce Bessel beams. The phase profile for a one-dimension Bessel-like beam can be expressed as:

$$\varphi(x) = |x|k_0 sin\theta \tag{4-9}$$

where θ represents the tilt angle of the phase profile. The coordinate origin is set at the center of the metasurface.

In this section, the phase distribution on the metasurface for the generation of 1D Airy beams and 1D zeroth-order Bessel-like beams is described. By applying the appropriate

phase profile on the metasurface, the corresponding beam can be achieved. In the next section, I will study the 1D diffraction-free beam utilizing the 1D reconfigurable metasurface.

4.3 Diffraction beams generation based on 1D reconfigurable metasurface

In this section, I will explore the generation and manipulation of diffraction-free beams using the 1D reconfigurable metasurface.

4.3.1 1D Airy beams generation and manipulation

4.3.1.1 Parametric study of 1D Airy beams

The theory of 1D Airy beams and the method to calculate the phase profile of these Airy beams have been described in the second section. In this part, parameter *b* that is related to the curvature of Airy beams is studied for the generation of Airy beams with a fixed parameter *a*. The curvature of 1D Airy beams increases with the parameter *b* according to the equation (4-2). The reason why I do not study parameter *a* is that I use the phase-only modulation method for generating Airy beams and parameter *a* has no influence on the phase distribution of Airy beams as shown in Figure 4-8(b), where the zero points of the electric envelopes do not change with the variation of the parameter *a*.

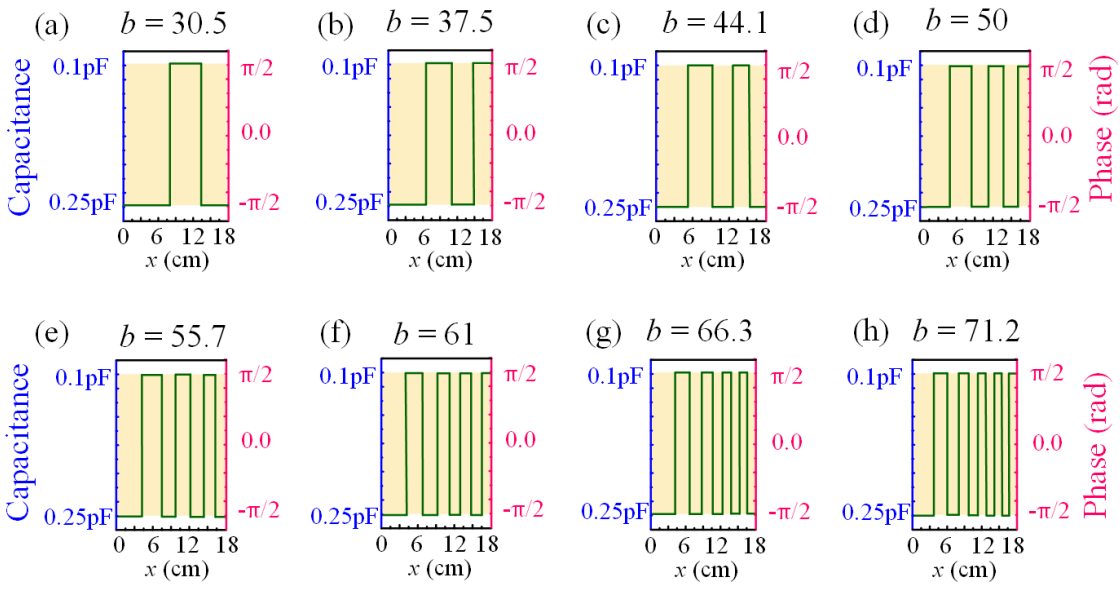

Figure 4.9 Phase distributions of Airy beams with different parameter values of *b* and fixed parameter *a* = 4. The section of the phase profile increases with the value of parameter *b*.

First, I calculate the phase profiles of the 1D Airy beams according to equation (4-4). For our Airy beam generator, the phase modulation is along the *x*-direction and there is no modulation in the *y*-direction. Eight parameter values of *b* are selected for the Airy beams generation with the decay factor *a* fixed as 4. The phase profile applied to the metasurface is represented by the green lines as presented in Figures 4-9(a)-(h). The phase profile of the Airy beam with parameter $b = 30.5$ is composed of three sections, including 30 unit cells in total. The section of the phase profile increases from 3 to 10 with the variation of parameter *b* from 30.5 to 71.2.

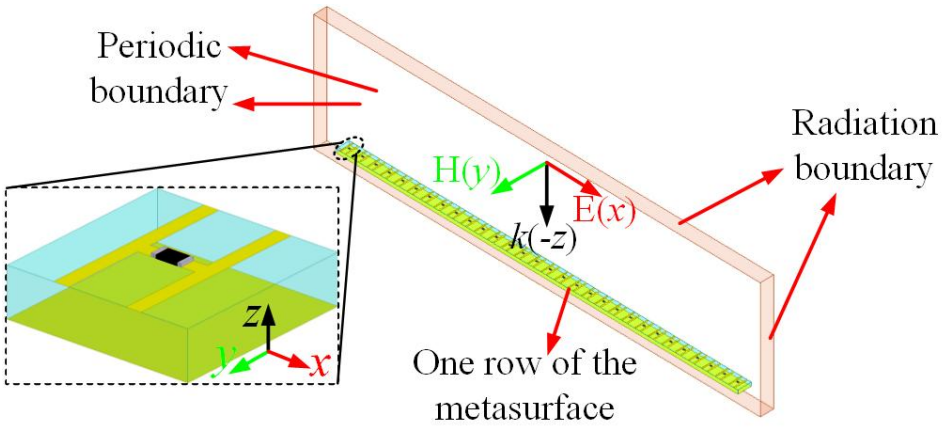

Figure 4.10 Schematic of the reconfigurable metasurface with only one line used for the 1D Airy beam generation. Inset shows the schematic of the tunable unit cell.

Then, I numerically investigate the 1D Airy beams with the different values of parameter *b*. To reduce the simulation time, a single row (30 × 1 unit cells) of the 1D reconfigurable metasurface (30 × 30 unit cells) are used for the simulations in HFSS, as shown in Figure 4-10. Periodic boundary conditions are applied on the two faces that are parallel to the *x*-axis and radiation boundary conditions are set on others faces represented by orange color. By applying the appropriate capacitance values on the metasurface, the numerical simulations of the 1D Airy beams are performed at 10 GHz. The corresponding simulated results of eight values of parameter *b* are depicted in Figure 4-11, where the white dotted lines in the bottom of subfigures represent the position of the metasurface. It is clear that the propagation trajectory of the main lobe of a 1D Airy beam is a curve. As parameter *b* increases, the degree of bending effect of the main lobe also increases. Besides, it is essential to point out that Airy beams are inherently paraxially limited. Therefore, when an Airy beam propagates along a parabolic trajectory and eventually bends into a large angle,

it will leave its domain of existence and diffraction eventually takes over. The curvature of the Airy beam with parameter $b = 71.2$ is so large that it reaches the paraxial approximation limit at a short propagating distance and diffracts quickly. However, the curvature of the Airy beam with parameter $b = 30.5$ is small and not easy to identify. Therefore, I select four from the eight Airy beams ($b = 44.1$, 50, 55.7, and 61) for the experimental validation.

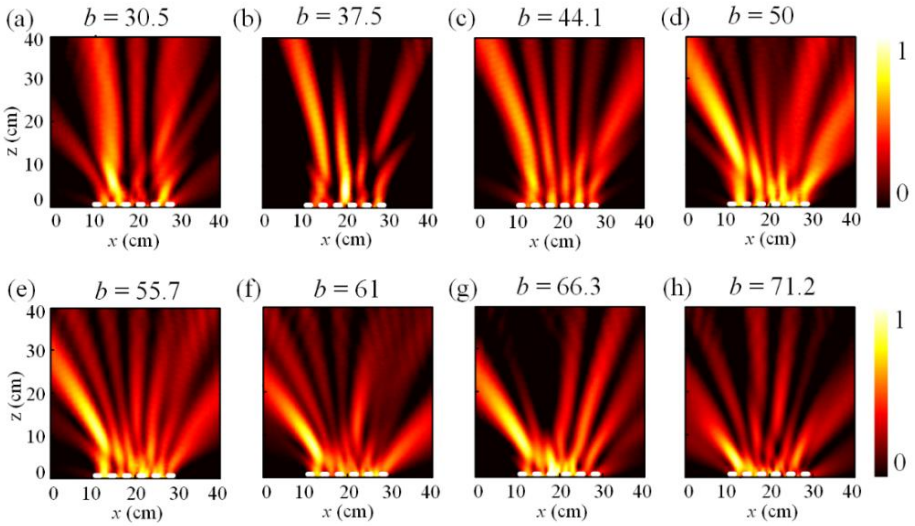

Figure 4.11 Simulated electric field distributions of the 1D Airy beams with eight values of parameter b at 10 GHz.

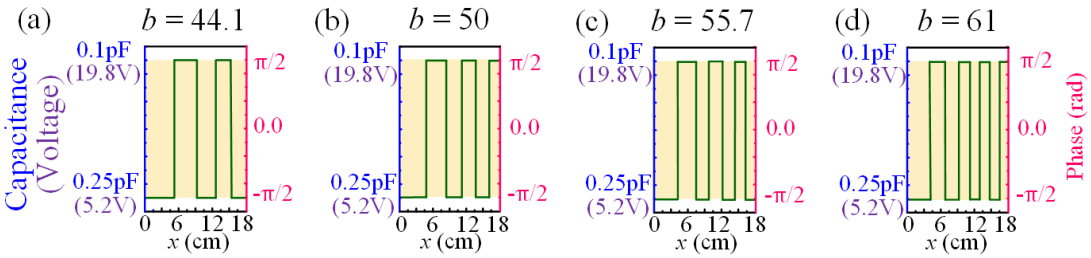

Figure 4.12 Phase, capacitance, and voltage profiles of the 1D Airy beams with four selected values of parameter b.

The fabricated 1D reconfigurable metasurface is used for the experimental verification of the propagation trajectory upon the value of parameter b. Four values of parameter b containing 44.1, 50, 55.7, and 61 are selected for the measurements of Airy beams in the anechoic chamber. The voltage profiles of the four values are calculated using Matlab

according to the relationship extracted between phase and voltage of the unit cell, and are denoted in Figure 4-12. The experimentally measured electric field distributions at 10 GHz are depicted in Figure 4-13. It is distinct that Airy beams are generated for the four values and the degree of curvature of the main lobe increases with an increasing value of *b*. The measured results show a good agreement with the numerical simulations. These results exhibit the influence of parameter *b* on the propagation trajectory of the 1D Airy beams and verify the dynamic control ability of our reconfigurable metasurface.

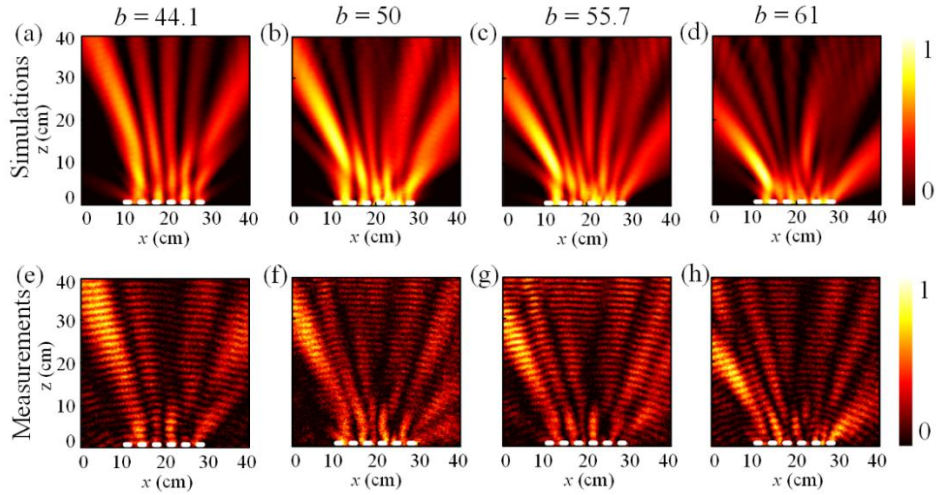

Figure 4.13 Normalized near-field results of Airy beam with four different values of parameter *b* at 10 GHz. (a)-(d) Simulated electric field distributions in *xoz* plane. (e)-(h) Measured electric field distributions in *xoz* plane.

4.3.1.2 Study of three properties of Airy beams

In this part, I investigate the properties of Airy beams, including diffraction-free, self-healing, and self-bending properties. The diffraction-free characteristic of Airy beams shows that the electric field distribution of the main lobe can remain unchanged during its propagation. The self-bending property means that the main lobe of Airy beams propagates along a parabolic trajectory. The self-healing property exhibits that the main lobe of Airy beams can rapidly be reconstructed after passing through a small metallic obstacle placed on the propagation path of the main lobe. The Airy beam with parameter $b = 44.1$ at 10 GHz is taken as an example.

First, I investigate the diffraction-free characteristic, which can be evaluated by the full width at half maximum (FWHM) of the main lobe of Airy beams. The simulated and measured values of FWHM versus the propagation distance are shown in Figure 4-14. We

can see that the average value of FWHM for the main lobe is around 3 cm at the initial stage of propagation. The diffraction-free region is defined as the zone where the maximum FWHM value is below 1.5 times the average FWHM value[170]. The diffraction-free property is evident in spite of a slight oscillation of FWHM appearing when the main lobe propagates. The yellow shadow represents the diffraction region. The diffraction-free property of the Airy beam with parameter $b = 44.1$ at 10 GHz can be well maintained within the propagation distance of $8.6\lambda_o$ along the z-direction (λ_o @10 GHz).

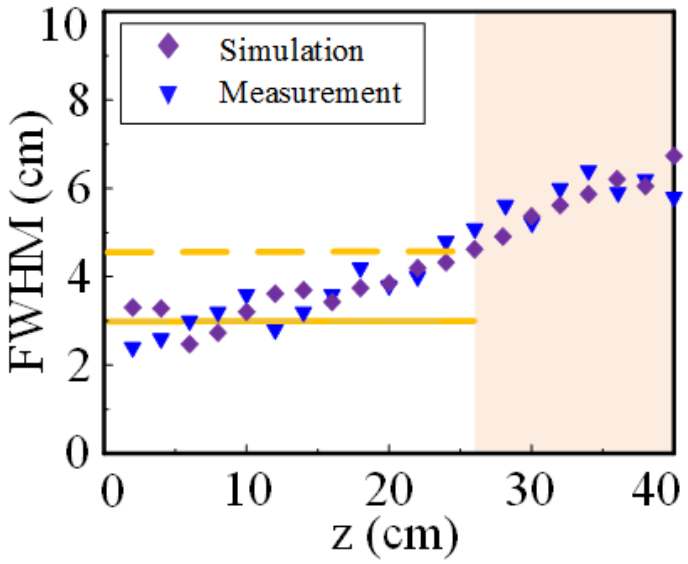

Figure 4.14 The FWHM of the main lobe of the Airy beam with parameter $b = 44.1$ at 10 GHz.

Different from the straight-line propagation properties of traditional waves in free space, the self-bending feature of Airy beams means that the trajectory of the main lobe is a curve, allowing a transverse offset of the main lobe. I use the deflection offset of the main lobe of Airy beams in the x-direction to evaluate the self-bending feature of Airy beams, which can be calculated by the difference between the center position of the main lobe and the initial position $x = 13$ cm ($b = 44.1$). The deflection offset Δd of the main lobe can be theoretically calculated as[152]:

$$\Delta d = \frac{z^2}{4k_0^2 x_0^3} \tag{4-10}$$

where $x_0 = 1/b \approx 22.7$ mm and k_0 is the wavenumber in free space. The theoretical prediction of the deflection offset of the main lobe is represented by the continuous pink

curve as shown in Figure 4-15. The simulated and measured deflection offsets are represented by purple rhombus and blue inverted triangle, respectively. The deflection offset non-linearly increases with the propagation distance, which reveals the parabolic trajectory of the main lobe of the Airy beam. We can see a good agreement among the simulation, measurement, and theoretical prediction, which verify the self-bending characteristic of Airy beams.

The self-healing property of Airy beams is typically demonstrated by placing a small metallic obstacle on the propagation path of the main lobe as shown in Figure 4-16(a). The metallic obstacle located at (x, y, z) = (12.4 cm, 0 cm, 2.6 cm) is a copper-based cube with dimensions $\lambda_o/2 \times \lambda_o/2 \times \lambda_o/2$ (λ_o @10 GHz). It is observed that the Airy beam is scattered by the obstacle locally and then recovers quickly after passing the obstacle with its diffraction-free characteristic well maintained in the simulation. The experimental measurement of the Airy beam with a metallic obstacle placed on the propagation path of the main lobe is carried out as shown in Figure 4-16(b). To reduce the complexity of the measurement, I measured the field beyond the obstacle and the recovered main lobe can also be clearly observed. Besides, the FWHM and deflection of the main lobe of the restructured Airy beam with parameter b = 44.1 is displayed in Figure 4-16(c) and (d), which agrees with the original Airy beam. The self-healing characteristic is well verified by our simulation and measurement.

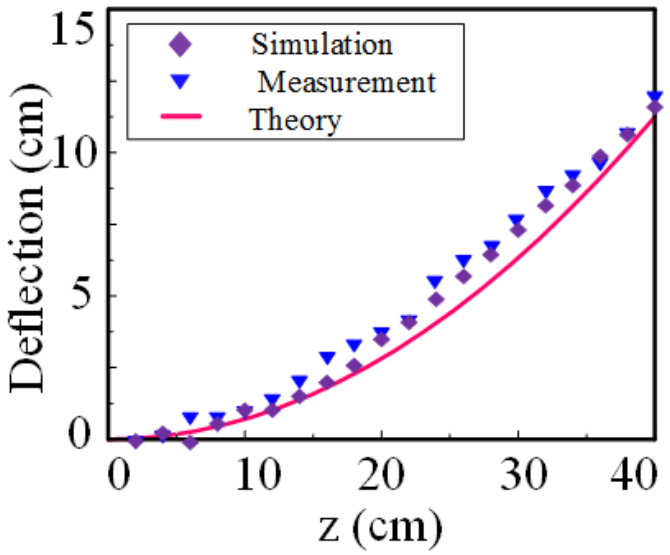

Figure 4.15 Self-bending property evaluated by the deflection offset of the main lobe of the Airy beam for parameter b = 44.1 at 10 GHz.

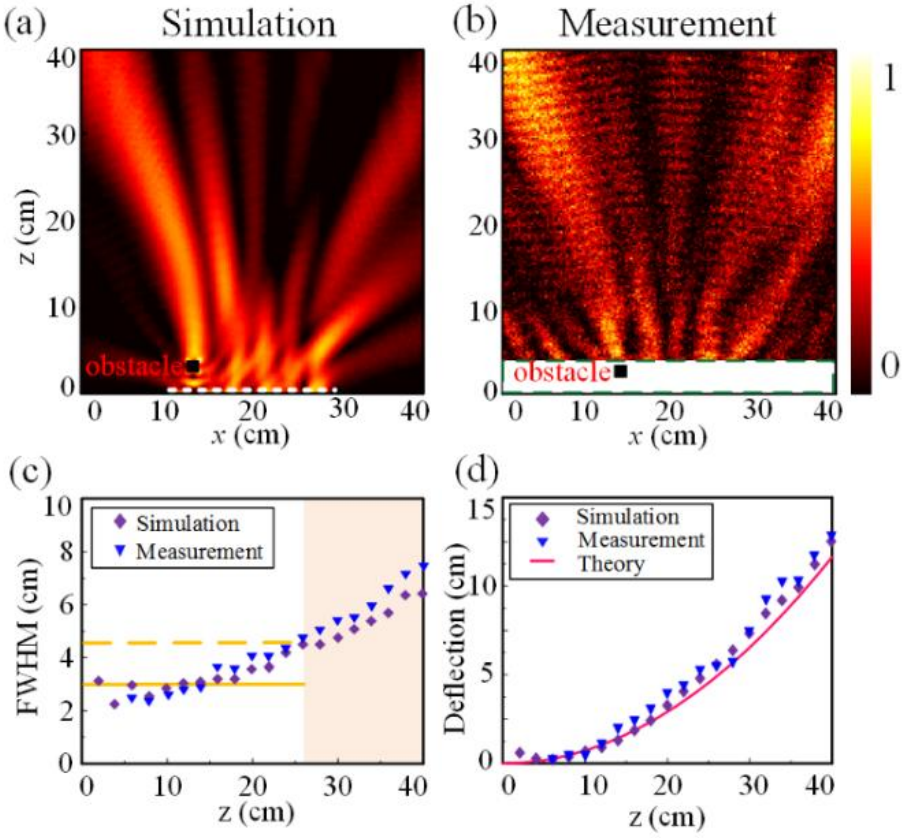

Figure 4.16 Simulated and Measured results of the Airy beam for parameter b = 44.1 with a metallic obstacle placed on the propagation path of the main lobe. (a) Simulated electric field distribution. (b) Measured electric field distribution. (c) FWHM of the main lobe. (d) Deflection of the main lobe in the x-direction.

However, all these studies above were fulfilled at a fixed frequency of 10 GHz. As our metasurface is reconfigurable, I will present the 1D Airy beam generation at multiple frequencies in the next part.

4.3.1.3 Frequency agility of the 1D Airy beam generator

Compared to the Airy beam generator based on passive metasurfaces, our Airy beam is generated utilizing the reconfigurable metasurface whose resonance frequency can be dynamically adjusted. In this part, I verify the frequency agility of the 1D Airy beam generator by realizing the Airy beams with the fixed parameter b = 44.1 over a wide frequency band varying from 9 to 12 GHz. The phase, capacitance, and bias voltage profiles of Airy beams with parameter b = 44.1 at different frequencies are calculated and presented in Figure 4-17. The green lines are the phase profiles with the phase alternating between -π/2 and π/2. The numerical simulations and experimental measurements of the Airy beams

are carried out at 9, 10, 11, and 12 GHz as shown in Figures 4-18. The results show that the distinct parabolic trajectory at different operating frequencies. The deflection offset of the main lobe of Airy beams decreases slightly with the operating frequency increases, which is due to the fact that the deflection of the main beam of Airy beams is inversely proportional to the operating frequency according to equation (4-10). Good agreement between the simulations and measurements can be observed. The good frequency agility of the Airy beam generator based on the reconfigurable metasurface is validated.

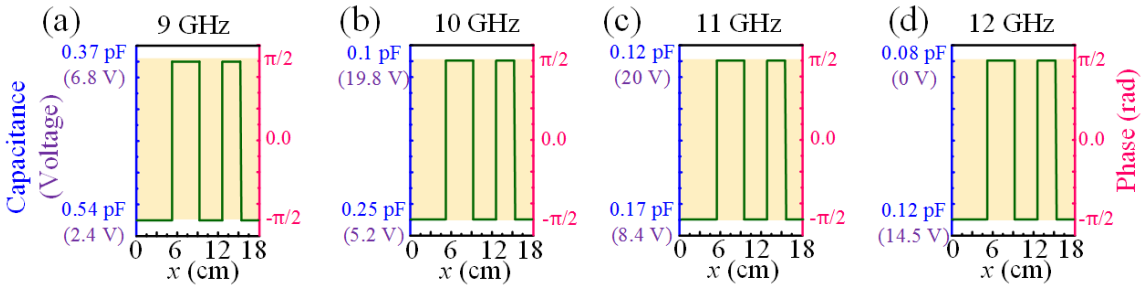

Figure 4.17 Phase, capacitance, and bias voltage profiles of the Airy beams with parameter b = 44.1 at 9, 10, 11, and 12 GHz.

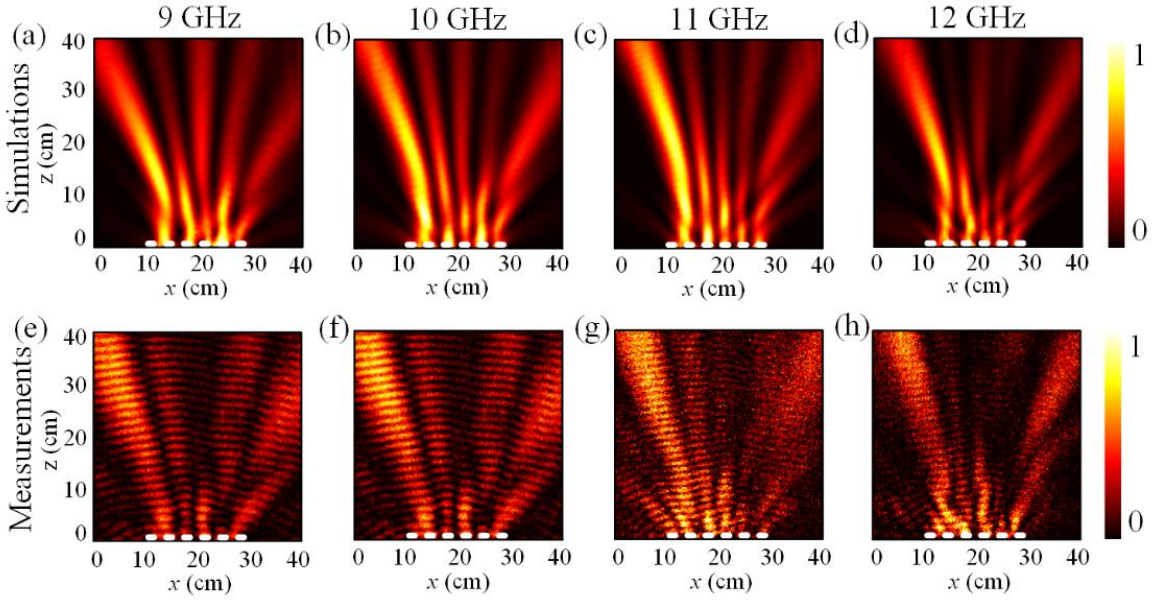

Figure 4.18 Simulations and measurements of the Airy beams with parameter b = 44.1 at 9 GHz, 10 GHz, 11 GHz, and 12 GHz. (a)-(d) Simulated near-field results in *xoz* plane. (e)-(h) Measured near-field results in *xoz* plane.

Table 4.1 Efficiency of the whole 1D Airy beams.

Frequency	Simulations	Measurements
9 GHz	36%	31.13%
10 GHz	38.61%	34.87%
11 GHz	38.11%	32.91%
12 GHz	32.79%	30.56%

Furthermore, I quantitatively evaluate the quality of the 1D Airy beam generated by our reconfigurable metasurface. The efficiency of the Airy beam with parameter b = 44.1 is calculated using the following formula:

$$\eta = \frac{P_{Airy}}{P_{inc}} \tag{4-11}$$

where P_{Airy} and P_{inc} respectively represents the power of the generated Airy beam and incident plane wave. The efficiency of the simulated and measured Airy beam at different frequencies is extracted from the data in the *xoz* plane and shown in Table 1. Due to the resonant nature of the elementary cell and ohmic losses caused by the inclusion of varactor diodes, the reflection amplitude varies slightly when the capacitance is changed. The inhomogeneous reflection amplitude along the metasurface can explain the low efficiency. The difference between measured and simulated efficiencies is mainly due to the incorrect consideration of the resistance value of the varactor diode in the simulations. Using plane wave incidence in simulations and a horn antenna in experiments can also explain the difference. Then, I make a comparison between my design with several passive metasurfaces as shown in Table 4.2.

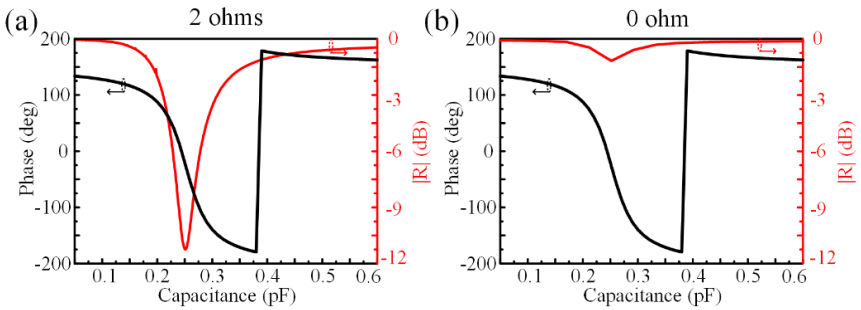

Figure 4.19 Reflection phase and magnitude curves varying with capacitance for different ohmic loss at 10 GHz. (a) 2 ohms. (b) 0 ohm.

Table 4.2 Comparison of Airy beam generation.

Works	Frequency	Type	Efficiency
Ref. [171]	200 THz	passive	25%
Ref. [172]	Sub THz	passive	13.7%
Ref. [173]	8.5 GHz	passive	30%
My work	10 GHz	active	38.61%

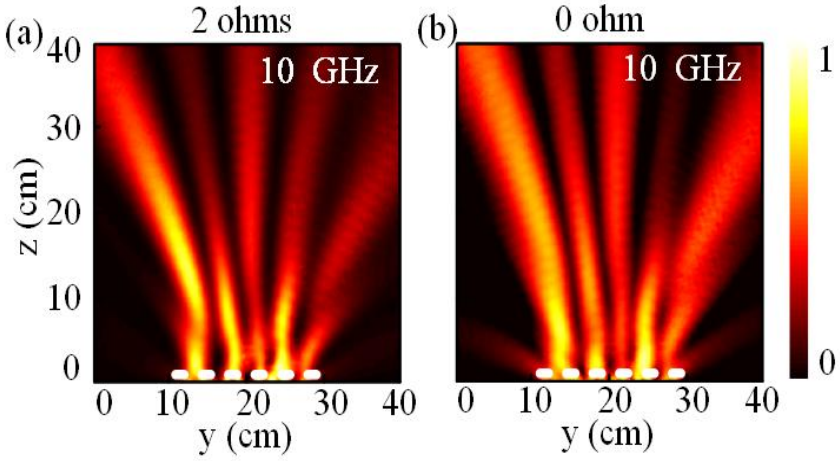

Figure 4.20 Simulated electric field distribution for parameter b = 44.1 with 1-bit coding phase arranged as -90° and 90° with different ohmic losses of varactor diodes at 10 GHz. (a) 2 ohms. (b) 0 ohm.

To address this issue of the low efficiency of the reconfigurable metasurface, I can use varactors with lower ohmic losses and substrates with lower dielectric losses to improve the efficiency of the reconfigurable metasurface. Here, I take the ohmic losses of varactor diodes as an example. Two resistance values of the varactor diode (R = 0 ohm and 2 ohms) are chosen for this numerical study. The phase and amplitude curves of the 1D tunable unit cell versus the capacitance value at 10 GHz are displayed in Figure 4-19, which exhibit the reflection magnitude variation with the resistance value. Since the 1-bit phase-coding scheme is utilized for the Airy beam generation in this chapter, I only consider the magnitude at the 1-bit coding phases of 90° and -90°. The magnitude at 90° and -90° are -1.6 dB and -8.7 dB, respectively, for R = 2 ohms as illustrated in Figure 4-19(a). Similarly, the magnitude at phase 90° and -90° are -0.14 dB and -0.5 dB for the case R = 0 ohm. The simulation results for the two resistance values are presented in Figure 4-20 at 10 GHz. According to equation (4-11), the efficiency is 62.47%, 38.61% for R = 0 ohm and 2 ohms, respectively. The efficiency decreases considerably with an increase in resistance of the varactor diode.

All these results validate the frequency reconfigurability mechanism. Additionally, to date, all the studies of 1D Airy beams have been carried out with a vertical launch angle. However, it would also be interesting to study the excitation of the 1D Airy beams with arbitrary launching angles that would benefit in near-field communication systems.

4.3.1.4 Beam steering of 1D Airy beams

To realize the arbitrary launch angle of the Airy beam, I investigate the dynamic steering of the 1D Airy beam with b = 44.1 at 10 GHz. According to the generalized Snell's law[43], the phase gradient used for the beam steering for Airy beams can be easily derived. The phase profile φ_{def} for an Airy beam with a desired deflection angle θ_{def} can be described as:

$$\varphi_{def} = \text{angle}[\phi(x, z = 0)] - \frac{\pi}{2} + xk_0 sin\theta_{def} \tag{4-12}$$

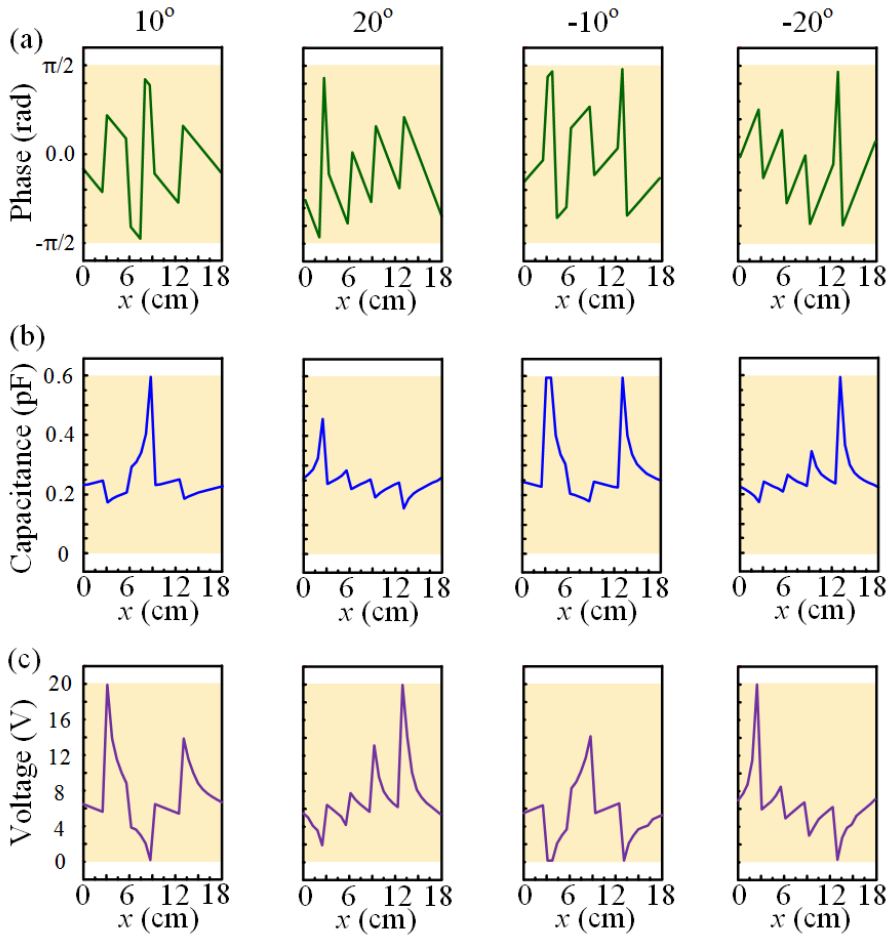

Figure 4.21 Phase, capacitance, voltage profiles of the beam steering of the Airy beam for parameter b = 44.1 at 10 GHz. (a) Phase profiles. (b) Capacitance profiles. (c) Voltage profiles.

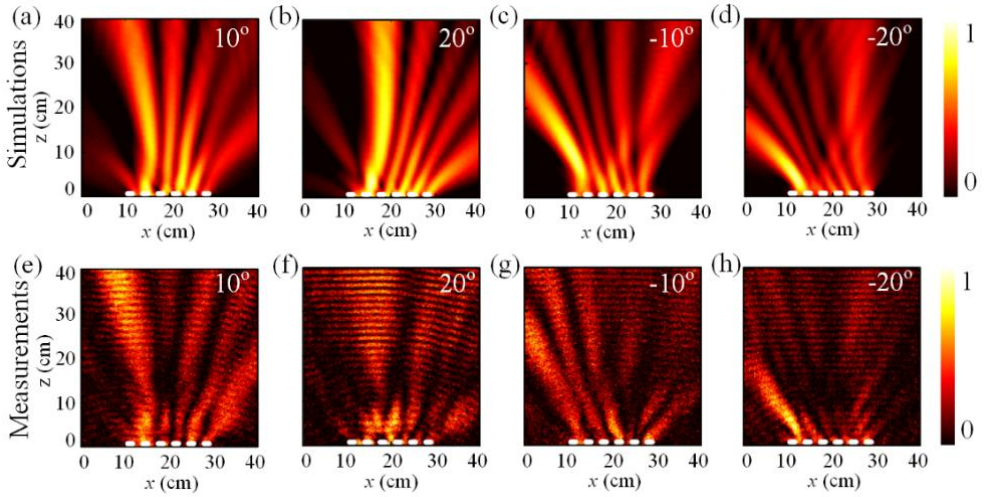

Figure 4.22 Simulations and measurements of the Airy beams with parameter b = 44.1 at different deflection angles. (a) Simulated electric field distribution in *xoz* plane. (b) Measured electric field distribution in *xoz* plane.

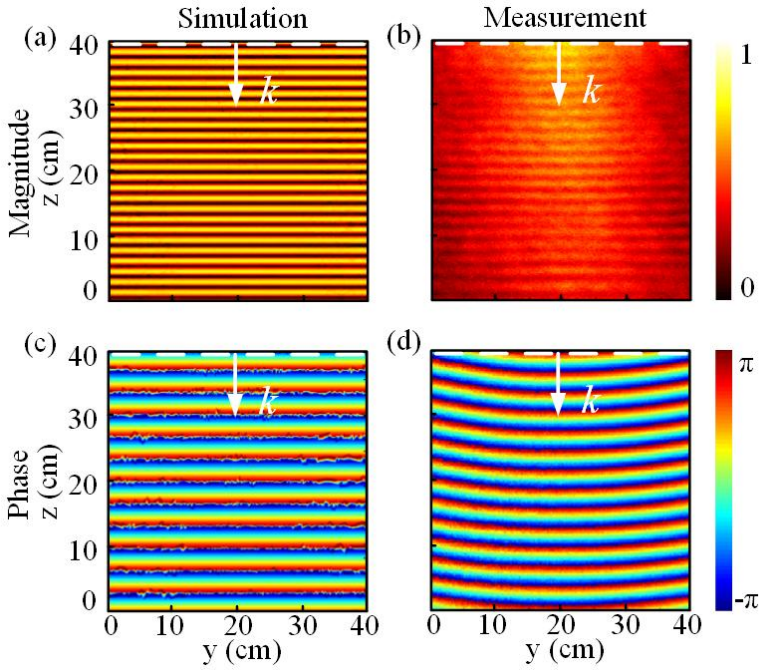

Figure 4.23 Magnitude and phase distributions of the incidence in simulation and measurement. (a)-(b) Magnitude distributions (c)-(d) Phase distributions.

Four phase profiles for the Airy beams with deflection angles of 10°, 20°, -10°, and -20° are calculated according to equation (4-12) and are plotted in Figure 4-21(a). The corresponding capacitance and voltage profiles are depicted in Figures 4-21(b) and (c). The simulations and measurements for the Airy beams with the deflection angles 10°, 20°, -10°,

and -20° are performed at 10 GHz by applying the capacitance and voltage profiles on the metasurface. The corresponding simulated electric field distributions in *xoz* plane are shown in Figures 4-22(a)-(d). The whole Airy beams including side lobes are deflected towards the right side for the negative values θ_{def} = 10° and 20° with the clear parabolic trajectory. Similarly, the whole Airy beam is deflected towards the left side for the positive values θ_{def} = -10° and -20°. Figures 4-22(e)-(h) show the measured electric field distributions of Airy beams with different deflection angles in *xoz* plane at 10 GHz. The fabrication error and imperfect quasi-plane wave emitted from the horn antenna cause the difference between the simulations and measurements. The comparison of the incident wave in simulations and measurements is shown in Figure 4-23. As displayed in Figure 4-23 (b), the incident wave emitted from the horn antenna seems a quasi-plane wave. However, we can observe that the isophase surface is not planar in the measurements, which is different with the plane wave used in simulations.

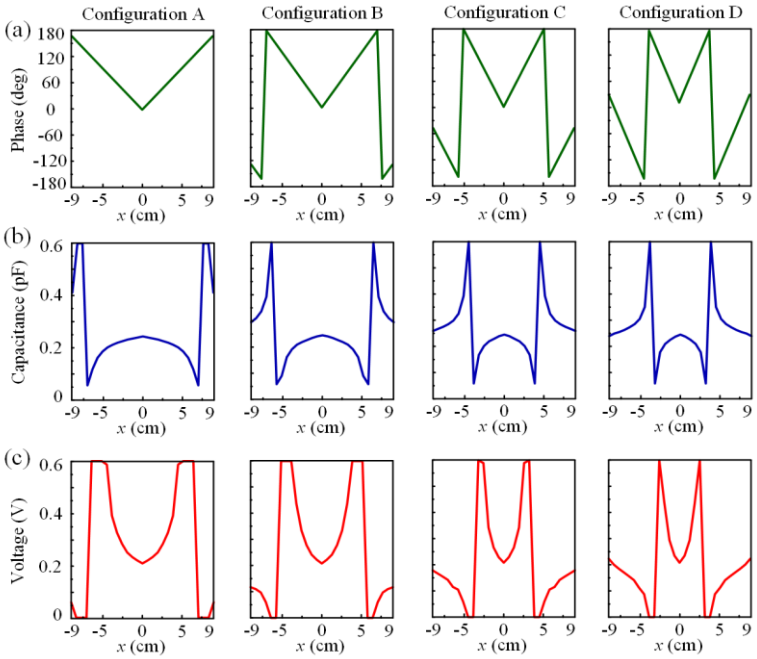

Figure 4.24 Phase, capacitance, and voltage profiles of four configurations 'A' to 'D' corresponding to the phase tilt angle θ of 10°, 13°, 18°, and 22°, respectively, at 10 GHz. (a) Phase profiles. (b) Capacitance profiles. (c) Voltage profiles.

The dynamic generation and manipulation of the 1D Airy beams are achieved based on the 1D reconfigurable metasurface. The three properties of Airy beams have been demonstrated. I also have presented the Airy beam generation over a wide frequency band.

4.3.2 Zeroth-order Bessel-like beams generation and manipulation

In this subsection, the dynamic generation and manipulation of zeroth-order Bessel-like beams will be explored using the one-dimensional reconfigurable metasurface.

4.3.2.1 Parametric study of Zeroth-order Bessel-like beams

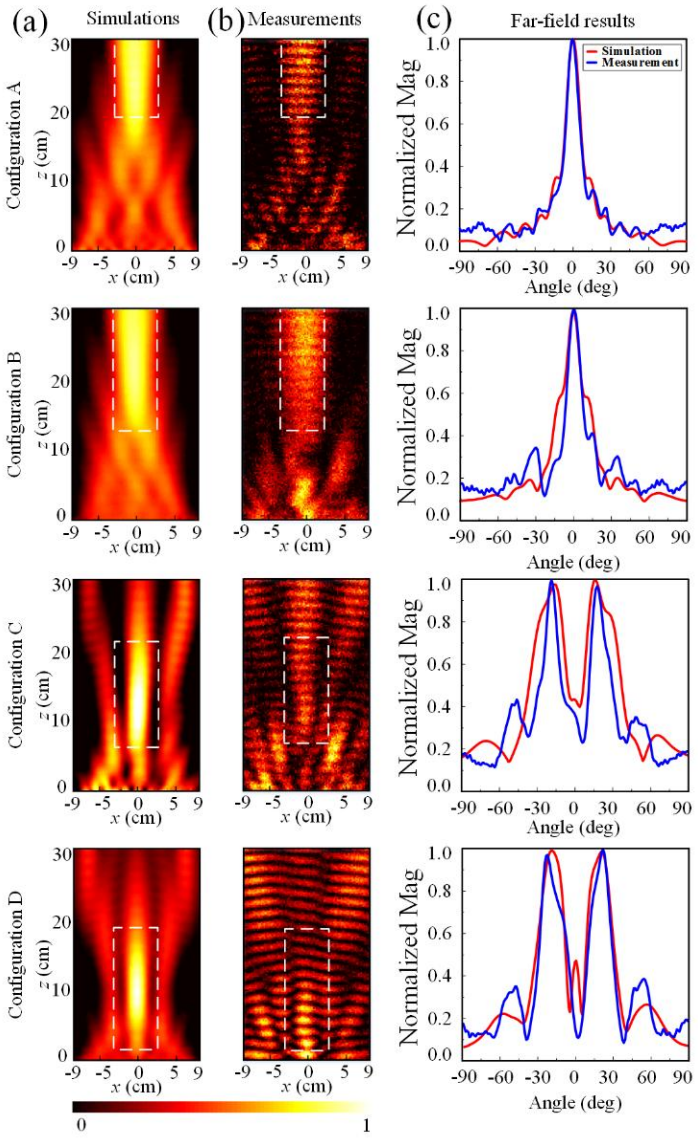

Figure 4.25 Simulated and measured results of the Bessel-like beams for phase configurations 'A' to 'D' at 10 GHz. (a) Simulated near-field electric field distribution. (b) Measured near-field electric field distribution. (c) Simulated and measured far-field radiation patterns.

To study the influence of parameter θ on the position of diffraction-free area of Bessel-like beam, four phase configurations 'A' to 'D', corresponding to the phase tilt angle θ of 10°, 13°, 18°, and 22°, are designed and shown in Figure 4-24 (a). The corresponding

capacitance and voltage profiles required to fulfill the phase distributions are depicted in Figures 4-24(b) and (c). A single row (30 × 1 unit cells) of the 1D reconfigurable metasurface (30 × 30 unit cells) is adopted for the simulation of 1D Bessel-like beams generation, as presented in Figure 4-10. The numerical simulations for the generation of Bessel-like beams with four different tilt angles are performed at 10 GHz as shown in Figure 4-25 (a), where the white dotted rectangles represent the diffraction-free areas of the generated zeroth-order Bessel beams. The starting positions of the diffraction-free zone of Bessel beams with phase configurations 'A' to 'D' in numerical simulations are 190, 135, 80, and 20 mm on the *z*-axis, respectively, which means the diffraction-free zone of zeroth-order Bessel-like beams is flexibly manipulated in the near-field at 10 GHz. The experimental measurements of the Bessel-like beams with configurations 'A' to 'D' are carried out using the fabricated 1D reconfigurable metasurface. The measured results of zeroth-order Bessel-like beams at 10 GHz as presented in Figure 4-25(b). We can see that the diffraction-free zones start from different position on the *z*-axis for configurations 'A' to 'D', which are consistent with simulations. In addition, it is clear that the diffraction-free area is closer to the metasurface as the phase tilt angle θ increases, which is consistent with the theory. Compared to the results of phase configurations A and B, it is also distinct that the two side lobes appear in the two sides of main beam of zeroth-order Bessel-like beams for configurations C and D.

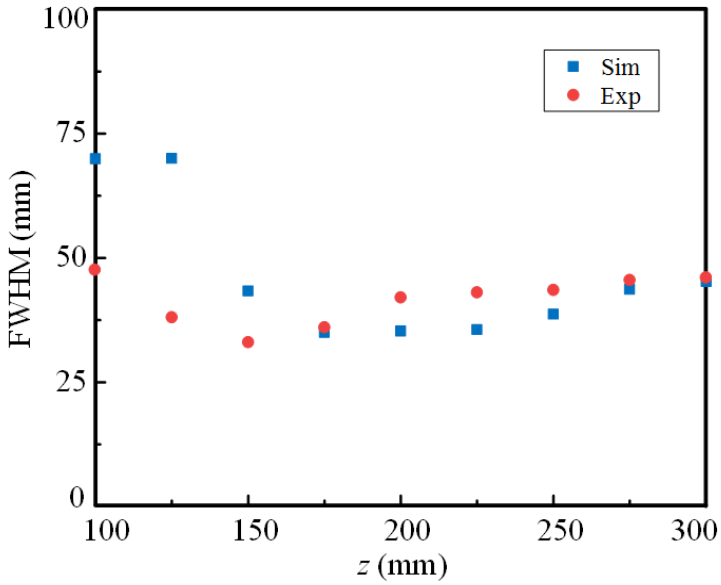

Figure 4.26 Simulated and measured FWHM of zeroth-order Bessel beams with configuration 'B' at 10 GHz.

The normalized far-field results of the different configurations in *xoz* plane are depicted in Figure 4-25(c). It is worth noting that it is a single beam appearing at 0° in the far-field for phase configurations 'A' and 'B' while there are two beams for phase configurations 'C' and 'D'. The dual-beam appear at around $\pm 18°$ and $\pm 22°$ for phase configurations 'C' and 'D', respectively. The zeroth-order Bessel beam produced by an axicon can be considered as the synthesis of Gaussian beams whose axes uniformly lie on a cone. The far-field pattern is determined by two opposing effects of these Gaussian beams[198]. One effect is that the overleaping of any two Gaussian beams decreases with propagation distance due to the angular separation of their axes. This effect is related to the angular aperture of the cone corresponding to the phase tilt angle θ. The other effect is that the spot-size of each Gaussian beam increases with respect to the propagation axis, and hence contribute to the overlapping of the various beams. Consequently, the far-field pattern is determined by the ratio between the angular spread of a single Gaussian beam and the angular aperture of the cone. When the phase tilt angle is small, such as configurations 'A' and 'B', the ratio is smaller than unity. Thus, all the component Gaussian beams keep overlapping and interfering in the far-field to form a single beam. Conversely, when the ratio is greater than 1, such as configurations 'C' and 'D', no intensity appears in the center of the far-field pattern. Therefore, an annular pattern can be observed in the far-field region. It should be noticed that the zeroth-order Bessel beams with a hollow structure for phase configuration 'C' and 'D' are not vortex beams because they do not carry any orbital angular momentum. This issue will be discussed in next section.

In summary, the flexible manipulation of the diffraction-free zone of Bessel-like beams is validated at 10 GHz by changing the phase profiles of different values of parameter θ in this part. The phenomenon of the two types of far-field radiation patterns of zeroth-order Bessel beams is explained.

4.3.2.2 Study of the two properties of zeroth-order Bessel-like beams

In this part, I demonstrate the two properties of zeroth-order Bessel beams, including diffraction-free and self-healing properties. The diffraction-free property means that the full width at half maximum (FWHM) of Bessel beams maintains constant in the diffraction-free region. The simulated and measured FWHM of the zeroth-order Bessel beam with phase configuration 'B' at 10 GHz are presented in Figure 4-26, where the nearly constant FWHM starts from z = 135 mm for both simulation and measurement, validating the diffraction-free property.

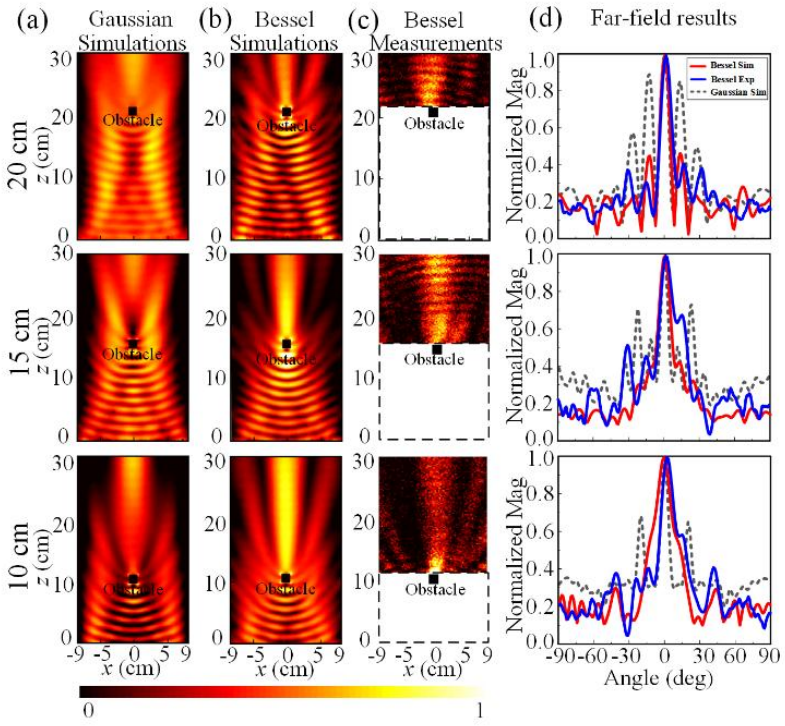

Figure 4.27 Self-healing property validation of the Bessel-like beam using configuration 'B' with the metallic obstacle placed in the propagating path of Bessel-like beams at 10 GHz. (a) Simulations of Gaussian beam as a reference. (b) and (c) are the near-field simulations and measurements of the Bessel-like beam. (d) Corresponding far-field results.

The self-healing property means that the propagation of the zeroth-order Bessel beam is not affected by a small metallic obstacle placed in the propagating path, which is verified by putting a metallic obstacle ($\lambda_0/2 \times \lambda_0/2 \times \lambda_0/2$) in the propagating path of the Bessel-like beam with configuration 'B' at 10 GHz. In the first case, I place the obstacle at z = 20 cm on the z-axis. Compared to the Gaussian beam in Figure 4-27(a), the zeroth-order Bessel beam restructures quickly after passing through the obstacle as presented in Figure 4-27(b). The near-field measurement is performed in the region beyond the obstacle in the propagation path to reduce the complexity of measurement, as shown in Figure 4-27(c). The clear restructured zeroth-order Bessel beam can be observed after the beam passes through the obstacle. Besides, in order to show that the self-healing property of the zeroth-order Bessel beam is insensitive to the position change of the obstacle placed in the propagating path, I then place the obstacle at z = 10 cm and z = 15 cm on the z-axis. Similarly, the Bessel beam restructures after passing through the obstacle in both simulations and measurements.

To further demonstrate the self-healing property of Bessel-like beams with phase configuration 'B', the far-field results are explored in both simulations and measurements at

10 GHz with an obstacle placed in the propagating path. Figure 4-27(d) depicts two non-negligible side lobes for the Gaussian beam with the obstacles placed at different positions. However, the far-field results of Bessel-like beams show the distinct single beams at around 0° with negligible side lobes when the obstacle is placed at z = 10 cm, which indicates the self-healing property of the Bessel beam. A spreading of the lobe with an approximate amplitude of 0.6 can be observed at around 15° when the obstacle is placed at z = 10 cm and 15 cm. This side lobe may be mainly due to the fact that the obstacle is difficult to be perfectly placed in the center along the x-axis in the experimental measurement, such that a part of the wave is scattered to the off-axis direction.

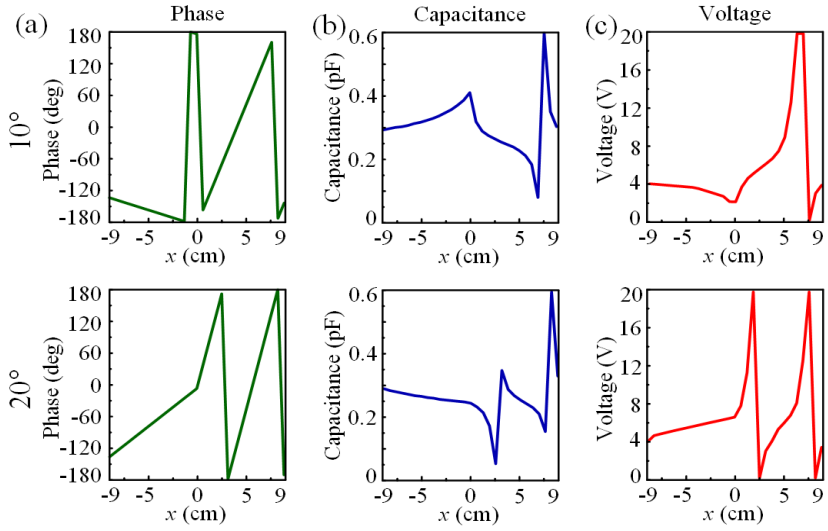

Figure 4.28 Phase, capacitance, and voltage profiles of the Bessel-like beams with the deflection angles of 10° and 20° at 10 GHz.

4.3.2.3 Beam steering of Bessel-like beams

In the above parts, the Bessel-like beams with a vertically launched angle have been explored. However, it is more beneficial to achieve an arbitrary launch angle for the Bessel-like beams in a wireless communication system. In this part, the beam steering of the Bessel-like beam with configuration 'B' is explored at 10 GHz. To begin with, I describe the theory of the beam steering of Bessel-like beams. According to generalized Snell's law [43], beam steering can be achieved by applying a predesigned phase gradient to the metasurface. Here, I set the incident angle of a plane wave as 0° since the incident wave is in the normal direction of the metasurface in this thesis. To realize the deflection of Bessel-like beams, the deflection phase profile should be superposed to the phase profile of Bessel-like beams. Thus, the phase

profile for a Bessel beam with a deflection angle θ_r can be expressed as:

$$\varphi_{deflection}(x) = 2n\pi + xk_0 sin\theta_r + |x|k_0 \sin\theta \tag{4-13}$$

where n is an integer.

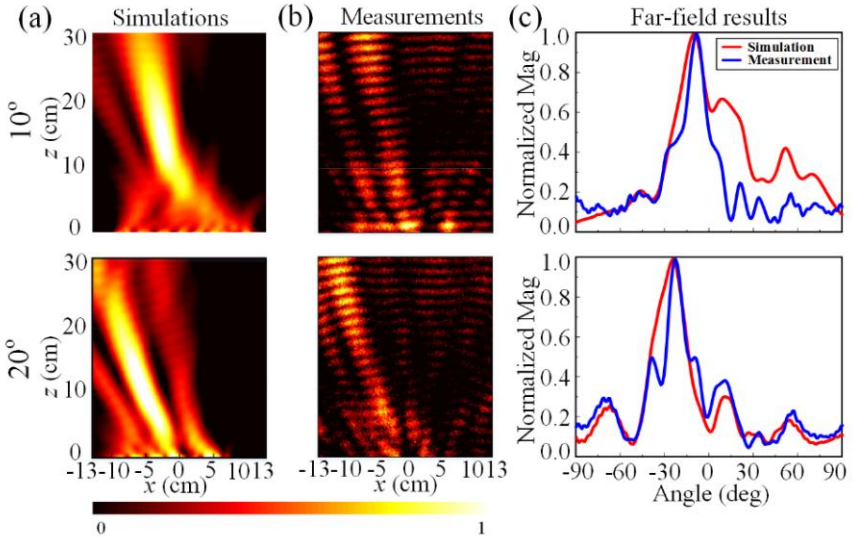

Figure 4.29 The beam steering of the Bessel-like beam with configuration 'B' at 10 GHz for deflection angle of 10° and 20°. (a) Simulated near-field results. (b) Measured near-field results. (c) Far-field results.

To realize the beam deflection of zeroth-order Bessel-like beams, I consider and calculate two phase profiles for the deflection angles of 10° and 20° from equation (4-13), as shown in Figure 4-28(a). Figures 4-28(b) and (c) present the corresponding capacitance and voltage profiles that allow to fulfill such phase modulations. The near-field simulations and measurements of Bessel-like beams with different deflection angles are presented in Figures 4-29(a) and (b), respectively. The results depict distinct diffraction-free zeroth-order Bessel-like beams deflected to 10° and 20°, respectively, which agree with the theoretical predictions. Figure 4-29(c) displays the far-field radiation patterns of the beam steering characteristics at 10 GHz. The Bessel-like beam is deflected to 10° and around 20°, respectively, which is consistent with near-field results and theoretical predictions. Therefore, the beam steering of zeroth-order Bessel-like is validated at 10 GHz. Such possibility of controlling the emission direction will inevitably enable the design and implementation of directional communication systems between connected objects.

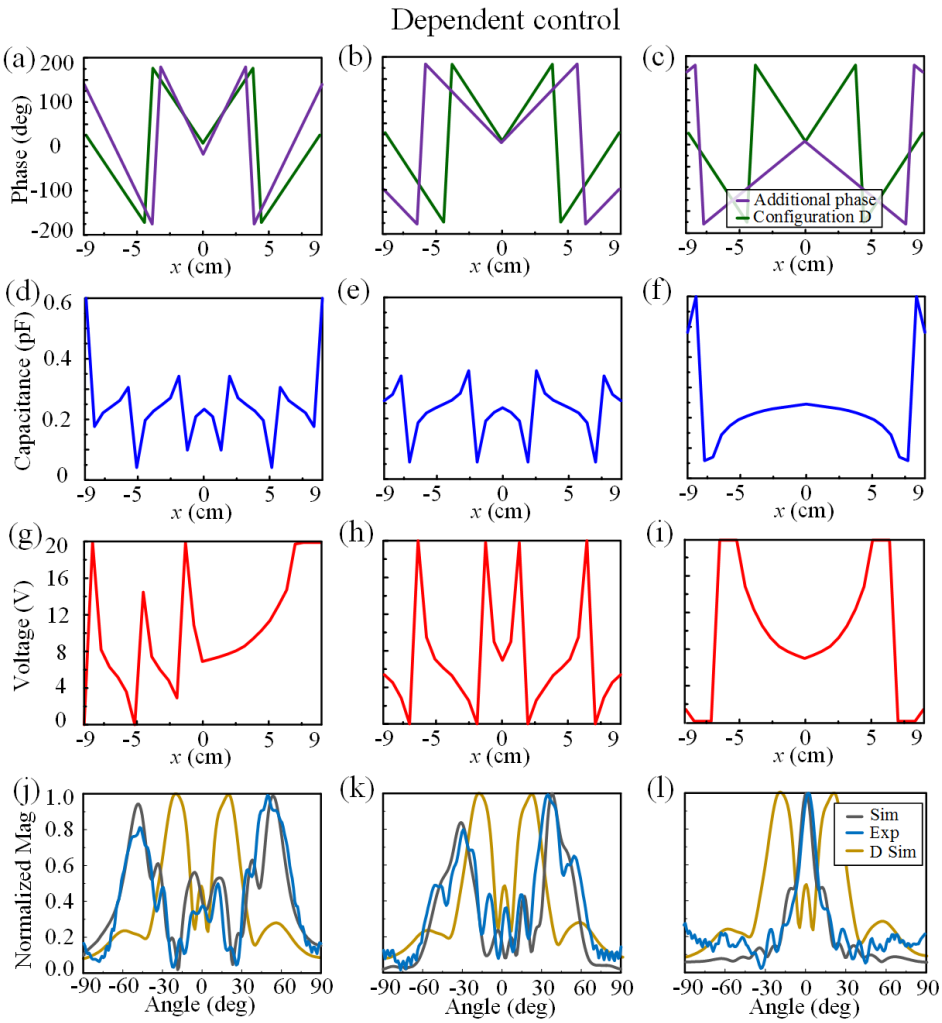

Figure 4.30 Far-field results of flexible manipulating Bessel-like beams for the phase configuration D at 10 GHz in the dependent way. (a)-(c) Additional phase profiles represented by purple lines. (d)-(f) Capacitance profiles. (g)-(i) Voltage profiles. (j)-(l) Far-field results in the *xoz* plane.

4.3.2.4 Beam manipulation of Bessel-like beams in the far-field

From the description in part 4.3.2.1, we know that there are two beams in *xoz* plane of the far-field region for the Bessel-like beam with configuration 'D'. In this part, I demonstrate the flexible control of these two beams. It is worth highlighting that the two far-field beams of configuration 'D' can be controlled in both dependent and independent ways by superposing an additional appropriate phase profile to the axicon phase profile.

Firstly, I validate the dependent control of the two far-field beams in the *xoz* plane. Two types of additional phase profiles; one having the same trend as the phase configuration 'D' and the other one having the opposite trend, are chosen and symmetrically assigned along the *x*-axis for this study. For the phase profiles having the same trend with configuration 'D',

the corresponding phase tilt angles are set as 30° and 15°, as respectively shown in Figure 4-30(a) and (b). The capacitance and voltage profiles corresponding to the total superimposed phase for the dependent control are exhibited in Figures 4-30(d)-(i). By superposing the additional symmetrical phase profiles with phase tilt angles of 30° and 15° to the phase profile of configuration 'D', the Bessel-like beams in the far-field appear at ±52° and ±37°, respectively. When the phase tilt angle of the additional phase profile reversed with regard to the phase configuration 'D' is set as -22° as displayed in Figure 4-30(c), a single beam is observed at 0°. This single beam is expected since the additional phase profile of -22° compensates the original steering of the Bessel-like beam of ±22°.

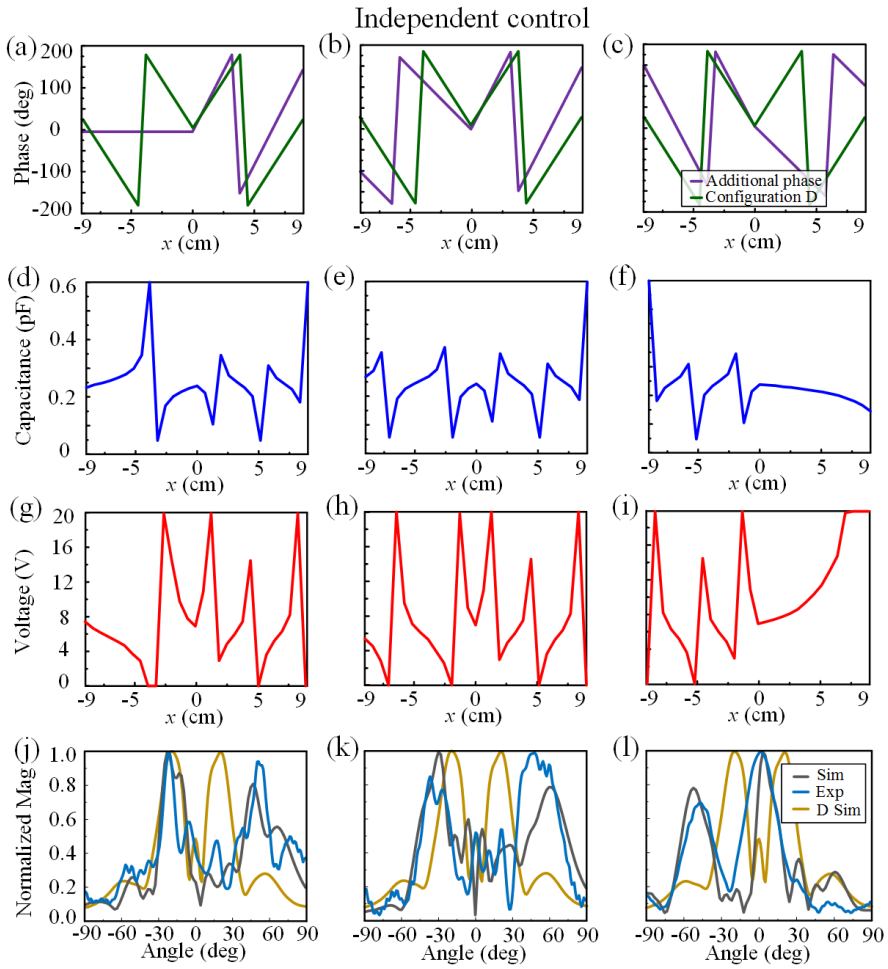

Figure 4.31 Far-field results of flexible manipulating Bessel-like beams for the phase configuration D at 10 GHz in the independent way. (a)-(c) Phase profiles. (d)-(f) Capacitance profiles. (g)-(i) Voltage profiles. (j)-(l) Far-field results in *xoz* plane.

Secondly, I demonstrate the independent control of two beams in the far-field region by

adding the asymmetric phase profiles to phase configuration 'D' as shown in Figures 4-31(a)-(c). For the first case, I intend to control only one beam out of the dual-beam. I preset the phase tilt angles of the additional phase on the left and right sides as 0° and 30°, respectively, as shown in Figure 4-31(a). In this way, the left beam is fixed and the right beam is expected to appear at 52°. The simulated and measured results in Figure 4-31(j) show the left and right beams appear at around 22° and 52°, which is in agreement with the theoretical prediction. Similarly, for the second case, I set the phase tilt angles of the additional phase on the left and right sides as 15° and 30°, respectively, as displayed in Figure 4-31(b). Thus, the left and right beams are adjusted to 37° and 52° as shown in Figure 4-31(k). For the third case, the phase tilt angles of the additional phase on the left and right sides are set as 30° and -15°, as depicted in Figure 4-31(c). Therefore, two beams appear at around 52° and 7°, respectively, as presented in Figure 4-31(l). These results validate the independent control of the far-field patterns of configuration 'D'.

In this part, both the dependent and independent control of the Bessel-like beam in the far-field region with phase configuration 'D' are well demonstrated at 10 GHz using the 1D reconfigurable metasurface.

4.4 Diffraction-free beams generation using 2D reconfigurable metasurface

In this section, I explore the generation and manipulation of diffraction-free beams using the 2D reconfigurable metasurface.

4.4.1 2D Airy beams generation and manipulation

In this subsection, I realize 2D Airy beams using the 1-bit phase-coding metasurface based on the 2D reconfigurable metasurface. 2D Airy beams can be synthesized by the two 1D Airy beams accelerating along two non-parallel directions. In this thesis, I only discuss the 2D Airy beams composed of two orthogonal 1D Airy beams. The electric field distribution of the 2D Airy beam should then satisfy[152]:

$$\phi(x, y, \xi = 0) = \mathrm{Ai}(b_x x)\mathrm{Ai}\left(b_y y\right)\exp(a_x x)\exp\left(a_y y\right) \tag{4-14}$$

where the two 1D Airy beam components accelerate along the *x*- and *y*-direction, respectively. The phase profile of the 2D Airy beam can be expressed as:

$$\varphi = \arg[\phi(x, y, \xi = 0)] - \pi/2 \tag{4-15}$$

4.4.1.1 Implementation of 2D Airy beams

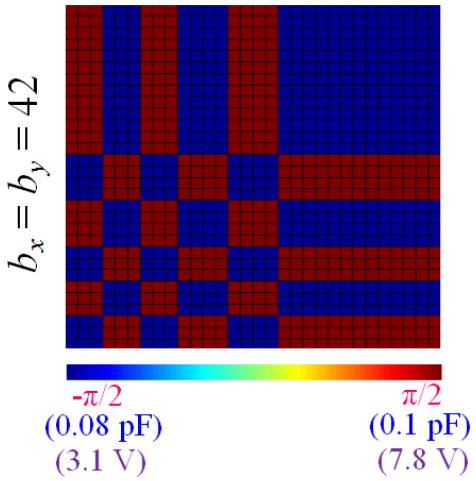

Figure 4.32 Phase, capacitance, and voltage profiles of the 2D Airy beams with parameters $a_x = a_y = 1$ and $b_x = b_y = 42$ at 9.5 GHz.

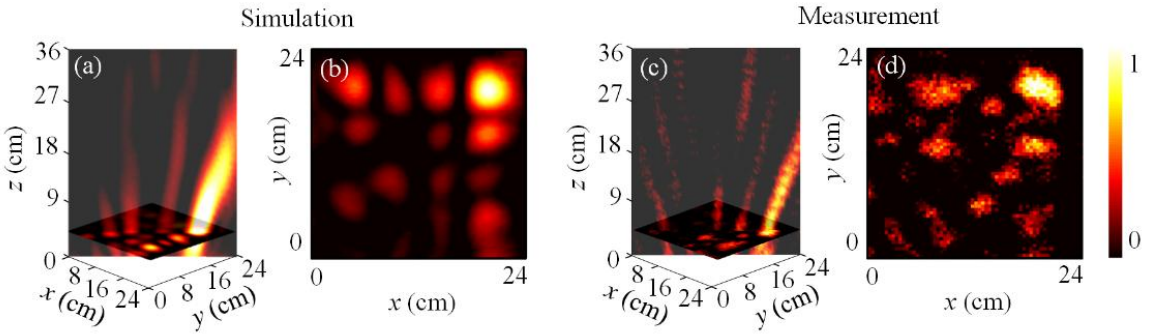

Figure 4.33 Simulated and measured electric field distributions of the 2D Airy beam with parameters $a_x = a_y = 1$ and $b_x = b_y = 42$ at 9.5 GHz. (a) 3D view of the simulated electric field distribution. (b) Simulated electric field distribution in the transverse plane at $z = 6$ cm. (c) 3D view of the measured electric field distribution. (d) Measured electric field distribution in the transverse plane at $z = 6$ cm.

According to the theory of 2D Airy beams as described in equation (4-14), I set the parameters $a_x = a_y$ and $b_x = b_y$ such that the two 1D Airy beam components have the same features, allowing a 2D Airy beam to accelerate along the 45° direction with respect to the x-axis. The parameters $a_x = a_y = 1$ and $b_x = b_y = 42$ is utilized to show the parabolic trajectorie of the main beam of the 2D Airy beam at 9.5 GHz. The corresponding phase profile is presented in Figures 4-32. Since the 1-bit coded phase has two values $\pi/2$ and $-\pi/2$, the

corresponding capacitance value shifts between two values, 0.08 pF and 0.1 pF, and the bias voltage shifts between 3.1 V and 7.8 V.

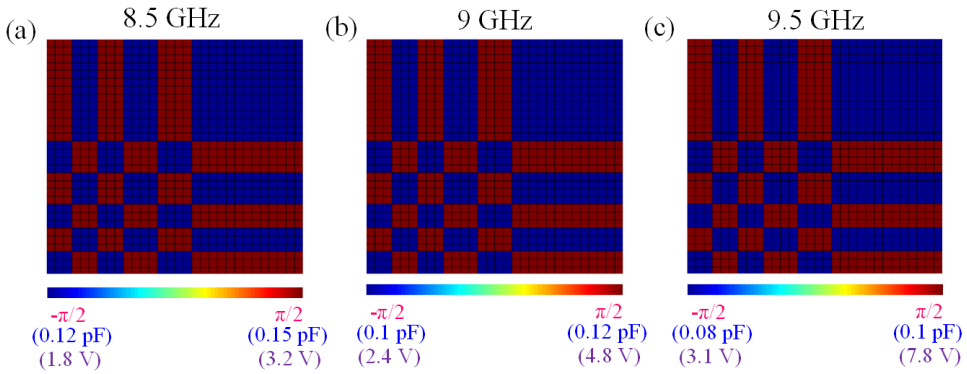

Figure 4.34 Phase, capacitance, and voltage profiles of the 2D Airy beam with parameters $b_x = b_y = 42$ at 8.5 GHz, 9 GHz, and 9.5 GHz.

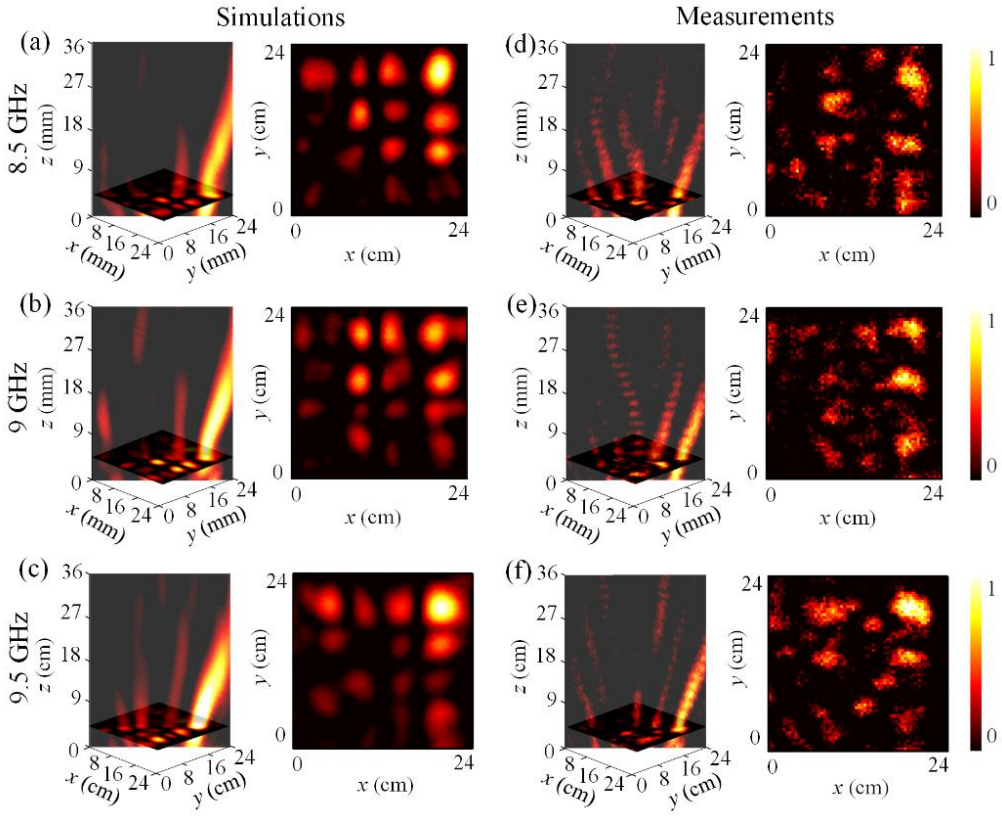

Figure 4.35 Normalized electric field distributions of the simulated and measured 2D Airy beam with parameters $b_x = b_y = 42$ at 8.5 GHz, 9 GHz, and 9.5 GHz. (a-c) Simulated electric field distributions. (d-f) Measured electric field distributions.

The simulated 3D electric field distribution of the 2D Airy beam with parameter $b_x = b_y = 42$, which is composed of one transverse plane and one longitudinal plane, is depicted in Figure 4-33(a). It is evident that the 2D Airy beam accelerates along the diagonal of the *xoy* plane. The electric field distribution of the 2D Airy beam with parameter $b_x = b_y = 42$ in the transverse plane at $z = 6$ cm is presented in Figure 4-33(b), which shows the 2D Airy beam can be considered as a synthesis of two 1D Airy beams accelerating along different directions. Figures 4-33(c) and (d) present the corresponding measured results. The deviation between the simulation and measurement mainly from the imperfect quasi-plane incident waves emitted from the horn antenna and the fabrication error.

4.4.1.2 Frequency agility of the 2D Airy beam generator

To achieve the frequency agility of the 2D Airy beam generator based on the two-dimensional reconfigurable metasurface, I intend to generate the 2D Airy beams with parameters $a_x = a_y = 1$ and $b_x = b_y = 42$ at 8.5, 9, and 9.5 GHz. The corresponding phase, capacitance, and voltages profiles are presented in Figures 4-34. By applying the appropriate capacitance and voltage profiles on the metasurface, the 2D Airy beams are generated at different frequencies as displayed in Figure 4-35. We can see nearly the same parabolic trajectories of the three 2D Airy beams at 8.5, 9, and 9.5 GHz in the 3D view of the simulations and measurements. The simulated results in the transverse plane exhibit that the highest energy spot is located at the upper right corner and the two components accelerating along the *x*- and *y*-axes. The measured electric field distributions of the 2D Airy beams show a good agreement with the simulations, demonstrating the frequency agility of the 2D Airy beam generator.

Then, I quantitatively evaluate the performance of the 2D Airy beam generator. The efficiency of the 2D Airy beams at the different frequencies, extracted from the data in the longitudinal plane located at the diagonal of the *xoy* plane, can be calculated according to equation (4-11) and summarized in Table2. Since the imperfect quasi-plane incident wave emitted from the horn antenna and fabrication error, the experimental efficiency is lower than numerical efficiency. Besides, the difficulty to correctly consider the resistance value of varactor diodes in the simulation also contributes to the deviation between simulated and measured efficiencies. Furthermore, the efficiency of our reconfigurable metasurface is not very high due to the ohmic losses of the varactor diodes and the dielectric losses of the substrate, as it has been highlighted in the part of 4.3.1.3.

Table 4.3 Efficiency of the whole 2D Airy beams

Frequency	Simulations	Measurements
8.5 GHz	29.96%	21.85%
9 GHz	29.13%	25.72%
9.5 GHz	31.13%	27.27%

4.4.2 Bessel beams generation and manipulation

The zeroth-order Bessel beam can be regarded as the rotational symmetry of the 1D Bessel-like beam along the central axis. One of the methods of generating a zeroth-order Bessel beam is to mimic the phase distribution of the plane wave passing through an axicon using a flat metasurface. Therefore, the phase profile applied on the metasurface for the zeroth-order Bessel beam generation should satisfy the following equation:

$$\varphi_B(x,y) = k_0\sqrt{|x|^2+|y|^2}\sin\theta \tag{4-16}$$

4.4.2.1 Parametric study of Bessel beams

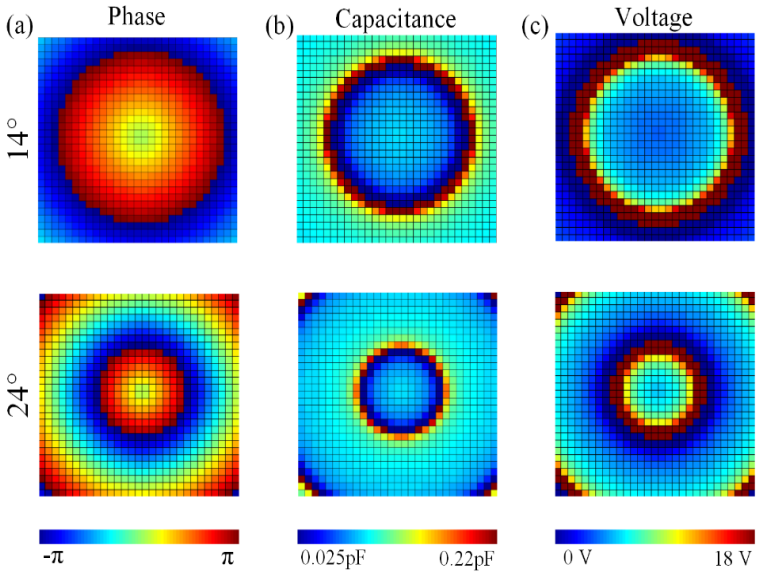

Figure 4.36 Phase, capacitance, and voltage profiles of the zeroth-order Bessel beams with different parameter θ = 14° and 24° at 9.5 GHz.

For the study of the influence of parameter θ on the zeroth-order Bessel beam generation using the two-dimensional reconfigurable metasurface, I choose two parameter values of θ (14° and 24°) for the generation of zeroth-order Bessel beams. The phase profiles

for the generation of zeroth-order Bessel beams with θ = 14° and θ = 24° at 9.5 GHz are obtained from the equation (4-16). The corresponding capacitance and voltage profiles are presented in Figure 4-36.

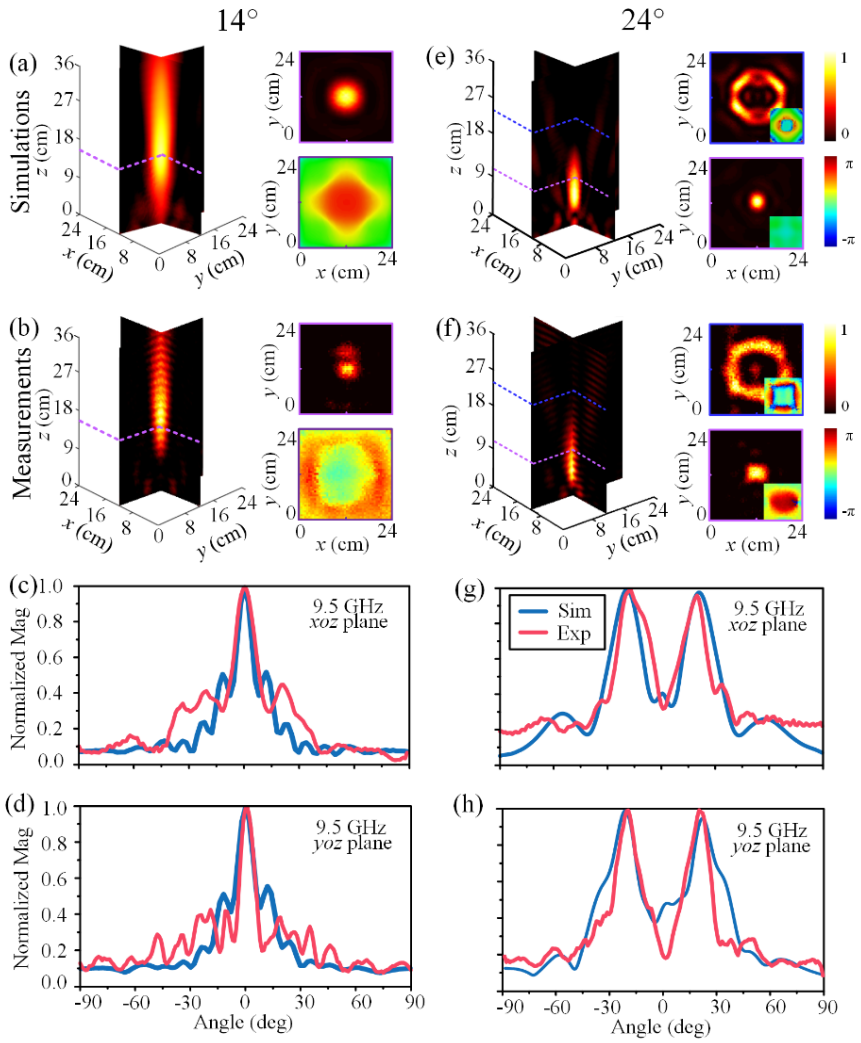

Figure 4.37 Simulated and measured results of the zeroth-order Bessel beams with parameter θ = 14° and 24° at 9.5 GHz. (a)-(d) Near-field and far-field results of the zeroth-order Bessel beams with parameter θ = 14°. (e)-(h) Near-field and far-field results of the zeroth-order Bessel beams with parameter θ =24°.

Figures 4-37(a) and (b) show the simulated and measured near-field results of the zeroth-order Bessel beam with θ = 14°. We can observe the distinct diffraction-free region in the 3D views. The normalized intensity and phase distributions in the transverse plane at z = 15 cm are shown in the two right subfigures. To make a comparison, the electric field distributions of the zeroth-order Bessel beam with tilt angle θ = 24° are depicted in Figures

4-37(e) and (f). The intensity distributions at the transverse plane z = 10 cm of the zeroth-order Bessel beam with θ = 24° is a central focusing spot. However, the transverse intensity distribution of the zeroth-order Bessel beam with θ = 24° is a doughnut-shaped structure. It should be noticed that the zeroth-order Bessel beam with θ = 24° is not a vortex beam since there is no helical phase profile in the transverse phase distribution as shown in the subfigure.

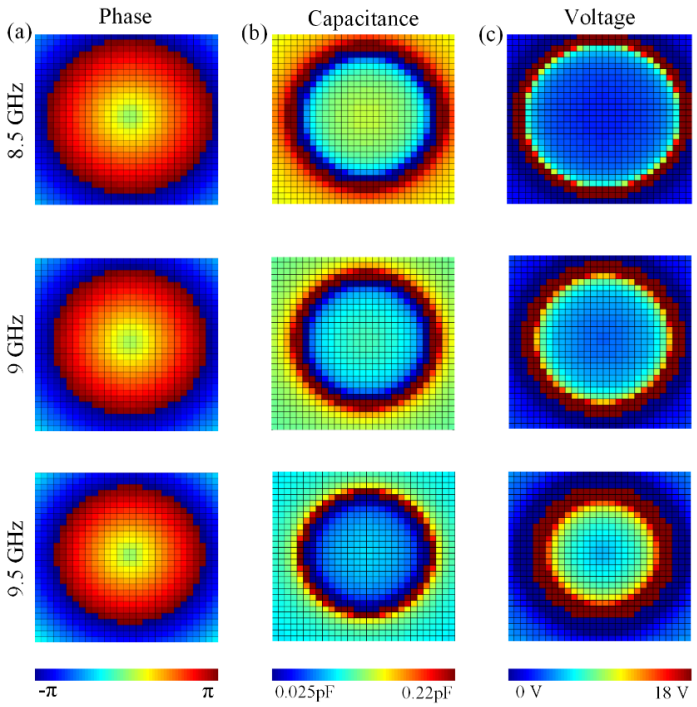

Figure 4.38 Phase, capacitance, and voltage profiles of the zeroth-order Bessel beams with different parameter θ = 14° at 8.5, 9, and 9.5 GHz.

The far-field results of the Bessel beams with different values of θ are plotted in two planes (*xoz* and *yoz* planes). A single beam appears at 0° for phase tilt angle θ = 14°, while there are two beams for phase tilt angle θ = 24°. The results in the *xoz* and *yoz* planes are consistent, which means the generated zeroth-order Bessel beams are rotationally symmetric along the *z*-axis. The different radiation patterns of the zeroth-order Bessel beams with θ = 14° and 24° can also be explained by the ratio between the angular spread of a single Gaussian beam and the angular aperture of the cone, as described in the part of 4.3.2.1. When the phase tilt angle is small, such as θ = 14°, the ratio is smaller than unity. Thus, all the component Gaussian beams keep overlapping and interfering in the far-field to form a single beam. Conversely, when the ratio is larger than 1, such as for θ = 24°, no intensity appears in the center of the far-field. Therefore, the annular pattern can be observed in the far-field.

4.4.2.2 Frequency agility of the Bessel beam generator

The frequency agility of the Bessel beam generator based on the two-dimensional reconfigurable metasurface is discussed in this part. I choose the zeroth-order Bessel beam with θ = 14° for this study. The phase, capacitance, and voltage profiles of the zeroth-order Bessel beam with θ = 14° at different frequencies are illustrated in Figure 4-38. The simulated and measured results are presented in Figure 4-39. The clear diffraction-free regions with the nearly same feature in the propagation direction can be observed at 8.5, 9, and 9.5 GHz. The transverse electric field distributions are also similar for the results at different frequencies. These results verify the generation of the Bessel beam over a wide frequency band ranging from 8.5 to 9.5 GHz.

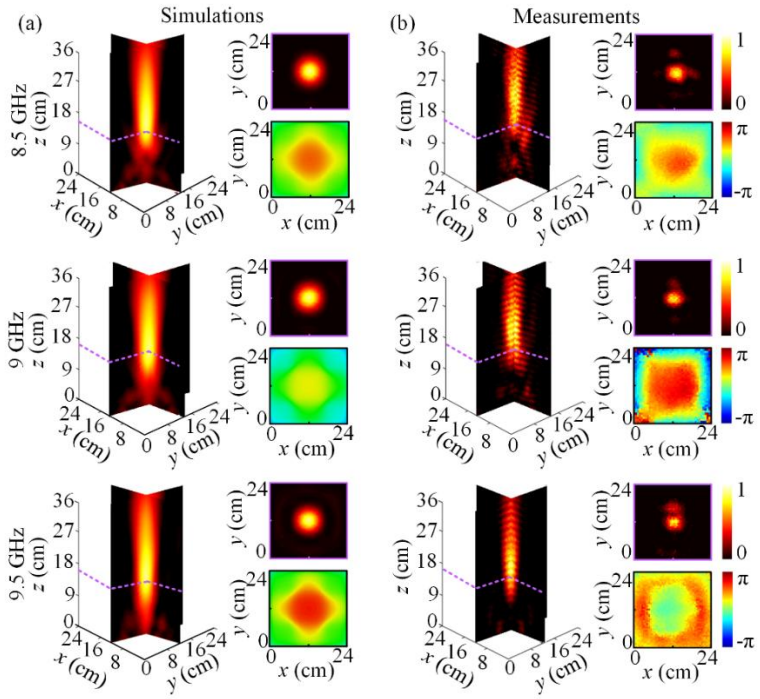

Figure 4.39 Simulated and measured near-field results of the zeroth-order Bessel beams with parameter θ = 14° at 8.5, 9, and 9.5 GHz. (a) Numerical simulations. (b) Experimental measurements.

4.5 Conclusion

In this chapter, I demonstrated the generation and manipulation of diffraction-free Airy beams and zeroth-order Bessel beams using both the 1D and 2D reconfigurable metasurfaces. By utilizing the 1D reconfigurable metasurface, I firstly explored the 1D Airy beam through the parameter b, representing a transverse scale, at 10 GHz. The parabolic trajectory of the

main lobe of 1D Airy beams can be flexibly adjusted by changing the phase profiles corresponding to different values of the *b*. Then, the diffraction-free, self-bending, and self-healing properties of Airy beams were demonstrated at 10 GHz. Besides, the 1D Airy beams were generated over a broad frequency band ranging from 9 to 12 GHz. Furthermore, the flexible control of the launch angle of the 1D Airy beams was validated by superposing an additional phase gradient to the phase profile of 1D Airy beam. To our best knowledge, this is the first demonstration of the concept of dynamic generation and manipulation of Airy beams using a reconfigurable metasurface in the microwave domain. Secondly, I explored Bessel-like beams using the same 1D reconfigurable metasurface. The flexible manipulation of diffraction-free areas of the 1D Bessel-like beam was validated by using different phase configurations. The diffraction-free property of Bessel beams was evaluated by the full width at half maximum (FWHM) of the main beam, and the self-healing property of Bessel beams was investigated by putting a metallic obstacle in the propagating path of the main beam. Beam steering of Bessel-like beams was also studied by superposing an additional phase gradient to the original phase profile. Although 1D Airy beam and 1D Bessel-like beam are achieved in one plane, we can still see the non-diffracting area from the generated 1D beams, which means they have the diffraction-free property.

By using the 2D reconfigurable metasurface, firstly, I explored the 2D Airy beam. The generation of the 2D Airy beam, synthesized by two similar 1D Airy beams accelerating along orthogonal directions, was demonstrated at 9.5 GHz. Then, the 2D Airy beams were fulfilled over a wide frequency band varying from 8.5 to 9.5 GHz. Secondly, I explored the zeroth-order Bessel beam. The 2D Bessel beam with different phase tilt angles was studied and the frequency agility of the Bessel beam generator was validated.

The attractive Airy beams propagating along a parabolic trajectory and having the advantage of energy concentration can be potentially exploited in applications of near-field communications, non-line-of-sight communications and underground exploration without directly passing through the obstacle. However, there are some aspects that still need to be exploited for the 2D Airy beam generator, such as the 2D Airy beams synthesized by two 1D Airy beams accelerating along non-orthogonal directions.

Compared to other diffraction-free beams, Bessel beams have higher directivity. The Bessel beam has potential application in the fields of near-field precise detection, near-field communication systems, covert communications, medical imaging, and wireless power transfer. It should be noticed that the zeroth-order Bessel beam can also be utilized to produce a higher-order Bessel beam by superposing its phase profile to the profile of a vortex beam.

Chapter 5 Vortex beams generation and manipulation

In recent years, the speed and capacity requirements of wireless communication systems have sharply increased since more and more smart terminals are connected to Internet. Therefore, wireless communication systems are subjected to the problem of scarcity of spectrum resources. To solve this problem, plenty of methods, including code division multiple access (CDMA), orthogonal frequency division multiplexing (OFDM), multi input multi output (MIMO), and so on, are proposed. The channel capacity and spectrum utilization are close to the Shannon limit. It is difficult to further improve the channel capacity using the conventional modulation of amplitude, phase, frequency, and polarization. However, the emergence of vortex beams carrying orbital angular momentum (OAM) provides a new freedom to modulate electromagnetic waves. In this chapter, I will explore another type of complex beam, the vortex beam, using the designed 2D reconfigurable metasurface.

5.1 Introduction

The momentum of electromagnetic waves is composed of linear momentum and angular momentum. The angular momentum is mainly of two types, spin angular momentum and orbital angular momentum[199]. The spin angular momentum is related to the polarization containing linear polarization, left-handed polarization and right-handed polarization. However, the orbital angular momentum is associated with the helical transverse phase structure denoted by $\exp(jl\phi)$, where l is the OAM mode and can be any integer. The relation of vortex beams carrying different modes can be expressed as:

$$\int_0^{2\pi} e^{jl_1\theta} \cdot \left[e^{jl_2\theta}\right]^* d\theta = \begin{cases} 2\pi & l_1 = l_2 \\ 0 & l_1 \neq l_2 \end{cases} \tag{5-1}$$

The vortex beams carrying the different OAM modes are orthogonal to each other. The orbital angular momentum is a new freedom for signal modulation and it allows multiple signals to be sent at the same frequency in different modes at the same time. Due to this feature of OAM, the spectrum efficiency of the signal will be greatly improved, so that the network capacity and communication security are further improved.

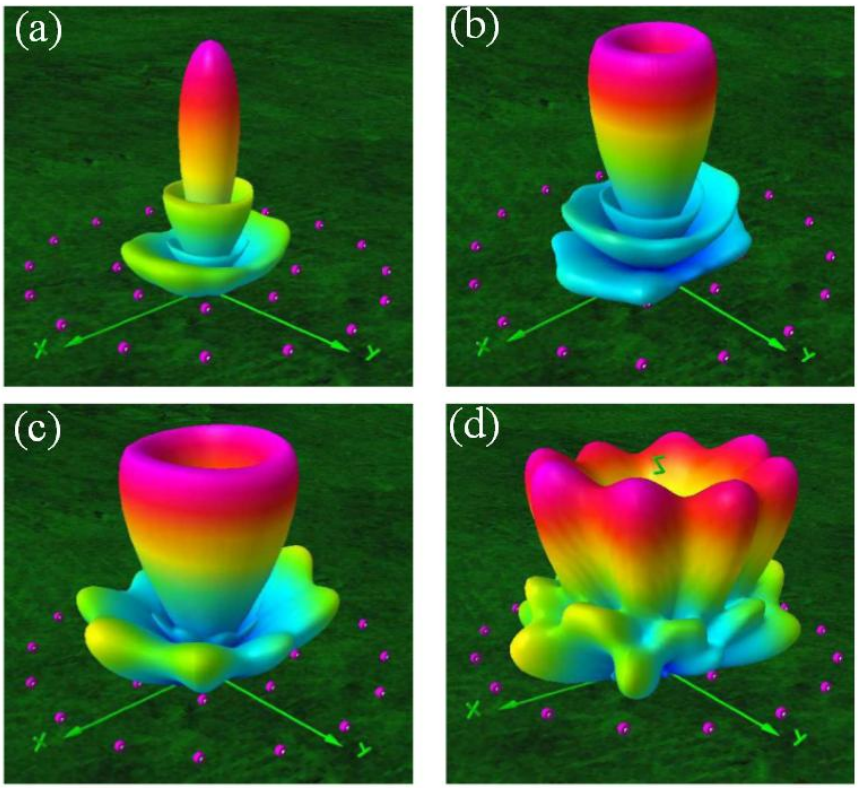

Figure 5.1 Radiation pattern for different OAM modes l = 0, 1, 2, and 3 at radio frequency domain[204].

It has been a long process from discovery to the application of vortex beams. J. H. Poynting predicted that electromagnetic waves had angular momentum in 1909 when he was studying the fluctuation characteristics of the rotating shaft[200]. In 1936, this prediction was verified by R. A. Beth *et al.* using the elaborately designed apparatus to detect and measure the angular momentum of light[201]. In 1992, the Dutch physicist L. Allen *et al.* proved that the Laguerre-Gauss beam possess the orbital angular momentum with the phase factor $e^{jl\theta}$[202]. Then, in 2004, G. Gibson proposed to use different OAM modes to encode data in optical communication, which offers a level of security since it is difficult to read the data without positioning the detector directly in the path of the intended receiver[203].

In 2007, B. Thidé *et al.* introduced OAM in the microwave frequency domain. Vortex beams with different OAM modes were numerically generated by using an antenna array in the radio frequency band[204]. The simulated vortex beams carrying different OAM modes are presented in Figure 5-1. The clear hollow areas with null intensity can be observed in the center of vortex beams with a mode $l \neq 0$. In 2011, for the first time, F. Tamburini *et al.* experimentally verified vortex beams in the radio frequency range in San Marco of Venice, Italy, as presented in Figure 5-2[205]. In this milestone experiment, an helicoidal parabolic antenna is used to transmit the signal and two Yagi antennas are used as receivers, which

realizes the simultaneous transmission of signals corresponding to different modes of 0 and 1 at 2.41 GHz. The significance of this experiment is that vortex beams with different modes at the same frequency can be transmitted simultaneously.

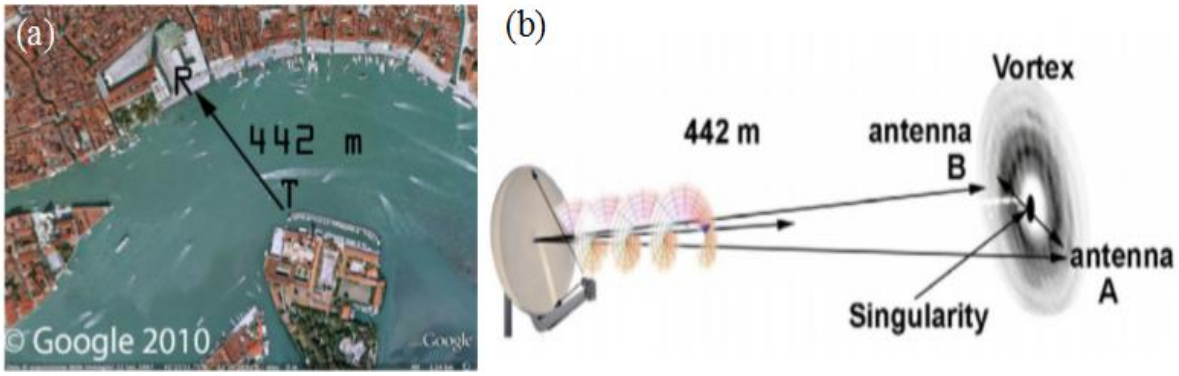

Figure 5.2 (a) Experiment place of the San Marco in Venice, Italy. (b) Schematic of the experiment. The helicoidal parabolic antenna is used as a transmitter while the Yagi-Uda antenna A and B are used as receiver[205].

Since then, the vortex beam carrying orbital angular momentum has attracted enormous attention and has been applied to versatile applications, including radio communications[206-209], radars[210-215], and object identification[216]. Plenty of methods, which contain spiral phase plates[216-220], spiral and twisted reflectors[221-224], circular phased arrays[225-230], and metasurfaces[231-237], are proposed to generate the vortex beam carrying OAM.

The spatial phase plate is derived from optics and has the advantages of simple structure and easy implementation. Since the spatial phase plate is generally an all-dielectric device realized by mechanical machining, it is not sensitive to polarization of illuminating waves. Transmissive spatial phase plates can be divided into three categories, as shown in Figure 5-3[217]. The thickness changes with the azimuth angle for the first two spatial phase plates. When the plane wave passes through the spiral phase plate, the transmitted wave has a path difference due to the different thickness of the medium at different positions of the helical phase plate, allowing to change the wavefront of the transmitted wave. Therefore, this device can convert conventional plane waves into vortex beams carrying OAM with a spiral phase factor $\exp(jl\varphi)$. For the third spatial phase plate, the thickness is constant, but the equivalent dielectric constant changes with the azimuth angle such that different equivalent dielectric constants correspond to different phase delays. However, the disadvantage of spatial phase plates is their bulky size. In addition, once the sample is manufactured, only a single OAM mode with limited functions can be generated.

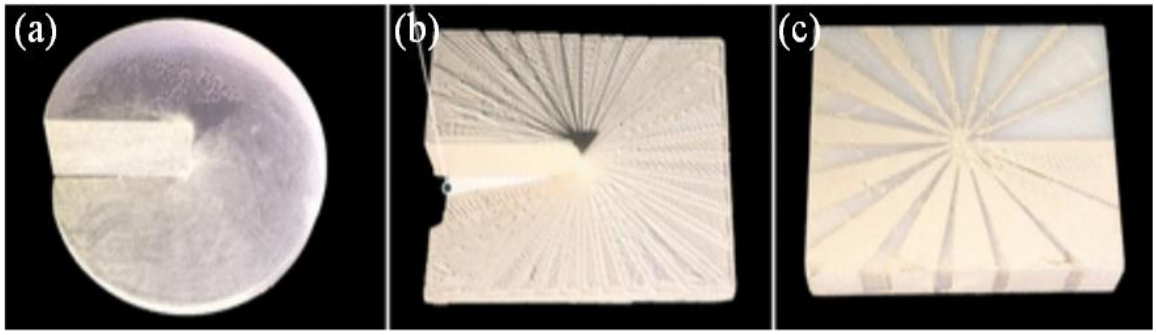

Figure 5.3 Three different kinds of 3D-printed spiral phase plate: (a) The thickness continuously varies. (b) The thickness has a staircase structure. (c) The thickness is fixed with a gradient refractive index versus the azimuth angle[217] .

The reflector antenna can also be used to generate vortex beams in the microwave domain. E. Mari *et al.* designed a twisted spiral parabolic reflector antenna based on an ordinary parabolic antenna as shown in Figure 5-4(a)[221]. The installation of the feed of the twisted spiral parabolic reflector antenna is the same as the standard Cassegrain antenna. The body of the antenna is made of photopolymerized ceramic material and copper with the 0.1 mm thickness is plated on the surface of the ceramic to reflect electromagnetic waves. F. Tamburini *et al.* proposed a planar reflector antenna with a discrete eight-step ladder to generate OAM based on the spiral phase plate[222]. As shown in Figure 5-4(b), eight polystyrene foam blocks covered with an electrically conductive and reflective surfaces are trimmed into a stepped structure.

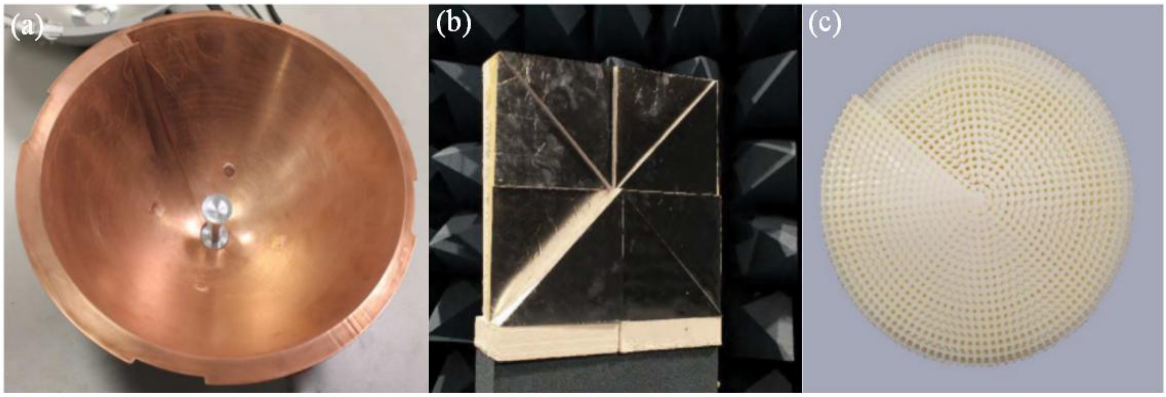

Figure 5.4 (a) Twisted spiral parabolic reflector antenna. (b) Staircase reflective antenna. (c) All-dielectric reflective lens[221-223].

J. Yi *et al.* designed a vortex beam generation lens with a flat cylindrical shape based on the transformation optics concept, as shown in Figure 5-4(c)[223]. The lens manufactured by 3D printing technology mimics a spiral parabolic antenna by transforming the uniform

free space above the spiral paraboloid area into a flat cylindrical space with inhomogeneous permittivity distribution. When electromagnetic waves pass through different areas of the lens and reflected by the backed metal plate, a phase difference will be produced due to the different permittivity distribution and then a vortex beam is generated. The lens is made of all-dielectric material such that it is not sensitive to the polarization of the incident wave and can realize the generation of vortex electromagnetic waves with arbitrary polarization. Besides, this all-dielectric lens can work in a wide frequency band. However, those devices are also subjected to the issue of bulk size and limited functionality.

The circular array antenna is another method to realize vortex beams carrying OAM, by adjusting the phase difference between the radiation elements. Q. Bai *et al.* designed a standard uniform circular array (UCA)[225], where the N element antennas are equidistantly placed on a circle with radius a and around the beam axis. In order to generate vortex beams with the OAM mode l, each element is fed with signals of equal amplitude and different phases. However, this type of array antenna requires a complicated microstrip line feed network. There is a mathematical relationship between the number of circular array antenna elements and the largest OAM mode that can be generated is $|l| < N/2$. The vortex beams generated by all these devices generally show inherent divergence characteristics.

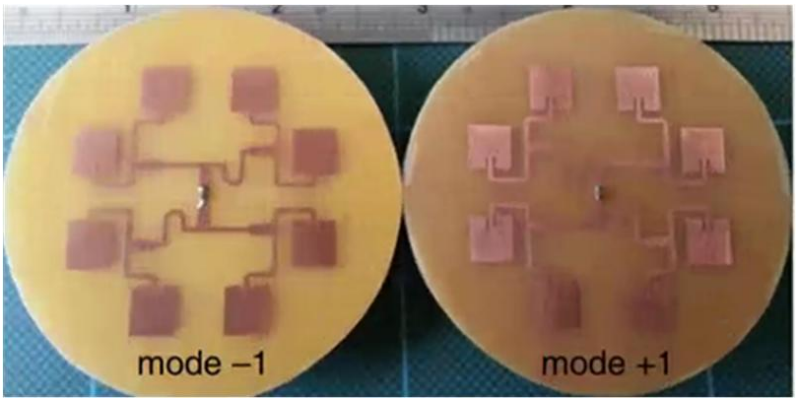

Figure 5.5 Photography of the typical UCA antenna using for vortex beam generation[225].

To solve the problem of the bulk size and limited design freedom, ultrathin metasurfaces have been proposed for the generation of vortex beams. As stated in chapter 1, a metasurface is composed of the artificial periodic or quasi-periodic structure with subwavelength dimensions, allowing it to accurately control the phase, magnitude, and polarization of electromagnetic waves. S. Yu *et al.* designed a reflective metasurface to effectively generate vortex beams as depicted in Figure 5-6(a). A reflective unit cell composed of three metallic strips was designed. By changing the length of the strips and the size ratio between the three

strips, 360° phase coverage can be realized with high reflectivity. Then, a reflective metasurface consisting of 20 × 20 unit cells is designed and fabricated for the numerical and experimental vortex beam generation with OAM mode l = 2. W. Luo *et al.* proposed a transmissive PB metasurface. The unit cell is composed of three metallic layers. The top layer and third layer are rectangular strips, and the middle layer is a holey metallic layer coupled with a rectangular strip in the center of the hole. The 360° phase coverage can be achieved by turning the orientation of the rectangle patch according to the theory of the PB phase. Three different vortex beams with OAM modes l = 1, 2, and 3 are generated utilizing three different metasurfaces of this type at 10.5 GHz.

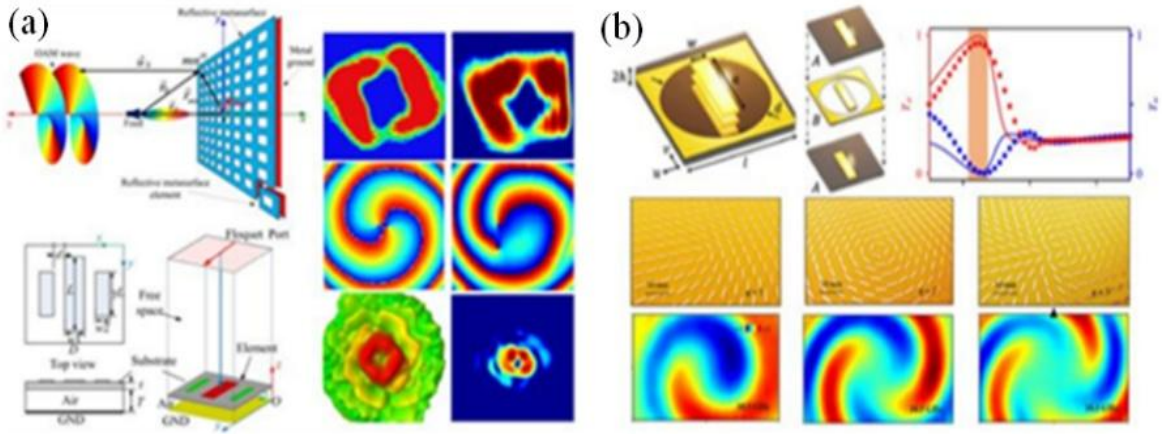

Figure 5.6 (a) Reflective metasurface used for the vortex beam generation[231]. (b) Transmissive metasurface utilized for the vortex beam generation[232].

However, these passive vortex beam generators suffer from the problems of limited functionalities and narrow bands. In this chapter, I will explore the dynamic generation of vortex beams carrying OAM using the designed 2D reconfigurable metasurface. The vortex beams with different OAM modes can be flexibly switched as desired by adjusting the bias voltage applied to the metasurface. This multi-functional vortex beam generator present potential applications in radar imaging, target detection, and wireless communication systems.

5.2 Vortex beams generation

The orbital angular momentum provides a new freedom for signal modulation. Therefore, it is more meaningful when the device can dynamically generate vortex beams carrying different OAM modes. In this section, I will demonstrate the dynamic realization

of three types of vortex beams with different OAM modes using a reconfigurable metasurface.

5.2.1 Laguerre-Gaussian beam

In this thesis, the plane wave is adopted as an illuminating source in HFSS. For the experimental measurements, the source antenna is placed 2 m away from the metasurface as described in chapter 2, such that the wave illuminating the metasurface can be considered as a quasi-plane wave. Therefore, the phase influence of the source antenna is not taken into account in the calculation of the phase profile applied to the metasurface for both simulation and measurements. In order to generate the Laguerre-Gaussian vortex beam carrying OAM mode, the spiral-like phase profile in the azimuthal direction should be applied to the metasurface, which can be expressed as[238]:

$$\varphi_l(x,y) = l \cdot \arctan(y/x) \tag{5-2}$$

where x and y denote the coordinate of the unit cell located in the metasurface. l is the OAM mode and it can be an arbitrary integer. The difference between positive modes and negative modes is only the direction of wavefront rotation. In this chapter, I only select positive modes for demonstration.

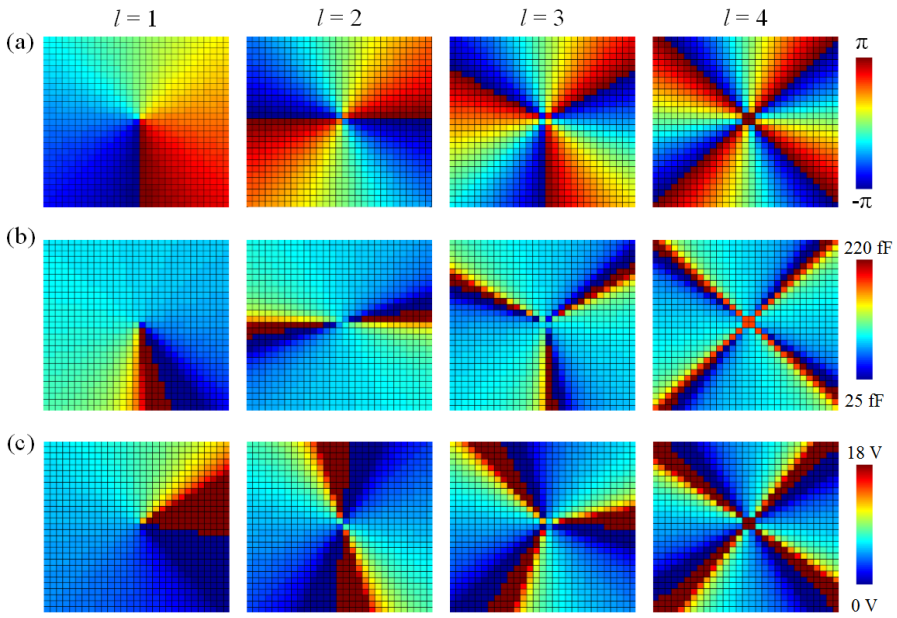

Figure 5.7 Phase, capacitance, and bias voltage profiles of Laguerre-Gaussian beams with different OAM modes l = 1, 2, 3, and 4 at 9.5 GHz. (a) Phase profiles. (b) Capacitance profiles. (c) Bias voltage profiles.

To explore the generation of Laguerre-Gaussian beams carrying OAM in the normal direction of metasurface, four positive modes l = 1, 2, 3, and 4 are selected for the numerical and experimental investigation. The phase profiles for Laguerre-Gaussian beams with different OAM modes l = 1, 2, 3, and 4 can be obtained from equation (5-5) as shown in Figure 5-7(a). The corresponding capacitance and voltage profiles are displayed in Figures 5-7(b) and (c). The numerical simulations of the Laguerre-Gaussian beams are carried out to generate different OAM modes at 9.5 GHz using the HFSS configuration presented in Figure 2-2 of chapter 2.

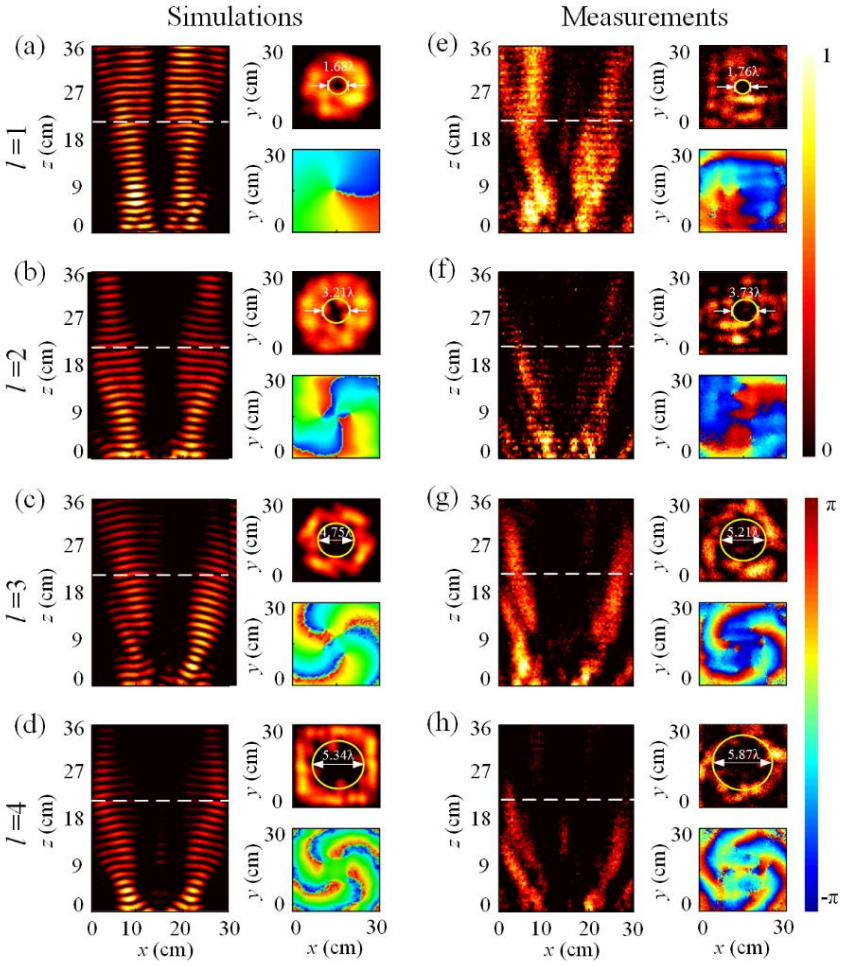

Figure 5.8 Numerical simulations and experimental measurements of the Laguerre-Gaussian beams with different OAM modes l = 1, 2, 3, and 4 at 9.5 GHz. (a)-(d) Simulated electric field distributions. (e)-(h) Measured electric field distributions. The two subfigures show the electric field distributions in the *xoy* plane at z = 22 cm.

Figures 5-8(a)-(d) show the electric field distributions of Laguerre-Gaussian beams with different OAM modes. We can see a clear hollow region with null intensity in the center

of the *xoz* plane for the four Laguerre-Gaussian beams, and it can be noted that the Laguerre-Gaussian beams diverge along the propagation distance. The divergence of the vortex beams increases with the number of OAM modes. These phenomena are consistent with the inherent divergent property of Laguerre-Gaussian beams. Besides, the subfigures in the right side of Figures 5-8(a)-(d) depict the simulated electric field distributions in the *xoy* plane at z = 22 cm. The doughnut-shaped structure can be seen and the diameters of the doughnut-shaped structure are approximately 1.68λ, 3.21λ, 4.75λ, and 5.34λ for the OAM modes l = 1, 2, 3, and 4, respectively. It is noticed that the diameter of the doughnut-shaped structure is in direct proportion to OAM modes l, which is another inherent tendency of vortex beams. In addition, we can observe the helical twist phase patterns of the Laguerre-Gaussian beams with different modes, which completely conform to $l \cdot 2\pi$.

Then, the fabricated 2D reconfigurable metasurface is used to experimentally validate the generation of Laguerre-Gaussian beams with the desired OAM modes l = 1, 2, 3, and 4. Figures 5-8(e)-(h) depict the measured results of Laguerre-Gaussian beams with different OAM modes at 9.5 GHz. The diameters of the four measured ring-shaped electric field distributions are around 1.76λ, 3.731λ, 5.21λ, and 5.87λ for the OAM modes l = 1, 2, 3, and 4, respectively. The deviation between the simulation and experimental measurement mainly comes from the fabrication error of the metasurface. The quasi-plane wave illuminating the metasurface also has a small influence on the measurement compared to the plane wave utilized in simulations as described in Chapter 4. Besides, since the voltage resolution of the electronic control board is 0.1 V, it is not easy to confirm that all the 900 unit cells are applied with the precise voltage value corresponding to the calculated phase, and therefore, this issue also contributes to a deteriorated measurement. Although the measurements show the deterioration to some slight extent, we can still clearly distinguish the modes of the generated vortex beams.

5.2.2 Focusing vortex beam

The divergence along propagation direction is an inherent property of the Laguerre-Gaussian beam. In order to optimize the divergence shortcoming of the vortex beam at a specific distance, I consider combining a focusing phase profile to the phase profile of Laguerre-Gaussian beams. The phase distribution of such focusing vortex beam on the metasurface can be expressed as[238]:

$$\varphi_{FOAM}(x,y) = l \cdot \arctan(y/x) + k(\sqrt{x^2 + y^2 + f^2} - |f|) \tag{5-3}$$

where f is the focal length.

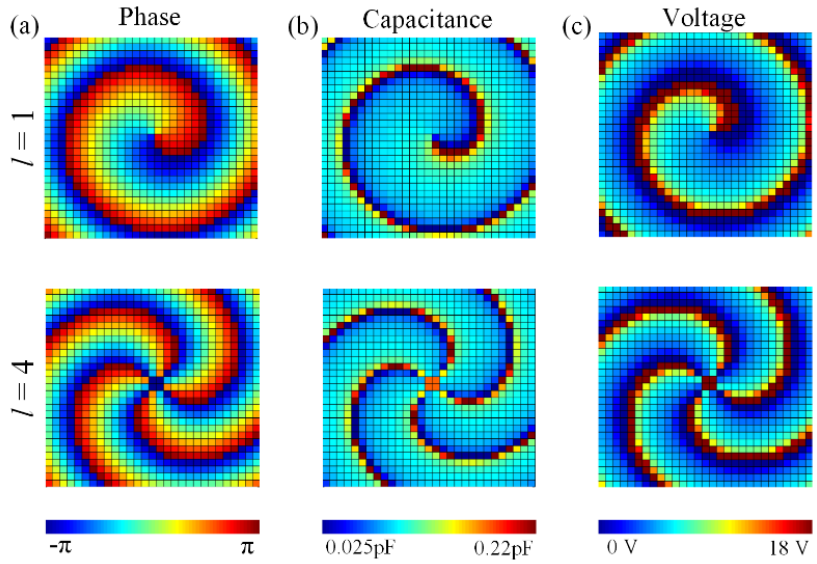

Figure 5.9 Phase, capacitance, and bias voltage profiles of the focusing vortex beams with different OAM modes l = 1 and 4 at 9.5 GHz. (a) Phase profiles. (b) Capacitance profiles. (c) Bias voltage profiles.

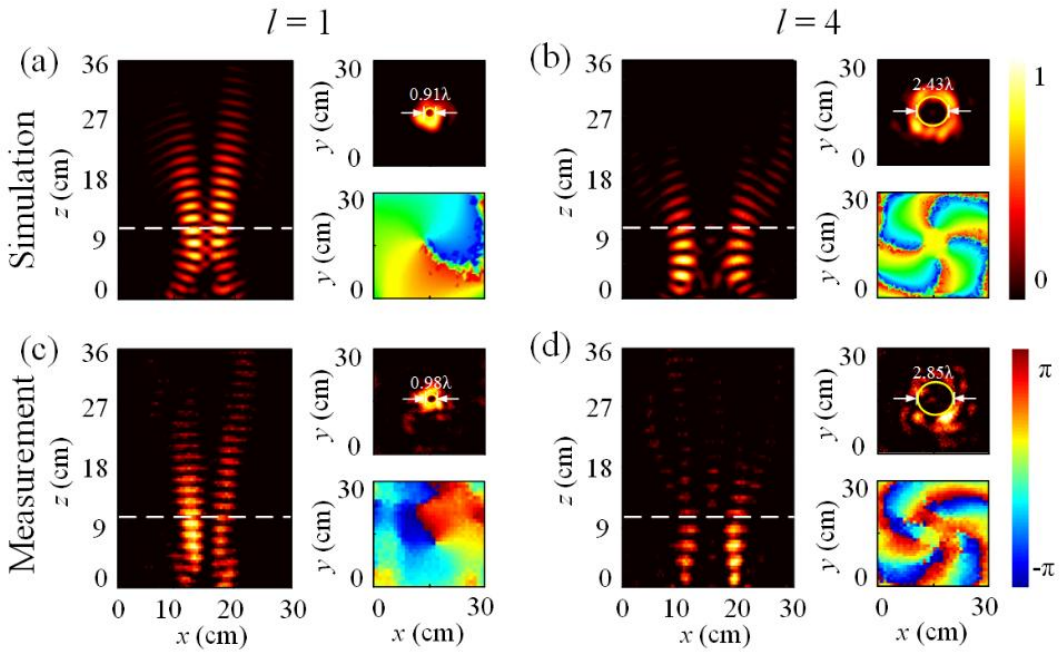

Figure 5.10 Numerical simulations and experimental measurements of the focusing vortex beams with different OAM modes l = 1 and 4 at 9.5 GHz. (a)-(b) Simulated electric field distributions. (c)-(d) Measured electric field distributions. The two subfigures show the electric field distributions in the xoy plane at z = 10 cm.

In this subsection, I explore the focusing vortex beam with different OAM modes and focal distance of f = 100 mm at 9.5 GHz. To simply validate the focusing vortex beam generation, only OAM modes 1 and 4 are selected. According to equation (5-3), the phase, capacitance, voltage profiles of the focusing vortex beams with the focal distance f = 100 mm for OAM modes l = 1 and 4 at 9.5 GHz are determined and displayed in Figures 5-9(a)-(c). Then, the corresponding simulations of focusing vortex beams are performed at 9.5 GHz as depicted in Figures 5-10(a) and (b). The energy convergence of two beams at nearly z = 100 mm is visible and the hollow structure can also be observed from the electric field distributions in *xoz* planes. The results extracted from the transverse plane at z = 10 cm (dotted with line in *xoz* plane) are also presented in the right two subfigures of Figures 5-10(a) and (b). The diameters of the ring-shaped electric field distributions in *xoy* plane of the two focusing vortex beams are 0.91λ and 2.43λ for the OAM modes l = 1 and 4, respectively. In addition, we can also observe that the helical twist phase distributions in *xoy* plane of the two focusing vortex beams. The results obtained from measurements are shown in Figures 5-10(c) and (d), which agree with the simulations, demonstrating the vortex beam can be focused in a specific distance by superposing a preset focusing phase profile. It is worth noting that the beam decays rapidly along the propagation direction beyond the focal point.

5.2.3 Non-diffracting vortex beam

The focusing vortex beam can overcome the divergence of the Laguerre-Gaussian beam. However, this type of vortex beam is usually practical for a near-field OAM wireless communication system. To realize a far-field OAM wireless communication system, one has to achieve a non-diffracting vortex beam whose energy is concentrated around the central axis along the propagation direction. For this purpose, I propose to combine the non-diffracting zeroth-order Bessel beam phase profile as described in Chapter 4 to the Laguerre-Gaussian vortex beam phase profile, realizing a non-diffracting vortex beam. Therefore, the phase profile of the non-diffracting vortex beam should satisfy the following equation[238]:

$$\varphi_{BOAM}(x,y) = l \cdot \arctan(y/x) + k\sqrt{|x|^2 + |y|^2}\sin\theta \tag{5-4}$$

where the parameter θ is the tilt angle of the phase profile of the zeroth-order Bessel beam.

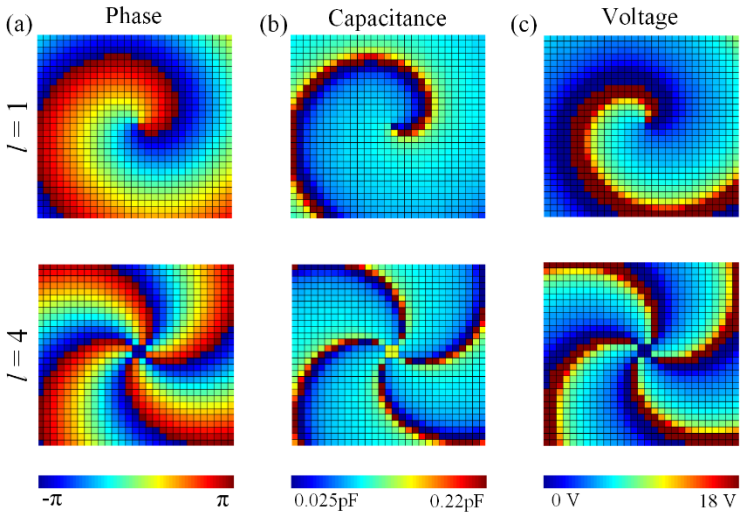

Figure 5.11 Phase, capacitance, and bias voltage profiles of the non-diffracting vortex beams with different OAM modes $l = 1$ and 4 at 9.5 GHz. (a) Phase profiles. (b) Capacitance profiles. (c) Bias voltage profiles.

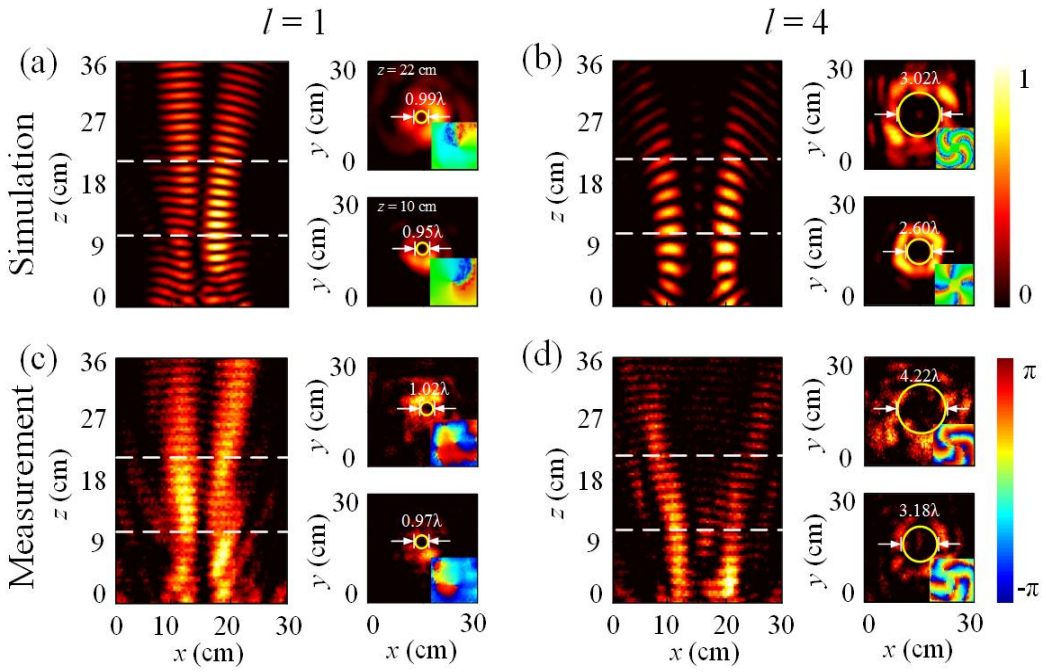

Figure 5.12 Numerical simulations and experimental measurements of non-diffracting vortex beams with different OAM modes $l = 1$ and 4 at 9.5 GHz. (a)-(b) Simulated electric field distributions. (c)-(d) Measured electric field distributions. The insets in the right two subfigures show the helical twist phase distributions.

The phase, capacitance and bias voltage profiles required to demonstrate the generation of non-diffracting vortex beams with different modes are calculated and presented in Figure

5-11. The non-diffracting vortex beams with different OAM modes l = 1 and 4 are numerically and experimentally generated at 9.5 GHz. The simulated electric field distributions of the two non-diffracting vortex beams are shown in Figures 5-12(a) and (b). These results show hollow beams with a null in the center for the non-diffracting vortex beams. The ring-shaped electric field distributions of the two non-diffracting vortex beams in *xoy* planes at z = 10 and 22 cm are displayed in the two subfigures of Figures 5-12(a) and (b), where the insets show the corresponding helical twist phase patterns. To further validate the non-diffracting vortex beam, the diameter of the non-diffracting vortex beams at different propagation distances is displayed in the subfigures. The diameters of the two non-diffracting vortex beams at z = 22 cm are around 0.99λ and 3.02λ for the OAM modes l = 1 and 4, respectively. The diameters of the two non-diffracting vortex beams at z = 10 cm are 0.95λ and 2.60λ for the OAM modes l = 1 and 4, respectively. The diameters of the ring-shaped structure at the transverse plane have a small change with the propagation of non-diffracting vortex beams due to the effect of the combined non-diffracting zeroth-order Bessel beam phase profile. The measurements of the two non-diffracting vortex beams are depicted in Figures 5-12(c)-(d). We can see the diameters of non-diffracting vortex beams in *xoy* plane present a small change at the two positions of z = 10 cm and z = 22 cm. The fabrication error and quasi-plane wave emitted from horn antenna explain the deteriorated measurements.

5.2.4 Comparison among the three different kinds of vortex beams

In the above subsection, I have verified the realization of the Laguerre-Gaussian, focusing, and non-diffracting vortex beams at 9.5 GHz. In this subsection, I consider comparing the three different types of vortex beams carrying OAM mode l = 1. The near-field results are presented in Figures 5-13(a)-(f). Compared to the Laguerre-Gaussian, the diameter of the ring-shaped electric field distributions in *xoy* plane at z = 22 cm is smaller for non-diffracting vortex beams due to the combined non-diffracting zeroth-order Bessel phase profiles. The concentrated energy around the central axis along the propagation direction can be clearly observed for the non-diffracting vortex beam. In addition, the far-field results of the three different kinds of vortex beam with OAM mode l = 1 are depicted in Figures 5-13(g)-(h), which exhibits the non-diffracting vortex beams have the smallest divergent angle and the two main beams of the non-diffracting vortex beam appear at around $\mp 10°$. Compared to the other two types of vortex beams, the non-diffracting vortex beam can be considered more suitable for wireless communication. In the next subsection, I will

explore the generation of non-diffracting vortex beams over a wide frequency band.

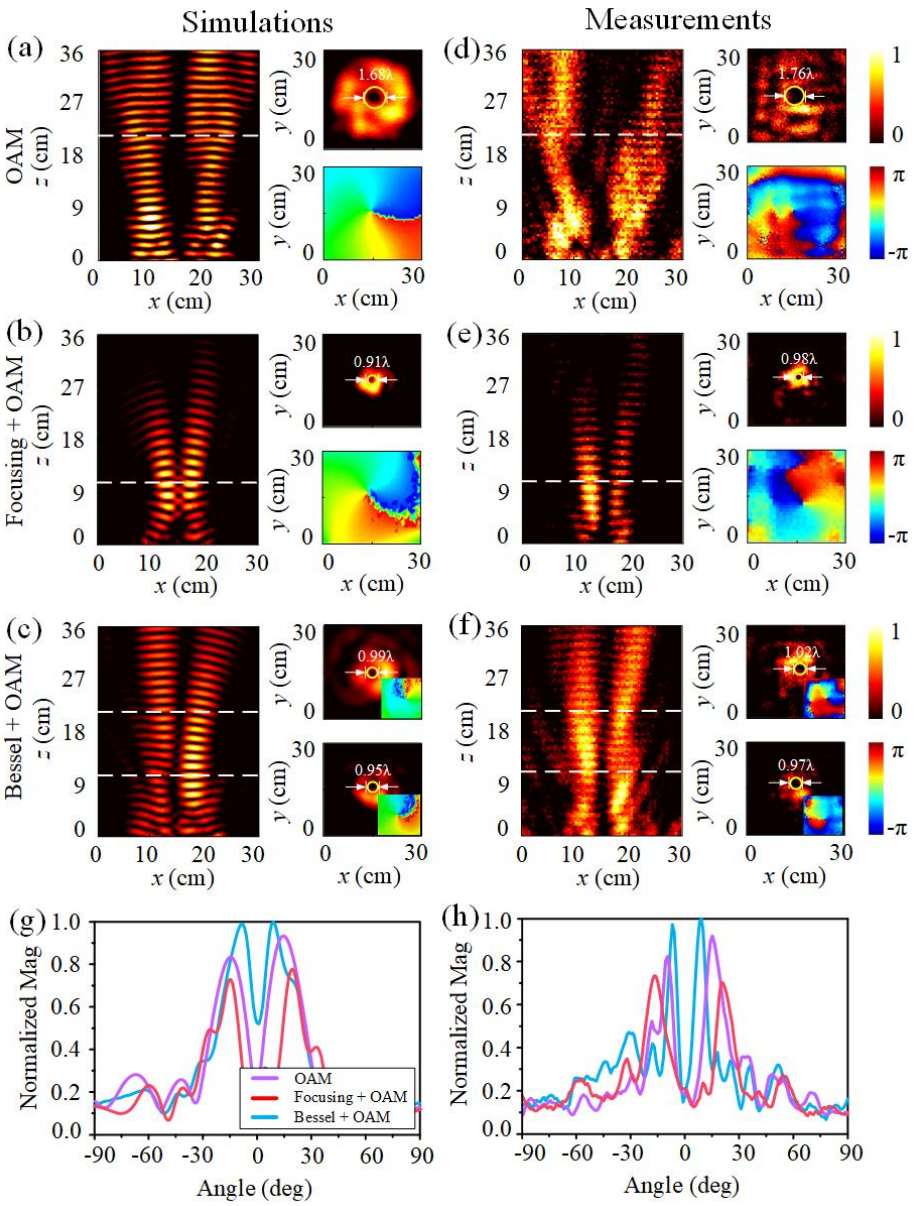

Figure 5.13 Numerical simulations and experimental measurements of Laguerre-Gaussian, focusing, and nondiffracting vortex beams with OAM mode $l = 1$ at 9.5 GHz. (a)-(c) Numerical near-field simulations. (d)-(f) Experimental near-field measurements. (g) Numerical far-field simulations in *xoz* plane. (g) Experimental far-field measurements in *xoz* plane [239].

5.3 Non-diffracting vortex beams generation in a wide frequency band

I start by recalling that traditional antenna systems and passive metasurfaces can only generate vortex beams with limited OAM modes in a narrow band. The results deteriorate when the frequency moves away from the preset operating frequency point. However, the

phase profile of our reconfigurable metasurface can be dynamically adjusted, allowing the operating frequency point to move in a wide frequency band without the deterioration of results.

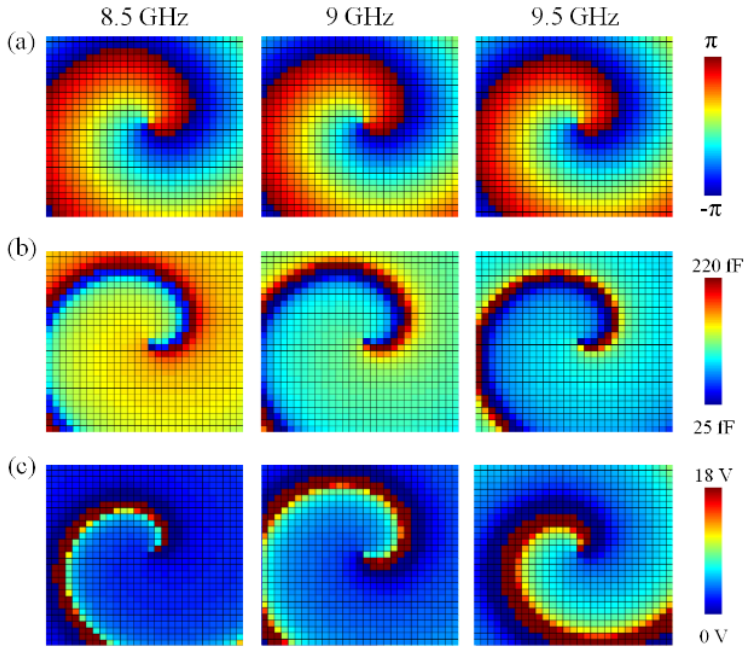

Figure 5.14 Phase, capacitance, and bias voltage profiles of the non-diffracting vortex beams with OAM mode $l = 1$ at 9.5 GHz. (a) Phase profiles. (b) Capacitance profiles. (c) Bias voltage profiles.

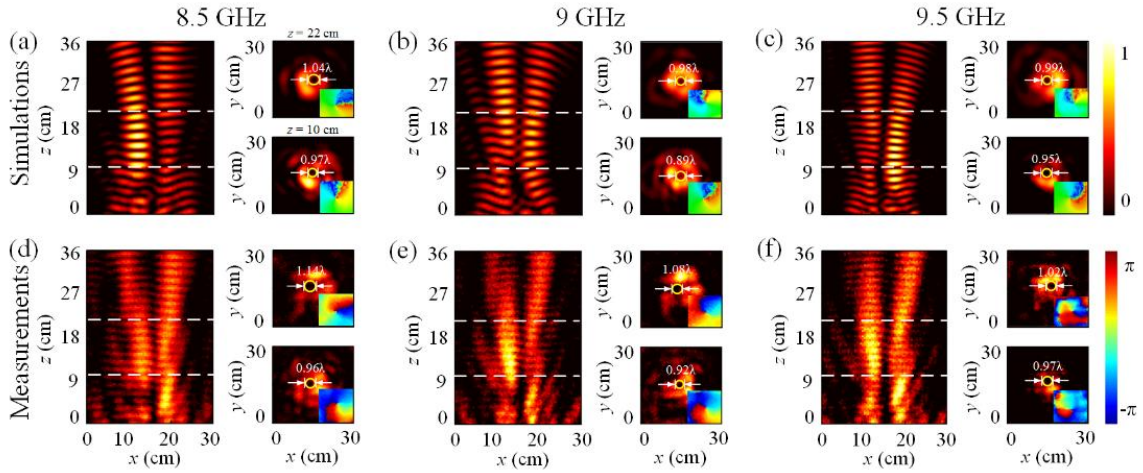

Figure 5.15 Numerical simulations and experimental measurements of the non-diffracting vortex beams with OAM mode $l = 1$ at 8.5, 9, and 9.5 GHz. (a)-(c) Simulated electric field distributions. (d)-(f) Measured electric field distributions. The insets show the helical twist phase distributions.

In this subsection, I demonstrate the generation of non-diffracting vortex beams with OAM mode $l = 1$ over a non-narrow operating frequency band ranging from 8.5 to 9.5 GHz. The phase, capacitance, and bias voltage profiles used for the simulations and measurements are shown in Figure 5-14. The simulations and measurements of the non-diffracting vortex beams with OAM mode $l = 1$ are carried out at 8.5, 9, and 9.5 GHz, respectively. The related results of non-diffracting vortex beams at three operating frequencies are presented in Figures 5-15. We can see that the near-null intensity in the center along the *z*-axis for the three vortex beams in the *xoz* plane. The nearly constant diameter of ring-shaped electric field distributions in the two detecting *xoy* planes at $z = 10$ cm and 22 cm can be observed. Measurements have a good agreement with the simulations. These results demonstrated the good frequency agility of the designed vortex beam generator based on the two-dimensional reconfigurable metasurface. However, it should be noticed that the vortex beam generated by the reconfigurable metasurface at each frequency point is still narrowband.

In this section, I validated the dynamic generation of vortex beams carrying different OAM modes at different frequency points using the 2D reconfigurable metasurface, which presents a potential application for the OAM mode modulation and operating frequency modulation of an OAM-based wireless communication system.

5.4 Multiple vortex beams generation

Compared to traditional antennas that can only realize a single vortex beam from one aperture, the ultrathin metasurface generator has the specific advantage of achieving multiple vortex beams simultaneously in different directions from one shared aperture. The multiple vortex beams method can effectively increase communication capacity and signal coverage of the orbital angular momentum wireless communication system, and can be applied to the modulation and multiplexing of different signals in one system. In this section, I will validate the proof of concept of the single-mode and quad-mode multiple vortex beams generations using the 2D reconfigurable metasurface.

5.4.1 Principle of multiple vortex beams

In this section, the method for four vortex beams is achieved by dividing the square metasurface into four equal regions, allowing the independent control of the modes of four vortex beams.

To begin with, I describe the principle of the second method that can be used to generate

four vortex beams simultaneously carrying either similar mode or different modes in the four channels. By dividing the square metasurface into four equal regions, vortex beams with arbitrary OAM modes can be independently generated in four channels. The phase profile of the quad-mode vortex beams can be expressed as:

$$\varphi(x,y)=\begin{cases} l_1\cdot\arctan\left(\frac{y}{x}\right)+k\left(\sqrt{x^2+y^2+f^2}-|f|\right), & \left(0<x\ll\frac{M}{2},\ 0<y\ll\frac{M}{2}\right) \\ l_2\cdot\arctan\left(\frac{y-M/2}{x}\right)+k\left(\sqrt{x^2+\left(y-\frac{M}{2}\right)^2+f^2}-|f|\right), & \left(0<x\ll\frac{M}{2},\ \frac{M}{2}<y\ll M\right) \\ l_3\cdot\arctan\left(\frac{y}{x-M/2}\right)+k\left(\sqrt{\left(x-\frac{M}{2}\right)^2+y^2+f^2}-|f|\right), & \left(\frac{M}{2}<x\ll M,\ 0<y\ll\frac{M}{2}\right) \\ l_4\cdot\arctan\left(\frac{y-M/2}{x-M/2}\right)+k\left(\sqrt{\left(x-\frac{M}{2}\right)^2+\left(y-\frac{M}{2}\right)^2+f^2}-|f|\right), & \left(\frac{M}{2}<x\ll M,\ \frac{M}{2}<y\ll M\right) \end{cases} \tag{5-8}$$

where l_1, l_2, l_3, and l_4 are the OAM modes in the corresponding channels. f is the focal distance. M is the side length of a square metasurface. The phase profile for the independent deflection can be written as:

$$\varphi_{def}(x,y)=\begin{cases} x\sin\theta_2+y\sin\theta, & \left(0<x\ll\frac{M}{2},\ 0<y\ll\frac{M}{2}\right) \\ x\sin\theta_2-(y-\frac{M}{2})\sin\theta, & \left(0<x\ll\frac{M}{2},\ \frac{M}{2}<y\ll M\right) \\ (x-\frac{M}{2})\sin\theta_2+y\sin\theta, & \left(\frac{M}{2}<x\ll M,\ 0<y\ll\frac{M}{2}\right) \\ (x-\frac{M}{2})\sin\theta_2-(y-\frac{M}{2})\sin\theta, & \left(\frac{M}{2}<x\ll M,\ \frac{M}{2}<y\ll M\right) \end{cases} \tag{5-9}$$

where θ is the deflection angle of the vortex beam with respect to the z-axis. In this thesis, the quad-mode vortex beams are preset with the same deflection angle for the proof of concept. It is worth noting that the deflection angles of the quad-mode vortex beams can be set to different values. The phase profile of the quad-mode vortex beams with independent deflection angles can thus be expressed as:

$$\varphi_{total}(x,y) = \varphi_{def}(x,y) + \varphi(x,y) \tag{5-10}$$

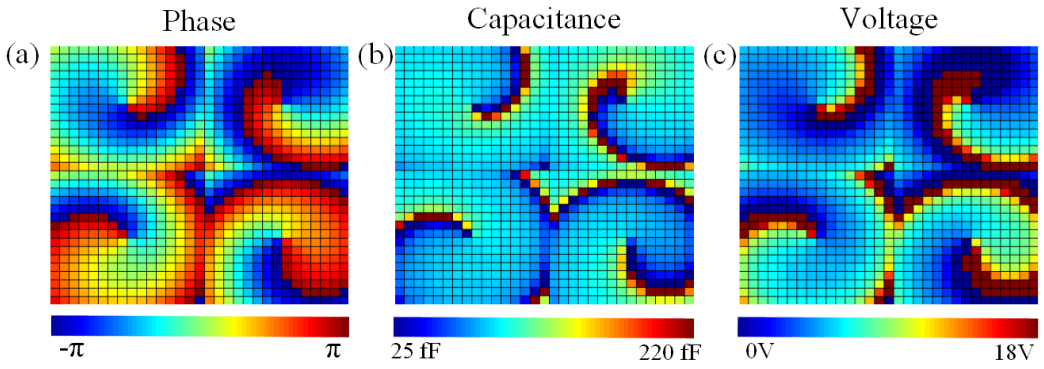

Figure 5.16 Phase and capacitance profile of the four vortex beams with same OAM mode l = 1 and focal distance f = 10 cm using method of dividing one metasurface into four equal parts. (a) Phase profile. (b) Capacitance profile. (c) Voltage profile.

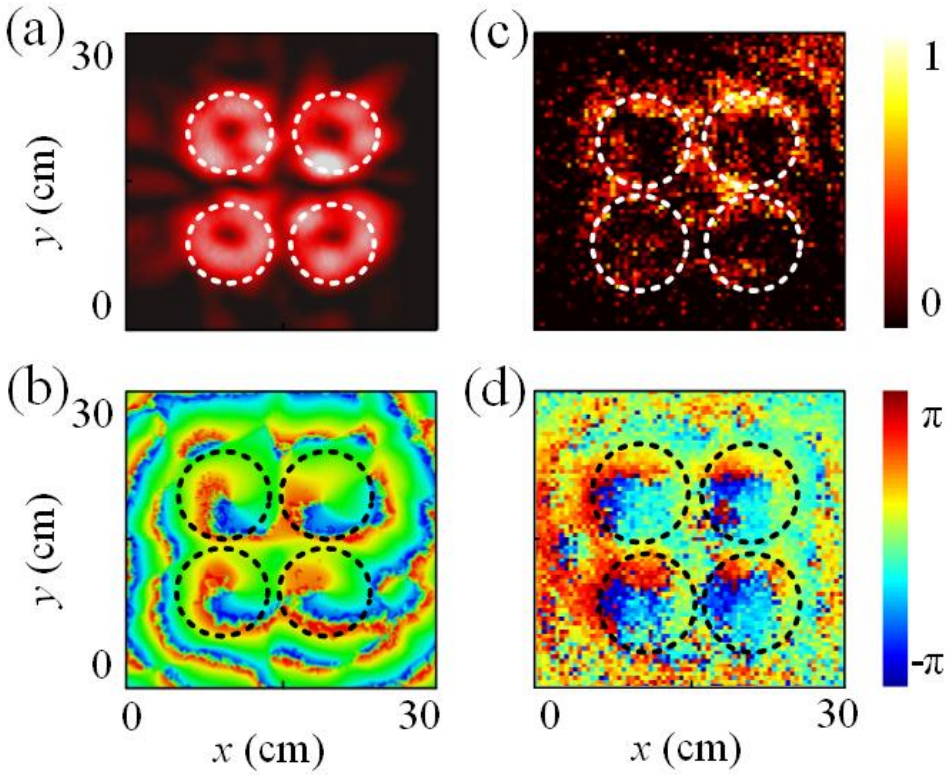

Figure 5.17 Numerical simulated and experimental measured electric field distributions of the four vortex beams with same mode l =1 in the transverse plane of z = 100 mm at 9.5 GHz using method of dividing one metasurface into four equal parts. (a) Simulated electric field distribution. (b) Simulated phase distribution. (c) Measured electric field distribution. (d) Measured phase distribution.

5.4.2 Four vortex beams carrying similar OAM mode

In this subsection, I demonstrate the generation of four vortex beams carrying the same OAM mode at 9.5 GHz using the proposed method, which is to divide the metasurface into four equal parts as described in equation (5-8). I preset the OAM modes of the four vortex beams with focal distance f = 10 cm as $l_1 = l_2 = l_3 = l_4 = 1$. The phase, capacitance, and voltage profiles are calculated and displayed in Figure 5-16. By applying the capacitance profiles to the metasurface, the simulation is performed at 9.5 GHz. The results in the transverse plane z = 10 cm are presented in Figures 5-17(a) and (b), where we can observe the four doughnut-shaped electric field distributions and four clear helical twist phase patterns. Figures 5-17(c) and (d) show the corresponding measured results, where four identical vortex beams can be seen. The concept of four vortex beams generation with the same mode by dividing the metasurface into four equal parts is demonstrated.

5.4.3 Four vortex beams carrying different OAM mode

I further validate the generation of four vortex beams with different OAM mode in different channels at the same time. According to equation (5-10), I calculate the phase profile of four vortex beams with OAM modes 0, 1, 2, and 3 by dividing the metasurface into four equal parts, as displayed in Figure 5-18(a). The calculated capacitance profile is obtained from the phase response versus the capacitance of the corresponding tunable unit cell and is exhibited in Figure 5-18(b). Figure 5-18(c) shows the voltage profile. The simulation and measurement of the four vortex beams with different OAM modes are carried out at 9.5 GHz and the results are shown in Figure 5-19. The normalized intensity distribution in the transverse plane z = 10 cm shows one focusing spot corresponding to mode l = 0 and three ring-shaped structures for the modes 1,2 and 3, which means the vortex beams with different OAM modes are generated simultaneously. The inherent tendency of the intensity ring radius in direct proportion to the OAM mode can be observed. We can also observe one quasi-plane phase distribution and three helical twist phase distributions in Figure 5-19(b) and (d). Due to the overlap and interference between the four vortex beams, we can see the measurement is deteriorated. However, the four vortex beams with different OAM modes can still be easily distinguished. These results demonstrated the concept of four vortex beams with different OAM modes by dividing the metasurface into four equal parts.

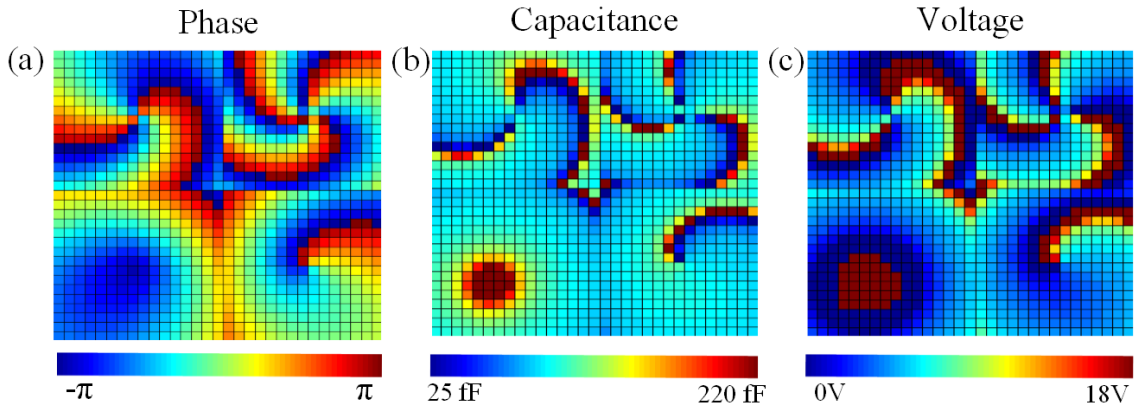

Figure 5.18 Phase and capacitance profile of the four vortex beams with different OAM modes including 0, 1, 2, and 3, and focal distance f = 10 cm using method of dividing one metasurface into four equal parts. (a) Phase profile. (b) Capacitance profile.

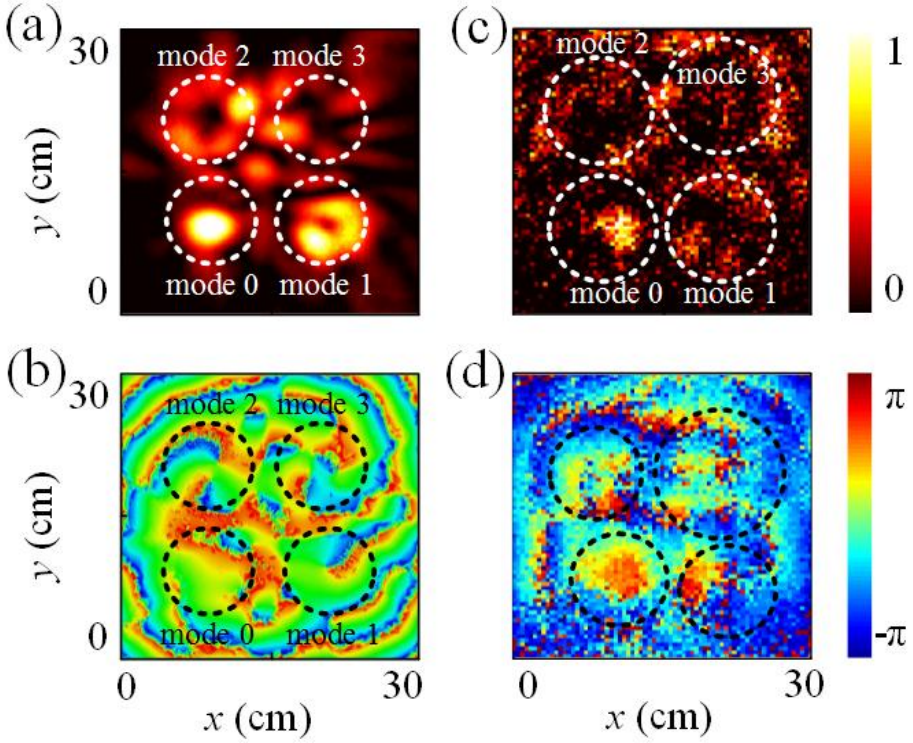

Figure 5.19 Numerical simulated and experimental measured electric field distributions of the four vortex beams with different OAM modes including 0, 1, 2, and 3, and focal distance f = 10 cm at 9.5 GHz using method of dividing one metasurface into four equal parts. (a) Simulated electric field distribution. (b) Simulated phase distribution. (c) Measured electric field distribution. (d) Measured phase distribution.

5.5 Conclusion

In this chapter, I explored the dynamic generation of vortex beams carrying OAM mode using the 2D reconfigurable metasurface. First, the dynamic generation of three types of vortex beams carrying OAM, including Laguerre-Gaussian beam, focusing vortex beam, and non-diffracting vortex beam, were demonstrated. Compared to other vortex beams, the non-diffracting vortex beam has the smallest divergence angle. Then, the realization of non-diffracting vortex beam over a wide frequency band was achieved. Additionally, I studied multiple vortex beams generation. By superposing appropriate phase profiles to the focusing vortex beam, several vortex beams carrying similar or different OAM modes are generated simultaneously.

Only phase modulation can be realized using our two-dimensional reconfigurable metasurface. Therefore, only the mode and operating frequency of vortex beams can be adjusted. It can be necessary to design a reconfigurable metasurface whose phase and amplitude can be individually adjusted to realize both phase and amplitude modulations of vortex beams, which is more applicable in wireless communication. In the next chapter, I will explore holographic imaging and spatial energy allocation, which has a potential application in security, near-field wireless communication.

Chapter 6 Digital holographic imaging generation

Different from traditional optical devices for holographic imaging, ultrathin metasurfaces have the unique ability to control the phase, amplitude, and polarization of illuminating waves as described in chapter 1, providing the possibility of holographic imaging technology with high resolution and imaging efficiency. Holographic imaging based on metasurfaces opens an avenue for applications such as industrial detection sensors, wireless energy transmission, radio frequency identification, and near-field communication. In this chapter, I will explore the digital holographic imaging using the designed 2D reconfigurable metasurface.

6.1 Introduction

As a vital method to fully engineer the wavefronts of the EM waves, holography was first proposed by D. Gabor in the research of improving the revolution of microscopes in 1947[240], allowing him to be awarded the 1971 Nobel Prize in Physics. The basic principle of holography is divided in two steps, wavefront recording and wavefront reconstruction. The process of wavefront recording is achieved by the interference on the hologram plate between the object light, which is the light scattered from an object, and the reference light that illuminates the hologram plate. The hologram plate can record all the information about the amplitude and phase of the object light corresponding to the 3D information of the object. When the hologram plate is illuminated with only an incident light similar to the reference light used in the wavefront recording process, it acts as a diffraction grating to produce a three-dimensional image of the original object. This process is known as wavefront reconstruction. However, the traditional holographic technology requires a complicated optical system, including a photosensitive process and a real object.

In 1966, A.W. Lohmann and D.P. Paris proposed the method to generate hologram using computers, known as Computer Generated Holography (CGH)[241]. Compared to traditional holography, the wavefront recording process of CGH is completed by a computer such that the complex coherent light illumination systems, photosensitive processes, and natural objects are not required. Consequently, CGH provides a way to image virtual objects that may not exist in nature. The recording process of CGH is generally realized through theoretical calculations based on interference or diffraction, which can avoid producing

conjugate images and significantly improve the imaging quality of holography. The mechanism of CGH is to use a specific optical device to realize the calculated phase distribution hologram, and the required imaging can be obtained from the optical device under the illumination of incident waves. However, the traditional optical devices suffer from the bulky size and high losses.

The emergence of metasurfaces exhibiting characteristics of low thickness and low loss provides a powerful tool for holography with unprecedented resolution, low noise, and high precision of the images. Thus, holography based on metasurface has attracted enormous attention for high-quality holographic imaging. Metasurface holography can be classified into phase-only metasurface holography[242-246] and complex amplitude metasurface holography[247-250].

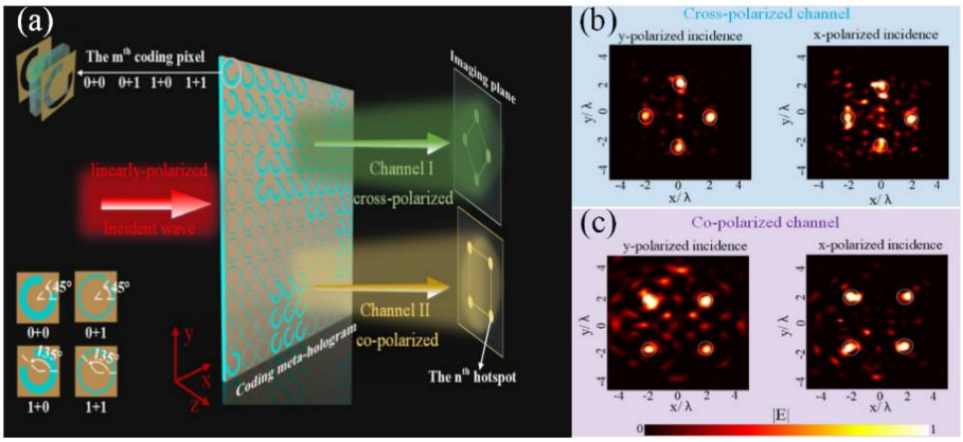

Figure 6.1 (a) Schematic of holography generation using a phase-only dual-polarized metasurface in microwave frequency domain. (b) The simulation and measurement for the cross-polarized component. (c) The simulation and measurement for the co-polarized component[244].

By utilizing an iterative or point source algorithm to optimize the uniform intensity distribution of images, the phase-only metasurface holography can achieve imaging using only phase without the amplitude information[251]. L. Huang *et al.* demonstrated 3D imaging using a metasurface, composed of a metallic nanorod array, illuminated by the circularly polarized incident wave[242]. The nearly 360° phase coverage and uniform amplitude are realized based on the PB phase principle through changing the orientation of metallic nanorods. By appropriately assigning the orientation of the nanorods on the metasurface, the 3D image appears in the Fresnel range at the visible and near-infrared bands. Similarly, X. Zhang *et al.* proposed the phase-only metasurface holography based on the PB phase principle over a wide frequency band[243]. In the microwave frequency domain, a phase-only

coding metasurface for holography generation is realized by C. Guan *et al.* as shown in Figure 6-1[244]. The split rings are adopted for the unit cell design, which allows the 1-bit phase coding with a phase change between 0 and π and a nearly constant amplitude. Two different holographic images are achieved under linear polarized incident waves in two channels corresponding to the cross-polarized and co-polarized components.

The complex amplitude metasurface holography means that the incoming wavefront is modulated in both phase and amplitude, which can reconstruct the image of objects without information loss. X. Ni *et al.* verified the high-resolution and low-noise metasurface hologram in the visible range with both amplitude and phase modulation by an ultra-thin (λ/23) metasurface composed of V-shaped nano-elements[247]. Q. Wang *et al.* adopted the C-shaped split rings in the unit cell design, which can simultaneously and independently manipulate the phase and amplitude by changing the geometrical parameters such as split opening angle, orientation angle and radius of split ring, which greatly simplifies the metasurface design[248]. The metasurface hologram with complex amplitude modulation is realized and the corresponding results are shown in Figure 6-2.

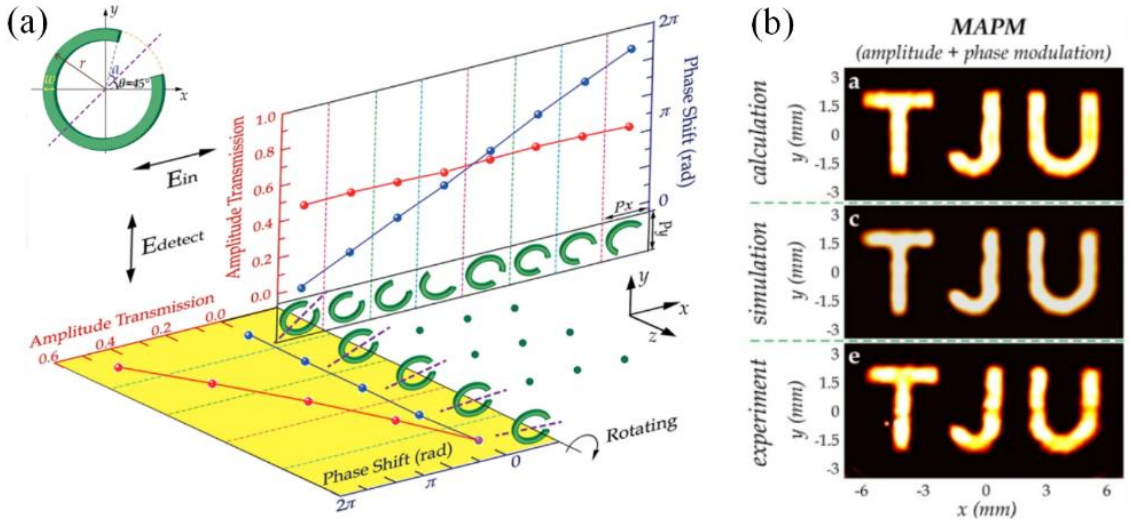

Figure 6.2 (a) Phase and amplitude response of the C-shaped element. (b) The corresponding results for the complex amplitude modulation[248].

The passive metasurfaces introduced above are limited in terms of functionalities and reconfigurability. To realize holographic images that can be tuned in real time, several types of tunable components, such as phase-transition materials[252–259], 2D materials[260–264], diodes[265-267], and liquid metal[268,269], were used for the reconfigurable metasurface design. In the microwave domain, T. J. Cui *et al.* designed a reconfigurable holographic metasurface

integrated PIN diodes as shown in Figure 6-3[265]. The reconfigurable metasurface is composed of tunable unit cells that can be individually addressed on a two-dimensional scale. The tunable unit cell can achieve the binary phase coding by switching the state of the PIN diodes between "ON" and "OFF". The phase profile applied to the reconfigurable metasurface is changed by a field-programmable gate array (FPGA) program board. Therefore, the high-resolution holographic images are achieved in real-time. Then, T. J. Cui *et al.* proposed another reconfigurable metasurface also loaded with PIN diodes. This metasurface can realize full-space EM wave control, allowing holographic imaging generation in both reflection and transmission modes[266]. However, the metasurface integrating PIN diodes can only achieve binary phase states. The low phase-quantization has a non-negligible influence on the image quality[270].

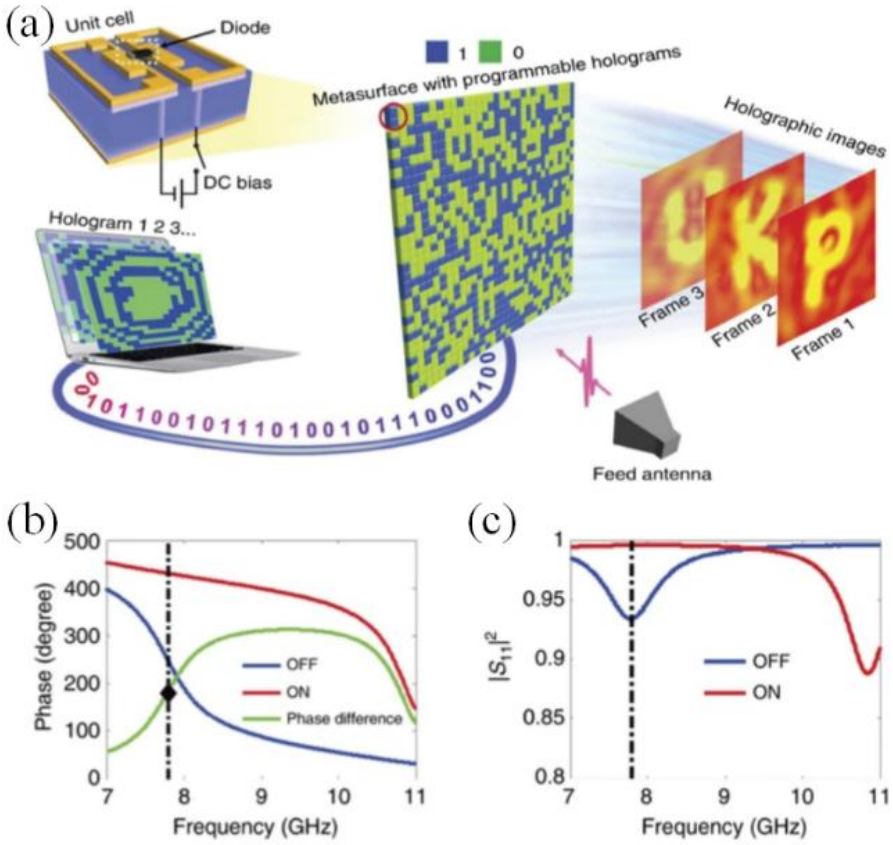

Figure 6.3 (a) Schematic of the holographic imaging system using the 1-bit coding metasurface. (b) Phase response of the unit cell. (c) The reflection efficiency of the unit cell[265].

In this chapter, I present the dynamic holographic imaging system utilizing the varactor-based two-dimensional reconfigurable metasurface whose phase can be continuously controlled. Therefore, high phase-quantization can be realized to generate a holographic

image with good quality. Three different types of holographic images including focal spots, Arabic numbers, and Alphabet letters are generated at different frequencies and distances based on the modified weighted Gerchberg-Saxton (GSW) algorithm. Then, the multibit spatial energy modulation in different channels is also demonstrated.

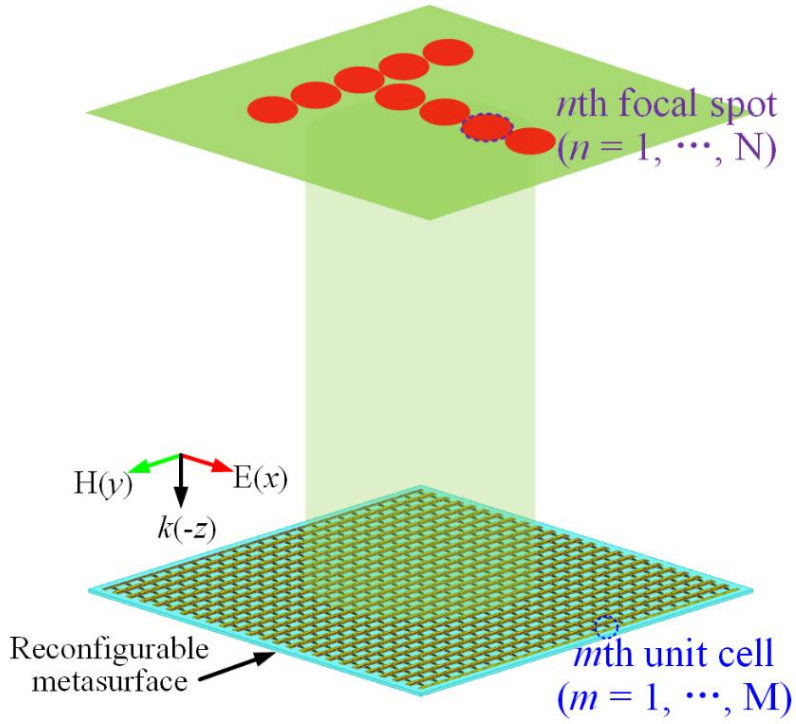

Figure 6.4 Schematic of the holographic imaging using the reflective reconfigurable metasurface.

6.2 Principle of holographic imaging

In this chapter, the dynamic holographic imaging is realized by utilizing the modified weighted Gerchberg-Saxton algorithm. The holographic imaging is performed in the near-field such that the focal distance is limited compared to the operating wavelength. Therefore, the propagation formula of EM waves is characterized by Green's function instead of Fraunhofer diffraction due to the fact that the propagation of EM waves does not satisfy the paraxial approximation[271]. We assume there are N focal spots in the imaging plane and M unit cells constituting the metasurface as shown in Figure 6-4. E_n is defined as the electric field of the n^{th} focal spot. φ_m is the reflection phase of the m^{th} unit cell. To achieve the maximum efficiency for a general holographic imaging, the sum of all the focal amplitude $\sum_{n=1}^{N}|E_n|$ is expected to be maximum. For the weighted Gerchberg-Saxton algorithm, the

weighted factor w_n is introduced to optimize the holographic imaging efficiency and the energy ratio between *N* desired focal spots, which result in the new sum of all the focal amplitude $\sum_{n=1}^{N}|w_nE_n|$. By differentiating $\sum_{n=1}^{N}|w_nE_n|$ with respect to φ_m, the maximum condition satisfies:

$$\varphi_m = \arg\left(\sum_{n=1}^{N}\frac{e^{ikr_m^n}}{r_m^n}\frac{w_nE_n}{|E_n|}\right) \tag{6-1}$$

where r_m^n denotes the distance between the *n*th focal spot and *m*th unit cell. *k* is the phase constant in free space. Equation (6-1) is an implicit form since E_n is related to φ_m. Therefore, an iterative procedure should be introduced to obtain the phase distribution φ_m. The iterative procedure of the phase calculation satisfies the following equations[270]:

$$\varphi_m^p = \arg\left(\sum_{n=1}^{N}\frac{e^{ikr_m^n}}{r_m^n}\frac{w_n^pE_n^{p-1}}{\left|E_n^{p-1}\right|}\right) \tag{6-2}$$

$$E_n^p = \sum_{m=1}^{M}\frac{e^{-ikr_m^n+i\varphi_m^p}}{r_m^n} \tag{6-3}$$

$$w_n^p = w_n^{p-1}\frac{\sum_{n=1}^{N}\left|E_n^{p-1}\right|}{\left|E_n^{p-1}\right|}\frac{q_n}{\sum_{n=1}^{N}q_n} \tag{6-4}$$

where the superscript *p* denotes the number of iterations. The parameter q_n corresponds to the preset value of the intensity ratio of the *n*th focal spot. In order to run the algorithm successfully, the initial value of the parameters φ and *w* should be given, which can be expressed as:

$$w_n^0 = 1,\ \ \varphi_m^0 = \frac{2\pi m}{M} \tag{6-5}$$

To quantitatively evaluate the quality of the generated holographic images, the total efficiency is calculated and can be written as:

$$\eta_{\text{total}} = \frac{P_{image}}{P_{inc}} \tag{6-6}$$

where P_{image} denotes the power of carried by the effective focusing spots or image. P_{inc} represents the power incident on the metasurface.

6.3 Imaging of focusing spots

The theory of holographic imaging has been discussed in the above section. In this section, I will verify the holographic images generation of different focusing spots with uniform amplitude in different detecting planes at 8.5 GHz as illustrated in Figure 6-5. It should be noticed that the three holographic images are generated at different time sequences. Besides, by adjusting the energy ratio parameter w_n of the focusing spots according the GSW algorithm, 1-bit and 2-bit energy modulation of different focusing spots in different channels are also validated.

6.3.1 Dynamic generation of focusing spots

To begin with, the holographic images of two focusing spots with uniform amplitude at the focal distance z = 7 cm is demonstrated at 8.5 GHz (λ = 3.53 cm). According to the modified GSW algorithm, the code for the holographic reconstruction and phase calculation is written in Matlab. By setting the number of focal spots as 2 in the code and the corresponding positions (0.9λ, 0, 7 cm) and (-0.9λ, 0, 7 cm), the phase profile composed of 30 × 30 pixels is depicted in Figure 6-6(a). The capacitance and voltage profiles for the numerical and experimental validation are calculated and shown in Figure 6-6(d) and (g). Figure 6-7(b) shows the simulated result, where the clear two focusing spots with uniform amplitude can be observed in the imaging plane at z = 7 cm. The measured result is displayed in Figure 6-7(c). Although there are useless field in the measured image, we can clearly observe two focal spots as in simulation.

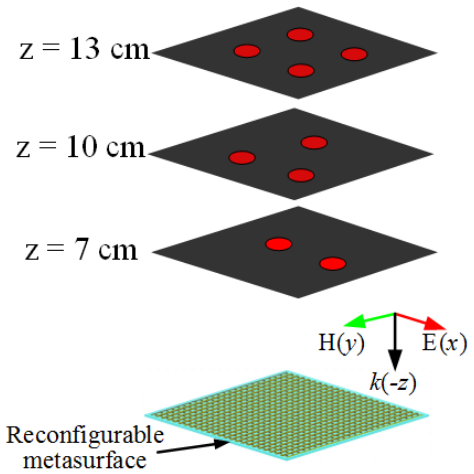

Figure 6.5 Schematic of holographic imaging of different focus spots in different detecting planes at 8.5 GHz.

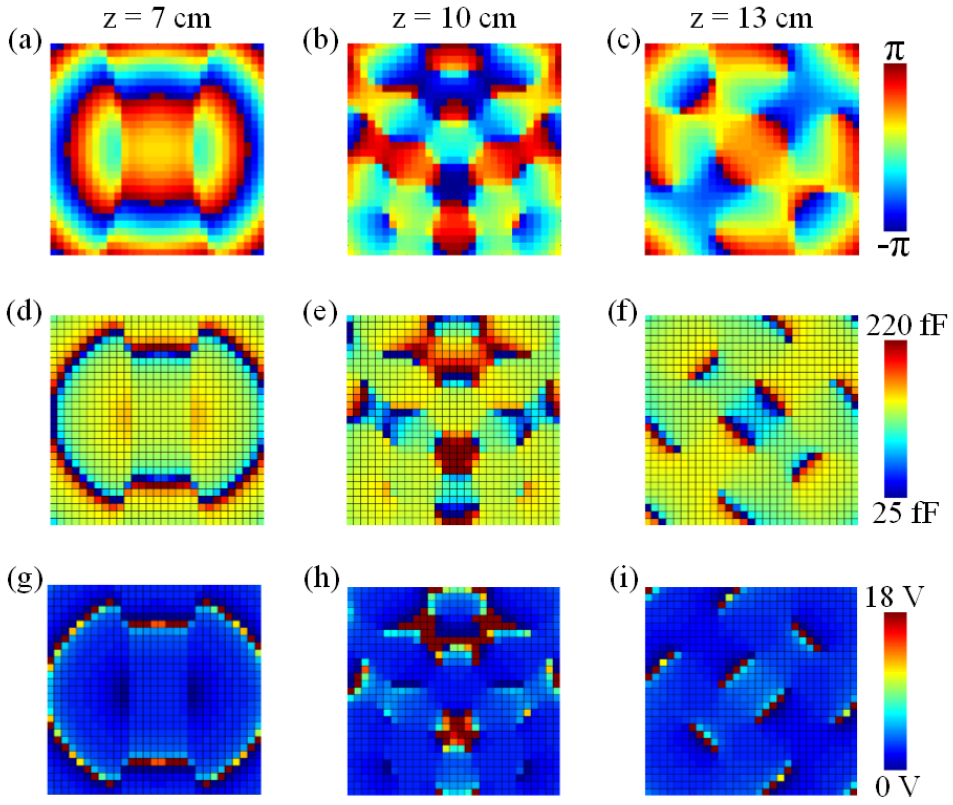

Figure 6.6 Phase, capacitance, and voltage profiles of the holographic images composed of different focal spots at different focal distances at 8.5 GHz. (a)-(c) Phase profiles. (d)-(f) Capacitance profiles. (g)-(i) Voltage profiles.

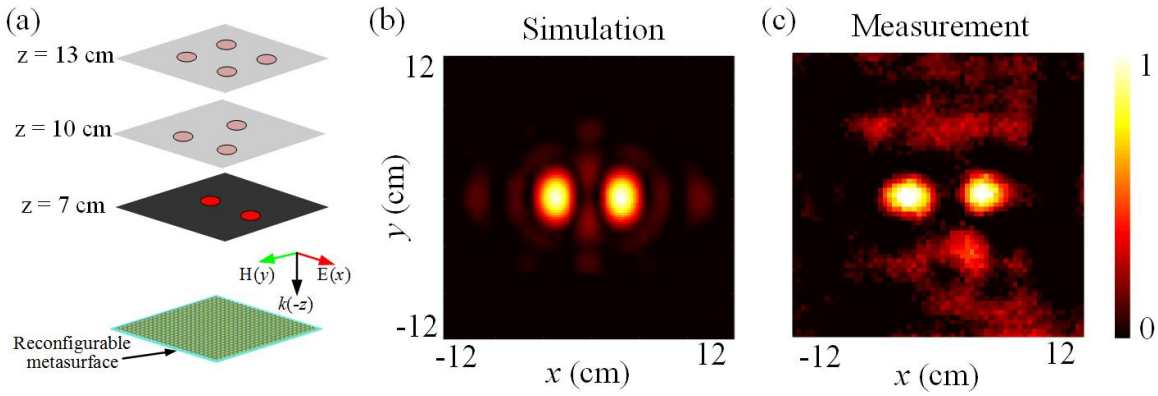

Figure 6.7 Numerical simulation and experimental measurement of the holographic image composed of two focal spots in the detecting plane z = 7 cm at 8.5 GHz. (a) Schematic of the holographic image composed of two focal spots. (b) Simulated result. (c) Measured result.

Then, the number of focal spots in holographic image is increased to 3. The position of

the three focal spots are preset at (1.8λ, -1.8λ, 10cm), (0, 1.8λ, 10cm), and (-1.8λ, -1.8λ, 10cm), which are arranged on the three vertices of a triangle in the plane z = 10 cm as illustrated in Figure 6-8(a). For the demonstration purpose, the phase profile, capacitance, and voltage profiles are calculated at 8.5 GHz and depicted in Figures 6-6(b), (e), and (h), respectively. Both the simulation and measurement of the holographic image composed of three focal spots are performed to validate the predesigned imaging. The simulated and measured results are shown in Figure 6-8(b) and (c), respectively. The three focusing points with nearly uniform amplitude can be observed, which is consistent with the theory.

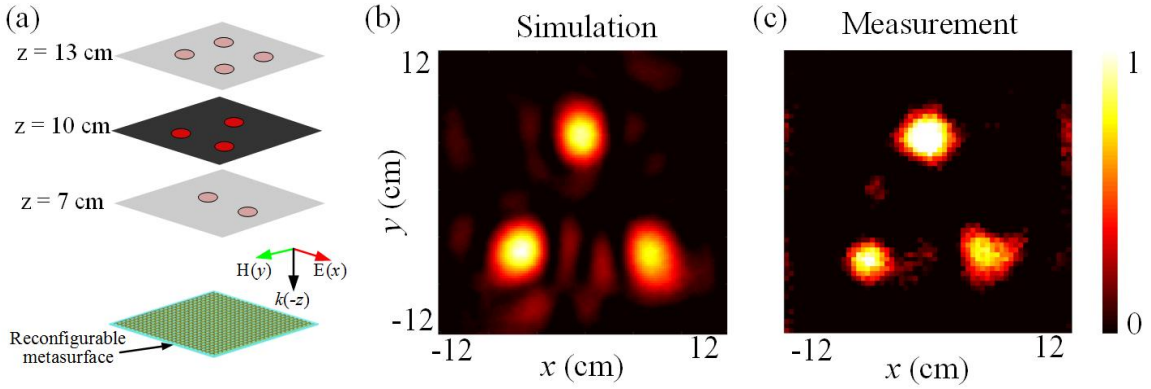

Figure 6.8 Numerical simulation and experimental measurement of the holographic image composed of three focal spots in the detecting plane z = 10 cm at 8.5 GHz. (a) Schematic of the holographic image composed of two focal spots. (b) Simulated result. (c) Measured result.

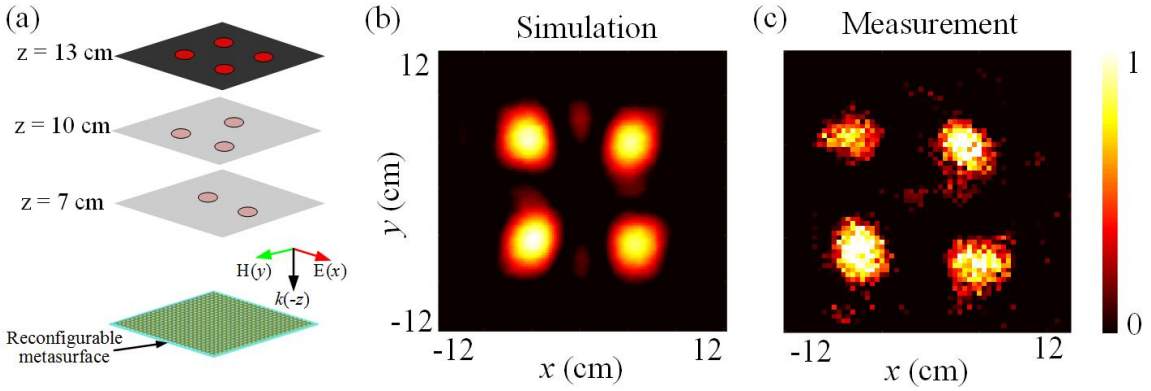

Figure 6.9 Numerical simulation and experimental measurement of the holographic image composed of four focal spots in the detecting plane z = 13 cm at 8.5 GHz. (a) Schematic of the holographic image composed of two focal spots. (b) Simulated result. (c) Measured result.

Besides, as presented in Figure 6-9(a), the implementation of holographic image composed of four focal spots, which are arranged on the four vertices of a rectangle, is demonstrated at 8.5 GHz in the plane z = 13 cm. The position of the four focal spots are preset at (1.5λ, 1.5λ, 13cm), (-1.5λ, 1.5λ, 13cm), (1.5λ, -1.5λ, 13cm), and (-1.5λ, -1.5λ, 13cm). The corresponding phase profile, capacitance, and voltage profiles are displayed in Figures 6-6(c), (f), and (i), respectively. The simulated and measured results are shown in Figure 6-9(b) and (c). The clear holographic image of 4 focal spots at 8.5 GHz are generated in the imaging plane z = 13 cm.

In summary, the dynamic generation of holographic images composed of different focal spots with uniform amplitude at different distances have been validated at 8.5 GHz from a single metasurface. The measured total efficiency of the three holographic images composed of 2, 3, and 4 focal spots is 24.34%, 26.85%, and 26.91%, respectively. The deviation between the near-field simulations and measurements come mainly from the fabrication error and quasi-plane incident wave emitted from the horn antenna as explained in Chapter 4. Furthermore, the energy ratio of the focusing points in a holographic image can be adjusted as desired using the modified GSW algorithm. It is interesting to investigate the energy modulation of the focusing points.

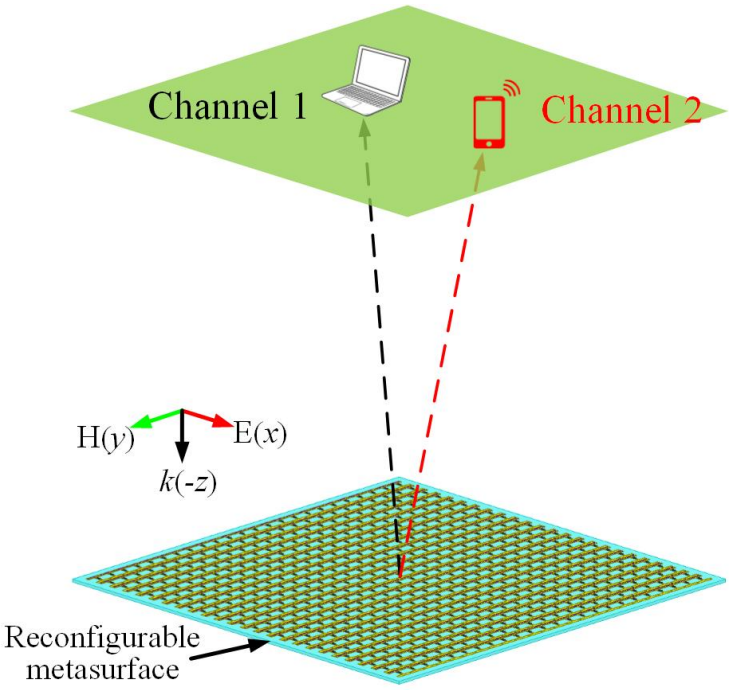

Figure 6.10 Schematic of the 1-bit energy modulation in two channels at 8.5 GHz. The focal distance is z = 7 cm.

6.3.2 Energy modulation of focusing spots

It is worth noting that the holography technology based on the 2D reconfigurable metasurface has potential application in the microwave field, such as near-field wireless energy transfer and near-field communications. By changing the factor q_n of the modified GSW algorithm, the energy ratio of N focal spots can be flexibly controlled. The concept of digital coding can be introduced into the spatial energy modulation in different channels to realize the multibit energy coding. In this subsection, I demonstrate the multibit spatial energy modulation in different channels at 8.5 GHz.

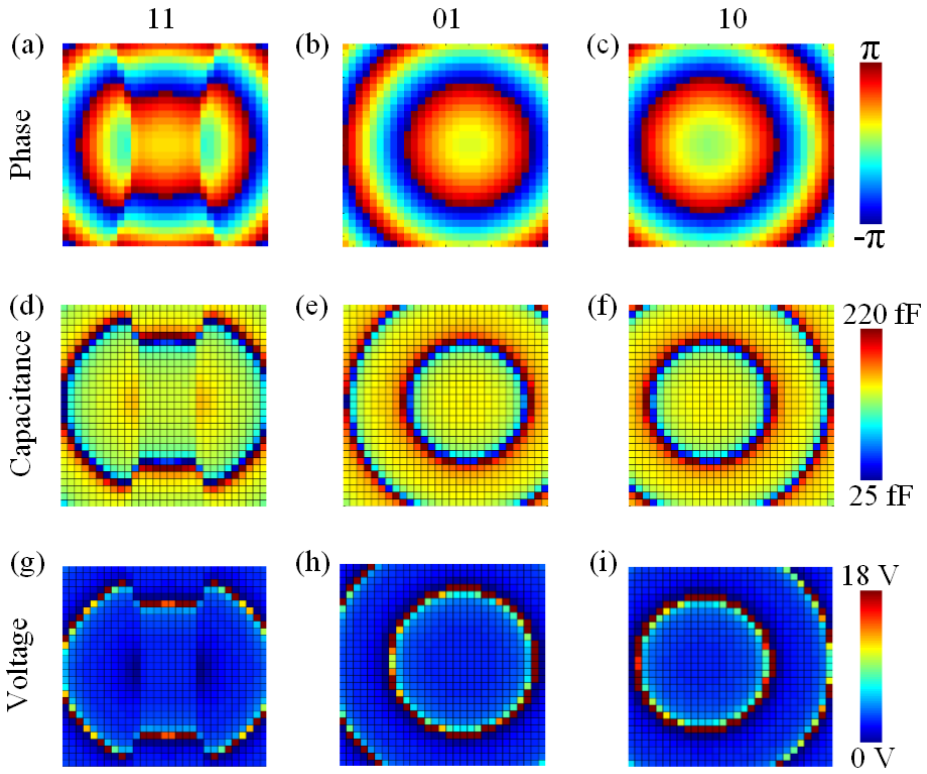

Figure 6.11 Phase, capacitance, and voltage profiles of the 1-bit energy modulations in two channels at 8.5 GHz and the detecting plane z = 7 cm. (a-c) Phase profiles. (d-f) Capacitance profiles. (g-i) Voltage profiles.

In a first step, the 1-bit energy modulation in two channels at 8.5 GHz is validated, as illustrated in Figure 6-10. The detecting plane is set as z = 7 cm. By presetting the intensity ratio of two channels as 1:1, the two focusing spots with quasi similar amplitude is expected. The phase, capacitance, and voltage profiles corresponding to the states "11" are calculated and presented in Figures 6-11(a), (d), and (g). Both simulations and measurements are carried out at 8.5 GHz. The simulated and measured results are shown in Figures 6-12(a)

and (d). The normalized magnitude in the two channels are nearly equal, as illustrated in Figure 6-12(g). It should be noted that the digital symbol “0” and “1” of the 1-bit magnitude coding is represented by the measured normalized amplitude located in the region of 0 to 0.5 and 0.5 to 1.0, respectively.

Then, the intensity ratio of two channels are preset as 0:1 and 1:0 corresponding to the states “01” and “10”, respectively. The simulated and measured results of the state “01” are shown in Figures 6-12(b) and (e). The normalized magnitude is nearly 0 in channel 1 and nearly 1 in channel 2 for the state “01”. Figures 6-12(c) and (f) show the simulation and measurement of the electric field distribution of the energy modulation for the state “10”. The energy is nearly 1 in channel 1 and nearly 0 in channel 2 for the state “10”. Therefore, the concept of 1-bit energy modulation in two channels is validated.

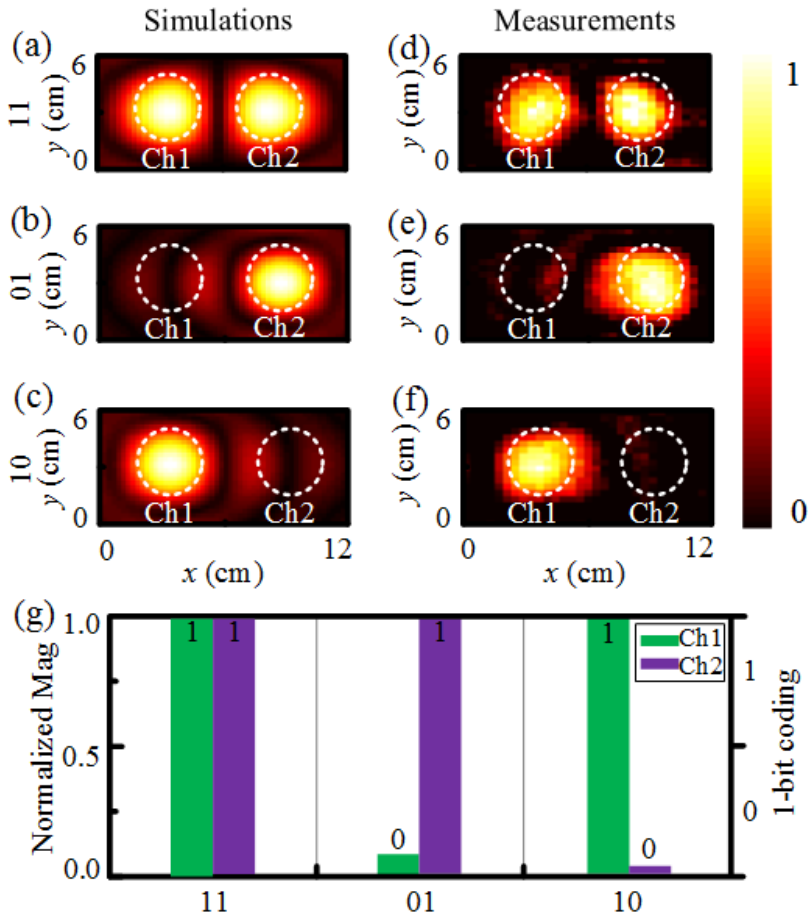

Figure 6.12 Numerical simulations and experimental measurements of the 1-bit spatial energy modulation in two channels at 8.5 GHz for a detecting plane set as z = 7 cm. (a-c) Simulations of the three states of “11”, “01”, and “10”. (d-f) Measurements of the three states. (g) Measured normalized magnitude of the three states.

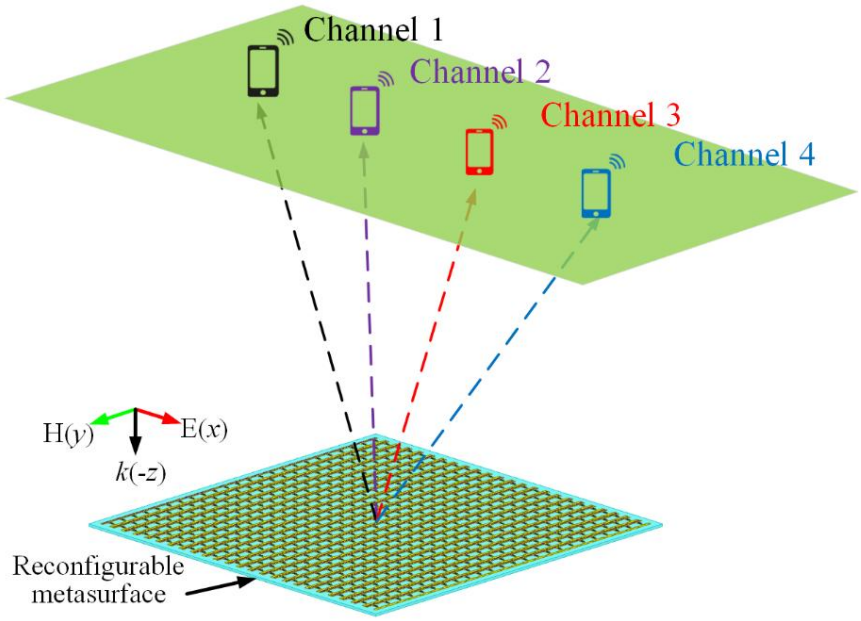

Figure 6.13 Schematic of the 2-bit spatial energy modulation in four channels at 8.5 GHz. The focal distance is z = 10 cm.

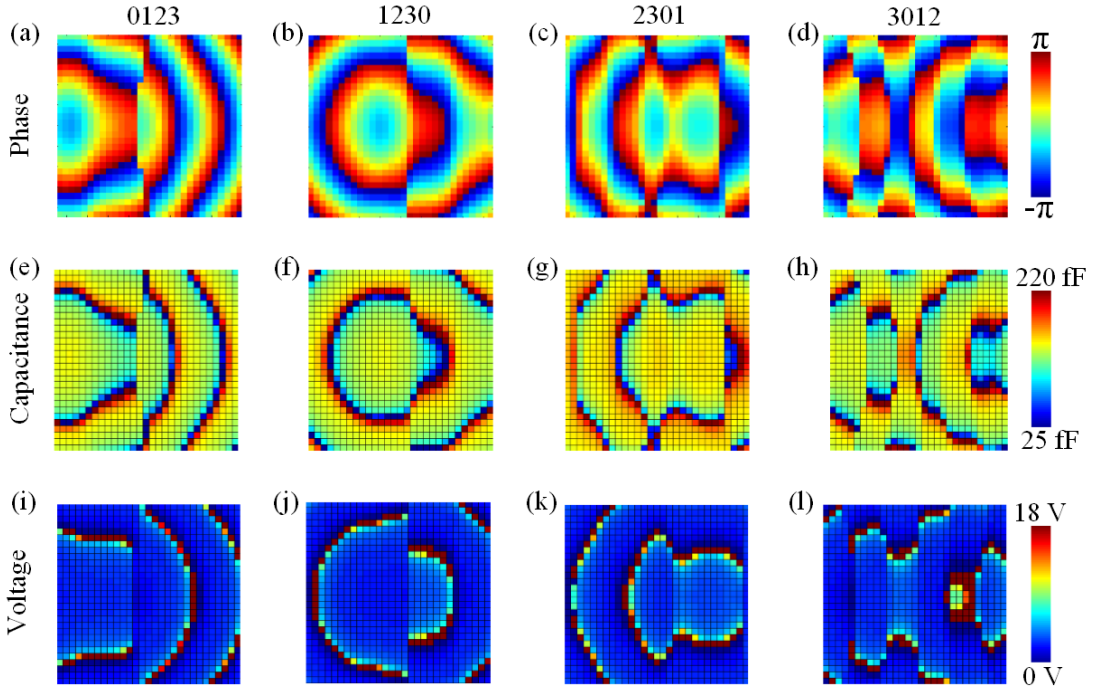

Figure 6.14 Phase, capacitance, and voltage profiles of the 2-bit energy modulations in four channels assigned along a line at 8.5 GHz and the detecting plane z = 10 cm. (a)-(d) Phase profiles. (e)-(h) Capacitance profiles. (i)-(l) Voltage profiles.

Next, I study the 2-bit spatial energy modulation in four different channels assigned in

a line through changing the parameter q_n (n = 1, 2, 3, 4) of the modified GSW algorithm, as displayed in Figure 6-13. The intensity ratio of the four channels are preset as 0:1:2:3, 1:2:3:0, 2:3:0:1, and 3:0:1:2, corresponding to the four 2-bit coding states of "0123", "1230", "2301", and "3012", respectively. Figure 6-14 shows the phase, capacitance, and voltage profiles of the four states. Both simulations and measurements are carried out at 8.5 GHz using the 2D reconfigurable metasurface and the results are exhibited in Figure 6-15. As shown in Figures 6-15(a) and (e), we can see that the amplitude increases from channel 1 to channel 4 for the state "0123". The measured normalized magnitude of four states is presented in Figure 6-15(i). The digital symbol "0" of 2-bit coding is defined as the normalized magnitude located at 0 to 0.25. Similarly, the digital symbols "1", "2", and "3" of 2-bit coding represent the normalized magnitude located at 0.25 to 0.5, and 0.5 to 0.75, and 0.75 to 1, respectively. The target energy ratio in four channels are also realized for the three coding states "1230", "2301", and "3012".

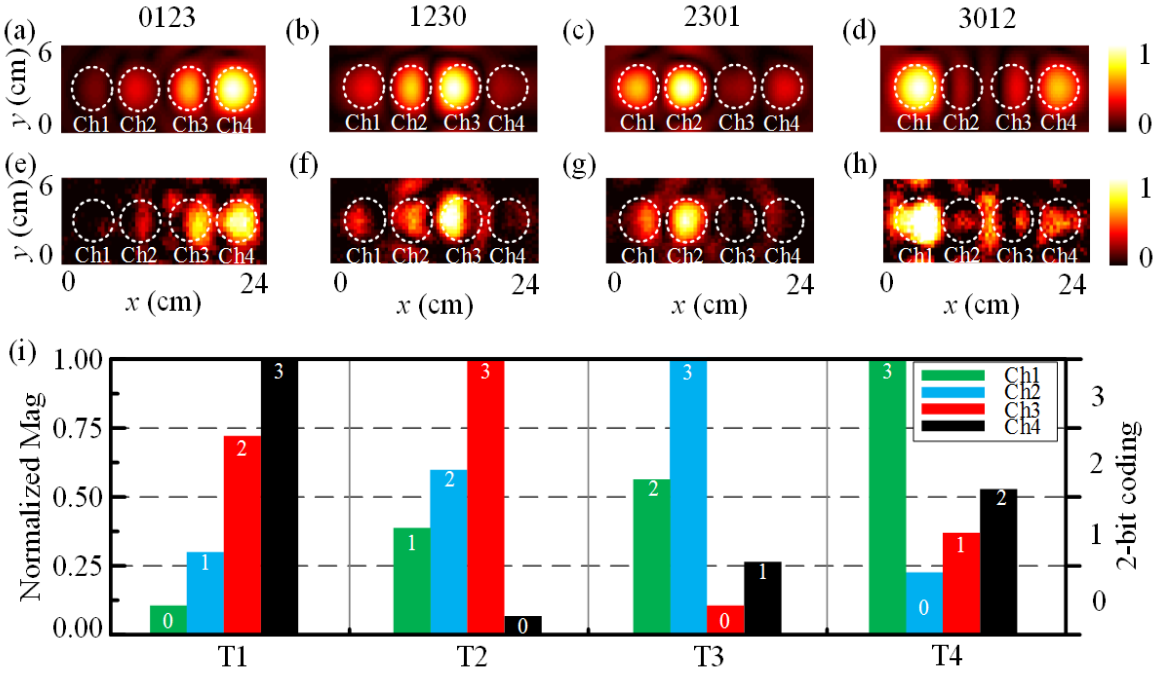

Figure 6.15 Numerical simulations and experimental measurements of the 2-bit spatial energy modulation in four channels assigned along a line at 8.5 GHz for an imaging plane set at z = 10 cm. (a)-(d) Simulations of the 2-bit energy modulation. (e)-(h) Measurements of the 2-bit energy modulation. (i) Measured normalized magnitude of the 2-bit energy modulation.

To further verify the effectiveness of the 2-bit energy coding in different channels in free space, we assign the four channels in the four corners of a square, as illustrated in Figure

6-16. Four states of 2-bit coding, including “0123”, “1230”, “2301”, and “3012”, are investigated and the corresponding four phase profiles are displayed in Figures 6-17(a)-(d). The capacitance and voltage profiles are calculated and displayed in Figures 6-17(e)-(l). The numerical simulations and experimental measurements are implemented at 8.5 GHz for an imaging plane set at z = 10 cm. The electric field distributions of the four coding states are shown in Figure 6-18. The intensity increases from channel 1 to channel 4 can be observed for the coding state “0123” as presented in Figures 6-18(a) and (e). Similarly, the corresponding intensity ratio of the coding states “1230”, “2301”, and “3012” in the four channels assigned to four corners of a square are also realized, which reveals the 2-bit energy coding in four channels is well performed in free space.

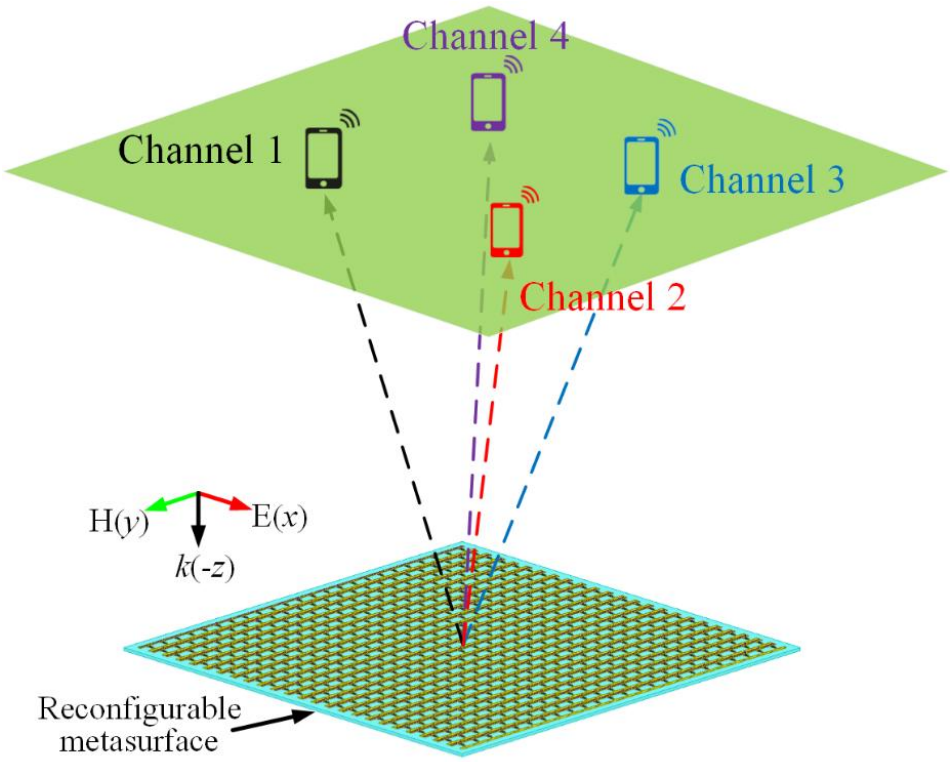

Figure 6.16 Schematic of the 2-bit spatial energy modulation in four channels arranged in the four corners of a square at 8.5 GHz. The focal distance is set at z = 10 cm.

In this subsection, the concept of 1-bit and 2-bit spatial energy modulation based on the modified GSW algorithm have been fully validated. It should be noted that the spatial energy modulation technique can be generalized to multibit configuration so as to freely realize the modulation of focal energy distribution in multiple channels, which can really benefit to a near-field communication systems.

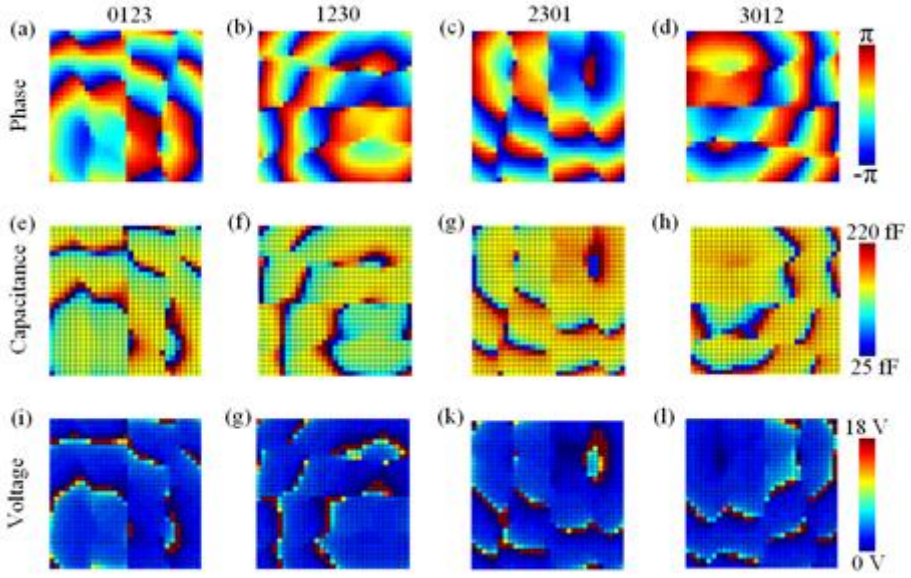

Figure 6.17 Phase, capacitance, and voltage profiles of the 2-bit energy modulations in four channels assigned at the four corners of a square at 8.5 GHz and the detecting plane z = 10 cm. (a)-(d) Phase profiles. (e)-(h) Capacitance profiles. (i)-(l) Voltage profiles.

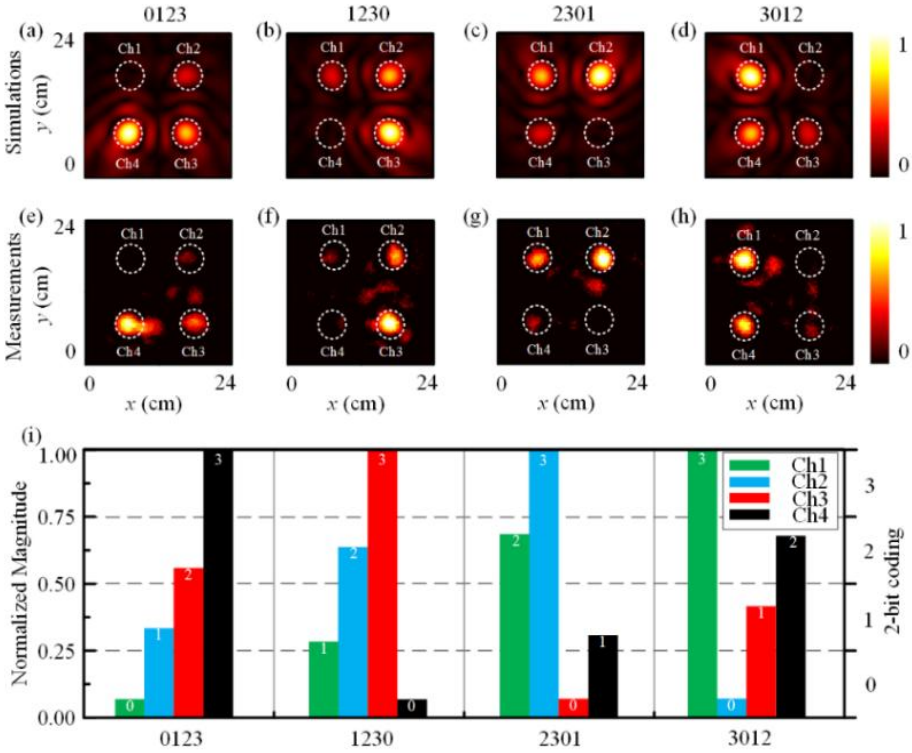

Figure 6.18 Numerical simulations and experimental measurements of the 2-bit energy modulation in four channels assigned at the four corners of a square at 8.5 GHz and the imaging plane z = 10 cm. (a)-(d) Simulations of the 2-bit energy modulation. (e)-(h) Measurements of the 2-bit energy modulation. (i) Measured normalized magnitude of the 2-bit energy modulation.

6.4 Holographic images of Arabic numbers

The simple holographic images of focal spots have been discussed above. In this section, I demonstrate the generation of the complex holographic images of the Arabic numbers at different focal distances at 9 GHz. To generate the desired holographic images of numbers, several non-superposing focal spots are elaborately assigned on the imaging plane to constitute the imaging of numbers.

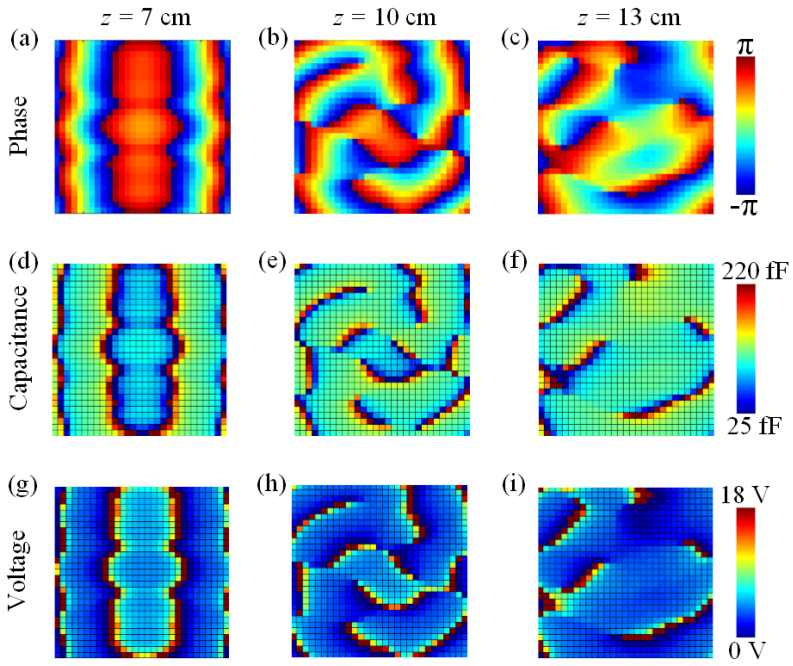

Figure 6.19 Phase, capacitance, and voltage profiles of the holographic imaging of Arabic numbers of "1", "2", and "3" at different distances and 9 GHz. (a)-(d) Phase profiles. (e)-(h) Capacitance profiles. (i)-(l) Voltage profiles.

By appropriately assigning the focal spots according to the modified GSW algorithm, the phase profile of Arabic number "1" is shown in Figure 6-19(a). Then, the corresponding capacitance and voltage profiles are exhibited in Figures 6-19(d) and (g), respectively. By performing the simulation and measurement, the simulated and measured electric field distributions of the holographic image of Arabic number "1" at 9 GHz are obtained and displayed in Figures 6-20(a) and (d), where the imaging plane is located at z = 7 cm. The clear Arabic number "1" can be observed, validating the theory. Then, I appropriately assign the focal spots in the path of Arabic numbers "2" and "3" and the corresponding simulations and measurements are carried out at 9 GHz. The results of the Arabic numbers "2" and "3" at the imaging planes located at z = 10 cm and z = 13 cm, respectively, are shown in Figure

6-20. Compared to the simple number '1', the measured results of numbers '2' and '3' are deteriorated due to the complex electric field distribution. The measured total efficiency of the three holographic images of Arabic numbers "1", "2", and "3" is calculated as 33.23%, 41.20%, and 43.14%, respectively, which shows the good quality of the generated holographic images based on the reconfigurable metasurface, which inherently presents losses due to the implementation of the electronic components.

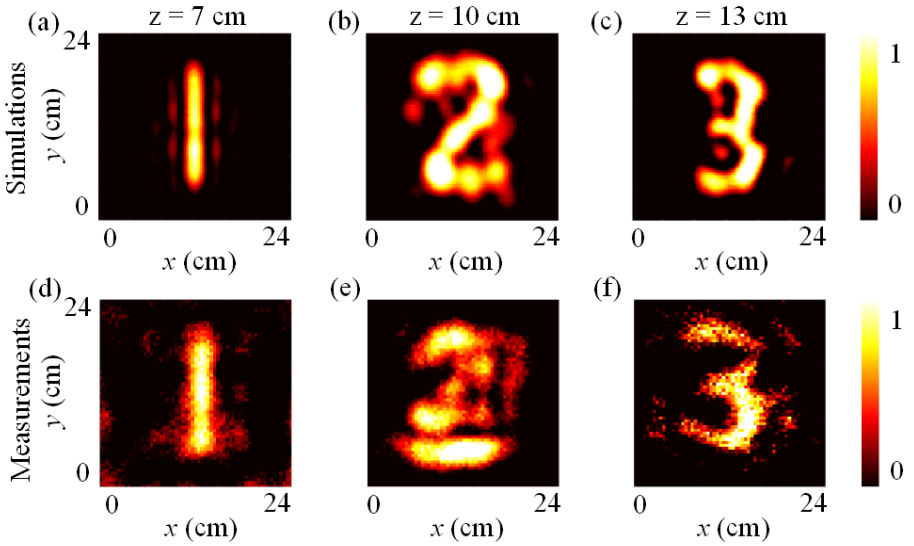

Figure 6.20 Numerical simulations and experimental measurements of the holographic images of Arabic numbers at 9 GHz and different imaging planes. (a)-(c) Simulations of the Arabic numbers. (d)-(f) Measurements of the Arabic numbers.

6.5 Holographic images of Alphabet letters

In this section, the holographic images of the alphabet letters at 9.5 GHz and different detecting planes is demonstrated. The phase profiles of the holographic images of alphabet letters, such as "C", "T", and "L", are depicted in Figures 6-21(a)-(c). The capacitance and voltage profiles are shown in Figures 6-21(d)-(i). The corresponding electric field distributions of the holographic images of the alphabet letters in the plane z = 7 cm, z = 10 cm, and z = 13 cm, are shown in Figure 6-22. We can observe clear holographic images of the alphabet letters at 9.5 GHz and in different detecting plane. Good agreement between the simulations and measurements can be observed, demonstrating the concept of the holographic images of the alphabet letters. The measured total efficiency of the three holographic images of the letters "C", "T", and "L" is 43.97%, 43.71%, and 35.92%, respectively. All these results lead us to conclude that the 2D reconfigurable metasurface can

be used as a dynamic holographic image generator. Different holographic imaging can be achieved in different detecting planes over a wide frequency band ranging from 8.5 GHz to 9.5 GHz.

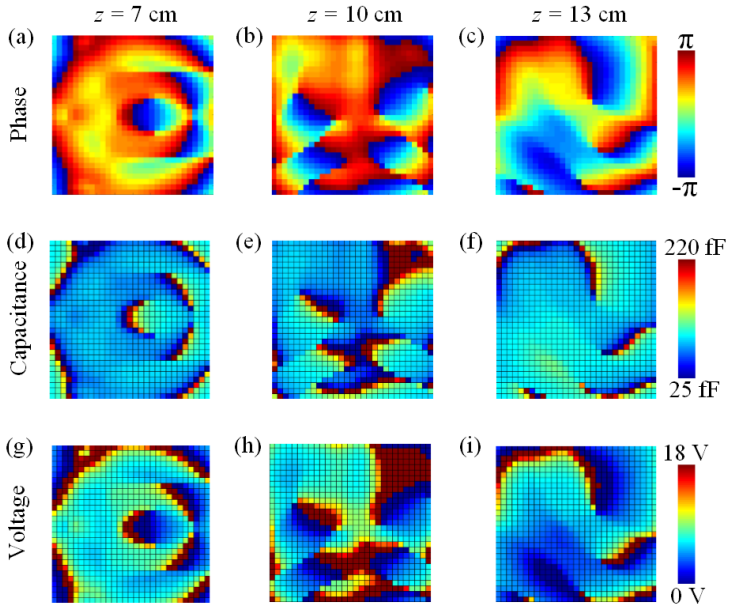

Figure 6.21 Phase, capacitance, and voltage profiles of the holographic images of Alphabet letters of "C", "T", and "L" at different distances at 9.5 GHz. (a)-(d) Phase profiles. (e)-(h) Capacitance profiles. (i)-(l) Voltage profiles.

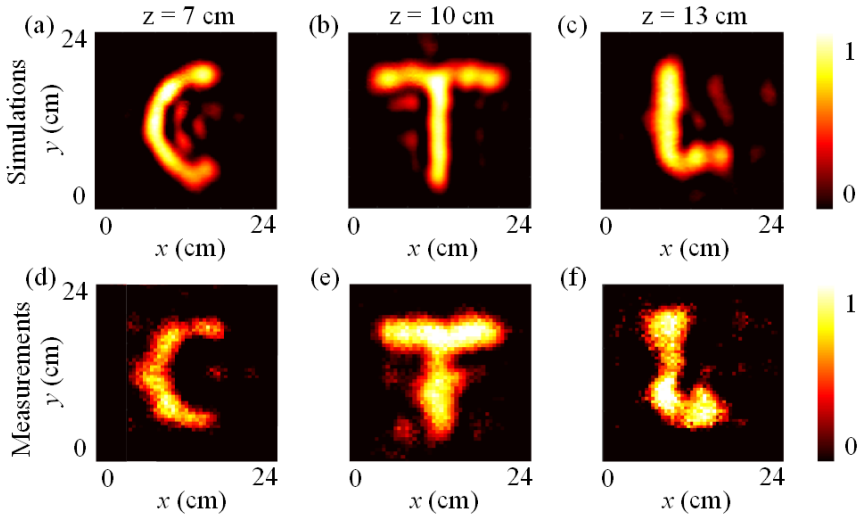

Figure 6.22 Numerical simulations and experimental measurements of the holographic images of Alphabet letters of "C", "T", and "L" at different distances at 9.5 GHz. (a)-(c) Simulations of the Alphabet letters. (d)-(f) Measurements of the Alphabet letters.

6.6 Conclusion

In this chapter, I presented the dynamic generation of different holographic images based on the modified GSW algorithm by utilizing the 2D reconfigurable metasurface whose unit cell can be individually addressed and can achieve continuous phase control. Firstly, I demonstrated that holographic images of different focal spots, including 2, 3, and 4 spots, can be realized in different detecting planes at a single frequency. Besides, the 1-bit and 2-bit energy modulation in different channels were also validated at 8.5 GHz, which shows the ability of energy control in the free space using the 2D reconfigurable metasurface.

Secondly, I verified the generation of complex holographic images. The holographic images of Arabic numbers at 9 GHz and alphabet letters at 9.5 GHz were achieved in different imaging planes located at $z = 7$ cm, $z = 10$ cm, and $z = 13$ cm, respectively. In theory, any holographic image can be realized using the designed reconfigurable metasurface.

General Conclusions and Outlooks

In this thesis, two designs of reconfigurable metasurfaces based on the electrically tunable mechanism have been presented. Five applications are conceived and experimentally tested. I will simply summarize the contents of this thesis.

In the first chapter, the state of art of metamaterials and metasurfaces has been described in detail. The reconfigurable metasurface with different tunable mechanisms has been discussed by listing corresponding representative works.

In the second chapter, I have presented the related softwares used for the whole thesis, the simulation configurations, and the measurement setups. Then, the design of the 1D and 2D reconfigurable metasurfaces has been discussed in detail.

In the third chapter, the directional beaming of electromagnetic waves through a subwavelength aperture surrounded by the reconfigurable metasurface has been proposed. The principle of the direction beaming has been firstly discussed. By symmetrically applying appropriate phase gradients on both sides of the subwavelength aperture, beaming at boresight direction has been realized over a wide frequency band spanning from 9 GHz to 12 GHz. Then, off-axis beaming at 20°, 30° and 40° have also been achieved by assigning the asymmetric phase profiles on the sides of the aperture.

In the fourth chapter, diffraction-free beams, including Airy beams and Bessel beams, have been investigated using both metasurfaces. The two metasurfaces can be utilized as a reconfigurable 1-bit coding metasurface. 1D Airy beams and Bessel-like beams with different parameters have been analyzed at 10 GHz. The generation of 1D Airy beams has been developed over a frequency band from 9 to 12 GHz. The properties of the 1D Airy beams and 1D Bessel-like beam have been demonstrated at 10 GHz. In addition, the beam steering of 1D Airy beams and Bessel-like beams has been also verified at 10 GHz by superposing additional phase gradients to the original diffraction-free beam phase profile. The two different far-field radiation modes of the zeroth-order Bessel beams under different scenarios have been highlighted and explained. Then, the Bessel beams have also been parametrically studied at 9.5 GHz utilizing the 2D reconfigurable metasurface. The generation of 2D Airy beams and 2D Bessel beams in the frequency band ranging from 8.5 to 9.5 GHz has been achieved.

In the fifth chapter, the dynamic generation and manipulation of vortex beams has been presented. First, three different types of vortex beams, including Laguerre-Gaussian beam,

focusing vortex beam, and non-diffracting vortex beam, have been developed to achieve a single-beam vortex beam in the boresight direction. Then, a comparison among the three types of vortex beams with the same mode has been implemented. The non-diffracting vortex beam has the smallest divergent angle. Besides, the generation of non-diffracting vortex beam with mode 1 has been validated over 8.5 to 9.5 GHz frequency band.

In the sixth chapter, three different types of holographic imaging, including focusing spots, Aribia numbers, and Alphabet letters, have been achieved in different imaging planes and at different frequencies using the modified GSW algorithm. First, the holographic images of 2, 3, and 4 focusing spots have been realized at 8.5 GHz in three different imaging planes. Then, multibit spatial energy allocation in different channels has been fulfilled at 8.5 GHz. In addition, more complex holographic images of Arabic numbers, and Alphabet letters have been implemented in different imaging planes at 9 GHz and 9.5 GHz, respectively.

However, due to the limited time of the thesis and knowledge, there are still many problems to be solved, whether it concerns the metasurface design or complex beam study. In the future, focus can be put on the following aspects:

1. The efficiency of the proposed reconfigurable metasurfaces is not very high. This can be further improved by using the substrate with low dielectric loss.

2. In this thesis, both reconfigurable metasurfaces operate in reflection mode. The EM waves can be flexibly controlled in only half-space. In a first step, a transmissive reconfigurable metasurface with quasi-continuous phase modulation can be considered. Then, a full-space reconfigurable metasurface showing capabilities in both reflection and transmission can be envisaged.

3. The vortex beams carrying OAM constitute a very important tool to improve the channel capacity. It provides new freedom to modulate electromagnetic waves. Achieving non-diffraction over long distances with such vortex beams can inevitably enhance channel capacities to improve data rates in communication systems.

4. The diffraction-free beams have a potential application in wireless communication. There are also other types of diffraction-free beams that can be analyzed, such as Mathieu beams and Weber beams.

References

[1] Veselago V G. The electrodynamics of substances with simultaneously negative values of ε and μ[J]. Physics-Uspekhi, 1968, 10(4): 509-514.

[2] Pendry J B, Holden A J, Stewart W J, et al. Extremely low frequency plasmons in metallic mesostructures[J]. Physical review letters, 1996, 76(25): 4773.

[3] Pendry J B, Holden A J, Robbins D J, et al. Magnetism from conductors and enhanced nonlinear phenomena[J]. IEEE transactions on microwave theory and techniques, 1999, 47(11): 2075-2084.

[4] Shelby R A, Smith D R, Schultz S. Experimental verification of a negative index of refraction[J]. science, 2001, 292(5514): 77-79.

[5] Pendry J B, Schurig D, Smith D R. Controlling electromagnetic fields[J]. science, 2006, 312(5781): 1780-1782.

[6] Lai Y, Ng J, Chen H Y, et al. Illusion optics: the optical transformation of an object into another object[J]. Physical review letters, 2009, 102(25): 253902.

[7] Li C, Meng X, Liu X, et al. Experimental realization of a circuit-based broadband illusion-optics analogue[J]. Physical review letters, 2010, 105(23): 233906.

[8] Xu Y, Du S, Gao L, et al. Overlapped illusion optics: a perfect lens brings a brighter feature[J]. New Journal of Physics, 2011, 13(2): 023010.

[9] Li C, Liu X, Liu G, et al. Experimental demonstration of illusion optics with “external cloaking” effects[J]. Applied Physics Letters, 2011, 99(8): 084104.

[10] Lai Y, Ng J, Chen H Y, et al. Illusion optics[J]. Frontiers of Physics in China, 2010, 5(3): 308-318.

[11] Rahm M, Schurig D, Roberts D A, et al. Design of electromagnetic cloaks and concentrators using form-invariant coordinate transformations of Maxwell’s equations[J]. Photonics and Nanostructures-fundamentals and Applications, 2008, 6(1): 87-95.

[12] Zhang K, Wu Q, Fu J H, et al. Cylindrical electromagnetic concentrator with only axial constitutive parameter spatially variant[J]. JOSA B, 2011, 28(6): 1573-1577.

[13] Li T, Huang M, Yang J, et al. Three dimensional electromagnetic concentrators with homogeneous material parameters[J]. Progress In Electromagnetics Research M, 2011, 18: 119-130.

[14] Pendry J B. Negative refraction makes a perfect lens[J]. Physical review letters, 2000, 85(18): 3966.

[15] Tsang M, Psaltis D. Magnifying perfect lens and superlens design by coordinate transformation[J]. Physical Review B, 2008, 77(3): 035122.

[16] Yan M, Yan W, Qiu M. Cylindrical superlens by a coordinate transformation[J]. Physical Review

B, 2008, 78(12): 125113.

[17] Guenneau S, Ramakrishna S A. Negative refractive index, perfect lenses and checkerboards: Trapping and imaging effects in folded optical spaces[J]. Comptes Rendus Physique, 2009, 10(5): 352-378.

[18] Gaillot D P, Croënne C, Zhang F, et al. Transformation optics for the full dielectric electromagnetic cloak and metal–dielectric planar hyperlens[J]. New Journal of Physics, 2008, 10(11): 115039.

[19] Wee W H, Pendry J B. Shrinking optical devices[J]. New Journal of Physics, 2009, 11(7): 073033.

[20] Ng J, Chen H, Chan C T. Metamaterial frequency-selective superabsorber[J]. Optics letters, 2009, 34(5): 644-646.

[21] Yang T, Chen H, Luo X, et al. Superscatterer: enhancement of scattering with complementary media[J]. Optics express, 2008, 16(22): 18545-18550.

[22] Zang X, Jiang C. Two-dimensional elliptical electromagnetic superscatterer and superabsorber[J]. Optics Express, 2010, 18(7): 6891-6899.

[23] Yang C, Yang J, Huang M, et al. Two-dimensional electromagnetic superscatterer with arbitrary geometries[J]. Computational Materials Science, 2010, 49(4): 820-825.

[24] Ng J, Chen H, Chan C T. Metamaterial frequency-selective superabsorber[J]. Optics letters, 2009, 34(5): 644-646.

[25] Ginis V, Tassin P, Danckaert J, et al. Creating electromagnetic cavities using transformation optics[J]. New Journal of Physics, 2012, 14(3): 033007.

[26] Yu G X, Cao L, Zhou M. Design of miniaturization resonant cavities using metamaterial[J]. Central European Journal of Physics, 2012, 10(1): 140-144.

[27] Ginis V, Tassin P, Soukoulis C M, et al. Confining light in deep subwavelength electromagnetic cavities[J]. Physical Review B, 2010, 82(11): 113102.

[28] Wang Z, Luo Y, Cui W, et al. Controlling the field distribution in waveguides with transformation optics[J]. Applied Physics Letters, 2009, 94(23): 234101.

[29] Tichit P H, Burokur S N, de Lustrac A. Waveguide taper engineering using coordinate transformation technology[J]. Optics Express, 2010, 18(2): 767-772.

[30] Landy N I, Padilla W J. Guiding light with conformal transformations[J]. Optics express, 2009, 17(17): 14872-14879.

[31] Ma Y G, Wang N, Ong C K. Application of inverse, strict conformal transformation to design waveguide devices[J]. JOSA A, 2010, 27(5): 968-972.

[32] Zhang J, Luo Y, Chen H, et al. Guiding waves through an invisible tunnel[J]. Optics Express, 2009, 17(8): 6203-6208.

[33] Shalaev V M. Transforming light[J]. Science, 2008, 322(5900): 384-386.

[34] Valentine J, Li J, Zentgraf T, et al. An optical cloak made of dielectrics[J]. Nature materials, 2009, 8(7): 568-571.

[35] Ergin T, Stenger N, Brenner P, et al. Three-dimensional invisibility cloak at optical wavelengths[J]. science, 2010, 328(5976): 337-339.

[36] Zhang B, Luo Y, Liu X, et al. Macroscopic invisibility cloak for visible light[J]. Physical Review Letters, 2011, 106(3): 033901.

[37] Gharghi M, Gladden C, Zentgraf T, et al. A carpet cloak for visible light[J]. Nano letters, 2011, 11(7): 2825-2828.

[38] Li J, Pendry J B. Hiding under the carpet: a new strategy for cloaking[J]. Physical review letters, 2008, 101(20): 203901.

[39] Zhang P, Lobet M, He S. Carpet cloaking on a dielectric half-space[J]. Optics Express, 2010, 18(17): 18158-18163.

[40] Schurig D, Mock J J, Justice B J, et al. Metamaterial electromagnetic cloak at microwave frequencies[J]. Science, 2006, 314(5801): 977-980.

[41] Jiang W X, Qiu C W, Han T C, et al. Broadband All-Dielectric Magnifying Lens for Far-Field High-Resolution Imaging[J]. Advanced Materials, 2013, 25(48): 6963-6968.

[42] Ma H F, Cui T J. Three-dimensional broadband and broad-angle transformation-optics lens[J]. Nature communications, 2010, 1(1): 1-7.

[43] Yu N, Genevet P, Kats M A, et al. Light propagation with phase discontinuities: generalized laws of reflection and refraction[J]. science, 2011, 334(6054): 333-337.

[44] Grady N K, Heyes J E, Chowdhury D R, et al. Terahertz metamaterials for linear polarization conversion and anomalous refraction[J]. Science, 2013, 340(6138): 1304-1307.

[45] Cong L, Xu N, Gu J, et al. Highly flexible broadband terahertz metamaterial quarter-wave plate[J]. Laser & Photonics Reviews, 2014, 8(4): 626-632.

[46] Cong L, Xu N, Zhang W, et al. Polarization control in terahertz metasurfaces with the lowest order rotational symmetry[J]. Advanced Optical Materials, 2015, 3(9): 1176-1183.

[47] Pfeiffer C, Zhang C, Ray V, et al. High performance bianisotropic metasurfaces: asymmetric transmission of light[J]. Physical review letters, 2014, 113(2): 023902.

[48] Pfeiffer C, Zhang C, Ray V, et al. Polarization rotation with ultra-thin bianisotropic metasurfaces[J]. Optica, 2016, 3(4): 427-432.

[49] Pfeiffer C, Grbic A. Metamaterial Huygens' surfaces: tailoring wave fronts with reflectionless sheets[J]. Physical review letters, 2013, 110(19): 197401.

[50] Zhang L, Ding J, Zheng H, et al. Ultra-thin high-efficiency mid-infrared transmissive Huygens meta-optics[J]. Nature communications, 2018, 9(1): 1-9.

[51] Tian J, Yang Y, Qiu M, et al. All-dielectric KTiOPO 4 metasurfaces based on multipolar resonances in the terahertz region[J]. Optics Express, 2017, 25(20): 24068-24080.

[52] Kita S, Takata K, Ono M, et al. Coherent control of high efficiency metasurface beam deflectors with a back partial reflector[J]. Apl Photonics, 2017, 2(4): 046104.

[53] Zhang Q, Li M, Liao T, et al. Design of beam deflector, splitters, wave plates and metalens using photonic elements with dielectric metasurface[J]. Optics Communications, 2018, 411: 93-100.

[54] Wang G, Gao Z, Tang S, et al. Microwave absorption properties of carbon nanocoils coated with highly controlled magnetic materials by atomic layer deposition[J]. ACS nano, 2012, 6(12): 11009-11017.

[55] Shrekenhamer D, Chen W C, Padilla W J. Liquid crystal tunable metamaterial absorber[J]. Physical review letters, 2013, 110(17): 177403.

[56] Zhu J, Ma Z, Sun W, et al. Ultra-broadband terahertz metamaterial absorber[J]. Applied Physics Letters, 2014, 105(2): 021102.

[57] Liu S, Chen H, Cui T J. A broadband terahertz absorber using multi-layer stacked bars[J]. Applied Physics Letters, 2015, 106(15): 151601.

[58] Huang Y W, Chen W T, Tsai W Y, et al. Aluminum plasmonic multicolor meta-hologram[J]. Nano letters, 2015, 15(5): 3122-3127.

[59] Zheng G, Mühlenbernd H, Kenney M, et al. Metasurface holograms reaching 80% efficiency[J]. Nature nanotechnology, 2015, 10(4): 308-312.

[60] Wang Z, Ding X, Zhang K, et al. Huygens metasurface holograms with the modulation of focal energy distribution[J]. Advanced Optical Materials, 2018, 6(12): 1800121.

[61] Ding X, Wang Z, Hu G, et al. Metasurface holographic image projection based on mathematical properties of Fourier transform[J]. PhotoniX, 2020, 1(1): 1-12.

[62] Hu Y, Li L, Wang Y, et al. Trichromatic and tripolarization-channel holography with noninterleaved dielectric metasurface[J]. Nano letters, 2019, 20(2): 994-1002.

[63] Zhang X, Tian Z, Yue W, et al. Broadband terahertz wave deflection based on C-shape complex metamaterials with phase discontinuities[J]. Advanced Materials, 2013, 25(33): 4567-4572.

[64] Pancharatnam S. Generalized theory of interference and its applications[C]//Proceedings of the Indian Academy of Sciences-Section A. Springer India, 1956, 44(6): 398-417.

[65] Berry M V. Quantal phase factors accompanying adiabatic changes[J]. Proceedings of the Royal Society of London. A. Mathematical and Physical Sciences, 1984, 392(1802): 45-57.

[66] Jisha C P, Alberucci A, Beeckman J, et al. Self-trapping of light using the Pancharatnam-Berry phase[J]. Physical Review X, 2019, 9(2): 021051.

[67] Driscoll T, Kim H T, Chae B G, et al. Memory metamaterials[J]. Science, 2009, 325(5947): 1518-

1521.

[68] Singh R, Azad A K, Jia Q X, et al. Thermal tunability in terahertz metamaterials fabricated on strontium titanate single-crystal substrates[J]. Optics letters, 2011, 36(7): 1230-1232.

[69] Wang B X, Zhai X, Wang G Z, et al. Frequency tunable metamaterial absorber at deep-subwavelength scale[J]. Optical Materials Express, 2015, 5(2): 227-235.

[70] Ou J Y, Plum E, Zhang J, et al. Giant nonlinearity of an optically reconfigurable plasmonic metamaterial[J]. Advanced Materials, 2016, 28(4): 729-733.

[71] Ou J Y, Plum E, Jiang L, et al. Reconfigurable photonic metamaterials[J]. Nano letters, 2011, 11(5): 2142-2144.

[72] Chen H T, O'hara J F, Azad A K, et al. Experimental demonstration of frequency-agile terahertz metamaterials[J]. Nature Photonics, 2008, 2(5): 295-298.

[73] Huber A J, Kazantsev D, Keilmann F, et al. Simultaneous IR Material Recognition and Conductivity Mapping by Nanoscale Near-Field Microscopy[J]. Advanced Materials, 2007, 19(17): 2209-2212.

[74] Deng L, Teng J, Liu H, et al. Direct optical tuning of the terahertz plasmonic response of InSb subwavelength gratings[J]. Advanced Optical Materials, 2013, 1(2): 128-132.

[75] Zhu Y, Hu X, Fu Y, et al. Ultralow-power and ultrafast all-optical tunable plasmon-induced transparency in metamaterials at optical communication range[J]. Scientific reports, 2013, 3(1): 1-7.

[76] Zhu Y, Hu X, Yang H, et al. Ultralow-power all-optical tunable double plasmon-induced transparencies in nonlinear metamaterials[J]. Applied Physics Letters, 2014, 104(21): 211108.

[77] Zhang F, Hu X, Zhu Y, et al. Ultrafast all-optical tunable Fano resonance in nonlinear metamaterials[J]. Applied Physics Letters, 2013, 102(18): 181109.

[78] Zhou Y, Hu X, Li C, et al. All-optical tunable dual Fano resonance in nonlinear metamaterials in optical communication range[J]. Journal of Modern Optics, 2018, 65(2): 206-212.

[79] Si G, Leong E S P, Jiang X, et al. All-optical, polarization-insensitive light tuning properties in silver nanorod arrays covered with photoresponsive liquid crystals[J]. Physical Chemistry Chemical Physics, 2015, 17(20): 13223-13227.

[80] Shcherbakov M R, Liu S, Zubyuk V V, et al. Ultrafast all-optical tuning of direct-gap semiconductor metasurfaces[J]. Nature communications, 2017, 8(1): 1-6.

[81] Lapine M, Shadrivov I V, Powell D A, et al. Magnetoelastic metamaterials[J]. Nature materials, 2012, 11(1): 30-33.

[82] Zheludev N I, Kivshar Y S. From metamaterials to metadevices[J]. Nature materials, 2012, 11(11): 917-924.

[83] Valente J, Ou J Y, Plum E, et al. A magneto-electro-optical effect in a plasmonic nanowire material[J]. Nature communications, 2015, 6(1): 1-7.

[84] Liu Q, Cui Y, Gardner D, et al. Self-alignment of plasmonic gold nanorods in reconfigurable anisotropic fluids for tunable bulk metamaterial applications[J]. Nano letters, 2010, 10(4): 1347-1353.

[85] Zhang F, Kang L, Zhao Q, et al. Magnetically tunable left handed metamaterials by liquid crystal orientation[J]. Optics Express, 2009, 17(6): 4360-4366.

[86] Pryce I M, Aydin K, Kelaita Y A, et al. Highly strained compliant optical metamaterials with large frequency tunability[J]. Nano letters, 2010, 10(10): 4222-4227.

[87] Kamali S M, Arbabi E, Arbabi A, et al. Highly tunable elastic dielectric metasurface lenses[J]. Laser & Photonics Reviews, 2016, 10(6): 1002-1008.

[88] Gupta B, Pandey S, Nahata A, et al. Bistable physical geometries for terahertz plasmonic structures using shape memory alloys[J]. Advanced Optical Materials, 2017, 5(7): 1601008.

[89] Zaichun C, Rahmani M, Yandong G, et al. Realization of Variable Three-Dimensional Terahertz Metamaterial Tubes for Passive Resonance Tunability[J]. Advanced Materials, 2012, 24(23): OP143-OP147.

[90] Ee H S, Agarwal R. Tunable metasurface and flat optical zoom lens on a stretchable substrate[J]. Nano letters, 2016, 16(4): 2818-2823.

[91] Tao H, Strikwerda A C, Fan K, et al. Reconfigurable terahertz metamaterials[J]. Physical review letters, 2009, 103(14): 147401.

[92] Hum S V, Perruisseau-Carrier J. Reconfigurable reflectarrays and array lenses for dynamic antenna beam control: A review[J]. IEEE Transactions on Antennas and Propagation, 2013, 62(1): 183-198.

[93] Debogovic T, Perruisseau-Carrier J. MEMS-reconfigurable metamaterials and antenna applications[J]. International Journal of Antennas and Propagation, 2014, 2014.

[94] Arbabi E, Arbabi A, Kamali S M, et al. MEMS-tunable dielectric metasurface lens[J]. Nature communications, 2018, 9(1): 1-9.

[95] Meng C, Thrane P C V, Ding F, et al. Dynamic piezoelectric MEMS-based optical metasurfaces[J]. Science Advances, 2021, 7(26): eabg5639.

[96] Chen H T, Padilla W J, Cich M J, et al. A metamaterial solid-state terahertz phase modulator[J]. Nature photonics, 2009, 3(3): 148-151.

[97] Huang Y W, Lee H W H, Sokhoyan R, et al. Gate-tunable conducting oxide metasurfaces[J]. Nano letters, 2016, 16(9): 5319-5325.

[98] Ou J Y, Plum E, Zhang J, et al. An electromechanically reconfigurable plasmonic metamaterial

operating in the near-infrared[J]. Nature nanotechnology, 2013, 8(4): 252-255.

[99] Ju L, Geng B, Horng J, et al. Graphene plasmonics for tunable terahertz metamaterials[J]. Nature nanotechnology, 2011, 6(10): 630-634.

[100] Lee S H, Choi M, Kim T T, et al. Switching terahertz waves with gate-controlled active graphene metamaterials[J]. Nature materials, 2012, 11(11): 936-941.

[101] Bian Y, Wu C, Li H, et al. A tunable metamaterial dependent on electric field at terahertz with barium strontium titanate thin film[J]. Applied Physics Letters, 2014, 104(4): 042906.

[102] Chang T K, Langley R J, Parker E A. Active frequency-selective surfaces[J]. IEE Proceedings-Microwaves, Antennas and Propagation, 1996, 143(1): 62-66.

[103] Zhu B, Feng Y, Zhao J, et al. Switchable metamaterial reflector/absorber for different polarized electromagnetic waves[J]. Applied Physics Letters, 2010, 97(5): 051906.

[104] Zhang L, Wang Z X, Shao R W, et al. Dynamically realizing arbitrary multi-bit programmable phases using a 2-bit time-domain coding metasurface[J]. IEEE Transactions on Antennas and Propagation, 2019, 68(4): 2984-2992.

[105] Tao Z, Wan X, Pan B C, et al. Reconfigurable conversions of reflection, transmission, and polarization states using active metasurface[J]. Applied Physics Letters, 2017, 110(12): 121901.

[106] Sievenpiper D F, Schaffner J H, Song H J, et al. Two-dimensional beam steering using an electrically tunable impedance surface[J]. IEEE Transactions on antennas and propagation, 2003, 51(10): 2713-2722.

[107] Burokur S N, Daniel J P, Ratajczak P, et al. Tunable bilayered metasurface for frequency reconfigurable directive emissions[J]. Applied Physics Letters, 2010, 97(6): 064101.

[108] Chen K, Feng Y, Monticone F, et al. A reconfigurable active huygens' metalens[J]. Advanced materials, 2017, 29(17): 1606422.

[109] Lee S H, Choi M, Kim T T, et al. Switching terahertz waves with gate-controlled active graphene metamaterials[J]. Nature materials, 2012, 11(11): 936-941.

[110] Bonaccorso F, Sun Z, Hasan T, et al. Graphene photonics and optoelectronics[J]. Nature photonics, 2010, 4(9): 611-622.

[111] Koppens F H L, Chang D E, Garcia de Abajo F J. Graphene plasmonics: a platform for strong light–matter interactions[J]. Nano letters, 2011, 11(8): 3370-3377.

[112] Chen H, Lu W B, Liu Z G, et al. Microwave programmable graphene metasurface[J]. Acs Photonics, 2020, 7(6): 1425-1435.

[113] Chen H, Lu W B, Liu Z G, et al. Microwave programmable graphene metasurface[J]. Acs Photonics, 2020, 7(6): 1425-1435.

[114] Zhang F, Zhao Q, Zhang W, et al. Voltage tunable short wire-pair type of metamaterial infiltrated

by nematic liquid crystal[J]. Applied Physics Letters, 2010, 97(13): 134103.

[115] Shrekenhamer D, Chen W C, Padilla W J. Liquid crystal tunable metamaterial absorber[J]. Physical review letters, 2013, 110(17): 177403.

[116] Chen H T, Padilla W J, Zide J M O, et al. Active terahertz metamaterial devices[J]. Nature, 2006, 444(7119): 597-600.

[117] HFSS. https://www.ansys.com/products/electronics/ansys-hfss. [accessed: December 2021].

[118] MATLAB. https://ww2.mathworks.cn/en/products/matlab.html. [accessed: December 2021].

[119] FLANN DP240 horn antenna. https://flann.com/products/antennas/dual-polarised-horn-series-dp240/. [accessed: December 2021].

[120] EFS-105-12 electro-optical probe. http://www.enprobe.de/products_FO-Antennas.htm. [accessed: accessed: December 2021].

[121] Ratni B E. Étude et conception d'antennes à base de métasurfaces destinées aux applications spatiales et aéronautiques[D]. Université Paris-Saclay (ComUE), 2017.

[122] Ratni B, de Lustrac A, Piau G P, et al. Reconfigurable meta-mirror for wavefronts control: applications to microwave antennas[J]. Optics express, 2018, 26(3): 2613-2624.

[123] Ratni B, de Lustrac A, Piau G P, et al. Active metasurface for reconfigurable reflectors[J]. Applied Physics A, 2018, 124(2): 1-8.

[124] Ratni B, de Lustrac A, Piau G P, et al. Electronic control of linear-to-circular polarization conversion using a reconfigurable metasurface[J]. Applied Physics Letters, 2017, 111(21): 214101.

[125] MGV125-08. https://www.macom.com/products/product-detail/MGV125-08. [accessed: December 2021].

[126] Bethe H A. Theory of diffraction by small holes[J]. Physical review, 1944, 66(7-8): 163.

[127] Lee B, Kim S, Kim H, et al. The use of plasmonics in light beaming and focusing[J]. Progress in Quantum Electronics, 2010, 34(2): 47-87.

[128] Pendry J B, Martin-Moreno L, Garcia-Vidal F J. Mimicking surface plasmons with structured surfaces[J]. science, 2004, 305(5685): 847-848.

[129] Devaux E, Ebbesen T W, Weeber J C, et al. Launching and decoupling surface plasmons via micro-gratings[J]. Applied physics letters, 2003, 83(24): 4936-4938.

[130] Anttu N, Xu H Q. Scattering matrix method for optical excitation of surface plasmons in metal films with periodic arrays of subwavelength holes[J]. Physical review B, 2011, 83(16): 165431.

[131] Laluet J Y, Devaux E, Genet C, et al. Optimization of surface plasmons launching from subwavelength hole arrays: modelling and experiments[J]. Optics express, 2007, 15(6): 3488-3495.

[132] Lalanne P, Silberstein E. Fourier-modal methods applied to waveguide computational problems[J]. Optics Letters, 2000, 25(15): 1092-1094.

[133] Kim H, Lee I M, Lee B. Extended scattering-matrix method for efficient full parallel implementation of rigorous coupled-wave analysis[J]. JOSA A, 2007, 24(8): 2313-2327.

[134] Kim H, Lee B. Pseudo-Fourier modal analysis of two-dimensional arbitrarily shaped grating structures[J]. JOSA A, 2008, 25(1): 40-54.

[135] Kim H, Lee B. Mathematical modeling of crossed nanophotonic structures with generalized scattering-matrix method and local Fourier modal analysis[J]. JOSA B, 2008, 25(4): 518-544.

[136] Kim S, Kim H, Lim Y, et al. Off-axis directional beaming of optical field diffracted by a single subwavelength metal slit with asymmetric dielectric surface gratings[J]. Applied physics letters, 2007, 90(5): 051113.

[137] Otto A. Excitation of nonradiative surface plasma waves in silver by the method of frustrated total reflection[J]. Zeitschrift für Physik A Hadrons and nuclei, 1968, 216(4): 398-410.

[138] Hickernell R K, Sarid D. Optical bistability using prism-coupled, long-range surface plasmons[J]. JOSA B, 1986, 3(8): 1059-1069.

[139] Vinogradov A P, Dorofeenko A V, Pukhov A A, et al. Exciting surface plasmon polaritons in the Kretschmann configuration by a light beam[J]. Physical Review B, 2018, 97(23): 235407.

[140] Dostalek J, Čtyroký J, Homola J, et al. Surface plasmon resonance biosensor based on integrated optical waveguide[J]. Sensors and actuators B: Chemical, 2001, 76(1-3): 8-12.

[141] Ditlbacher H, Galler N, Koller D M, et al. Coupling dielectric waveguide modes to surface plasmon polaritons[J]. Optics express, 2008, 16(14): 10455-10464.

[142] Fisher C, Botten L C, Poulton C G, et al. Efficient end-fire coupling of surface plasmons in a metal waveguide[J]. JOSA B, 2015, 32(3): 412-425.

[143] Xu Y, Zhang J, Song G. Slow surface plasmons in plasmonic grating waveguide[J]. IEEE Photonics Technology Letters, 2013, 25(5): 410-413.

[144] Dallapiccola R, Dubois C, Gopinath A, et al. Near-field excitation and near-field detection of propagating surface plasmon polaritons on Au waveguide structures[J]. Applied Physics Letters, 2009, 94(24): 243118.

[145] Hecht B, Bielefeldt H, Novotny L, et al. Local excitation, scattering, and interference of surface plasmons[J]. Physical review letters, 1996, 77(9): 1889.

[146] Sun S, He Q, Xiao S, et al. Gradient-index meta-surfaces as a bridge linking propagating waves and surface waves[J]. Nature materials, 2012, 11(5): 426-431.

[147] Xu J J, Zhang H C, Zhang Q, et al. Efficient conversion of surface-plasmon-like modes to spatial radiated modes[J]. Applied Physics Letters, 2015, 106(2): 021102.

[148] Feng R, Ratni B, Yi J, et al. Electronically-engineered metasurface for directional beaming of electromagnetic waves through a subwavelength aperture[J]. Optics express, 2019, 27(24): 35774-

35783.

[149] Kang Y, Zhang Y, Li C, et al. Nonparaxial accelerating electron beams[J]. IEEE Journal of Quantum Electronics, 2017, 53(2): 1-6.

[150] Berry M V, Balazs N L. Nonspreading wave packets[J]. American Journal of Physics, 1979, 47(3): 264-267.

[151] Siviloglou G A, Christodoulides D N. Accelerating finite energy Airy beams[J]. Optics letters, 2007, 32(8): 979-981.

[152] Siviloglou G A, Broky J, Dogariu A, et al. Observation of accelerating Airy beams[J]. Physical Review Letters, 2007, 99(21): 213901.

[153] Zhang P, Prakash J, Zhang Z, et al. Trapping and guiding microparticles with morphing autofocusing Airy beams[J]. Optics letters, 2011, 36(15): 2883-2885.

[154] Zhao Z, Zang W, Tian J. Optical trapping and manipulation of Mie particles with Airy beam[J]. Journal of Optics, 2016, 18(2): 025607.

[155] Singh B K, Nagar H, Roichman Y, et al. Particle manipulation beyond the diffraction limit using structured super-oscillating light beams[J]. Light: Science & Applications, 2017, 6(9): e17050-e17050.

[156] Baumgartl J, Mazilu M, Dholakia K. Optically mediated particle clearing using Airy wavepackets[J]. Nature photonics, 2008, 2(11): 675-678.

[157] Cheng H, Zang W, Zhou W, et al. Analysis of optical trapping and propulsion of Rayleigh particles using Airy beam[J]. Optics express, 2010, 18(19): 20384-20394.

[158] Călin B Ș, Preda L, Jipa F, et al. Laser fabrication of diffractive optical elements based on detour-phase computer-generated holograms for two-dimensional Airy beams[J]. Applied Optics, 2018, 57(6): 1367-1372.

[159] Manousidaki M, Fedorov V Y, Papazoglou D G, et al. Ultrashort ring-Airy laser beams for advanced materials engineering[C]//Advanced Manufacturing Technologies for Micro-and Nanosystems in Security and Defence II. International Society for Optics and Photonics, 2019, 11168: 1116802.

[160] Mathis A, Courvoisier F, Froehly L, et al. Micromachining along a curve: Femtosecond laser micromachining of curved profiles in diamond and silicon using accelerating beams[J]. Applied Physics Letters, 2012, 101(7): 071110.

[161] Bongiovanni D, Wetzel B, Hu Y, et al. Optimal compression and energy confinement of optical Airy bullets[J]. Optics Express, 2016, 24(23): 26454-26463.

[162] Wu Z, Wang Z, Guo H, et al. Self-accelerating Airy-Laguerre-Gaussian light bullets in a two-dimensional strongly nonlocal nonlinear medium[J]. Optics Express, 2017, 25(24): 30468-30478.

[163] Abdollahpour D, Suntsov S, Papazoglou D G, et al. Spatiotemporal Airy light bullets in the linear and nonlinear regimes[J]. Physical review letters, 2010, 105(25): 253901.

[164] Peng Y, Chen B, Peng X, et al. Self-accelerating Airy-Ince-Gaussian and Airy-helical-Ince-Gaussian light bullets in free space[J]. Optics Express, 2016, 24(17): 18973-18985.

[165] He H, Kong C, Tan X J, et al. Depth-resolved volumetric two-photon microscopy based on dual Airy beam scanning[J]. Optics Letters, 2019, 44(21): 5238-5241.

[166] Tan X J, Kong C, Ren Y X, et al. Volumetric two-photon microscopy with a non-diffracting Airy beam[J]. Optics Letters, 2019, 44(2): 391-394.

[167] Jia S, Vaughan J C, Zhuang X. Isotropic three-dimensional super-resolution imaging with a self-bending point spread function[J]. Nature photonics, 2014, 8(4): 302-306.

[168] Vettenburg T, Dalgarno H I C, Nylk J, et al. Light-sheet microscopy using an Airy beam[J]. Nature methods, 2014, 11(5): 541-544.

[169] Chremmos I D, Fikioris G, Efremidis N K. Accelerating and abruptly-autofocusing beam waves in the fresnel zone of antenna arrays[J]. IEEE transactions on antennas and propagation, 2013, 61(10): 5048-5056.

[170] Hao W, Deng M, Chen S, et al. High-efficiency generation of airy beams with Huygens' metasurface[J]. Physical Review Applied, 2019, 11(5): 054012.

[171] Li Z, Cheng H, Liu Z, et al. Plasmonic airy beam generation by both phase and amplitude modulation with metasurfaces[J]. Advanced Optical Materials, 2016, 4(8): 1230-1235.

[172] Lin Z, Guo X, Tu J, et al. Acoustic non-diffracting Airy beam[J]. Journal of Applied Physics, 2015, 117(10): 104503.

[173] Chen D C, Zhu X F, Wei Q, et al. Broadband acoustic focusing by Airy-like beams based on acoustic metasurfaces[J]. Journal of Applied Physics, 2018, 123(4): 044503.

[174] Durnin J, Miceli Jr J J, Eberly J H. Diffraction-free beams[J]. Physical review letters, 1987, 58(15): 1499.

[175] Egmason. Bessel beam. https://en.wikipedia.iwiki.eu.org/wiki/Bessel_beam. [accessed: December 2021]

[176] Meyer R, Jacquot M, Giust R, et al. Single-shot ultrafast laser processing of high-aspect-ratio nanochannels using elliptical Bessel beams[J]. Optics letters, 2017, 42(21): 4307-4310.

[177] Stoian R, Bhuyan M K, Zhang G, et al. Ultrafast Bessel beams: advanced tools for laser materials processing[J]. Advanced Optical Technologies, 2018, 7(3): 165-174.

[178] Grojo D, Mouskeftaras A, Delaporte P, et al. Limitations to laser machining of silicon using femtosecond micro-Bessel beams in the infrared[J]. Journal of Applied Physics, 2015, 117(15): 153105.

[179] Bhuyan M K, Courvoisier F, Lacourt P A, et al. High aspect ratio nanochannel machining using single shot femtosecond Bessel beams[J]. Applied Physics Letters, 2010, 97(8): 081102.

[180] Dudutis J, Pipiras J, Stonys R, et al. In-depth comparison of conventional glass cutting technologies with laser-based methods by volumetric scribing using Bessel beam and rear-side machining[J]. Optics Express, 2020, 28(21): 32133-32151.

[181] Meinert T, Rohrbach A. Light-sheet microscopy with length-adaptive Bessel beams[J]. Biomedical optics express, 2019, 10(2): 670-681.

[182] Hu Y, Chen Z, Xiang L, et al. Extended depth-of-field all-optical photoacoustic microscopy with a dual non-diffracting Bessel beam[J]. Optics Letters, 2019, 44(7): 1634-1637.

[183] Grillo V, Harris J, Gazzadi G C, et al. Generation and application of bessel beams in electron microscopy[J]. Ultramicroscopy, 2016, 166: 48-60.

[184] Gao L, Shao L, Chen B C, et al. 3D live fluorescence imaging of cellular dynamics using Bessel beam plane illumination microscopy[J]. Nature protocols, 2014, 9(5): 1083-1101.

[185] Chen B, Huang X, Gou D, et al. Rapid volumetric imaging with Bessel-Beam three-photon microscopy[J]. Biomedical optics express, 2018, 9(4): 1992-2000.

[186] Costanzo S, Di Massa G, Borgia A, et al. Microwave Bessel beam launcher for high penetration planetary drilling operations[C]//2016 10th European Conference on Antennas and Propagation (EuCAP). IEEE, 2016: 1-4.

[187] Gautam G D, Pandey A K. Pulsed Nd: YAG laser beam drilling: A review[J]. Optics & Laser Technology, 2018, 100: 183-215.

[188] Johnson W J. Bessel beam radar system using sequential spatial modulation: U.S. Patent 5,093,649[P]. 1992-3-3.

[189] Costanzo S, Di Massa G. Near-field focusing technique for enhanced through-the-wall radar[C]//2017 11th European Conference on Antennas and Propagation (EUCAP). IEEE, 2017: 1716-1717.

[190] Li Z, Alici K B, Caglayan H, et al. Generation of an axially asymmetric Bessel-like beam from a metallic subwavelength aperture[J]. Physical review letters, 2009, 102(14): 143901.

[191] Cox A J, Dibble D C. Nondiffracting beam from a spatially filtered Fabry–Perot resonator[J]. JOSA A, 1992, 9(2): 282-286.

[192] Herman R M, Wiggins T A. High-efficiency diffractionless beams of constant size and intensity[J]. Applied optics, 1994, 33(31): 7297-7306.

[193] Scott G, McArdle N. Efficient generation of nearly diffraction-free beams using an axicon[J]. Optical Engineering, 1992, 31(12): 2640-2643.

[194] Cai B G, Li Y B, Jiang W X, et al. Generation of spatial Bessel beams using holographic

metasurface[J]. Optics express, 2015, 23(6): 7593-7601.

[195] Wang Z, Dong S, Luo W, et al. High-efficiency generation of Bessel beams with transmissive metasurfaces[J]. Applied Physics Letters, 2018, 112(19): 191901.

[196] Durnin J. Exact solutions for nondiffracting beams. I. The scalar theory[J]. JOSA A, 1987, 4(4): 651-654.

[197] Temme N M. Special functions: An introduction to the classical functions of mathematical physics[M]. John Wiley & Sons, 1996.

[198] Gori F, Guattari G, Padovani C. Bessel-gauss beams[J]. Optics communications, 1987, 64(6): 491-495.

[199] Allen L, Beijersbergen M W, Spreeuw R J C, et al. Orbital angular momentum of light and the transformation of Laguerre-Gaussian laser modes[J]. Physical review A, 1992, 45(11): 8185.

[200] Poynting J H. The wave motion of a revolving shaft, and a suggestion as to the angular momentum in a beam of circularly polarised light[J]. Proceedings of the Royal Society of London. Series A, Containing Papers of a Mathematical and Physical Character, 1909, 82(557): 560-567.

[201] Beth R A. Mechanical detection and measurement of the angular momentum of light[J]. Physical Review, 1936, 50(2): 115.

[202] Allen L, Beijersbergen M W, Spreeuw R J C, et al. Orbital angular momentum of light and the transformation of Laguerre-Gaussian laser modes[J]. Physical review A, 1992, 45(11): 8185.

[203] Gibson G, Courtial J, Padgett M J, et al. Free-space information transfer using light beams carrying orbital angular momentum[J]. Optics express, 2004, 12(22): 5448-5456.

[204] Thidé B, Then H, Sjöholm J, et al. Utilization of photon orbital angular momentum in the low-frequency radio domain[J]. Physical review letters, 2007, 99(8): 087701.

[205] Tamburini F, Mari E, Sponselli A, et al. Encoding many channels on the same frequency through radio vorticity: first experimental test[J]. New Journal of Physics, 2012, 14(3): 033001.

[206] Mohammadi S M, Daldorff L K S, Bergman J E S, et al. Orbital angular momentum in radio—A system study[J]. IEEE transactions on Antennas and Propagation, 2009, 58(2): 565-572.

[207] Wang J, Yang J Y, Fazal I M, et al. Terabit free-space data transmission employing orbital angular momentum multiplexing[J]. Nature photonics, 2012, 6(7): 488-496.

[208] Yan Y, Xie G, Lavery M P J, et al. High-capacity millimetre-wave communications with orbital angular momentum multiplexing[J]. Nature communications, 2014, 5(1): 1-9.

[209] Hui X, Zheng S, Chen Y, et al. Multiplexed millimeter wave communication with dual orbital angular momentum (OAM) mode antennas[J]. Scientific reports, 2015, 5(1): 1-9.

[210] Liu K, Cheng Y, Yang Z, et al. Orbital-angular-momentum-based electromagnetic vortex imaging[J]. IEEE Antennas and Wireless Propagation Letters, 2014, 14: 711-714.

[211] Lin M, Gao Y, Liu P, et al. Improved OAM-based radar targets detection using uniform concentric circular arrays[J]. International Journal of Antennas and Propagation, 2016, 2016.

[212] Lin M, Gao Y, Liu P, et al. Super-resolution orbital angular momentum based radar targets detection[J]. Electronics Letters, 2016, 52(13): 1168-1170.

[213] Bu X, Zhang Z, Chen L, et al. Implementation of vortex electromagnetic waves high-resolution synthetic aperture radar imaging[J]. IEEE antennas and wireless propagation letters, 2018, 17(5): 764-767.

[214] Bu X, Zhang Z, Liang X, et al. A novel scheme for MIMO-SAR systems using rotational orbital angular momentum[J]. Sensors, 2018, 18(10): 3511.

[215] Uribe-Patarroyo N, Fraine A, Simon D S, et al. Object identification using correlated orbital angular momentum states[J]. Physical review letters, 2013, 110(4): 043601.

[216] Schemmel P, Pisano G, Maffei B. Modular spiral phase plate design for orbital angular momentum generation at millimetre wavelengths[J]. Optics express, 2014, 22(12): 14712-14726.

[217] Isakov D, Wu Y, Allen B, et al. Evaluation of the Laguerre–Gaussian mode purity produced by three-dimensional-printed microwave spiral phase plates[J]. Royal Society open science, 2020, 7(7): 200493.

[218] Wang J, Cao A, Zhang M, et al. Study of characteristics of vortex beam produced by fabricated spiral phase plates[J]. IEEE photonics Journal, 2016, 8(2): 1-9.

[219] Miyamoto K, Kang B J, Kim W T, et al. Highly intense monocycle te-rahertz vortex generation by utilizing a Tsurupica spiral phase plate[J]. Scientific reports, 2016, 6(1): 1-7.

[220] Kotlyar V, Kovalev A, Porfirev A, et al. Orbital angular momentum of a laser beam behind an off-axis spiral phase plate[J]. Optics letters, 2019, 44(15): 3673-3676.

[221] Mari E, Spinello F, Oldoni M, et al. Near-field experimental verification of separation of OAM channels[J]. IEEE Antennas and Wireless Propagation Letters, 2014, 14: 556-558.

[222] Tamburini F, Mari E, Thidé B, et al. Experimental verification of photon angular momentum and vorticity with radio techniques[J]. Applied Physics Letters, 2011, 99(20): 204102.

[223] Yi J, Cao X, Feng R, et al. All-dielectric transformed material for microwave broadband orbital angular momentum vortex beam[J]. Physical Review Applied, 2019, 12(2): 024064.

[224] Feng R, Yi J, Burokur S N, et al. Orbital angular momentum generation method based on transformation electromagnetics[J]. Optics express, 2018, 26(9): 11708-11717.

[225] Bai Q, Tennant A, Allen B. Experimental circular phased array for generating OAM radio beams[J]. Electronics letters, 2014, 50(20): 1414-1415.

[226] Tennant A, Allen B. Generation of OAM radio waves using circular time-switched array antenna[J]. Electronics letters, 2012, 48(21): 1365-1366.

[227] Bai Q, Tennant A, Allen B, et al. Generation of orbital angular momentum (OAM) radio beams with phased patch array[C]//2013 Loughborough Antennas & Propagation Conference (LAPC). IEEE, 2013: 410-413.

[228] Wei W, Mahdjoubi K, Brousseau C, et al. Generation of OAM waves with circular phase shifter and array of patch antennas[J]. Electronics letters, 2015, 51(6): 442-443.

[229] Bai X, Liang X, Jin R, et al. Generation of OAM radio waves with three polarizations using circular horn antenna array[C]//2015 9th European Conference on Antennas and Propagation (EuCAP). IEEE, 2015: 1-4.

[230] Li L, Zhou X. Mechanically reconfigurable single-arm spiral antenna array for generation of broadband circularly polarized orbital angular momentum vortex waves[J]. Scientific reports, 2018, 8(1): 1-9.

[231] Yu S, Li L, Shi G, et al. Design, fabrication, and measurement of reflective metasurface for orbital angular momentum vortex wave in radio frequency domain[J]. Applied Physics Letters, 2016, 108(12): 121903.

[232] Luo W, Sun S, Xu H X, et al. Transmissive ultrathin pancharatnam-berry metasurfaces with nearly 100% efficiency[J]. Physical Review Applied, 2017, 7(4): 044033.

[233] Zhang Y, Lyu Y, Wang H, et al. Transforming surface wave to propagating OAM vortex wave via flat dispersive metasurface in radio frequency[J]. IEEE Antennas and Wireless Propagation Letters, 2017, 17(1): 172-175.

[234] Ran Y, Liang J, Cai T, et al. High-performance broadband vortex beam generator based on double-layered reflective metasurface[J]. Aip Advances, 2018, 8(9): 095201.

[235] Huang H F, Li S N. High-efficiency planar reflectarray with small-size for OAM generation at microwave range[J]. IEEE Antennas and Wireless Propagation Letters, 2019, 18(3): 432-436.

[236] Ran Y, Liang J, Cai T, et al. High-performance broadband vortex beam generator using reflective Pancharatnam–Berry metasurface[J]. Optics Communications, 2018, 427: 101-106.

[237] Wang H, Li Y, Han Y, et al. Vortex beam generated by circular-polarized metasurface reflector antenna[J]. Journal of Physics D: Applied Physics, 2019, 52(25): 255306.

[238] Zhang K, Yuan Y, Zhang D, et al. Phase-engineered metalenses to generate converging and non-diffractive vortex beam carrying orbital angular momentum in microwave region[J]. Optics express, 2018, 26(2): 1351-1360.

[239] Feng R, Ratni B, Yi J, et al. Versatile metasurface platform for electromagnetic wave tailoring[J]. Photonics Research, 2021, 9(9): 1650-1659.

[240] Gabor D. A new microscopic principle[J]. nature, 1948, 161: 777-778.

[241] Lohmann A W, Paris D P. Binary Fraunhofer holograms, generated by computer[J]. Applied optics,

1967, 6(10): 1739-1748.

[242] Huang L, Chen X, Mühlenbernd H, et al. Three-dimensional optical holography using a plasmonic metasurface[J]. Nature communications, 2013, 4(1): 1-8.

[243] Zhang X, Jin J, Wang Y, et al. Metasurface-based broadband hologram with high tolerance to fabrication errors[J]. Scientific Reports, 2016, 6(1): 1-7.

[244] Guan C, Liu J, Ding X, et al. Dual-polarized multiplexed meta-holograms utilizing coding metasurface[J]. Nanophotonics, 2020, 9(11): 3605-3613.

[245] Devlin R C, Khorasaninejad M, Chen W T, et al. Broadband high-efficiency dielectric metasurfaces for the visible spectrum[J]. Proceedings of the National Academy of Sciences, 2016, 113(38): 10473-10478.

[246] Huang K, Liu H, Garcia-Vidal F J, et al. Ultrahigh-capacity non-periodic photon sieves operating in visible light[J]. Nature communications, 2015, 6(1): 1-7.

[247] Ni X, Kildishev A V, Shalaev V M. Metasurface holograms for visible light[J]. Nature communications, 2013, 4(1): 1-6.

[248] Wang Q, Zhang X, Xu Y, et al. Broadband metasurface holograms: toward complete phase and amplitude engineering[J]. Scientific reports, 2016, 6(1): 1-10.

[249] Chong K E, Wang L, Staude I, et al. Efficient polarization-insensitive complex wavefront control using Huygens' metasurfaces based on dielectric resonant meta-atoms[J]. Acs Photonics, 2016, 3(4): 514-519.

[250] Overvig A C, Shrestha S, Malek S C, et al. Dielectric metasurfaces for complete and independent control of the optical amplitude and phase[J]. Light: Science & Applications, 2019, 8(1): 1-12.

[251] Huang L, Zhang S, Zentgraf T. Metasurface holography: from fundamentals to applications[J]. Nanophotonics, 2018, 7(6): 1169-1190.

[252] Michel A K U, Chigrin D N, Maß T W W, et al. Using low-loss phase-change materials for mid-infrared antenna resonance tuning[J]. Nano letters, 2013, 13(8): 3470-3475.

[253] Pogrebnyakov A V, Bossard J A, Turpin J P, et al. Reconfigurable near-IR metasurface based on Ge 2 Sb 2 Te 5 phase-change material[J]. Optical Materials Express, 2018, 8(8): 2264-2275.

[254] Chen Y, Li X, Sonnefraud Y, et al. Engineering the phase front of light with phase-change material based planar lenses[J]. Scientific reports, 2015, 5(1): 1-7.

[255] Wang L, Hong W, Deng L, et al. Reconfigurable multifunctional metasurface hybridized with vanadium dioxide at terahertz frequencies[J]. Materials, 2018, 11(10): 2040.

[256] Lee S Y, Kim Y H, Cho S M, et al. Holographic image generation with a thin-film resonance caused by chalcogenide phase-change material[J]. Scientific reports, 2017, 7(1): 1-8.

[257] Nouman M T, Hwang J, Faiyaz M, et al. Dynamic-metasurface-based cavity structures for

enhanced absorption and phase modulation[J]. Acs Photonics, 2018, 6(2): 374-381.

[258] Chu C H, Tseng M L, Chen J, et al. Active dielectric metasurface based on phase-change medium[J]. Laser & Photonics Reviews, 2016, 10(6): 986-994.

[259] Liu X, Wang Q, Zhang X, et al. Thermally dependent dynamic meta-holography using a vanadium dioxide integrated metasurface[J]. Advanced Optical Materials, 2019, 7(12): 1900175.

[260] Miao Z, Wu Q, Li X, et al. Widely tunable terahertz phase modulation with gate-controlled graphene metasurfaces[J]. Physical Review X, 2015, 5(4): 041027.

[261] Wu P C, Papasimakis N, Tsai D P. Self-affine graphene metasurfaces for tunable broadband absorption[J]. Physical Review Applied, 2016, 6(4): 044019.

[262] Yao W, Tang L, Wang J, et al. Spectrally and spatially tunable terahertz metasurface lens based on graphene surface plasmons[J]. IEEE photonics journal, 2018, 10(4): 1-8.

[263] Xu M, Liang T, Shi M, et al. Graphene-like two-dimensional materials[J]. Chemical reviews, 2013, 113(5): 3766-3798.

[264] Dabidian N, Kholmanov I, Khanikaev A B, et al. Electrical switching of infrared light using graphene integration with plasmonic Fano resonant metasurfaces[J]. Acs Photonics, 2015, 2(2): 216-227.

[265] Li L, Jun Cui T, Ji W, et al. Electromagnetic reprogrammable coding-metasurface holograms[J]. Nature communications, 2017, 8(1): 1-7.

[266] Wu L W, Ma H F, Wu R Y, et al. Transmission-Reflection Controls and Polarization Controls of Electromagnetic Holograms by a Reconfigurable Anisotropic Digital Coding Metasurface[J]. Advanced Optical Materials, 2020, 8(22): 2001065.

[267] Chen K, Feng Y, Monticone F, et al. A reconfigurable active huygens' metalens[J]. Advanced materials, 2017, 29(17): 1606422.

[268] Wu P C, Zhu W, Shen Z X, et al. Broadband wide-angle multifunctional polarization converter via liquid-metal-based metasurface[J]. Advanced Optical Materials, 2017, 5(7): 1600938.

[269] Chen J, Wang K, Long H, et al. Tungsten disulfide–gold nanohole hybrid metasurfaces for nonlinear metalenses in the visible region[J]. Nano Letters, 2018, 18(2): 1344-1350.

[270] Kim M K. Digital holographic microscopy[M]//Digital Holographic Microscopy. Springer, New York, NY, 2011: 149-190.

[271] Wang Z, Ding X, Zhang K, et al. Huygens metasurface holograms with the modulation of focal energy distribution[J]. Advanced Optical Materials, 2018, 6(12): 1800121.

Biography and Publications

1. Biography

I was born on 11 April, 1993 in Xinzhou, Shanxi Province, China. I am in the framework of the double degree agreement of University Paris-Saclay and Xidian University.

2. Education

2012.08～2016.07 Shandong University of Science and Technology, Bachelor, Communication Engineering

2016.08～2018.07 Xidian University，Master，Communication and Information Systems

2018.08～2022.07 Xidian University，PhD，Communication and Information Systems

2018.08～2022.05 Université Paris-Saclay，PhD，Electrical, electronics, photonics and systems engineering

3. Research results

3.1 Publications

Journal Publication:

[1] Guan C, **Feng R**, Ratni B, et al. Broadband tunable metasurface platform enabled by dynamic phase compensation[J]. Optics Letters, 2022, 47(3): 573-576.

[2] **Feng R**, Ratni B, Yi J, et al. Reprogrammable Digital Holograms and Multibit Spatial Energy Modulation Using a Reflective Metasurface[J]. ACS Applied Electronic Materials, 2021, 3(12): 5272-5277.

[3] **Feng R**, Ratni B, Yi J, et al. Versatile metasurface platform for electromagnetic wave tailoring[J]. Photonics Research, 2021, 9(9): 1650-1659.

[4] **Feng R**, Ratni B, Yi J, et al. Flexible Manipulation of Bessel-Like Beams with a Reconfigurable Metasurface[J]. Advanced Optical Materials, 2020, 8(23): 2001084.

[5] **Feng R**, Ratni B, Yi J, et al. Versatile Airy-beam generation using a 1-bit coding

programmable reflective metasurface[J]. Physical Review Applied, 2020, 14(1): 014081.

[6] **Feng R**, Ratni B, Yi J, et al. Electronically-engineered metasurface for directional beaming of electromagnetic waves through a subwavelength aperture[J]. Optics express, 2019, 27(24): 35774-35783.

[7] Yi J, Cao X, **Feng R**, et al. All-dielectric transformed material for microwave broadband orbital angular momentum vortex beam[J]. Physical Review Applied, 2019, 12(2): 024064.

[8] Yi J, Guo M, **Feng R**, et al. Design and validation of an all-dielectric metamaterial medium for collimating orbital-angular-momentum vortex waves at microwave frequencies[J]. Physical Review Applied, 2019, 12(3): 034060.

[9] Yi J, Li D, **Feng R**, et al. Design and validation of a metasurface lens for converging vortex beams[J]. Applied Physics Express, 2019, 12(8): 084501.

[10] **Feng R**, Yi J, Burokur S N, et al. Orbital angular momentum generation method based on transformation electromagnetics[J]. Optics express, 2018, 26(9): 11708-11717.

[11] Liu T, **Feng R**, Yi J, et al. All-dielectric transformation medium mimicking a broadband converging lens[J]. Optics Express, 2018, 26(16): 20331-20341.

[12] Yi J, Campbell S D, **Feng R**, et al. Realizable design of field taper via coordinate transformation[J]. Optics express, 2018, 26(1): 505-515.

International Conference：

[1] **Feng R**, Zhang H, Ratni B, et al. Tailoring Airy Beam from a Two-Dimensional Dynamic Metasurface[C]//2021 IEEE International Symposium on Antennas and Propagation and USNC-URSI Radio Science Meeting (APS/URSI). IEEE, 2021: 327-328.

[2] **Feng R**, Ratni B, Yi J, et al. Design and Experimental Characterization of a Two-Dimensional Reconfigurable Metasurface[C]//2021 15th European Conference on Antennas and Propagation (EuCAP). IEEE, 2021: 1-4.

[3] **Feng R**, Ratni B, Yi J, et al. Flexible Vortex Beam Generation Utilizing a Two-Dimensional Dynamic Metasurface[C]//2021 Fifteenth International Congress on Artificial Materials for Novel Wave Phenomena (Metamaterials). IEEE, 2021: 073-075.

[4] **Feng R**, Ratni B, Yi J et al. Metamirror for generation and control of Airy beams,

International Conference on Metamaterials, Photonic Crystals and Plasmonics, (Warsaw) Poland, July, 2021.

[5] **Feng R**, Ratni B, Yi J, et al. Generation and Control of Bessel Beam with a Reconfigurable Metasurface[C]//2020 IEEE International Symposium on Antennas and Propagation and North American Radio Science Meeting. IEEE, 2020: 959-960.

[6] **Feng R**, Ratni B, Yi J, et al. Reconfigurable Metasurface for Airy Beam Generation[C]//2020 IEEE International Symposium on Antennas and Propagation and North American Radio Science Meeting. IEEE, 2020: 851-852.

[7] **Feng R**, Ratni B, Yi J, et al. Phase-Gradient Metasurfaces for Efficient Conversion of Surface Wave to Propagating Wave[C]//2020 14th European Conference on Antennas and Propagation (EuCAP). IEEE, 2020: 1-5.

[8] **Feng R**, Ratni B, Yi J, et al. Metamirror for Generation and Control of Bessel Beam[C]//2020 Fourteenth International Congress on Artificial Materials for Novel Wave Phenomena (Metamaterials). IEEE, 406-408.

[9] **Feng R**, Ratni B, Yi J, et al. Transmission of Electromagnetic Waves through a Subwavelength Slit using a Reconfigurable Phase-Gradient Metasurface[C]//2020 International Workshop on Antenna Technology (iWAT). IEEE, 2020: 1-4.

[10] **Feng R**, Zhu L, Yi J, et al. Space Transformation for Vortex Beam Generation[C]//2018 IEEE International Symposium on Antennas and Propagation & USNC/URSI National Radio Science Meeting. IEEE, 2018: 943-944.

[11] **Feng R**, Yi J, Zhang H. et al. All-dielectric vortex beam converging lens, 2018 Biennial IEEE Conference on Electromagnetic Field Computation, Hangzhou (China), October, 2018.

[12] **Feng R**, Yi J, Zhang H. et al. Space transformation based multi-beam generation lens antenna, 8th International Conference on Metamaterials, Photonic Crystals and Plasmonics (META'17), Incheon (Korea), July, 2017.

3.2 Patents

[1] Method for designing orbital angular momentum vortex electromagnetic wave generating device: Yi J, **Feng R**, Cao X, Meng Y, Huang J, Zhang H, (201810233261.6), authorized；

[2] A device for vortex wave generation: Yi J, Cao X, **Feng R**, Meng Y, Zhang H, (201711350241.9), authorized；

[3] A device for vortex wave convergence: Yi J, Meng Y, Zhang H, Liang X, Cao X, **Feng R** (201810119942.X), authorized;

[4] A device for mode transformation of vortex wave: Yi J, **Feng R**, Cao X, Meng Y, Zhang H, (201810297114.5), unauthorized；

université PARIS-SACLAY

DOCTORAL SCHOOL
Electrical, Optical, Bio: Physics and Engineering (EOBE)

Titre : Métasurfaces reconfigurables pour le contrôle des fronts d'onde - Application à la génération de faisceaux complexes

Mots clés : métasurface reconfigurable, rayonnement directionnel, faisceaux non-diffractants, imagerie holographique faisceau vortex

Résumé : En raison de leur capacité à contrôler les ondes électromagnétiques, les métasurfaces ont suscité d'énormes intérêts en recherche au cours de ces deux dernières décennies. Cependant, la plupart des travaux concernent des métasurfaces passives qui ne permettent, dans la majorité des cas, qu'une seule fonctionnalité et qui fonctionnent sur une bande de fréquences étroite. Cette thèse de doctorat vise à fournir une flexibilité dans le contrôle des fronts d'onde grâce à la conception de métasurfaces reconfigurables. Les travaux ont été réalisés conjointement à l'Université Paris-Saclay et Xidian University. Dans un premier temps, des métasurfaces électroniquement reconfigurables incorporant des diodes varactor sont développées. Ensuite, plusieurs fonctionnalités de contrôle d'ondes électromagnétiques sont mises en œuvre et validées expérimentalement. Le rayonnement directionnel d'ondes électromagnétiques à travers une ouverture sub-longueur d'onde et où la direction du rayonnement peut être contrôlée, est réalisé avec succès à différentes fréquences.

Des plaques de phase permettant de générer des faisceaux non-diffractants d'Airy et de Bessel d'ordre zéro et des faisceaux vortex sont également implémentées en utilisant les métasurfaces reconfigurables conçues. Dans le cas des faisceaux vortex transportant un moment cinétique orbital, des propriétés de focalisation et de non-diffraction sont de plus superposées aux faisceaux vortex, générant des faisceaux vortex focalisés et non-diffractants et validant ainsi la polyvalence des métasurfaces reconfigurables proposées. De plus, la génération simultanée de quatre faisceaux vortex focalisés dans différentes directions est aussi réalisé. Enfin, trois types d'images holographiques, comprenant des points focaux, des nombres et des lettres de l'alphabet, et le codage d'énergie spatiale multibits dans différents canaux sont réalisés en se basant sur l'algorithme pondéré de Gerchberg-Saxton. Le mécanisme de reconfigurabilité permet d'implémenter plusieurs fonctions dans une seule métasurface, tout en ayant une certaine flexibilité dans le fonctionnement en fréquence.

Title : Reconfigurable metasurfaces for wavefronts control - Application to the generation of complex beams

Keywords : Reconfigurable metasurface, directional beaming, non-diffractive beams, holographic imaging, vortex beam

Abstract : Due to their capability to control electromagnetic waves, metasurfaces have attracted enormous research interests these last two decades. Nevertheless, most of the works concern passive metasurfaces which allow, in most cases, only a single functionality and operate on a narrow frequency band. This PhD thesis aims at providing flexibility in wavefronts control through the design of reconfigurable metasurfaces. The works have been done jointly between Université Paris-Saclay and Xidian University. In a first step, electronically reconfigurable metasurfaces incorporating varactor diodes are developed. Then, several functionalities for controlling electromagnetic waves are implemented and experimentally validated. Directional beaming of electromagnetic waves through a subwavelength aperture where the radiation direction can be controlled is successfully performed at different frequencies.

Phase plates allowing to generate diffraction-free Airy beams and zeroth-order Bessel beams and vortex beams are also implemented utilizing the designed reconfigurable metasurfaces. In the case of the vortex beams carrying orbital angular momentum, focusing and non-diffracting features are further superposed to the vortex beams, producing the focusing vortex beams and non-diffracting vortex beams and validating the versatility of the designed reconfigurable metasurface. Furthermore, the simultaneous generation of four focusing vortex beams in different directions is also achieved. Finally, three types of holographic images, including focusing spots, Arabic numbers, and Alphabet letters, and multibit spatial energy coding in different channels are realized based on the weighted Gerchberg-Saxton algorithm. The reconfigurability mechanism allows to implement several functionalities in a single metasurface, while having a certain flexibility in frequency operation.